

THE APPLICATION OF
SATELLITE RADAR INTERFEROMETRY
TO THE STUDY OF LAND SUBSIDENCE
OVER DEVELOPED AQUIFER SYSTEMS

A DISSERTATION
SUBMITTED TO THE DEPARTMENT OF GEOPHYSICS
AND THE COMMITTEE ON GRADUATE STUDIES
OF STANFORD UNIVERSITY
IN PARTIAL FULFILLMENT OF THE REQUIREMENTS
FOR THE DEGREE OF
DOCTOR OF PHILOSOPHY

Jörn Hoffmann
January 2003

© Copyright by Jörn Hoffmann 2003
All Rights Reserved

I certify that I have read this dissertation and that, in my opinion, it is fully adequate in scope and quality as a dissertation for the degree of Doctor of Philosophy.

Howard A. Zebker
(Principal Adviser)

I certify that I have read this dissertation and that, in my opinion, it is fully adequate in scope and quality as a dissertation for the degree of Doctor of Philosophy.

Steven M. Gorelick

I certify that I have read this dissertation and that, in my opinion, it is fully adequate in scope and quality as a dissertation for the degree of Doctor of Philosophy.

Mark D. Zoback

Approved for the University Committee on Graduate Studies:

Abstract

This dissertation investigates the application of interferometric synthetic aperture radar (InSAR) to the measurement and interpretation of surface displacements over developed aquifer systems. Land subsidence over developed groundwater systems has been observed in a wide variety of hydrogeologic settings worldwide. The phenomenon can be explained with elastic and inelastic deformation of water-bearing material at depth in response to declining pore pressures. The lack of observational data has made it difficult in the past to define the extent of the deforming areas, the magnitude of the surface displacements, and the time-history of the deformation process accurately. Consequently, this has also generally precluded the estimation of aquifer system storage or flow parameters, which relate the surface subsidence to the subsurface pore pressure changes.

The development of InSAR techniques using satellite radar data now provides the ability to map surface displacements with centimeter to millimeter precision over extensive areas with great spatial detail (10s of meters). I have used InSAR data to derive detailed maps of the time-varying surface displacement fields over the Las Vegas Valley, Nevada and Antelope Valley, California aquifer systems during several years in the 1990s. The achieved measurement accuracy in the two study areas was typically better than 1cm and was limited primarily by the effect of tropospheric signal delays in the radar images. The availability of satellite acquisitions from closely spaced orbits in the existing data catalog constrains the temporal sampling to 35 days or longer for ERS data.

For both aquifer systems studied the InSAR observations enabled a detailed and spatially complete characterization of the highly heterogeneous displacement fields. The structure of the observed subsidence in many cases reflected known or previously

unknown subsurface structure such as faults or changes in sediment thickness, emphasizing the value of these displacement maps in delineating subsurface units. A comparison of surface displacements derived from SAR data realizing different viewing geometries over Antelope Valley indicated that surface displacements related to inelastic compaction of compressible units in the aquifer system are primarily vertical, which has been a widely used, albeit hitherto generally untested assumption in basin-scale studies of land subsidence.

The observed displacement fields were temporally highly variable, reflecting the effects of both seasonal fluctuations and long-term trends of the stresses in the aquifer systems. By combining independent information on these stress variations with InSAR observations of the surface displacements I was able to estimate spatially variable storage parameters for the heterogeneous aquifer systems.

Using a one-dimensional compaction model I interpreted InSAR surface displacement observations in Las Vegas Valley in conjunction with water-level observations to estimate spatially varying aquifer system elastic skeletal storage coefficients between $4.2 \cdot 10^{-4}$ and $3.4 \cdot 10^{-3}$ in the elastically deforming parts of the aquifer system.

In the Antelope Valley aquifer system the drainage of thick low-conductivity units is delayed with respect to the drawdowns in the aquifers, causing continuing land subsidence for many years after the hydraulic head declines have ceased. I estimated inelastic skeletal storage coefficients up to 0.09 and compaction time constants for interbed compaction between 3 and 285 years in a three-dimensional groundwater flow and subsidence (MODFLOW) model. The parameter estimation was constrained both by InSAR subsidence observations and historical benchmark data.

I investigated the sensitivity of the parameter inversion to the accuracy and frequency of the subsidence observations and the stress changes in the aquifer system in a set of numerical simulations. The results indicated that InSAR-derived displacement maps are well suited to provide the displacement observations necessary to estimate storage parameters. However the parameter estimation proved to be severely limited by the poor reliability of subsurface pore pressure change estimates in regional aquifer systems.

This work is the first use of InSAR technology to investigate the time-dependent

deformation processes in developed aquifer systems; here I employ InSAR-derived displacement data to estimate spatially variable aquifer system parameters. Where applicable, InSAR provides a powerful tool for characterizing and simulating aquifer systems, which often are an important resource to the local communities.

Acknowledgements

Many people can justly claim partial responsibility for this dissertation. I gladly take the opportunity to acknowledge those who have helped me along the way and made this work possible through their tireless advice, comments, thought and support.

Howard A. Zebker has been an invaluable source of advice throughout the five years in which I have had the privilege of being his student. His profound knowledge of radar interferometry and his accessible character have made my studies at Stanford enjoyable and fruitful. While always being available for questions and discussion Howard has also given me plenty of room for trying out my ideas.

Much of my work would have foundered without the advice of Devin L. Galloway, whose keen interest and insightful suggestions have led me to develop new ideas and encouraged me to attempt the next step on several occasions. He has also been very helpful in directing me to others for further advice.

I thank Steven M. Gorelick for causing me numerous headaches during the early stages of this work, in retrospect, saving me from full-blown migraines. His inquisitive and initially quite critical approach to my work have forced me more than once to reconsider things or investigate a problem in more detail in order to steel myself for further discussions. Not only has this helped improve the work itself, but it has taught me a valuable lesson, for which I am indebted to Steve.

My work on the Las Vegas Valley aquifer system was inspired by previous work by Falk Amelung. Falk has helped me to get started by providing me with some of his data and offering advice during my initial tentative steps. Michael T. Pavelko and Randell J. Laczniaik provided me with water level data for Las Vegas Valley and offered helpful discussions of my work.

With respect to my work on Antelope Valley I am grateful to Steven Phillips

and David Leighton for providing me with their MODFLOW model, which I relied on heavily. They also provided me with data on water levels and historic subsidence measurements, and patiently answered my many questions regarding their groundwater flow model. Stanley Leake provided me with his IBS2 package, which was critical in conducting my work on Antelope Valley.

Much of my inspiration during my time at Stanford has stemmed from my interactions with the faculty and fellow students. I am glad to have had the opportunity to meet Sigurjón Jónsson, with whom I have not merely shared an office for five years, but who has also been a great first line of defense for me to bounce ideas off. Countless hours of discussions lasting from triple espressi to margaritas have part of the foundations of this dissertation and a lasting friendship.

Weber Hoen, Curtis Chen, Leif Harke, and Ramon Hanssen have also helped me with various aspects of this work.

I thank Mark D. Zoback for serving on my reading committee, and the Geophysics faculty, students and staff for creating the stimulating environment that I have enjoyed in the Geophysics department.

This work has been made possible through the generous support of several institutions. I have been fortunate to be a scholar of the German National Merit Foundation. Most of this work has been supported by NASA Headquarters under Earth System Science Fellowship Grant NGT5-30342. Additional funds were provided by the Stanford University Department of Geophysics and the Cecil Green Fellowship.

Working at Stanford has provided opportunities for me that extended far beyond my academic pursuits. I have had the privilege and pleasure to meet many wonderful people, several of whom have become good friends. Special thanks go to John Townsend, whose friendship has been an invaluable asset during the past few years. He has tirelessly helped me out in any aspect of the English language and often offered me good advice, taking a deep interest in my work. I also want to thank Darcy Karakelian, Eva Zanzerkia, Björn and Lena Lund, Rosalind Archer, Colin Doyle, and John Harrison for helping me live a life outside the office. I am grateful for the support of my family, my parents Ingrid Pahl-Hoffmann and Klaus Hoffmann, and my sisters Anke, Katja and Sarah.

Finally, I want to thank my wife Teresa for her loving support and patience. I hope she will forgive me the evenings and weekends that fell victim to this dissertation.

Contents

Abstract	v
Acknowledgements	ix
1 Introduction	1
1.1 Objective and contributions	5
1.2 Outline	6
2 Theoretical background	9
2.1 Aquifer system compaction and land subsidence	9
2.1.1 Measurement of land subsidence	10
2.1.2 Aquifer system deformation	11
2.1.3 Other mechanisms for surface displacements	22
2.2 InSAR - Background	26
2.2.1 InSAR fundamentals	28
2.2.2 Error contributions in InSAR-observed surface displacements .	33
3 Seasonal subsidence and rebound in Las Vegas Valley, Nevada	49
3.1 Introduction	49
3.2 InSAR observations	53
3.2.1 Time series analysis	53
3.2.2 Horizontal surface displacements	63
3.3 Accuracy	67
3.4 Estimation of aquifer system storage coefficients	71
3.5 Discussion	76

3.5.1	Seasonal deformations	77
3.5.2	Land subsidence from December 1997 to January 1999	78
3.5.3	Elastic storage coefficient estimates	79
3.5.4	Comparison of InSAR and extensometer measurements	80
3.6	Conclusions	83
4	Subsidence observations and estimation of parameters governing inelastic compaction in Antelope Valley, California	87
4.1	Introduction	87
4.1.1	The lay of the land	88
4.1.2	Historical settlement and water development	90
4.1.3	Description of the aquifer system	93
4.2	Subsidence observations	95
4.2.1	Recent subsidence observations from InSAR and borehole extensometer data	95
4.2.2	Historical subsidence observations from repeated benchmark surveys	101
4.3	Parameter estimation	106
4.3.1	The MODFLOW model	107
4.3.2	Simulation of compaction	109
4.3.3	Setting up the inverse model	113
4.3.4	Notes on the reliability of the resulting parameter estimates	120
4.4	Results	121
4.4.1	Final parameter estimates	121
4.4.2	Model fit	125
4.4.3	Aquifer heads	130
4.4.4	Results using kriged aquifer heads	131
4.5	Conclusions	138
5	Limitations in estimating inelastic compaction parameters	143
5.1	Introduction	143
5.2	Description of the simulated scenarios	145

5.3	Results	147
5.4	Conclusions	153
6	Horizontal displacements in Antelope Valley, California from ascending and descending SAR acquisitions	155
6.1	Sensitivity to horizontal displacements	156
6.2	Displacement estimation	159
6.2.1	Available SAR acquisitions	159
6.2.2	Estimating displacements from several interferograms	160
6.3	Comparison of ascending and descending images	165
7	Conclusions	175
7.1	Results and implications	175
7.2	Future research and applications	178
7.3	Closing remarks	179
A	Details of the Antelope Valley groundwater flow model	181
A.1	Model grid	182
A.2	Flow properties	183
A.2.1	Horizontal groundwater flow	183
A.2.2	Vertical groundwater flow	183
A.2.3	Storage	186
A.3	In- and outflow	192
A.3.1	Evapotranspiration	192
A.3.2	Recharge	192
A.3.3	Groundwater pumping	192
A.3.4	Irrigation return	194
A.4	Starting heads	194

List of Tables

2.1	Parameters for ERS data	27
3.1	Displacement magnitudes at 8 locations in Las Vegas Valley	59
3.2	Data used to study horizontal displacements	64
3.3	Atmospheric data for Las Vegas	66
3.4	Estimates of the elastic storage coefficient	75
4.1	Radar scenes used in Antelope Valley	96
4.2	Variogram sills used for kriging of benchmark data	103
4.3	Parameters required for IBS1 and IBS2/SUB	110
4.4	Number of estimated parameters	113
4.5	Constant SUB input parameters	117
4.6	Time constants estimated for Antelope Valley using simulated heads .	121
4.7	Time constants estimated for Antelope Valley using kriged heads . . .	137
5.1	Summary of interbed parameters at eight simulated locations	146
5.2	Summary of different simulated drawdown scenarios	147
6.1	Ascending interferograms used to study horizontal displacements . . .	160
6.2	Descending interferograms used to study horizontal displacements . .	161

List of Figures

2-1	Examples for subsidence-related damages	10
2-2	Benchmark and extensometer	11
2-3	Sketch of deforming aquifer system	12
2-4	Fissure in Antelope Valley	14
2-5	Compaction in layer due to step head decline	17
2-6	Idealized stress-strain relation	20
2-7	Typical tectonic displacement patterns	24
2-8	Surface displacements for shallow and deep compacting reservoirs	25
2-9	InSAR baseline geometry	30
2-10	Flow diagram of image processing	32
2-11	Example of temporal decorrelation	38
2-12	Examples of atmospheric disturbance signals	43
3-1	Location map of Las Vegas Valley	50
3-2	Interferometric baselines	54
3-3	Summer displacements in Las Vegas Valley	57
3-4	Winter displacements in Las Vegas Valley	58
3-5	Annual displacements in Las Vegas Valley	60
3-6	Displacement histories at three locations in Las Vegas Valley	62
3-7	Ascending and descending interferograms	65
3-8	Ascending and descending interferograms after correction	66
3-9	Displacements along three profiles in ascending and descending interferograms	68
3-10	Stress-strain plots at 6 well locations	73

3-10	Stress-strain plots at 6 well locations (continued)	74
3-11	Comparison of displacements derived from extensometer and InSAR data	81
4-1	Location map of Antelope Valley	89
4-2	Groundwater pumpage in Antelope Valley during 1915-95	91
4-3	Generalized cross-section of the Antelope Valley aquifer system	94
4-4	Interferogram time-series showing subsidence between 1996 and 1999	97
4-5	Interferograms formed for Antelope Valley	98
4-6	Two long-term interferograms	99
4-7	Comparison of surface displacements derived from InSAR and extensometer measurements	102
4-8	Experimental semivariograms for benchmark subsidence data	104
4-9	Maps of historical subsidence in Antelope Valley	105
4-10	Compaction 1995-99 simulated by Leighton and Phillips-model	108
4-11	Parameter zones used for estimation of compaction time constants	112
4-12	Flow-chart of parameter estimation	114
4-13	Estimated compaction time constants and inelastic skeletal storage coefficients	121
4-14	Cost as a function of time constants	123
4-15	Comparison of estimated storage coefficients with clay thickness estimate	124
4-16	Comparison of simulated subsidence with subsidence derived from benchmark observations	126
4-17	Comparison of simulated subsidence with subsidence derived from InSAR observations	127
4-18	Subsidence history at four locations	129
4-19	Well locations used to krig aquifer head	133
4-20	Variogram model for kriging of aquifer heads	134
4-21	Comparison of simulated and kriged hydraulic heads	135
4-22	Comparison of simulated and kriged drawdowns	136
4-23	Root-mean-square difference between kriged and simulated heads	137

4-24	Estimated parameters using kriged heads	137
4-25	Estimate for total S_{kv}^* error	139
5-1	Drawdown locations in Antelope Valley model	145
5-2	Objective functions for different head histories in inversion	148
5-3	Drawdowns scenarios 1-5 at eight locations	149
5-4	Drawdown scenarios 6-9 at eight locations	150
5-5	Drawdown scenarios 10-13 at eight locations	151
6-1	Sensitivity to horizontal displacements as a function of azimuth	158
6-2	Ascending and descending acquisitions and interferograms	159
6-3	Relationship between variances of wrapped and unwrapped phase values	164
6-4	Comparison of ascending and descending observations	166
6-5	Comparison of observations over subsidence bowl	168
6-6	Difference between displacement maps	169
6-7	Normalized differences and statistical significance	170
6-8	Displacements along profile A	171
6-9	Displacements along profile B	172
6-10	Displacements along profile C	173
A-1	IBOUND Arrays	182
A-2	Horizontal flow properties	184
A-3	Vertical flow properties	185
A-4	Specific yield, layer 1	186
A-5	Aquifer storage coefficients	187
A-6	Interbed storage, layer 1	189
A-7	No-delay interbed storage, layer 2	190
A-8	Delay interbed storage, layer 2	191
A-9	Groundwater recharge	193
A-10	Total withdrawals from wells	193
A-11	Starting heads	195

Chapter 1

Introduction

The growth of populations and agricultural activity in many arid and semi-arid regions worldwide have increased the importance of locally available groundwater resources over the last several decades. As the available surface water supplies have become insufficient to satisfy the growing demand for freshwater people have turned to the subsurface for additional water resources. Large aquifer systems underlying the often rapidly expanding centers of economic activity contain an estimated 30% of the global freshwater resources – about 100 times more than what is accounted for by lakes and rivers. Given that almost 70% of the global freshwater resources are in polar ice caps, glaciers and permanent snow cover, groundwater is by far the most important freshwater reservoir available to meet today's growing water needs.

The increasing reliance of irrigation agriculture and domestic water supply on water pumped from aquifers has in many cases led to aquifer system overdraft, as the volume of water pumped from the ground has exceeded natural recharge over extended periods of time. The resulting adverse effects have included declining hydraulic heads, water quality problems and the destruction of ecosystems. Meanwhile, the compaction of aquifer systems accompanying extensive drawdowns of hydraulic heads is a commonly observed but frequently neglected effect of groundwater development.

Widespread subsidence of the land surface has been observed in association with the development of groundwater resources in unconsolidated alluvial groundwater basins worldwide. It is an expression of often irrecoverable deformation in aquifer

systems that indicates a permanent reduction of aquifer system storage. Despite considerable damage to manmade structures such as well casings, railways, aqueducts, buildings or drainage systems, land subsidence has remained one of the least studied adverse impacts of groundwater development. In several low-lying coastal areas such as Houston, Texas or the Santa Clara Valley, California land subsidence has become the primary constraint to groundwater development [Galloway et al., 1999]. However, land subsidence in the affected areas is not merely a concern for engineers, but is an observable quantity containing valuable information about the physical properties of the material constituting the aquifer system at depth. Deformation of the porous materials constituting the aquifer system often accounts for most of the water pumped from confined aquifers. The compressibility of the aquifer system materials consequently determines their storage capacity. To assess the volume of water available in an aquifer system accurately, its mechanical properties must therefore be understood. The direct measurement of deformations in aquifer systems at depth is technically difficult and too expensive to be feasible at more than very few point locations. But even the accurate measurement of displacements at the land surface above deforming aquifer systems have been historically labor-intensive and consequently expensive to acquire. Analyses of land subsidence observations in terms of aquifer system properties have therefore generally been restricted to one or few point locations. The development of satellite radar interferometry (InSAR) and the recent availability of widely acquired data from civilian satellite missions now provide unprecedented opportunities to study land subsidence. In this dissertation I discuss the application of InSAR to the detection, monitoring and interpretation of land subsidence caused by aquifer system deformation.

The theoretical basis for aquifer system deformation due to pore pressure changes has historically been developed in different fields. Terzaghi [1925], a soil engineer by training, developed the ubiquitous (in aquifer mechanics) principle of effective stress. An investigation prompted by a lawsuit concerning land subsidence produced by oil and gas production in Galveston Island, Texas granted the principle legal recognition [Pratt and Johnson, 1926] identifying compaction of clay units due to decreasing

pressures as the cause of about 1 m of surface subsidence. Several hydrologic investigations over the 20th century [Meinzer, 1928; Jacob, 1940; Tolman and Poland, 1940; Riley, 1969; Helm, 1975] helped develop what is now often referred to as the aquitard-drainage model (see Holzer [1998] for a description of the theory and development). Jorgensen [1980] related this theory to equivalent equations in the field of soil mechanics. Though poroelastic theory has been formulated for three-dimensional isotropic [Biot, 1941] and anisotropic [Biot, 1955; Carroll, 1979] media, the one-dimensional theory of the aquitard-drainage model remains the most widely used to interpret aquifer system compaction (see section 2.1).

Numerical techniques to simulate aquifer system compaction have been developed as digital computers have become widely available and affordable [e.g. Gambolati, 1970, 1972a,b; Gambolati and Freeze, 1973; Helm, 1975, 1976; Narasimhan and Witherspoon, 1977; Neuman et al., 1982]. Leake and Prudic [1991] developed a package to simulate interbed compaction for use with the widely used groundwater flow simulator MODFLOW [McDonald and Harbaugh, 1988; Harbaugh et al., 2000], which has now been superseded for MODFLOW-2000 by the subsidence package (SUB) [Hoffmann et al., 2003b], formulated by Leake [1990]. Notwithstanding these developments of the simulation tools, field-scale investigations of land subsidence in the past have been impaired by the aforementioned lack of observational subsidence data. It is in this context that the work described herein originates.

The development of new technologies has often preceded and enabled the evolution of scientific understanding. Advances in measurement techniques have spurred investigations that would have been impossible without these developments and have allowed testing of hypotheses that had remained untested for the lack of suitable data. Spaceborne synthetic aperture radar interferometry is an example of such a development. A large number of new and exciting investigations into a variety of processes causing extensive displacements of the land surface have employed InSAR data in addition to or replacing more conventional geodetic observations.

Interferometric synthetic aperture radar was developed during the second half of the 20th century. Although the first experiments used airborne systems and optical processing [Graham, 1974], the general availability of inexpensive digital computers

promoted the shift to digital processing techniques in the 1980s [Goldstein et al., 1985; Zebker and Goldstein, 1986]. The first space-borne data successfully used in radar interferometry were SEASAT data [Li and Goldstein, 1987, 1990; Prati and F., 1990; Goldstein et al., 1988] and later the space shuttle's SIR-B data [Gabriel and Goldstein, 1988]. These first applications mostly focused on the measurement of surface topography from the interferograms. The extremely successful European Remote Sensing satellites ERS-1 (launched in 1991) and ERS-2 (1995) missions acquired data extensively used for a wide range of interferometric applications (section 2.2.1).

Galloway et al. [1998] first applied InSAR to the observation of land subsidence over an aquifer system, explaining observed subsidence as compaction of compressible sediments caused by declining groundwater levels. More recently, Amelung et al. [1999] presented InSAR subsidence observations of Las Vegas Valley, Hoffmann et al. [2001] (see Chapter 3) first studied seasonal subsidence signals, and Bawden et al. [2001] and Watson et al. [2002] discovered large seasonal subsidence signals masking tectonic deformation signals in the Santa Ana basin.

Probably the single most interesting property of InSAR measurements is their extensive spatial coverage at very high spatial resolution. A satellite system such as the SAR on ERS-1 and ERS-2 acquires imaging data at a resolution on the order of 10 meters over areas of 10,000 square kilometers. Where other surveying technologies have only provided point measurements, InSAR now enables spatially detailed mapping of surface deformation. Most successful applications of InSAR measurements have focused on interpreting spatially variable displacement fields, that previously were difficult or impossible to characterize by other observational techniques. Finally, another important advantage of using spaceborne satellite imaging has received more and more attention over the past few years:

The ability to make observations at the orbit repeat periods can be used to compile time series measurements of deformation patterns. I capitalize on both of these capabilities to apply InSAR observations to the study of subsidence patterns over aquifer systems.

1.1 Objective and contributions

Both complete spatial mapping and time-series information make InSAR data promising for the study of developed aquifer systems undergoing deformation in response to changing pore pressures or hydraulic heads. The inherent heterogeneity of aquifer systems requires spatially distributed parameter estimates. These can best be obtained from spatially dense observations, such as the displacement measurements provided by InSAR. Furthermore, developed aquifer systems respond dynamically to spatial and temporal changes in pumping rates, and natural or artificial recharge. In the arid and semi-arid southwestern United States, as in any region characterized by unreliable surface water supplies, groundwater constitutes a vital and often vigorously exploited resource of the regional community and economy. Thus, monitoring and interpreting the responses to changes in water use is an integral and important part of managing the groundwater resources responsibly.

Because accurate observations of surface displacements have historically been sparse, so were studies using displacement measurements in investigations of aquifer systems. Though aquifer system deformation has been theoretically described and has been known to occur in many developed aquifer systems for almost a century, most investigations into water resources have neglected the phenomenon. It is thus the prime objective of this work to apply satellite InSAR observations to detect, characterize and interpret surface displacements caused by aquifer system deformation. The main questions addressed here are

1. What characteristics of aquifer system deformation can be detected successfully with InSAR?
2. What additional information can be derived from these observations of surface displacements regarding aquifer system properties?
3. What are the main limitations of applying InSAR to aquifer system characterization?

This work constitutes the first systematic investigation into the application of InSAR to aquifer system deformation. My main contribution has been to demonstrate

and develop the technique for aquifer system applications. Specifically, I have

- developed extensive time-series of displacement maps from InSAR observations for the two study areas, Las Vegas Valley, Nevada and Antelope Valley, California measuring and visualizing the spatial and temporal characteristics of ongoing land surface deformation in these regions.
- verified the measurement accuracy in these areas by comparison to other geodetic observations, where these were available and quantified the common error sources in interferometric measurements.
- for the first time used InSAR time-series observations in conjunction with measurements of groundwater head to estimate spatially variable elastic storage coefficients of an aquifer system. This represents the first systematic use of InSAR time-series data in geophysical analyses.
- developed an approach to the use of surface displacement observations to estimate inelastic storage coefficients using a calibrated numerical model of groundwater flow and land subsidence.
- investigated the occurrence of substantial horizontal surface displacement accompanying land subsidence, testing the commonly made assumption that these horizontal displacements are negligible.

1.2 Outline

The questions laid out in the previous section are addressed in the following six chapters of this dissertation. Chapter 2 presents the theoretical background of both the fundamentals of aquifer system mechanics and the InSAR technique. Section 2.1 introduces the theory of aquifer system deformation. Section 2.2 introduces the InSAR technique and discusses the most important limitations and error sources. Chapter 3 reports a study of land subsidence in Las Vegas Valley, Nevada. It presents several years of InSAR subsidence data and demonstrates the estimation of spatially variable

elastic storage coefficients using seasonal subsidence observations from InSAR and water-level observations in wells. Chapter 4 includes a study of ongoing land subsidence in Antelope Valley, California using InSAR observations. It also contains the description of a new approach combining historical (benchmark leveling) subsidence observations with recent InSAR observations and hydraulic heads simulated by a previously calibrated numerical groundwater flow model to estimate compaction time constants and inelastic storage coefficients for compacting interbeds in the aquifer system. Chapter 5 investigates the usefulness of InSAR data hypothetically available in the future using the estimation approach proposed in Chapter 4. Chapter 6 explores the occurrence of horizontal surface displacements accompanying long-term land subsidence in Antelope Valley. Finally, Chapter 7 summarizes the conclusions from this work in view of the questions put forth in section 1.1 and suggests avenues for future research.

Chapter 2

Theoretical background

2.1 Aquifer system compaction and land subsidence

Economic development and population growth has led to an increase in groundwater withdrawals from many aquifer systems. This development has often created a pronounced imbalance between water withdrawals and natural recharge, sometimes termed groundwater overdraft. Where groundwater withdrawals exceed recharge water is temporarily or permanently removed from storage in the system. Particularly in confined aquifer systems a large part of the storage can be due to the compressibility of the aquifer system materials. When water is produced from a compacting aquifer system or returned into storage causing expansion of the grain matrix the storage due to deformation of the aquifer system is an important part of the water budget.

Widespread aquifer system overdraft in the southwestern United States during much of the 20th century has resulted in large and often rapid declines in groundwater levels [e.g. Snyder, 1955]. It was soon recognized that the drawdowns of the groundwater levels were often accompanied by subsidence of the overlying land surface [Meinzer and Hard, 1925; Meinzer, 1928] as the removal of water from storage in compressible materials caused compaction of the aquifer system. A large number of case studies [e.g. Poland, 1984; Borchers, 1998; Galloway et al., 1999] have documented the global occurrence of this phenomenon. In some cases adverse effects of the subsiding land surface, such as increasing susceptibility to flooding or damage to drainage systems, wells or buildings (fig. 2-1), have made subsidence a primary constraint on groundwater development.

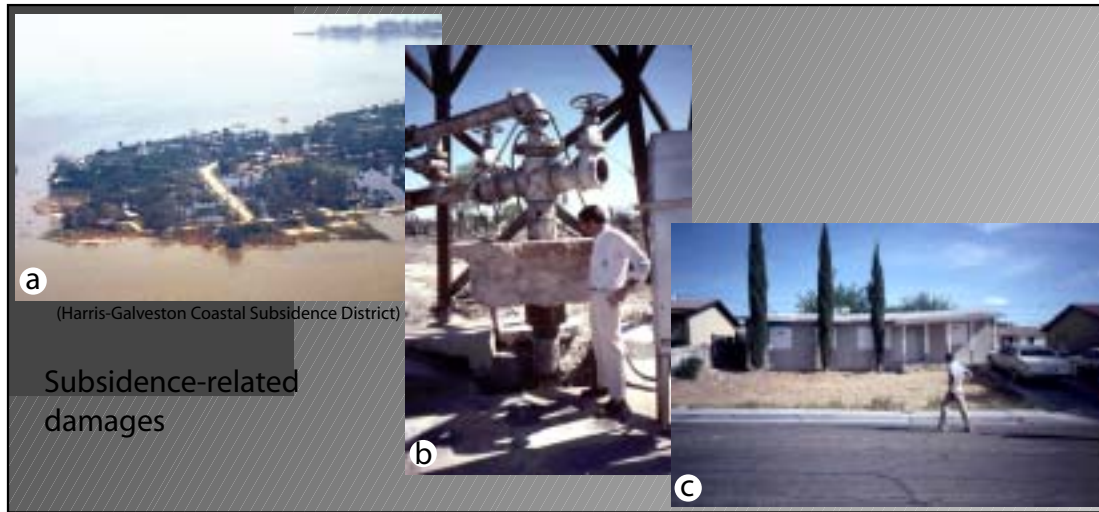


Figure 2-1: Examples for subsidence-related damages: (a) Flooding in Brownwood, Texas after hurricane Alicia (1983), (b) damaged wellhead in Las Vegas Valley (1997), and (c) damaged residential home in Windsor Park, Las Vegas Valley.

2.1.1 Measurement of land subsidence

Historically, land subsidence has been measured and monitored by repeatedly surveying geodetic benchmarks (fig. 2-2a) and contouring the elevation changes [e.g. Bell and Price, 1991; Ikehara and Phillips, 1994]. Recent investigations have also included elevation changes measured in GPS surveys [Ikehara and Phillips, 1994]. In some cases borehole extensometers (fig. 2-2b) have been installed to monitor aquifer system compaction continuously and with great accuracy. Recognizing the promise of using InSAR to measure land subsidence over compacting aquifer systems, Galloway et al. [1998] were the first to use an interferogram spanning two years from 1993 to 1995 to characterize the subsidence field in Antelope Valley, California. Amelung et al. [1999] presented subsidence maps for Las Vegas Valley, Nevada and noticed fluctuations in the subsidence rates during summer and winter seasons. This was analyzed in more detail by Hoffmann et al. [2001] (Chapter 3) using a large number of interferograms in a time-series analysis of the displacement field. This also represented the first time that InSAR subsidence observations were used to estimate aquifer system storage coefficients. Investigating surface displacements in the Santa Ana Basin, California

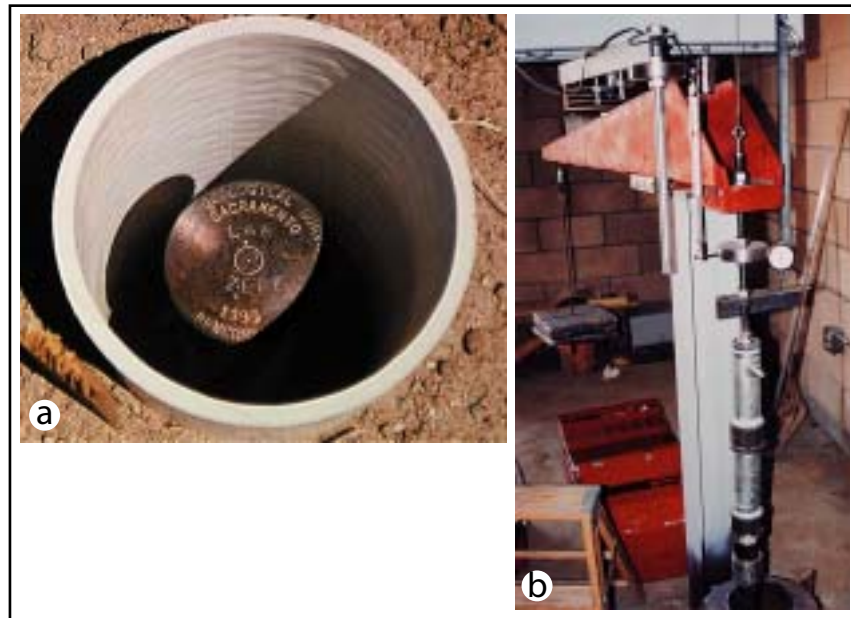


Figure 2-2: Benchmark (a) and extensometer (b) installed to monitor subsidence near Lancaster, Antelope Valley, California.

Bawden et al. [2001] and Watson et al. [2002] also found a seasonally fluctuating displacement field that corresponded to the seasonal pore pressure (pressure of the pore fluid) fluctuations induced by groundwater pumping. Hoffmann et al. [2003a] used InSAR-derived displacement maps to estimate inelastic storage coefficients and compaction time constants in a regional groundwater-flow and subsidence model for the Antelope Valley aquifer system in California.

2.1.2 Aquifer system deformation

The physical relationship between the displacements of the land surface measured by the various techniques and changes of the pore pressures in the aquifer system induced by groundwater pumping is presented in the remainder of this section. I focus here on land subsidence due to compaction in sedimentary aquifer systems as both aquifer systems studied for this dissertation fall into this category.

An unconsolidated sedimentary aquifer system typically constitutes a series of relatively flat lying aquifers interbedded with aquitards that confine fluid pressures

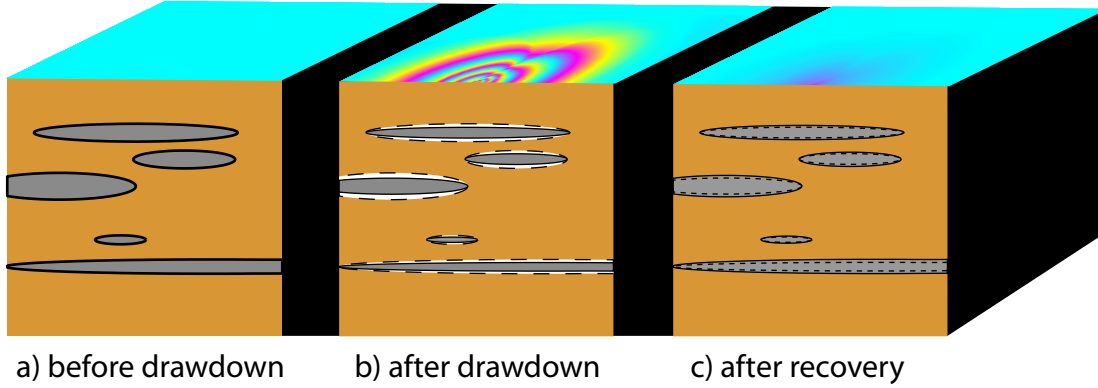


Figure 2-3: Sketch of deforming aquifer system. Highly compressible interbeds are interbedded with the usually less compressible aquifers. If drawdowns cause an increase in stress in the aquifer system, these interbeds compact, leading to land subsidence (b). Even if the head recovers to its previous level, the land surface does not return to its original location and only a comparatively small amount of uplift is measured at the land surface (c). Note that the color fringes at the surface in (b) and (c) indicate the surface displacements relative to the state at (a) and (b), respectively.

in the underlying aquifers. Land subsidence caused by the compaction of overdrafted aquifer systems occurs as a result of consolidation of aquitards (compressible silt and clay deposits) within the aquifer system. The aquifers usually consist of less compressible materials (sands, gravel), which do not yield as readily to stress changes and deform primarily elastically. This is shown schematically in figure 2-3.

Aquifer system materials deform under changes in effective stress, [Terzaghi, 1925]

$$\sigma'_{ij} = \sigma_{ij} - \delta_{ij}p, \quad (2.1)$$

where σ_{ij} are the components of the total stress tensor due to overburden and tectonic stresses, p is the pore pressure and δ_{ij} is the Kronecker delta function. Nur and Byerlee [1971] presented a modified version of 2.1,

$$\sigma'_{ij} = \sigma_{ij} - \tilde{\alpha}\delta_{ij}p, \quad \text{with} \quad \tilde{\alpha} = 1 - \frac{\tilde{B}}{\tilde{B}_s}, \quad (2.2)$$

where \tilde{B} and \tilde{B}_s are the bulk elastic moduli of the material matrix and the grains,

respectively. Equation 2.2 becomes identical to 2.1 if the bulk modulus of the grains becomes very large, i.e., the grains are incompressible. For typical aquifer system material, the coefficient $\tilde{\alpha}$ is very close to unity and equation 2.1 applies.

The Terzaghi principle of effective stress (eq. 2.1) states that for a constant total stress a change in pore pressure causes a change in effective stress of equal magnitude and opposite sign. The theory of poroelasticity, coupling the three-dimensional deformation field with pore pressure, was first developed by Biot [1941] and later extended to include anisotropic material properties [Biot, 1955; Carroll, 1979] and thermal effects [Palciauskas and Domenico, 1982; McTigue, 1986]. Assuming isotropic material properties, the validity of Darcy's Law and Hookes Law the pressure and strain fields in a saturated medium are described by the following system of coupled partial differential equations:

$$\frac{K}{\rho g} \nabla^2 p = \frac{\partial \varepsilon}{\partial t} + n\beta \frac{\partial p}{\partial t} \quad (2.3)$$

$$(\lambda + 2\mu) \nabla^2 \varepsilon = \nabla^2 p \quad (2.4)$$

Here K is the hydraulic conductivity, ρ is the density of the pore fluid, g is the gravitational constant, ε is the incremental volume strain, n is the porosity, β is the compressibility of the fluid, λ and μ are Lamé's constants and t is time. A nice derivation of these equations can be found in Verrujit [1969]. Equation 2.4 can be integrated to

$$(\lambda + 2\mu)\varepsilon = p + f(\vec{x}, p), \quad \text{with } \nabla^2 f = 0. \quad (2.5)$$

In one dimension this becomes [Verrujit, 1969]

$$(\lambda + 2\mu)\varepsilon = p. \quad (2.6)$$

Inserting 2.6 into 2.3 yields the one-dimensional diffusion equation

$$\frac{K_v}{\rho g} \frac{\partial^2}{\partial z^2} p = (\alpha + n\beta) \frac{\partial p}{\partial t}, \quad (2.7)$$

where K_v is the vertical hydraulic conductivity, z is the vertical coordinate, and α

is the compressibility of the material matrix. Equation 2.7 was derived prior to the Biot [1941] developments by Terzaghi [1925].

Horizontal deformation

In the study of aquifer system compaction equation 2.7 has been used extensively, neglecting any horizontal deformation. Although it has been criticized that horizontal displacements can be important near a pumping well in an aquifer system [Helm, 1994], most authors have ignored them [e.g. Riley, 1969; Galloway et al., 1998; Hoffmann et al., 2001].



Figure 2-4: The opening of surface fissure in Antelope Valley testifies to horizontal surface displacements.

The justification for neglecting horizontal deformation over extensive aquifer systems are often geometrical considerations. The compacting material is mostly contained in sub-horizontal layers that extend much farther laterally than vertically. Furthermore, the most compressive parts of the aquifer system are often clay and silt layers (either in confining units or interbedded), which have extremely low vertical hydraulic conductivities. The pressure gradient within these layers is therefore almost exactly vertical, suggesting the one-dimensional simplification. Also, the compacting layers cannot move freely in the horizontal direction. As they are in contact with over- and underlying

sediments and their lateral abutments, these may restrain the compacting units from undergoing significant horizontal deformation. However, according to the Biot equations (2.3, 2.4) the deformation field has a horizontal component even if the stress-change gradient is one-dimensional.

Treating the problem in one-dimension corresponds to assuming a Poisson ratio of zero. Opening of fissures over deforming aquifer systems in Las Vegas Valley [Bell and

Price, 1991], Antelope Valley [Blodgett and Williams, 1992] (fig. 2-4) and elsewhere [Holzer, 1984; Carpenter, 1993] evidence the existence of horizontal displacement, although they have not been clearly related to displacements in the confined part of the aquifer systems.

In the analyses in this work I have adopted the commonly used one-dimensional theory. While this was also a pragmatic choice, considering the fact that most of the tools available today for groundwater modeling and subsidence simulation employ the one-dimensional treatment, applying a fully three-dimensional theory instead would require the specification of additional parameters (e.g. Poisson's ratio, anisotropy, etc.). Unfortunately, these parameters are usually unknown for groundwater basins. Using poorly constrained assumptions for these parameters would likely have prevented the more realistic three-dimensional theory from yielding more reliable interpretations. Furthermore, I was able to support the assumption that at least horizontal surface displacements are indeed negligible for inelastic displacements in the Antelope Valley aquifer system by analyzing interferograms from ascending and descending satellite tracks (Chapter 6).

Hydraulic head

In hydrogeology pore pressures in the water-bearing formations are commonly discussed in terms of hydraulic head, defined as

$$h = h_z + \frac{p}{\rho g} = h_z + \frac{p}{\gamma_w}. \quad (2.8)$$

The first term on the right hand sides, h_z is called the elevation head, the distance to an arbitrary reference surface. The quantity $\gamma_w = \rho g$ is the specific weight (specific gravity) of water. When discussing changes in pore pressure or hydraulic head, the elevation head drops out and the hydraulic head changes are directly proportional to the changes in pore pressure. The advantage of using hydraulic head instead of pressure is that it is very easily related to the observable quantity, the level to which water rises in a well tapping the formation of interest.

Deformation and storage

Two other important quantities in discussing compaction of aquifer systems are the specific storage, S_s , and the storage coefficient, S . The specific storage is a material property defined as the volume of water expelled from a unit volume of the aquifer system due to a unit decline in hydraulic head [Todd, 1980]. In a confined aquifer system water is derived both from reduction of pore space (resulting in compaction of the system) and expansion of the pore water as the pore pressure declines:

$$S_s = \alpha\gamma_w + n\beta\gamma_w = S_{sk} + S_w \quad (2.9)$$

The first term on the right hand side, S_{sk} is called the skeletal specific storage. For the more compressible fine-grained sediments in the aquifer systems studied in this work, $S_{sk} \gg S_w$, so that $S_s \approx S_{sk}$ [Poland, 1984]. The storage coefficient, S , is defined as the volume of water expelled per unit area from a layer of thickness b due to a unit decline in hydraulic head. Thus, it is given as

$$S = bS_s. \quad (2.10)$$

Similarly to 2.9 the storage coefficient can be separated into the storage due to compaction of the layer, called the skeletal storage coefficient, $S_k = bS_{sk}$, and the storage derived from expansion of the water. Note that the definitions for S_s and S in equations 2.9 and 2.10 refer to the case of one-dimensional deformation.

Using the definitions in equations 2.8 and 2.9, the diffusion equation 2.7 can be written as

$$\frac{\partial^2 h}{\partial z^2} = \frac{S_s}{K_v} \frac{\partial h}{\partial t}. \quad (2.11)$$

For this simple one-dimensional form with constant parameters, the analytical solution for the head in a horizontal layer of thickness b_0 as a function of vertical position, $-b_0/2 < z < b_0/2$, and time t following a step decrease of hydraulic head at both layer boundaries at $\pm b_0/2$ at time $t = 0$ is given by the infinite series [Carslaw and

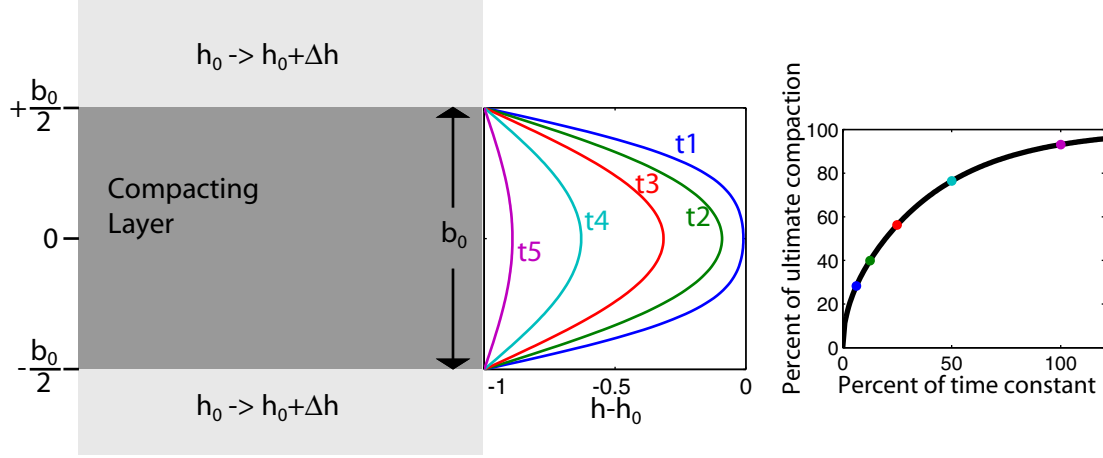


Figure 2-5: Compaction in a horizontal layer of thickness b_0 due to a unit step decline $\Delta h = -1$ of hydraulic head in the surrounding material. Head profiles across the layer are shown for several times, t_{1-5} (center), indicated by colored dots in the graph of subsidence over time on the right.

Jaeger, 1959],

$$h(z, t) - h_0 = \Delta h - \frac{4 \Delta h}{\pi} \sum_{k=0}^{\infty} \frac{(-1)^k}{2k+1} e^{-\frac{\pi^2}{4} \frac{t}{\tau_k}} \cos\left(\frac{(2k+1)\pi z}{b_0}\right), \quad (2.12)$$

where $\tau_k = \frac{\left(\frac{b_0}{2}\right)^2 S_s}{(2k+1)^2 K_v}$.

Here h_0 is the initial head throughout the layer and Δh is the instantaneous step change of head (fig. 2-5). A very good approximation to the exact expression in 2.12 is achieved with very few terms of the series. The value

$$\tau = \tau_0 = \frac{\left(\frac{b_0}{2}\right)^2 S_s}{K_v} \quad (2.13)$$

is called the compaction time constant. It is the time after which about 93% of the water that will drain from the layer in infinite time due to the step decline has drained from the layer. Thus, it is also the time after which 93% of the ultimate compaction due to the head change has been realized [Scott, 1963; Riley, 1969].

If a system of N layers with identical K_v and S_s but different thicknesses b_n

compacts due to the same head decline, Helm [1975] defined an equivalent thickness

$$b_{equiv} = \sqrt{\frac{1}{N} \sum_{n=1}^N b_n^2}, \quad (2.14)$$

which results in the correct time constant if used in equation 2.13 (i.e., the time after which about 93% of the cumulative compaction in all interbeds has occurred). Equation 2.14 enables much more efficient compaction computations for a system of interbeds. It is important to keep in mind though, that b_{equiv} as defined in 2.14 cannot be used in equation 2.10 to compute the total storage coefficient for all N interbeds, because b_{equiv} is generally smaller than the cumulative thickness of all interbeds for $N > 1$.

For the idealized layer for which the solution 2.12 was derived, the compaction can be computed by the integral

$$\begin{aligned} s(t) &= \int_{-b_0/2}^{b_0/2} S_{sk} \Delta h(t, z) dz = 2 \int_0^{b_0/2} S_{sk} \Delta h(t, z) dz \\ &= S_{sk} b_0 \Delta h \left(1 - \frac{8}{\pi^2} \sum_{k=0}^{\infty} \frac{e^{-\frac{\pi^2}{4} \frac{t}{\tau_k}}}{(2k+1)^2} \right), \end{aligned} \quad (2.15)$$

where τ_k is as defined in 2.12 and Δh is the step head decline at the boundaries of the layer. An important observation in equation 2.15 is that the compaction of the layer, $s(t)$ is directly proportional to the skeletal storage coefficient, $S_k = S_{sk} b_0$.

The deformation of geologic materials under applied stresses is described by their constitutive relations. The details of these relations are typically quite complex for geologic material and are rarely described accurately by analytical functions. Often the constitutive relations need to be idealized in order to incorporate them in physical or numerical models. For many unconsolidated fine-grained sediments, which constitute large portions of the aquifer systems under study, two dramatically different domains of deformation behavior have been observed. If the stress exceeds any stress previously experienced by the material, the grain matrix is rearranged and compacts as it yields to the increasing stress. This compaction is permanent. The often large

displacements resulting from these deformations are not recovered when the stress is released. Compaction occurring in this domain is termed “inelastic” or “virgin” compaction. If the stress changes without exceeding the maximum preexisting stress, called the preconsolidation stress, the deformations are much smaller and mostly elastic. This deformation behavior is often described by assigning two different skeletal specific storages:

$$S_{sk} = \begin{cases} S_{skv} & , \text{ for } \sigma' > \sigma'_{max} \\ S_{ske} & , \text{ for } \sigma' \leq \sigma'_{max}. \end{cases} \quad (2.16)$$

If the total stress due to the overburden and tectonic processes is assumed to remain constant, the preconsolidation stress, σ'_{max} , can be expressed by the preconsolidation head, h_{pc} , the lowest hydraulic head experienced by the material.

Figure 2-6 shows an idealized relation between effective stress change and compaction. In many cases the elastic deformations for coarse- and fine-grained sediments can be approximated by the linear relation

$$\Delta b = S_{ske} b_0 \Delta h = S_{ke} \Delta h \quad , \text{ for } h > h_{pc}, \quad (2.17)$$

or equivalently

$$S_{ke} = \frac{\Delta b}{\Delta h}. \quad (2.18)$$

Inelastic compaction of coarse-grained sediments that typically constitute the aquifers within these aquifer systems is negligible. For many fine-grained sediments the relationship between compaction and effective stress change has been observed to be approximately logarithmic [Jorgensen, 1980]:

$$\Delta b = b_0 C_c \frac{\Delta \log_{10} \sigma'}{1 + e_0} \quad \text{so that} \quad S_{skv} = \frac{C_c \gamma_w}{\ln 10 \cdot \sigma' \cdot (1 + e_0)}. \quad (2.19)$$

Here C_c is the compression index and e_0 is the void ratio. Equation 2.19 can be integrated to express the relation between the change in effective stress and thickness as

$$b = b_0 \left(\frac{\sigma'_0}{\sigma'} \right)^a \quad \text{with} \quad a = \frac{C_c}{\ln 10 (1 + e_0)} = \frac{S_{skv} \sigma'_0}{\gamma_w}. \quad (2.20)$$

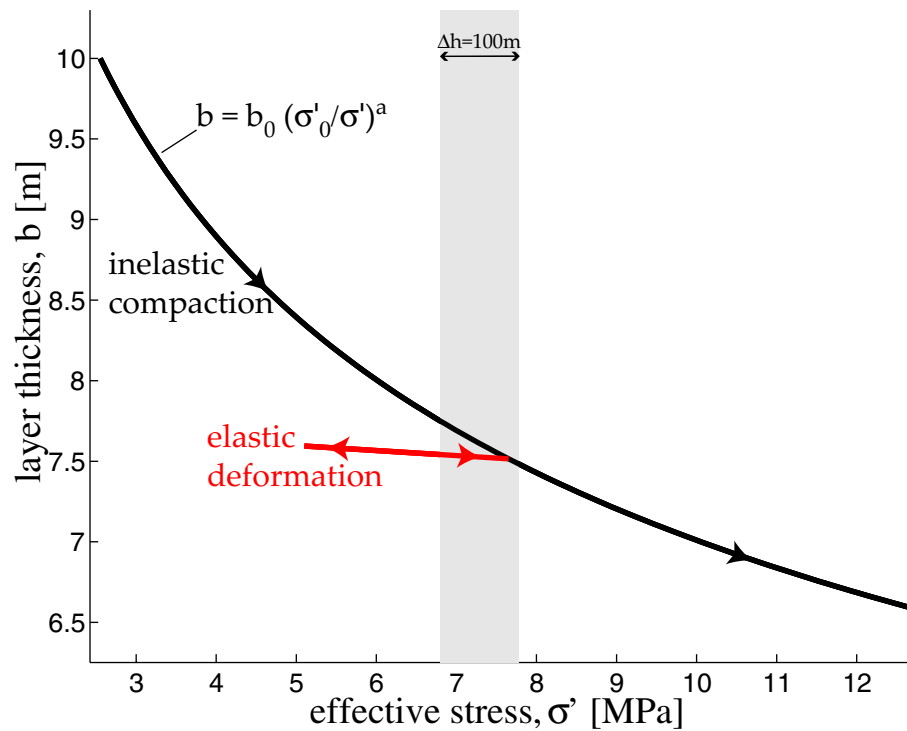


Figure 2-6: Idealized stress-strain relation for fine-grained sediments. The relationship is often approximately logarithmic for inelastic compaction (black) and approximately linear in the elastic range (red) of stresses. The width of the shaded area corresponds to a 100 m change in hydraulic head. For the small stress changes typically caused by changes in hydraulic head the constitutive relation is often approximately linear (eq. 2.22).

For small changes in effective stress, $\frac{\Delta\sigma'}{\sigma'_0} \rightarrow 0$, equation 2.20 can be linearized to

$$b - b_0 = \Delta b = b_0 \frac{S_{skv}}{\gamma_w} (\sigma'_0 - \sigma'). \quad (2.21)$$

If the change in effective stress is exclusively due to a change in hydraulic head, $\sigma'_0 - \sigma' = \gamma_w(h - h_0)$ (see equation 2.8), resulting in the same linear equation as in the elastic case (eq. 2.17):

$$\Delta b = S_{skv} b_0 \Delta h = S_{kv} \Delta h, \quad \text{for } h < h_{pc}. \quad (2.22)$$

It is important to keep in mind though that equations 2.17 to 2.22 assume that all deformation caused by the change in head, Δh , has been realized, i.e., the head throughout the entire layer thickness has equilibrated with the head at the layer boundaries. The time-scale on which this equilibration occurs is described by the compaction time constant (eq. 2.13). Because the time constant depends on the specific storage of the material, its value differs for elastic and inelastic compaction. In unconsolidated clayey or silty sediments (aquitard and confining unit materials) the values of S_{skv} are often tens to one hundred times larger than the values of S_{ske} [Riley, 1998]. Consequently the time constants for elastic deformations are usually on the order of days, whereas the time constants for inelastic compaction can be on the order of years, decades or longer.

Where time constants are large, the observed compaction can differ significantly from what would be expected from equations 2.17 to 2.22. Continuing compaction in the presence of non-declining and even recovering water levels can be observed where residual compaction, caused by previous drawdowns, is occurring in thick compressible layers.

Compaction and expansion in multiple layered units typically contribute to the observed surface displacements over unconsolidated alluvial aquifer systems. Depending on the stresses in the aquifer system with respect to the preconsolidation stress the observed surface displacements have to be interpreted in terms of elastic deformation or non-recoverable inelastic compaction. Large-magnitude land subsidence

observed over many aquifer systems is generally due to inelastic compaction of thick, highly compressible interbeds and confining units, consisting of compressible silt and clay deposits. The aquifer portions of an aquifer system are usually constituted of less compressible materials (sands, gravel) that deform mostly elastically, even when the preconsolidation stress is exceeded.

2.1.3 Other mechanisms for surface displacements

Up to this point I have focused the discussion on surface displacements caused by compaction and expansion of sediments in the confined part of an aquifer system caused by pore pressure changes. However, a number of different physical mechanisms can lead to measurable displacements of the land surface. The most important of these are mentioned briefly below. In each case I state briefly why I have not considered these mechanisms to be responsible for significant surface displacements observed in the studies presented in this dissertation.

Hydrocompaction

One mechanism that is known to cause extensive subsidence is that of hydrocompaction [Lofgren, 1969]. Hydrocompaction occurs in very porous ($> 45\%$) sediments or soils in arid or semi-arid environments that are cemented by clay. The clay loses its strength when it is wetted, e.g. during irrigation, resulting in the compaction of the sediments. This mechanism is very shallow and irreversible. The seasonal fluctuations in land surface position observed over the studied basins cannot be explained with this mechanism. The agreement of the subsidence trends observed using InSAR with the subsidence measured by borehole extensometers, which are constructed to exclude any potential deformation in the shallow sediments, also indicates that this mechanism is not important in the cases studied in this work. Finally, hydrocompaction occurs when the susceptible sediments are wetted for the first time. In the case of the agricultural areas in Antelope Valley any hydrocompaction would have occurred long ago. The same is also true for heavily urbanized areas, such as the Las Vegas Valley.

Soil swelling

Another mechanism causing surface displacements is soil swelling and shrinking. Similar to hydrocompaction this is a shallow mechanism requiring soils containing clays that expand when wetted [Rahn, 1996]. Where this is occurring the surface displacements as a function of time should be correlated with precipitation or irrigation practices. There should also be a noticeable correlation of the displacement signal with the vegetated areas. This has been observed over the Imperial Valley, California by Gabriel et al. [1989]. However, I have observed neither of these in the InSAR data examined for this dissertation. While I cannot exclude that soil shrinking and swelling may occur locally, it cannot explain the dominant displacement signals.

Construction and erosion

Two other agents potentially affecting the location of the land surface are construction activities and naturally occurring erosion processes. Both of these are unlikely to bias InSAR displacement measurements though, because they will render them impossible where they are significant. The interferometric phase difference is only meaningful where the signals in the two SAR acquisitions remain coherent (section 2.2.2). Construction, plowing, or significant erosion destroy this coherence by altering the geometry of the surface at the scale of the radar wavelength. Thus these processes may reduce the precision of the phase measurement or in serious cases even prevent any measurement of the surface displacement, but they cannot bias the displacement measurement. Both study sites showed generally high coherence values. Only decorrelation at isolated locations in Las Vegas valley (Chapter 3) may be attributable to construction activity.

Vegetation growth

The same reasoning applies in the case of vegetation growth. Growing lawns or crop fields are unlikely to mimic surface displacements in interferometric measurements because the growth of the plants will lead to decorrelation in the image where scattering from the growing plants contributes significantly to the measured signal. Some

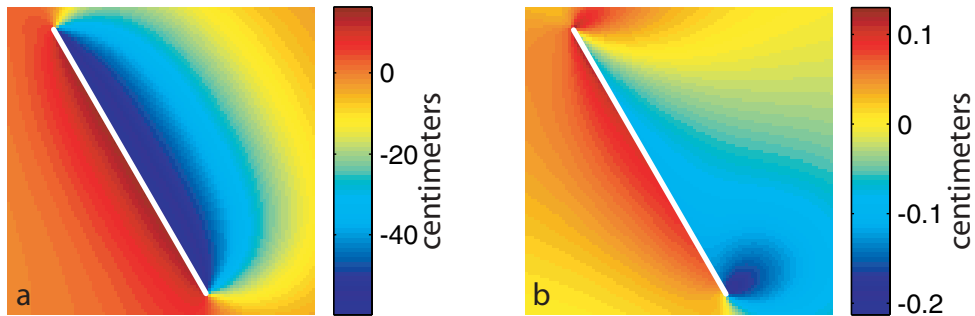


Figure 2-7: Typical displacement patterns for tectonic deformation processes as observed in a side-looking InSAR geometry. The figure shows the theoretically measured displacement on (a) a normal fault dipping 70° to the lower left for 50 cm dip-slip and (b) a vertical strike-slip fault for a 50 cm strike-slip. Positive values indicate motion towards the sensor. Patterns like these have been extensively studied and observations are therefore easily related to motion on faults.

loss of correlation over the farmed regions of the Antelope Valley (Chapter 4) illustrates this, although the correlated part of the radar signal, which is not affected by vegetation growth, usually remains strong enough to enable a phase measurement.

Tectonic deformation

Tectonic processes can cause dramatic surface displacements. In fact, the number of interferometric studies that has focused on aquifer system compaction to date is much smaller than that of studies focused on characterizing and analyzing tectonic processes by observing volcanic deformation and coseismic or interseismic displacements along active geologic faults. The areas actively deforming due to tectonic processes at appreciable rates are generally well known. Furthermore, the patterns of tectonic surface deformation are typically highly suggestive of the underlying process (fig. 2-7). The spatial extent and shape of the surface displacements observed in this work over aquifer systems strongly suggests the inferred relation to a deformation process in the groundwater reservoir. Other reservoirs, such as magma chambers or oil reservoirs do not exist under the areas studied here and therefore need not be considered. Very deep sources (much deeper than the aquifer system) for the deformation could not explain the observed small-scale structure of the displacement fields (fig. 2-8). The same is

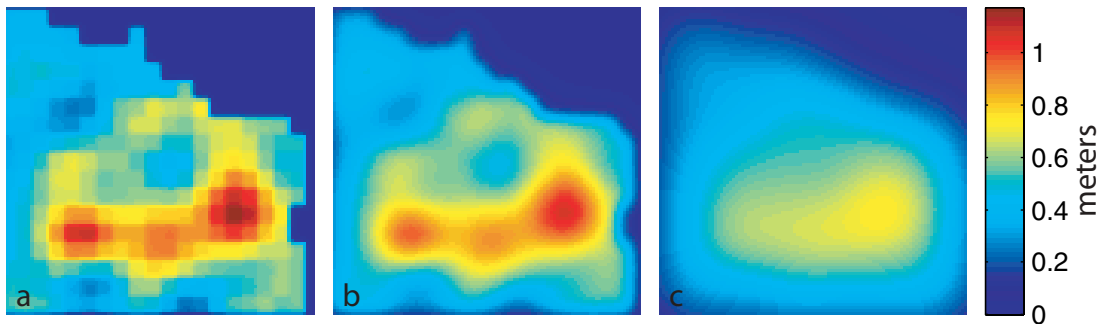


Figure 2-8: Theoretical observations of surface displacements over a heterogeneously compacting reservoir at 100 m (a), 500 m (b), and 2 km (c). The figure assumes the same amount of reservoir compaction for all three cases. Note that the degree of spatial detail declines with increasing depth of the reservoir.

true for processes related to the major fault lines, such as the San Andreas or the Garlock faults, both of which delineate the Antelope Valley. Any deformation related to these faults would affect the area broadly or be discontinuous across the fault. Neither of these are observed. However, in many cases the observed displacement field is strongly correlated with known geologic faults. Whether this corresponds to a activation of the fault by pore pressure changes, differential compaction on different sides of the fault or a superposition of these two needs to be investigated on a case by case basis.

In this section I have laid out the theory of aquifer system compaction caused by pore pressure changes in a developed aquifer system. Deformations in the aquifer system at depth can displace the overlying land surface, and thus become amenable to study by InSAR techniques as discussed in the next section. The described relationship between the stress changes due to pore pressure fluctuations and the resulting deformation is governed by the constitutive properties of the deforming material. Thus, conjunctive analyses of both, stress changes and surface deformation over developed aquifer systems, can yield valuable information about these properties.

2.2 InSAR - Background

A wide variety of geophysical investigations directed toward studying subsurface processes use observations made at or very near the earth's surface. One of the directly observable quantities containing information on subsurface processes is the displacement of the earth's surface itself. Until fairly recently however, making these observations frequently and accurately enough and with sufficiently dense spatial sampling to enable meaningful conclusions regarding the processes of interest at depth has been extremely difficult with the available geodetic techniques.

This has changed dramatically with the development of InSAR. Where applicable, InSAR techniques allow the measurement of one component of the surface displacement field at spatial resolutions on the order of meters or tens of meters with a precision on the order of millimeters to centimeters over large areas of up to thousands of square kilometers. The basic principles and the limitations of synthetic aperture radar (SAR) interferometry are presented in this chapter.

Applications of InSAR technology have multiplied since imaging radar data from civilian radar satellites, such as the European Remote Sensing Satellites ERS-1 and ERS-2, the Japanese Earth Resource Satellite JERS-1 or the Canadian RADARSAT have become available to the science community. Currently (2003) the only two fully operational space-borne civilian imaging radar sensors usable for InSAR are RADARSAT and the European Environment Satellite ENVISAT, but several new missions are planned. All of the imaging radar data used for this dissertation was acquired by the ERS-1 and ERS-2 satellites. Some important system parameters of these satellites and properties of the data they acquire are summarized in table 2.1.

Using data primarily from these satellites, interferometric techniques have been employed to create topographic maps [e.g. Zebker and Goldstein, 1986; Gabriel et al., 1989] (culminating in the Shuttle Radar Topography Mission [Jordan et al., 1996]), observe ocean currents [Goldstein and Zebker, 1987; Goldstein et al., 1989], measure volcanic surface displacements [e.g. Massonnet et al., 1995; Amelung et al., 2000] co-seismic and postseismic earthquake motion [e.g. Massonnet et al., 1993, 1994], aseismic fault creep [Rosen et al., 1998; Bawden et al., 2001], flow of glaciers and ice

Parameter	Value
Radar system:	
radar frequency, f_0	5.3 GHz (C-Band)
radar wavelength, λ	5.666 cm
radar pulse waveform	linear chirp
pulse bandwidth	15.55 MHz
pulse repetition frequency, prf	1679.9 Hz
Imaging geometry:	
orbit	polar
orbital elevation	790 km
orbit repeat time	35 days
look angle, Θ	$21^\circ - 26^\circ$
swath width	100 km
Data product:	
along-track resolution, δr_{az}	5 m
across-track ground resolution, δr_r	25 m
size of individual image scene	100 km by 100 km

Table 2.1: Some important parameters of ERS-1 and ERS-2 imaging radar data.

sheets [e.g. Goldstein et al., 1993; Joughin et al., 1995; Rignot, 1998], subsidence over geothermal fields [Massonnet et al., 1997], mining operations [Carnec et al., 1996], oil fields [Fielding et al., 1998], and aquifer systems [Galloway et al., 1998; Amelung et al., 1999; Hoffmann et al., 2001]. Extensive reference lists for many of the early publications using InSAR can be found in Massonnet and Feigl [1998] and Hanssen [2001].

2.2.1 InSAR fundamentals

In this section I present the fundamental background of SAR interferometry at the level necessary to discuss the observations derived from the interferometric phase measurements in this dissertation. After introducing the basic InSAR geometry and equations, I detail the image processing performed on the data used for this dissertation. Additional background on the methodology can be found in Massonnet and Feigl [1998] and Hanssen [2001]. A comprehensive presentation of SAR image formation can be found in Curlander and McDonough [1991].

The interferometric phase

The basic property of imaging radar acquisitions enabling interferometric measurements is the control and measurement of the phase of the complex-valued radar signal. The scattered radar signal returned to the radar antenna from every resolution element (about 5 by 25 m for ERS (table 2.1)) in a SAR image is the coherent sum of the echoes from all scattering interactions in the resolution element. The exact way in which the contributions from the different scatterers are added up in the observed signal is not predictable. In this sense the signal phase in a SAR image is effectively random. If two separate radar acquisitions are acquired realizing the same, or almost the same, viewing geometry over the same area, however, the summing of the contributions from individual scatterers is largely the same so that the phase difference between the two image acquisitions is not random. This can either be realized by using two physically separate antennas mounted on the same platform (single-pass interferometry) or two passes of the same antenna (repeat-pass interferometry). An

interferogram is formed from the two (complex) image signals, I_1 and I_2 , as

$$I = I_1 I_2^* = A_1 e^{i\phi_1} \cdot A_2 e^{-i\phi_2} = A_1 A_2 \cdot e^{i(\phi_1 - \phi_2)} = A \cdot e^{i\Phi}, \quad (2.23)$$

where $*$ denotes the complex conjugate. $A = A_1 A_2$ is the interferogram amplitude and $\Phi = \phi_1 - \phi_2$ is the interferogram phase, which is the principal measurement in InSAR. For an identical imaging geometry and imaged surface, the two acquisitions would be identical apart from system noise, hence, $I_1 = I_2$, and the interferometric phase would be exactly zero everywhere. However, this is never observed in practice. The measured phase can be written as the sum of contributions from different processes [Zebker et al., 1994; Ferretti et al., 2000]:

$$\Phi = \Phi_{\text{topo}} + \Phi_{\text{def}} + \Phi_{\text{atm}} + \Phi_n \quad (2.24)$$

Here, Φ_{topo} is a phase contribution due to viewing the topography from two (slightly) different angles, Φ_{def} is a phase contribution due to a possible movement of the imaged surface in the line-of-sight (LOS) direction, Φ_{atm} is a phase contribution due to a difference in the optical path-lengths due to changes in the refractivity along the signal path, and Φ_n is phase noise. Depending on the application, all of the first three terms on the right hand side of equation 2.24 may be considered “signal” or “noise”. Each of these terms are briefly discussed in the following paragraphs.

If the viewing geometry remains exactly the same for the two SAR acquisitions, Φ_{topo} is equal to zero. However, if the two antenna positions are separated by some distance B in the plane perpendicular to the antenna motion, called the interferometric baseline (fig. 2-9), different points on the surface will be at slightly different relative positions from the antennas. The interferometric phase contribution due to surface topography can be written as [Zebker et al., 1994; Hanssen, 2001]

$$\Phi_{\text{topo}} = -\frac{4\pi B_{\perp}}{\lambda r \sin \Theta} dz + \Phi_{\text{flat.earth}}, \quad (2.25)$$

where λ is the radar wavelength, r is the range (the distance between the radar and a point on the ground), Θ is the look angle (fig. 2-9), and dz is the surface

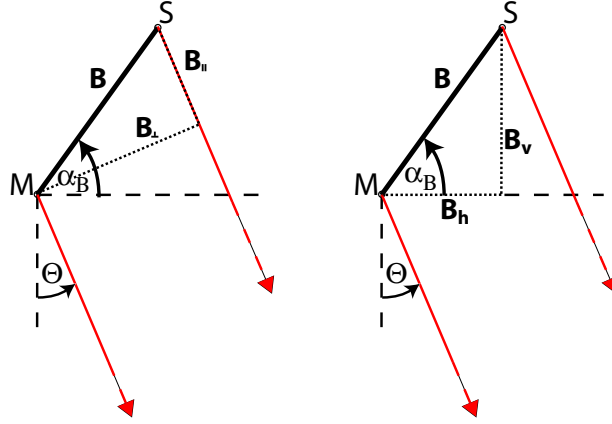


Figure 2-9: Different parameterizations of the InSAR baseline geometry. M and S are the two antenna positions in the plane perpendicular to the antenna flight path, B is the interferometric baseline, B_{\perp} , B_{\parallel} , B_h and B_v are the perpendicular, parallel, horizontal and vertical baselines, respectively, Θ is the look angle and α_B the baseline angle.

elevation above a reference elevation. The term $\Phi_{\text{flat.earth}}$ is a deterministic phase contribution due to the reference surface, which for satellite systems is typically the reference ellipsoid. According to equation 2.25 the topographic phase signal after removal of the reference surface is directly proportional to the surface elevation and the perpendicular baseline. This equation is used to develop topographic maps from interferometry. In the study of surface displacements equation 2.25 is used to remove the topographic phase contribution from the signal. To do this the imaged topography must be known either from a digital elevation (or terrain) model (DEM or DTM), or be estimated from a separate “topographic” interferogram.

If some process alters the position of the land surface between the two image acquisitions used to form the interferogram, the distance from the antenna to the scattering centers on the ground changes. If an area on the ground is displaced by Δr in the LOS direction of the radar, the path difference between the two acquisitions, $2\Delta r$, introduces an excess phase of

$$\Phi_{\text{def}} = \frac{4\pi}{\lambda} \Delta r. \quad (2.26)$$

Absolute displacements of the entire area imaged in a radar scene are only detectable to the precision to which the orbits are known. However, the power of the interferometric technique for deformation observations lies in the measurement of relative displacements between areas within the radar image. An ERS radar scene covers an area of about 100 km by 100 km, which is larger than the size of the surface expressions of many geophysical processes such as volcano inflations or deflations, most earthquakes, flowing glaciers, and compacting aquifer systems. Thus, significant areas in the image can often be assumed to be stable between the two image acquisitions. This yields a displacement measurement in the LOS direction that is only limited by the ability to measure the interferometric phase. Under favorable conditions (see section 2.2.2) this measurement can be made to millimeter precision.

A frequently emphasized, important advantage of remote sensing at radio frequencies is the transparency of clouds at these wavelengths. Thus, SAR images can be formed from acquisitions in all weather conditions. However different meteorological conditions in the atmosphere affect the propagation velocity of the radar signal, slightly modifying the optical path-length travelled by the signal. The difference of the path-lengths between the two acquisitions introduces the phase contribution

$$\Phi_{\text{atm}} = \frac{4\pi}{\lambda} \left[\int n_{r1} \vec{dp} - \int n_{r2} \vec{dp} \right] \approx \frac{4\pi}{\lambda} \int [n_{r1} - n_{r2}] \vec{dp}, \quad (2.27)$$

where n_{r1} and n_{r2} are the refractive indices at the times of the two acquisitions along the signal path, \vec{dp} . The approximation between the two expressions in equation 2.27 holds if ray bending is negligible, which is the case for all SAR data available today [Hanssen, 2001]. Although some studies have tried to exploit the atmospheric signal contribution for meteorological studies [e.g. Hanssen, 1998], it is typically considered an error source (see section 2.2.2) and presently constitutes one of the principal limitations of InSAR applications in deformation monitoring.

Interferometric processing

Figure 2-10 shows the image processing steps performed to derive the surface displacement maps in this dissertation from radar interferograms. After SAR image

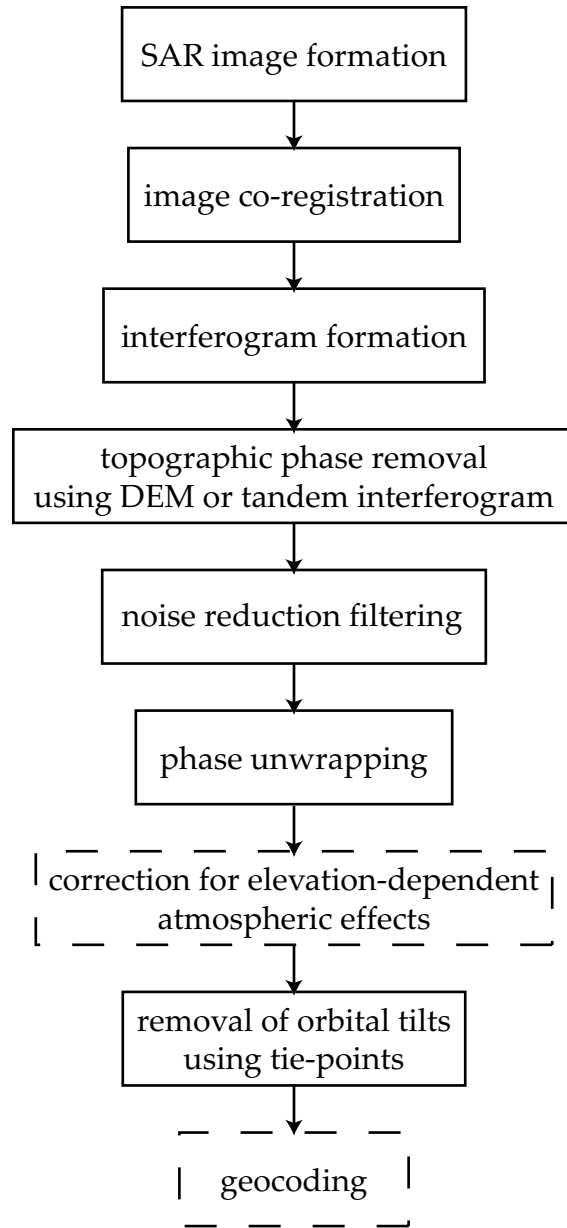


Figure 2-10: Image processing steps performed to obtain surface displacement maps from radar acquisitions. Steps in dashed boxes were not performed for all images.

formation, the two images are co-registered with high accuracy before the interferogram is formed (eq. 2.23). The topographic phase contribution (eq. 2.25) is removed, using a DEM or tandem interferogram (an interferogram using two SAR acquisitions separated by only one day in time, thereby likely excluding any significant contribution due to deformation). Because the phase values are measured in the interval $[0, 2\pi)$ (or in $[-\pi, \pi)$), they need to be integrated to determine the absolute phase differences between locations in the image. This integration is called phase unwrapping. Different algorithms for phase unwrapping exist. Chen [2001] reviews existing algorithms and provides a thorough discussion of the topic. The majority of the interferograms used in this dissertation were unwrapped using a minimum-cost network-flow (MCF) algorithm [Costantini, 1998]. For the successful and accurate unwrapping of the interferogram it is often necessary to reduce the phase noise in the interferogram prior to unwrapping. This can be done by a variety of filtering operations, such as moving-average (mean or median) filters. If significant residual phases are observed to correlate with topography in the image these can sometimes be removed by estimating the excess path length due to a layered atmosphere (eq. 2.35). However, as discussed in 2.2.2, this is usually not necessary over flat groundwater basins. Inaccurately known satellite orbits introduce, to first order, linear phase tilts across the image (2.2.2), which can be estimated and removed using a number of tie-points of known elevations distributed across the image. Finally, to remove geometric distortions due to the radar imaging geometry the image can be rectified and geocoded. Because topography in the groundwater basins studied here was insignificant, this step was not critical. However, the geocoding of the resulting images helps in analyzing the observations in their spatial relation to additional data (e.g., roads, buildings, benchmarks, well locations, etc.) from other sources.

2.2.2 Error contributions in InSAR-observed surface displacements

To interpret surface displacements measured with InSAR techniques quantitatively it is important to understand and quantify the errors affecting the measurement. Until

the mid-1990s most work related to InSAR focused on the applicability of the new technique to a variety of geophysical phenomena, generally overlooking or neglecting the issue of measurement reliability. Recent work has tried to further the understanding of errors and biases contained in interferometric phase measurements [e.g. Jónsson, 2002]. In this section I briefly describe the most important error sources and their implication for the accurate measurement of surface displacements, particularly under conditions typically encountered in desert basins in the southwestern United States. The following subsections are by no means meant to represent an exhaustive discussion of the various error sources. A very good and comprehensive treatment of errors in radar interferometry has been presented by Hanssen [2001], which I have relied on heavily for this section.

Most of the error contributions to deformation measurements with InSAR are not due to an inaccurate measurement of the interferometric phase. Rather, they derive from errors in relating the interferometric phase to the various signal contributions from surface topography, deformation, atmospheric delay, and changes in the refractive properties of the land surface. The most important error contributions in interferograms processed to measure surface displacements, phase noise and decorrelation, orbit errors, DEM errors, atmospheric errors, and projection errors are explained in the following subsections.

Phase noise and decorrelation

Phase noise and decorrelation are the most fundamental limitation to the interferometric measurement. As all interferometric techniques, radar interferometry relies on the coherence of the signals used to create the interference patterns. Incoherent signals cannot be used for an interferometric measurement. A number of effects reduce the signal coherence between two SAR acquisitions used to form an interferogram. They are usually discussed in terms of correlation between the two images, defined as

$$\rho = \frac{\langle I_1 I_2^* \rangle}{\sqrt{\langle I_1 I_1^* \rangle \langle I_2 I_2^* \rangle}}. \quad (2.28)$$

Here $\langle \rangle$ denotes the expected value and I and I^* are the complex image values and its complex conjugate, respectively. In interferograms the correlation value ρ is computed on a small sample of pixels around every location. By definition (2.28) the absolute values of ρ are between 0 and 1. A correlation value of 1 corresponds to perfect phase coherence between the two signals. Correlation values less than unity correspond to reduced phase coherence which results in a noisy measurement of the phase difference computed in the interferogram. A value of zero correlation indicates a meaningless phase-difference. This theoretical lower limit is usually not reached and interferograms with correlations below about 0.3 or 0.4 typically cannot be used for conventional interferometry.

The correlation term in equation 2.28 can be written in terms of the contributions of different processes causing decorrelation of the radar signals [Zebker and Villasenor, 1992]

$$\rho = \rho_{\text{thermal}} \cdot \rho_{\text{spatial}} \cdot \rho_{\text{temporal}}. \quad (2.29)$$

A more complete discussion might also include decorrelation terms for the processing itself and effects of different doppler centroids of the acquisitions, which introduce small amounts of decorrelation mostly in interpolation steps [Hanssen, 2001].

Thermal decorrelation is due to system noise and can be approximately related to the signal-to-noise ratio, SNR, of the radar system [Zebker and Villasenor, 1992]:

$$\rho_{\text{thermal}} = \frac{1}{1 + \text{SNR}^{-1}} \quad (2.30)$$

For the relatively high SNR of the ERS radar system, ρ_{thermal} is close to unity.

Spatial decorrelation occurs if the interferometric baseline, i.e., the spatial separation of the sensors (fig. 2-9) is not exactly zero. Because the signal received at the sensor is the coherent sum of scattered signals from different locations within a resolution element (section 2.2.1), these contributions are added slightly differently when viewed from a slightly different angle, reducing the signal coherence. Spatial decorrelation includes the effects of a slightly different incidence angle due to a non-zero perpendicular baseline, slightly non-parallel orbits, and volume scattering [Hoen, 2001]. If volume scattering and surface deformation effects can be neglected, and the

orbits are parallel, Zebker and Villasenor [1992] derived an expression for the spatial correlation factor,

$$\rho_{\text{spatial}} = 1 - \frac{2|B_h|R_y \cos^2 \Theta}{\lambda r}, \quad (2.31)$$

which can also be written as (fig. 2-9)

$$\rho_{\text{spatial}} = 1 - \frac{2|B_{\perp}|R_y \cos \Theta}{\lambda r}. \quad (2.32)$$

Here B_h and B_{\perp} are the horizontal and perpendicular baselines, R_y is the range resolution, Θ is the look angle of the two antennas, λ the signal wavelength and r the range from the antenna to any given resolution element. Equation 2.31 assumes that a chirp waveform is used in the SAR system and many about-equally strong scatterers are distributed throughout the resolution elements [Zebker and Villasenor, 1992]. Equations 2.31 or 2.32 also define the “critical baseline” as the baseline for which ρ_{spatial} becomes zero. The decrease of image correlation with increasing perpendicular baseline is inversely proportional to the signal wavelength (eq. 2.32). Thus, the effect is less severe for SAR sensors operating at longer wavelengths. Most SAR image data available today has been acquired at C-band (e.g. $\lambda = 0.05666$ m for ERS-1/2). Some sensors have applied shorter X-band wavelengths to achieve a higher resolution on the ground or the longer L-band wavelengths ($\lambda \approx 0.25$ m, e.g. J-ERS). Some of the planned SAR missions may employ L-band radars, which will enable the formation of coherent interferograms with much longer perpendicular baselines.

Temporal decorrelation has been the most problematic to characterize theoretically. The effect is due to changes of the imaged surface between the two radar acquisitions. Such changes may be due to geometrical changes like moving parts of vegetation or erosion of the land surface, agricultural activity or construction. Rain and snow also affect the reflectivity of the surface. Few quantitative treatments of temporal decorrelation have been attempted [e.g. Zebker and Villasenor, 1992; Hoen, 2001], but the results have been extremely site-specific and no general theory has been derived. However, it has been shown qualitatively that arid or semi-arid, sparsely vegetated or urban areas remain relatively well correlated over several years, while agricultural or heavily vegetated areas, as well as areas covered with perennial snow

are almost completely decorrelated after days to months (fig. 2-11). Because temporal decorrelation is due to changes of the land surface primarily at the scale of the radar signal wavelength, temporal decorrelation is also highly wavelength-dependent [Zebker and Villasenor, 1992]. Interferograms employing data acquired at longer radar wavelengths decorrelate much slower than data acquired at shorter wavelengths [Usai, 2001]. Thus, where temporal decorrelation in ERS C-band data has prevented the formation of usable interferograms over long time periods over some areas, future L-band missions may be more successful.

Simultaneously acquired images [Jordan et al., 1996] or techniques performing interferometry on a sparse grid of highly coherent scatterers [Ferretti et al., 2001; Usai, 2001] have been used to overcome the problem of decorrelation in interferograms. Fortunately the problem of temporal decorrelation is not prohibitive in most of the southwestern U.S. due to the semi-arid climate and sparse vegetation outside the irrigated areas.

Orbit errors

As the SAR image formation itself is based on a relative measure – the distance between the satellite and the earth’s surface – an accurate knowledge of the sensor position is necessary not just to form the image itself, but to determine the geographic location of the acquired image accurately. Knowledge of sensor position for an orbiting satellite is equivalent to accurate knowledge of the orbit, given by either the ephemeris or the state vector. Because an interferogram represents a difference measurement between two SAR acquisitions it is primarily the accurate knowledge of the relative position of the two orbits that affects the interferometric phase measurement. This relative position is parameterized by the interferometric baseline, \vec{B} , typically specified as either the baseline components parallel and perpendicular to the line of sight, B_{\parallel} and B_{\perp} , respectively, the horizontal and vertical components, B_h and B_v , or the baseline length, B , and orientation angle with respect to horizontal, α_B (fig. 2-9). As the orbits are generally not exactly parallel the baseline changes as a function of along-track location. For precise orbits determined from tracking data and gravity models the accuracies in across-track and vertical direction are about 8 cm

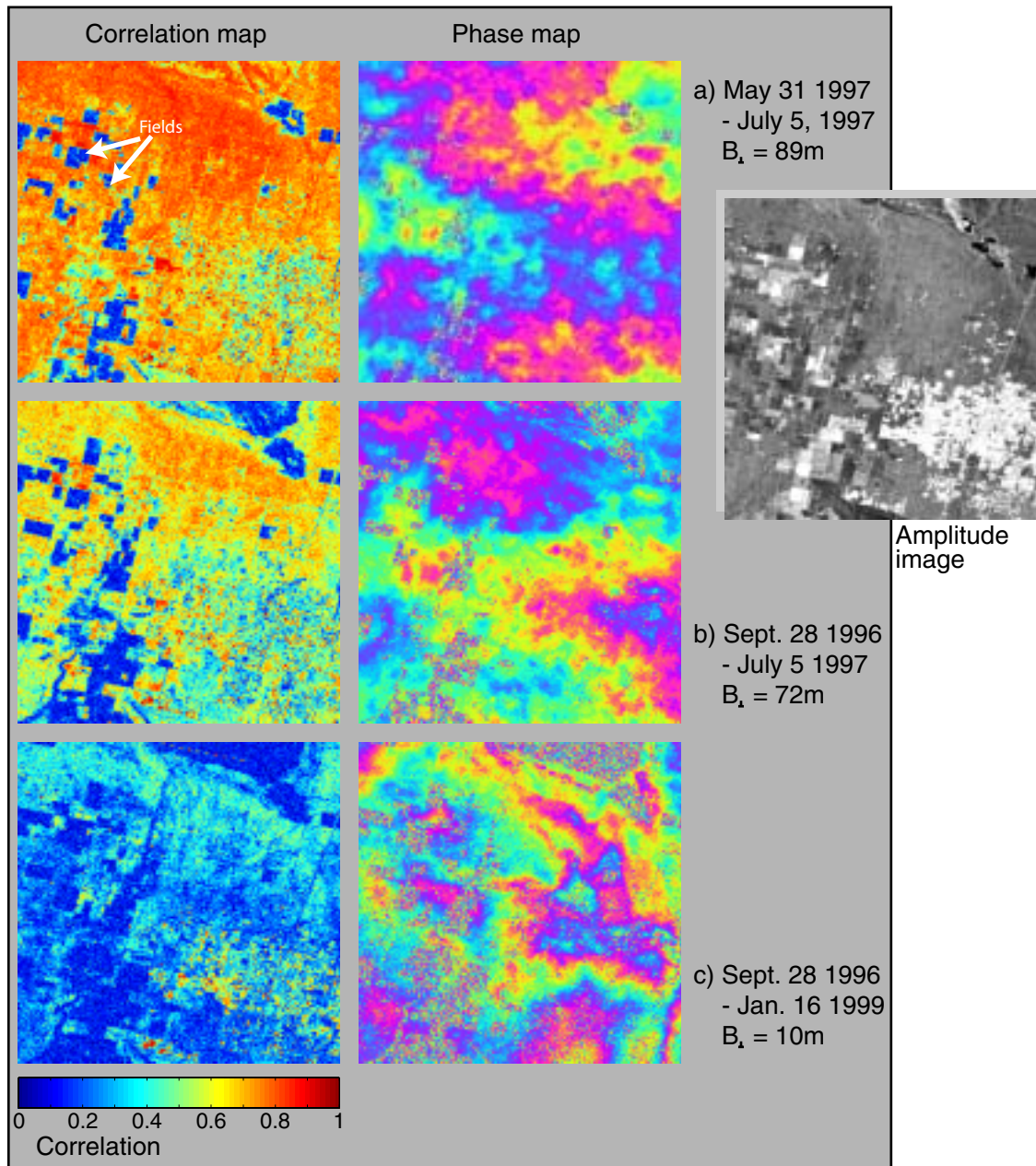


Figure 2-11: Example of temporal decorrelation. After one month (a) the correlation map (left) still shows generally high coherence values, although individual fields decorrelate. The coherence decreases markedly after 9 months (b) and 28 months (c). Coherence remains high over long time periods in urban areas. The loss of coherence appears as an increase in noise level in the interferometric phase in the phase maps.

and 5 cm, respectively [Scharroo and Visser, 1998]. Note that relative along-track errors are removed in the coregistration of the two SAR scenes prior to forming the interferogram (2.2.1). Using an inaccurate estimate of the interferometric baseline in the processing will result in a residual phase contribution from the earth's curvature and topography. Furthermore, an inaccurate estimate of the perpendicular baseline will bias any elevation estimate derived from the data (eq. 2.25).

Although it is, in principle, possible to estimate the error in the baseline from the residual phases in the interferogram, in practice this is often difficult due to the presence of other phase contributions from atmospheric effects or topography. However, to first-order, errors in the baseline components can be approximated by a linear or quadratic polynomial in range direction (the direction perpendicular to the flight path) [Hanssen, 2001]. This correction may vary slowly in along-track direction due to converging or diverging orbits. In the interferograms used for this dissertation I estimated and removed a bilinear correction in each image, using tie-points in areas outside the deforming regions. I assumed the interferometric phase at these tie-points to be zero. This may have introduced small systematic biases of the estimated displacement field due to signal noise, small local displacements, and, most importantly, atmospheric signal contributions. However due to the large number (typically > 100) and distribution of tie-points used I estimate that any such bias is probably smaller than 1 mm in the deforming areas.

DEM errors

Generation of digital elevation data has probably been the most important and economically most successful application of InSAR. The Shuttle Radar Topography Mission (SRTM) [Jordan et al., 1996] has revolutionized the availability of high-quality topography data (at least for those with security clearances – the actual availability of the data to the scientific community has become uncertain after the terrorist attacks in New York City on September 11, 2001). For deformation studies, however, the topographic phase-signature in interferograms usually needs to be removed prior to analyzing the deformation signal. This is done in one of two fashions, either using an existing digital elevation model (DEM) of the area (the so-called “two-pass”

method, as only two SAR acquisitions are required to form and correct one interferogram [Massonnet et al., 1993]), or by subtracting a scaled phase signal from a second interferogram assumed to contain only a topographic signal (the “three-pass” or “four-pass” method [Zebker et al., 1994], depending on the number of SAR scenes used). The influence of other interferometric error contributions on the DEM estimate can be reduced by combining several InSAR-derived DEMs [Ferretti et al., 1999]. Using the topographic information from either source the topographic phase signal is computed using equation 2.25 and subtracted from the interferogram. This correction can introduce errors depending on the method used to remove the topographic phase signature.

When a pre-existing DEM is used, any error in the elevation information will be mapped into a phase error of the estimated topographic phase and thus the corrected interferogram. The sensitivity of the phase error to the DEM elevation error is proportional to the perpendicular baseline (eq. 2.25)[Zebker et al., 1994]. For typical DEMs these errors occur primarily at high spatial frequencies. In addition, if the DEM used for correction is not sufficiently detailed, the required interpolation will introduce errors. A third effect can be important particularly for large-baseline interferograms. The elevation reported in DEMs is usually the elevation of the land surface. However, the surface imaged by the radar can differ by many meters from the land surface in urban areas (due to buildings) or areas of tall vegetation (due to the canopy). The difference between the elevation reported in the DEM and the elevation of the scattering center seen by the radar causes a phase error in the corrected interferogram. This is not an issue for the sparsely vegetated desert areas that make up much of the land surface above the aquifer systems studied in this dissertation.

When the three- or four-pass method is used to correct the topographic phase signature the principle error sources are non-topographic (e.g. atmospheric or deformation) phase contributions to the phase signal in the interferogram(s) used for topographic correction and errors in the estimated interferometric baselines. If several interferograms are combined to correct for the topography, the error of the elevation estimate can be reduced to about 5 m [Ferretti et al., 1999] which results

in a negligible phase error for all but the longest perpendicular baselines. Inaccurately estimated perpendicular baselines for both the topography-interferogram or the deformation-interferogram will result in a residual phase signal proportional to the elevation differences remaining in the corrected interferogram. This type of error is usually easy to detect and of little importance in the study of aquifer system deformation as the study areas of interest are usually very flat.

Atmospheric errors

A frequently cited advantage of radar remote sensing over optical remote sensing techniques is that electromagnetic energy at radar frequencies can penetrate clouds, enabling the all-weather imaging capability of SAR systems. However, as mentioned briefly in section 2.2.1, the propagation of electromagnetic radiation through a medium – such as the atmosphere – is affected by its refractive index. Spatial or temporal changes of the refractive index modify the propagation velocity of electromagnetic waves, which in turn affects the signal travel time measured by radar systems. SAR image formation is not visibly affected by the atmospheric effects because the relative delay differences within an image are much smaller than the range resolution of the system. Although atmospheric delay signals of several centimeters have been observed in radar interferograms [Hanssen, 2001], the effect is small compared to several meters of slant range resolution in typical radar systems. Interferometric measurements in contrast resolve propagation time differences on the order of a fraction of a nanosecond between two SAR acquisition, clearly accurate enough to measure changes in atmospheric propagation delay.

Because the changes in refractive index, n_r , are relatively small, these changes are typically discussed in terms of the refractivity

$$N = (n_r - 1)10^6. \quad (2.33)$$

As mentioned in section 2.2.1, the bending of radar signal paths due to changes of the refractivity in the atmosphere is negligible for all SAR data available today [Hanssen, 2001], so that the one-way signal delay along an incident ray path due to

the refractivity of the atmosphere can be written as

$$\Delta t = 10^{-6} \int_0^H \frac{N}{\cos \Theta_i} dh, \quad (2.34)$$

where H is the height of the atmosphere and Θ_i is the incidence angle. The refractivity depends on atmospheric pressure, temperature, the amount of water vapor, the electron number density and the amount of liquid water present [e.g. Smith and Weintraub, 1953]. Because the electron number density in the ionosphere changes very slowly in space, the importance of ionospheric effects in interferograms is typically much less important than tropospheric effects [Hanssen, 2001]. Furthermore, in the range of the typical variability, the refractivity is most sensitive to changes in tropospheric water vapor.

Although the physical mechanisms affecting the propagation of the radar waves through the atmosphere have been extensively studied, it is generally not possible to correct interferograms for the atmospheric delay signals. Such a correction would require knowledge of all the atmospheric parameters affecting the refractivity at the acquisition times of the images used to form the interferogram. While some observations of atmospheric pressure, surface temperature and surface relative humidity are often available, they are usually not obtained at the times of acquisition. More importantly, these parameters can vary significantly over the area of the interferogram and vertically. Hanssen [2001] therefore proposed a stochastic treatment of the atmospheric signal contributions.

Two types of atmospheric disturbance are frequently observed in radar interferograms. The first type, causing irregularly shaped phase artifacts at various spatial scales (fig. 2-12), has been related to turbulent mixing of the atmosphere [Hanssen, 2001]. The second type is expressed as a residual phase signal in the interferograms that is highly correlated with the topography. This type of delay signal can be explained with elevation-dependent changes in the refractivity in a layered atmosphere [Delacourt et al., 1998; Hanssen, 2001].

As the interferometric observations cannot simply be corrected for the atmospheric

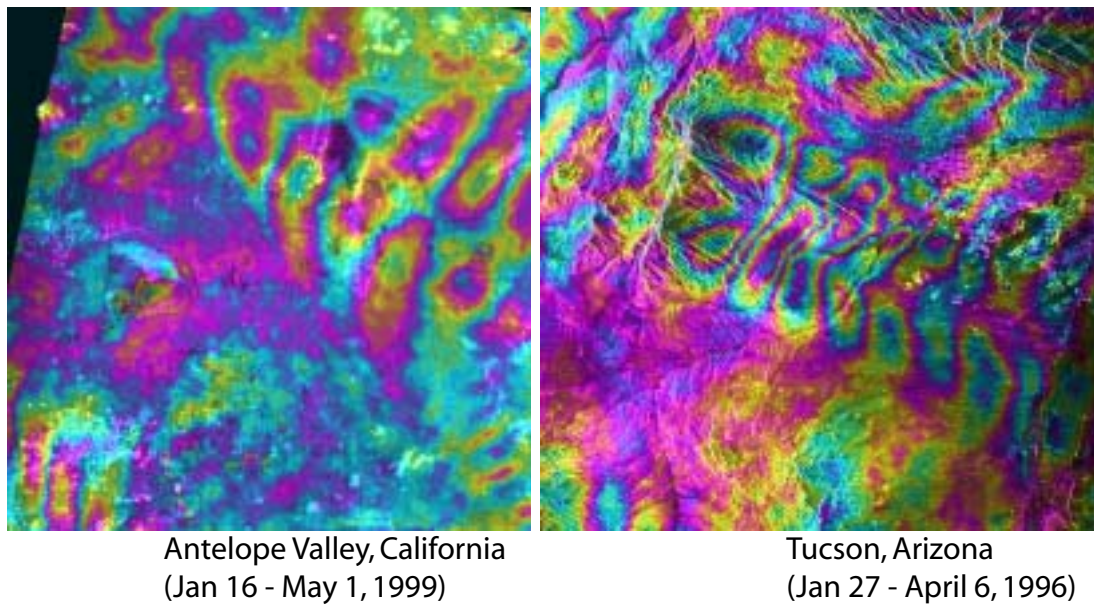


Figure 2-12: Two examples of atmospheric signals in InSAR phase measurements. In both cases one color-cycle corresponds to a round-trip difference in path-length of one wavelength (5.66 cm). Disturbances such as these are readily identified in images. Weaker or less characteristic patterns are much harder to recognize.

delay signals in absence of the large volumes of atmospheric data that would be required to do this, a more modest goal in InSAR applications has been to reliably distinguish atmospheric signals from deformation or topographic signals, to then exclude the areas affected by these “atmospheric artifacts” from subsequent analyses. A common approach has been to compare several independent interferograms over the same area. As turbulent atmospheric phenomena are assumed to be essentially uncorrelated in time after about a day or so, phase signatures that only appear in a single image are suspect of being caused by atmospheric contributions [e.g. Massonnet and Feigl, 1998]. Furthermore, if several interferograms are added (stacked), atmospheric contributions in different interferograms will cancel out, while the signal of interest (e.g. deformation or topography) will not. However, in differentiating between a deformation signal and an atmospheric signal this logic can only be used if the deformation process is temporally more correlated than the atmospheric signal, given the temporal sampling provided by the available SAR data. A subsidence signal contained in one interferogram followed by an uplift signal in the next cannot be differentiated from an atmospheric effect. Recent studies [Ferretti et al., 2000; Schmidt and Bürgmann, 2001] including large numbers of interferograms have used more elaborate temporal filtering techniques based on the same assumption of the spatial and temporal characteristics of the atmospheric signal. Ferretti et al. [2000] points out that this type of filtering can be optimized if *a priori* information about the statistics of the deformation process is available.

Another correction approach that relies on *a priori* information on the boundaries of the deforming area statistically characterizes the spatial correlation of the atmospheric signal in an (assumed) non-deforming area using measures such as the structure function or variogram. The spatial correlation of the atmospheric signal in the deforming areas allows the observed signal in the adjacent stable areas to be extrapolated to the deforming area. Crosetto et al. [2002] argue that this is a feasible strategy for removing the atmospheric signal in small subsiding areas, where the signal can be assumed to be approximately stationary.

Although atmospheric signals occur in interferograms at all spatial scales [Hanssen, 2001], their spectrum is altered in the image processing. Energy at the large-wavenumber

end of the spectrum is strongly reduced in correcting for residual orbit errors. As mentioned above, orbit errors can be approximated as linear phase ramps across the image. Such phase ramps are often removed using tie-points in the image for which the phase value is assumed to be known. This step essentially applies a high-pass filter to the signal, removing atmospheric signal contributions at these scales. Similarly, low-pass filtering is often applied to interferometric images to remove phase noise at the expense of resolution. While the kind of filtering applied varies from moving average (mean or median) filters to filters applied in the spectral domain, they all strongly reduce high-frequency atmospheric signal contributions. It is due to these processing steps that most atmospheric effects observed in images appear to have a “typical” extent in the images.

Signals from a layered atmosphere

The discussion in the previous paragraphs has focused on atmospheric signals caused by turbulent phenomena in the lower troposphere. Atmospheric signals correlated with topography have not received as much attention, although the effect can be significant (equivalent to several millimeters of surface displacement per 100 m of elevation difference) in the presence of topography [Delacourt et al., 1998; Hanssen, 2001]. To estimate the differential excess path-length causing the elevation-dependent phase signal in an interferogram, using only commonly available surface measurements of atmospheric conditions, Delacourt et al. [1998] proposed the expression

$$\Delta L = \frac{2.27 \cdot 10^{-3} \frac{\text{m}}{\text{mb}} (P_1 - P_2)}{\cos \Theta} (1 - 22.6 \cdot 10^{-6} m^{-1} \Delta z)^{5.26} + \frac{\nu}{\cos \Theta} (U_1 10^{\gamma(T_1 - k \Delta z)} - U_2 10^{\gamma(T_2 - k \Delta z)}). \quad (2.35)$$

Here,

- ΔL is the one-way excess path-length difference,
- P_1 and P_2 are the barometric pressures,
- U_1 and U_2 are the relative humidities (in percent), and

T_1 and T_2	are the temperatures (in $^{\circ}C$), all measured at the surface at the acquisition times of the two SAR scenes (indices 1 and 2). The temperature is assumed to decrease linearly with elevation (z). The values of the temperature gradient,
k ,	range from $0.0055^{\circ}C/m$ to $0.0072^{\circ}C/m$.
Δz	is the elevation difference between any point in the image and the reference elevation at which the atmospheric observations were made,
ν and γ	are empirical factors ranging from $0.4 \text{ mm}/\%$ to about $1 \text{ mm}/\%$ and $0.022^{\circ}C^{-1}$ to $0.029^{\circ}C^{-1}$, respectively, depending on the latitude and type of climate [Baby et al., 1988], and
Θ	is the look angle.

Although equation 2.35 allows the estimation of an elevation-dependent differential phase signal using generally available surface meteorological observations, the effectiveness of the correction is limited by the inherent assumptions about the atmospheric conditions. However, these elevation-dependent atmospheric signals are particularly limiting in studies of areas with high relief [e.g. Delacourt et al., 1998]. Over the typically very flat groundwater basins that are the focus of this dissertation the effects are small.

Displacement projection

Although not a measurement error in the narrow sense, a severe bias can be introduced when interpreting the line-of-sight radar observations as a three dimensional quantity. The problem arises because InSAR can only measure one component of the generally three-dimensional surface displacement field. Unfortunately this direction, along the radar line-of-sight, almost never carries any physical significance in the deformation process at hand. As a result, the LOS displacement observations are often interpreted in terms of displacements in three-dimensions, assuming a direction of the displacement. In the case of compacting aquifer systems the displacement has almost universally been assumed to be purely vertical [e.g. Riley, 1969; Galloway et al.,

1998; Hoffmann et al., 2001], based on geometrical and hydrological considerations for aquifer systems.

However, it has been pointed out that horizontal displacements may exist over aquifer systems [Helm, 1994], and they have been observed at the boundaries of a groundwater basin in southern California [Bawden et al., 2001]. Where the projection of horizontal surface displacements into the radar LOS are significant, assuming that the measured signal is caused by purely vertical displacements will introduce errors. Due to the steep incidence angle for ERS-acquired data the sensitivity of the LOS measurement to horizontal displacements is at most 42% of that to vertical displacements, somewhat limiting the relative importance of the bias. In Chapter 6 of this dissertation I analyze any occurrence of significant horizontal displacements accompanying land subsidence over several years comparing SAR data acquired on ascending and descending satellite tracks. The results indicate that horizontal displacements are in fact negligible for inelastic deformation processes in Antelope Valley. This suggests that horizontal displacements as observed by Bawden et al. [2001] in southern California may be largely restricted to the elastically deforming aquifers.

Chapter 3

Seasonal subsidence and rebound in Las Vegas Valley, Nevada

3.1 Introduction

In this chapter I analyze areal variations in the subsidence and rebound occurring over the Las Vegas Valley aquifer system in conjunction with measurements of the hydraulic head fluctuations causing these displacements. I present InSAR measurements of the typically small-magnitude, generally recoverable deformations of the aquifer system occurring at seasonal time scales. From these I derive estimates of the elastic storage coefficient for the aquifer system at several locations in Las Vegas Valley, using the concepts and equations presented in Chapter 2.

During the past several decades, Las Vegas, Nevada, (fig. 3-1) has experienced significant land subsidence due to compaction of the aquifer system. Though groundwater level declines had become apparent by 1912 [Maxey and Jameson, 1948] owing to discharging wells since the late 1800s, accelerated groundwater pumpage since the late 1940s to provide water for the currently fastest growing metropolitan area in the United States [U.S. Census Bureau, 2000] has lowered aquifer hydraulic heads over the entire valley. Maximum groundwater level declines in some areas exceeded 70 m between 1912 and 1972 [Morgan and Dettinger, 1991] and by 1990 the maximum decline exceeded 90 m [Burbey, 1995], although water levels had begun to recover in some areas. In 1998, accounting for artificial recharge of imported surface water, groundwater constituted about 14% of the municipal water supply [Coache, 1999].

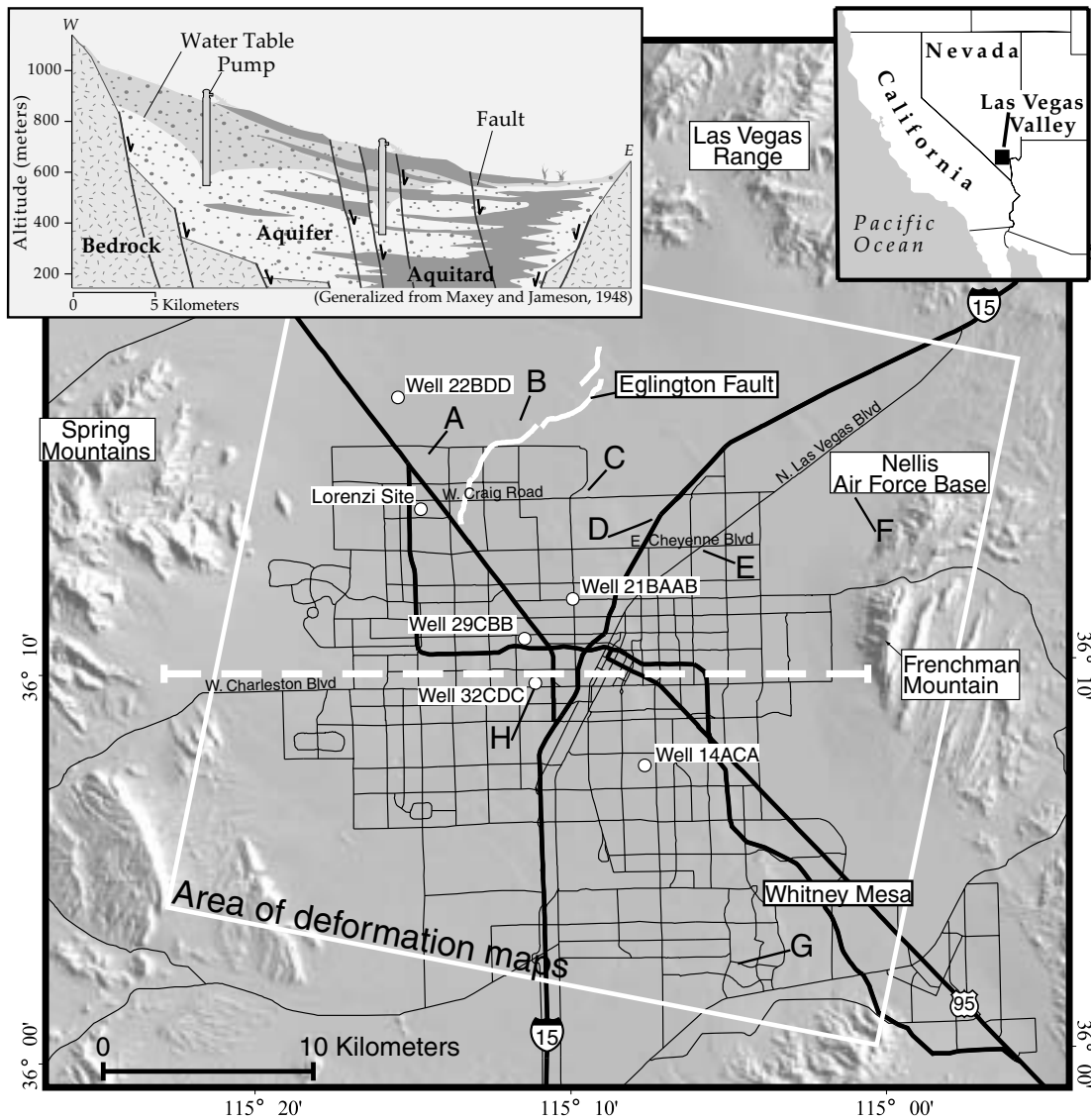


Figure 3-1: Location map of Las Vegas Valley. The white frame indicates the area displayed in figures 3-3, 3-4, and 3-5. The letters A-H label the same areas as in the displacement maps. The well and extensometer locations are shown as white dots. The inset on the top left shows a generalized stratigraphic cross section along the profile shown on the map (white dashed line).

The remainder was met with water imported from Lake Mead. In the central part of the valley declining heads in the aquifer system incorporating thick, highly compressible clay beds (aquitards) have led to subsidence rates of several centimeters per year during most of the 20th century, with resulting damage to structures and well casings. Differential subsidence has reactivated existing Quaternary faults and created new earth fissures [Bell and Price, 1991]. Recently, artificial recharge has become an increasingly important tool to store surplus surface water supplies and mitigate the negative effects of land subsidence due to overdrafting of the aquifer system in Las Vegas [Pavelko et al., 1999].

Subsidence in the Las Vegas area has previously been monitored using precise leveling surveys and a borehole extensometer installation, the Lorenzi Site, that was installed in 1994 [Pavelko, 2000]. Recently, Amelung et al. [1999] studied multi-year subsidence in Las Vegas Valley between 1992 and 1997 using interferometric techniques and satellite-borne synthetic aperture radar data. They delineated a subsidence bowl in northwest Las Vegas Valley where a maximum subsidence of 190 mm was measured between April 1992 and December 1997, and a central subsidence zone around the downtown area, where the maximum measured subsidence was about 110 mm in that time period. These results extended and enhanced the definition of these features, which had been previously mapped by leveling surveys in 1963 and 1987 [Bell and Price, 1991]. In addition, the InSAR imagery revealed that the Quaternary Eglinton Fault controls the spatial extent of the observed subsidence pattern along the southeastern boundary of the northwest subsidence bowl. The 1992-97 subsidence rates in the northwest subsidence bowl are significantly smaller than the 50 mm/yr measured from 1980 to 1982 by [Bell and Price, 1991]. Amelung et al. [1999] explained differences between interferograms spanning more than one year with differences in the contributions of periods of seasonal water level recovery relative to periods of water level decline. Interferograms that contained more winter season recovery showed less subsidence or relative uplift, while those with relatively more summer season decline showed more subsidence. However, they did not investigate the seasonal changes in the observed displacement patterns in detail or compare their magnitude to the observed multi-year subsidence.

Galloway et al. [1998] speculated that seasonal InSAR-derived displacement maps could be used in conjunction with hydraulic head measurements to compute the elastic storage coefficient of confined aquifer systems undergoing significant seasonal deformation (> 10 mm). Under the favorable radiometric conditions in Las Vegas Valley, relatively small ($\gtrsim 5$ mm) poroelastic deformations of the aquifer system in response to changes in aquifer head can be detected by InSAR within one month of the onset of the rapid drawdown and recovery of groundwater levels in response to the annual cycle of summer pumping and winter recharge. This capability, in addition to the importance of the valley fill aquifer system to the Las Vegas community, make this an interesting area of study.

The lack of spatially detailed hydrogeologic and geodetic information has limited the study of spatial heterogeneity in aquifer systems, which has been recognized to be an important factor in mitigating negative consequences of overdrafting [e.g. Carrillo-Rivera, 1999]. In this work, I present displacement maps derived from spaceborne radar measurements acquired by the European Remote Sensing satellites ERS-1 and ERS-2. These measurements can yield surface displacements accurate to subcentimeter levels at a spatial resolution of 20 m, over swaths 100 km in extent. The extensive coverage of Las Vegas Valley by the ERS satellites constitutes a catalog of accurate displacement measurements at unprecedented spatial resolution. It is my intent here to use these data to address the mechanics of deforming aquifer systems, and the controlling hydrogeologic parameters, in their spatial detail. This new constraint for hydrogeologic models promises to yield more information on the storage properties of the aquifer system. A better understanding of the areal variability of the aquifer system response to stress will be very useful in refining existing groundwater flow models and can improve the effectiveness of groundwater management schemes. It may further enable the identification of zones with a high potential of fissure formation, which would be valuable information in city planning.

The purpose of this chapter is threefold. First, I explicitly address seasonal-scale deformation in Las Vegas Valley by creating interferograms with temporal baselines on the order of a few months. Second, I document land subsidence during 1997-1999. Third, I use the InSAR-derived displacements and water level variations to obtain

an estimate of the elastic storage coefficients at six locations in the Las Vegas Valley aquifer system.

The material in this chapter is largely derived from a published paper [Hoffmann, Galloway, Zebker, and Amelung, 2001]. In addition to the material previously published there, this chapter includes a discussion of horizontal displacements analyzed in a comparison of ascending and descending data acquisitions (section 3.2.2) and some more detail on atmospheric artifacts (3.3). The theoretical background presented in the original paper has been omitted here as it was discussed at length in Chapter 2.

3.2 InSAR observations

3.2.1 Time series analysis

Measurements with high temporal and spatial resolution of both changes in aquifer hydraulic heads (measured as water level changes in wells) and resulting surface displacements can be used to improve estimates of the magnitude and distribution of storage coefficient values. In Las Vegas Valley coincident measurements of vertical displacement and hydraulic head are available only at the Lorenzi site (fig. 3-1). Presently, InSAR can map displacements at very high spatial resolution. Using the ERS satellites this can be done as frequently as every 35 days, the orbit repeat period of the satellites.

Las Vegas Valley offers favorable conditions for the application of InSAR because of its desert environment. The urban and sparsely vegetated dry surfaces that cover almost the entire Las Vegas Valley preserve the phase coherence of reflected radar signals over relatively long time periods, even though construction activities may cause a loss of phase coherence locally (section 2.2.2).

I used data from both ERS-1 and ERS-2 satellites, processed as 42 interferograms, spanning time periods between 2 and 35 months (fig. 3-2). The interferograms were used to create the displacement maps shown in figures 3-3, 3-4, and 3-5, and to construct the time series measurements shown in figures 3-6 and 3-11. I could not use any acquisitions between January 1994 and March 1995, when the ERS-1

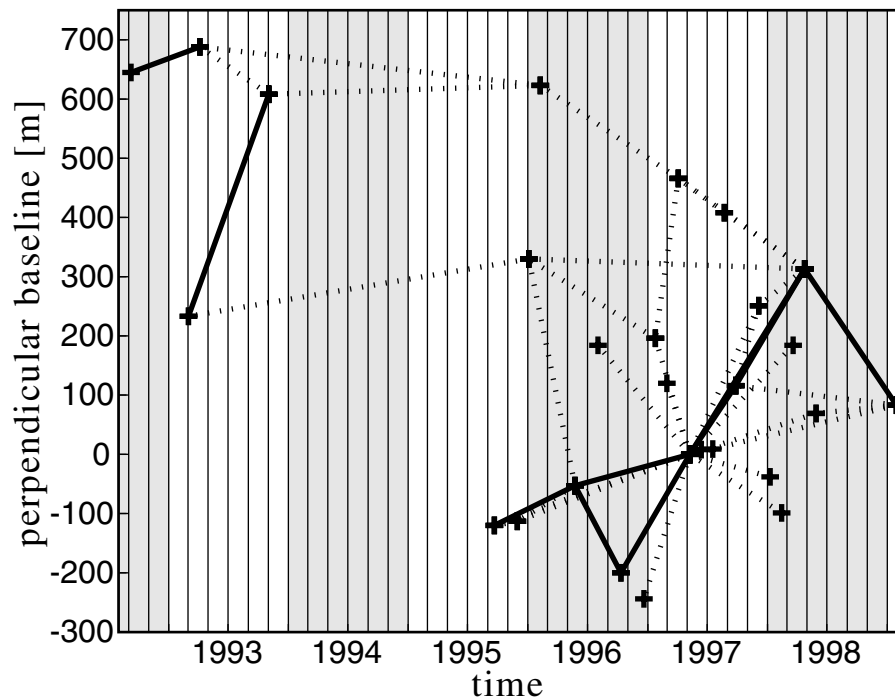


Figure 3-2: Plot of relative orbit location in space and acquisition times for the radar images used in this study. An interferogram is represented by a line connecting the “+” symbols representing the individual acquisitions. The differences between acquisitions along the ordinate indicates the interferometric perpendicular baseline (B_{\perp}), and the difference in time (abscissa) indicates the time interval spanned. The solid lines identify the interferograms used for the displacement maps shown in figures 3-3, 3-4, and 3-5. There are 42 interferograms in this plot. The largest perpendicular baseline is 320 m.

satellite was in different orbits. The spatial resolution of the images is initially about 4 m in the along-track direction (azimuth) and 20 m in the across-track direction (range). To eliminate some of the noise and reduce geometrical distortions I averaged (multilooked) the images, resulting in a 40 m resolution in both azimuth and range. The orbit repeat period of 35 days is the maximum temporal resolution using ERS-2 data.

The accuracy of the range change measurement in radar interferograms decreases with decreasing radar correlation. Correlation in the interferogram depends linearly on the component of the radar baseline perpendicular to the line of sight (called the perpendicular baseline, B_{\perp}) [Zebker and Villasenor, 1992] (eq. 2.32). Therefore, in the case of exceedingly long B_{\perp} , I combined (stacked) two or three interferograms with shorter B_{\perp} to span the same time period in order to maximize the accuracy in the displacement measurements. The longest B_{\perp} used was 320 m (fig. 3-2). In cases where I compared interferograms with long B_{\perp} to stacks of two or more images covering the same time periods, I found only insignificant differences in displacements, and an improvement in the measurement accuracy. Small residual tilts across the image that result from imprecise knowledge of the orbital geometries were corrected by subtracting a least-squares plane fit to residual displacement values at a large number of tie points distributed over parts of the valley where no significant subsidence was detected. The measured range changes were projected into the vertical dimension using the incidence angle of the ERS satellites (≈ 23 degrees).

The available ERS SAR images for Las Vegas Valley cover a wide range of time periods and allow the mapping of the displacement patterns related to groundwater withdrawal with high resolution in both space and time. I concentrated on interferograms covering time periods of up to a few months, in order to study the temporal variations in the displacement patterns within individual years. I found that the rates of seasonal displacement exceed the rates of yearly to multi-year displacement almost everywhere. For the following discussion, I assume that the observed range changes are caused by vertical ground displacements. Observed range increase is referred to as subsidence, and range decrease as uplift. Following Amelung et al. [1999], I refer to the deforming areas in the northwest and central part of Las Vegas Valley as the

northwest subsidence bowl and the central subsidence zone, respectively, despite the fact that the observed displacements in the central part of Las Vegas Valley are to a large extent uplift, particularly during the winters. Figures 3-3, 3-4, and 3-5 are displacement maps derived from the acquisition pairs shown as solid lines in figure 3-2. Extensive subsidence occurs during the summer over the entire Las Vegas Valley (fig. 3-3). Though subsidence is greatest in the northwest subsidence bowl, large parts of the central Las Vegas Valley and a few isolated locations in the eastern and southern parts of the valley also subside at detectable rates.

In Las Vegas Valley the summer drawdown season typically occurs during the period April to November, and the remainder of the year constitutes the winter recovery season. Figures 3-3 and 3-4 show the measured vertical displacements occurring during four summer seasons (1993, 1996, 1997, and 1998) and four winter seasons (1992-93, 1995-96, 1996-97, and 1997-98), respectively. The displacement map for the summer of 1998 (fig. 3-3d) also includes a large part of the following winter season because no SAR acquisition was available in the fall of 1998. In the figures, one color cycle corresponds to 20 mm of vertical displacement with turquoise being zero displacement (see colorscale). Uplift is characterized by blue-red-yellow-green-blue and subsidence is displayed with the reverse color order.

The large-scale subsidence patterns recur in all four summer seasons (fig. 3-3). However, the northwest subsidence bowl and the central subsidence zone are notably more defined in 1993 (fig. 3-3a) than in the three more recent summer seasons (fig. 3-3b-d). Subsidence during the summer of 1998 is least pronounced (fig. 3-3d), in particular in the central subsidence zone. This is, in part, caused by some summer subsidence being offset by some 1998-99 winter recovery in the interferogram.

During recent winters, subsidence seems to have been largely arrested over the entire valley and extensive uplift can be observed (fig. 3-4c, d), especially in the central subsidence zone. The uplifting areas are larger and the uplift is greater in the most recent winter season 1997-98 (fig. 3-4d) than in the earlier 1995-96 and 1996-97 images (fig. 3-4b, c). Although the maximum subsidence within the northwest subsidence bowl exceeds 10 mm in all observed winter seasons, the subsidence bowl is less defined in more recent winter seasons (fig. 3-4b-d). In the 1997-98 winter season,

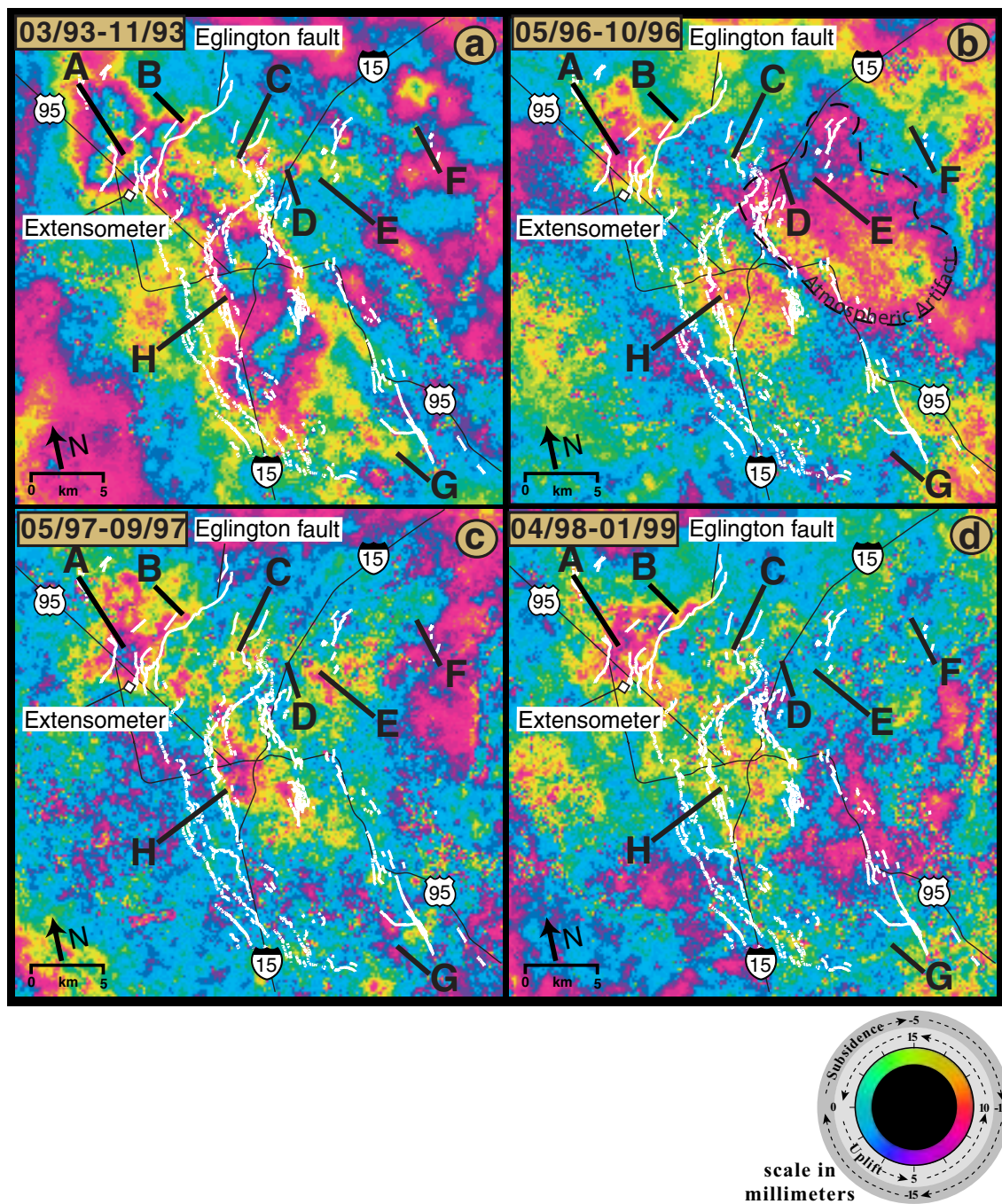


Figure 3-3: Comparison of the displacement patterns for four summer seasons. Uplift and subsidence are determined by the order of the colors: Uplift is characterized by blue-red-yellow-green-blue and subsidence is displayed with the reverse color order (see colorscale). Figure (d) also contains a significant part of a winter season. Most large scale patterns recur in all images, even though they exhibit varying magnitudes. Subsidence rates are generally decreasing in recent years. The large uplift seen in the eastern part of (circled pink color in (b)) is an atmospheric artifact. The northwest subsidence bowl includes areas A and B.

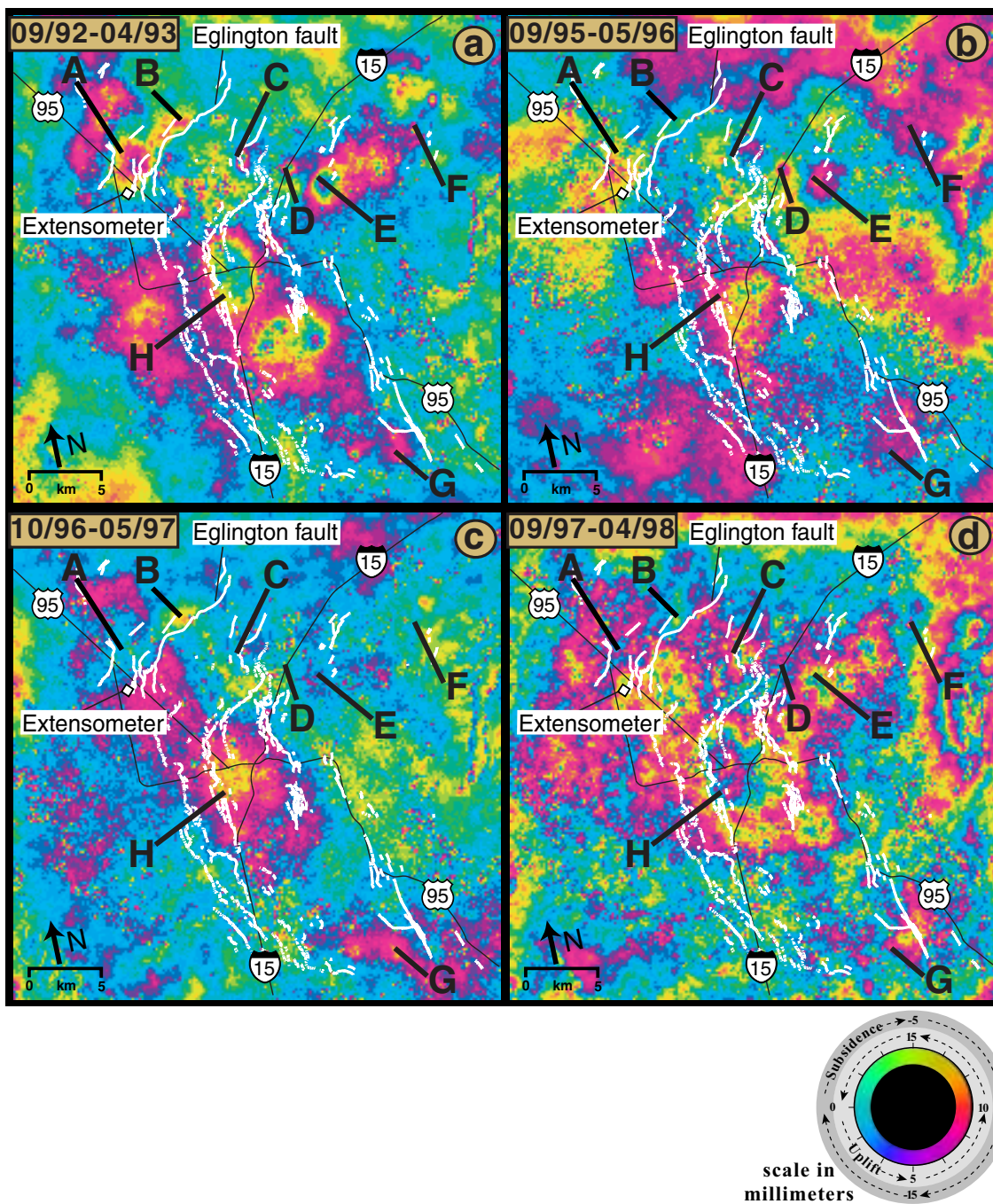


Figure 3-4: Displacement patterns for four winter seasons. The dominant deformation observed is uplift in the central subsidence zone. The subsidence in the northwest subsidence bowl (areas A and B) has almost entirely vanished in recent years. Note that the uplift in (d) is significantly stronger than in (b) and (c) and also somewhat larger than in (a).

	Summers				Winters				Years	
Figure	3-3a	3-3b	3-3c	3-3d	3-4a	3-4b	3-4c	3-4d	3-5a	3-5b
Area	04/06/93- 11/02/93	05/24/96- 10/11/96	05/09/97- 09/26/97	04/24/98- 01/29/99	09/08/92- 04/06/93	09/21/95- 05/24/96	10/11/96- 05/09/97	09/26/97- 04/24/98	05/24/96- 05/09/97	05/09/97- 04/24/98
A	+31	+16	+14	+16	+11	+5	+2	-2	+20	+14
B	+24	+11	+10	+17	+9	+5	+2	-1	+14	+9
C	+28	+12	+3	-5	-29	+2	-5	-19	+6	-18
D	+28	-4	+2	-2	-22	+20	+2	-3	-2	+11
E	+1	-12	+14	-1	-30	-12	0	-15	-11	-2
F	+16	+6	-2	+3	-20	-6	+1	-9	+6	-11
G	+7	-6	-6	+3	-9	-3	-11	-3	-16	-9
H	+12	+6	+11	+8	-13	-5	-14	-27	-2	-16

Table 3.1: Measured vertical displacement magnitudes for the locations labeled in figures 3-1, 3-3, 3-4, and 3-5. All values are in millimeters. Positive values are subsidence, negative values uplift. As discussed in section 3.3, displacement magnitudes smaller than 5 mm are probably insignificant.

there is some localized uplift (blue and pink areas) within the subsidence bowl (fig. 3-4d).

The maximum subsidence detected within the northwest subsidence bowl (area A) was 42 mm during the summer of 1993, almost twice the maximum subsidence measured in each of the summer seasons in 1996 (24 mm), 1997 (26 mm) and 1998 (24 mm). Peak subsidence of 19 mm, 26 mm, 19 mm, and 12 mm is detected during the winters of 1992-93, 1995-96, 1996-97, and 1997-98, respectively (fig. 3-4).

The vertical displacements measured at locations A-H in Figures 3-3, 3-4 and 3-5 are listed in Table 3.1. The measured displacements are averages over areas of about 20,000 m² (13 pixels) at each location. The northwest subsidence bowl (areas A and B) shows a dramatic decrease in summer subsidence since 1993, and remains constant from 1996-98. Winter subsidence in the northwest subsidence bowl has been decreasing linearly since 1992. Areas C through F show localized displacement patterns that may be related to local pumpage or recharge. The magnitudes of seasonal displacement are mostly decreasing with time in these areas. Note that values less

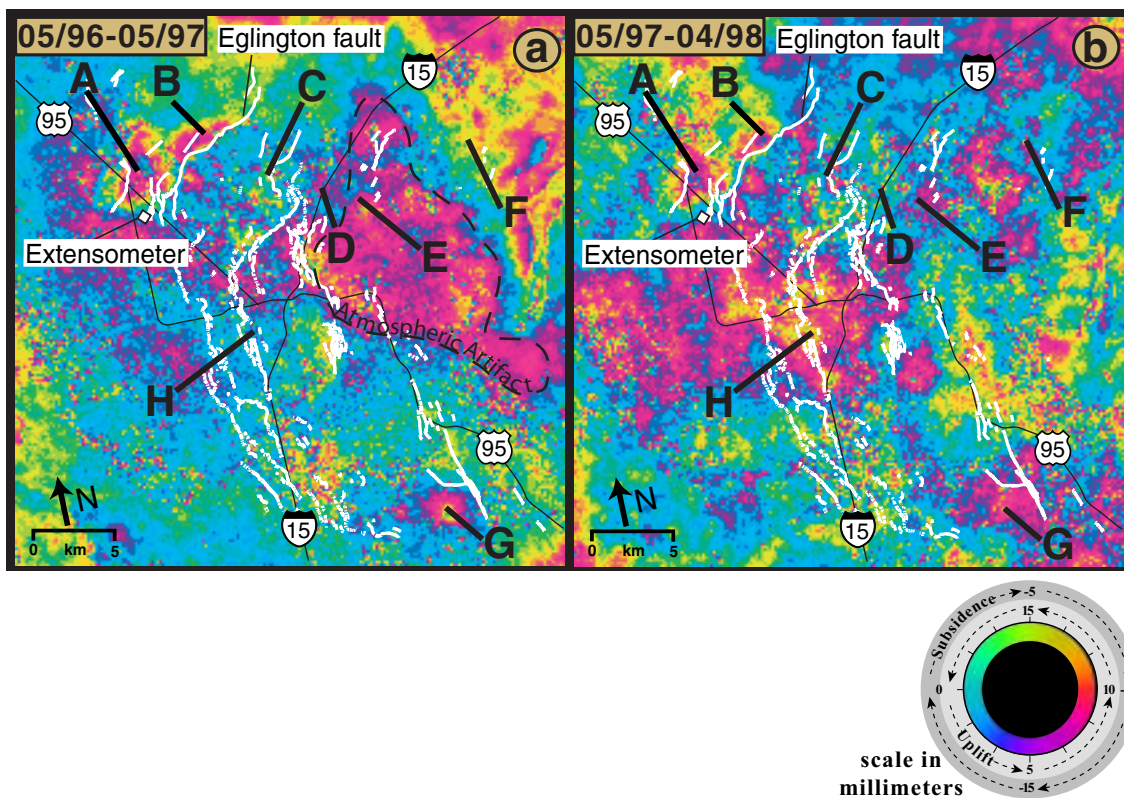


Figure 3-5: Displacement patterns compared for two consecutive annual periods. Residual subsidence is occurring in the northwest subsidence bowl while the central subsidence zone shows uplift in 1997-98 (b). The extended uplift indicated by the circled area in figure (a) is probably an atmospheric artifact.

than approximately 5 mm probably are not significant, as discussed in the following section. At area E, almost all displacements over the observed periods are uplift. At Whitney Mesa (area G), a curious variation in the displacement trends is observed, from decreasing subsidence (or increasing uplift) from summer 1993 to winter 1996-97, to comparable displacement magnitudes of opposite trend thereafter. The displacements at area H are typical for the central subsidence zone. Summer subsidence and winter uplift are relatively constant over the entire period of observation (table 3.1).

Figure 3-5 shows measured displacements for two consecutive annual periods. During the first annual period 1996-97 (fig. 3-5a) displacements are generally small in the central subsidence zone (including area H), although some small localized areas

show subsidence of about 19 mm. The northwest subsidence bowl (including areas A and B) is pronounced with a maximum subsidence of 28 mm. The moderate uplift seen over an extensive area in the eastern part of the valley (labeled) is likely an atmospheric artifact as it is unique to this particular interferogram. During the second annual period 1997-98 (fig. 3-5b), a large area of uplift in the central subsidence zone (area H) has a maximum uplift of approximately 23 mm. The northwest subsidence bowl is somewhat less developed than in the previous year, though the maximum subsidence values are about the same, 29 mm. In some interferograms an apparent displacements on the order of 20–30 mm is observed in areas of high relief, especially at Frenchman Mountain, in the east, and the Spring Mountains in the west (fig. 3-3b, 3-4d, 3-5a). For reasons discussed in sections 2.2.2 and 3.3, these relatively strong signals in the mountainous areas do not discredit the accuracy of the measurements on the valley floor. Figure 3-6 shows the InSAR derived displacements at area A in the northwest subsidence bowl, the central subsidence zone (about 2 km east of H) and at Whitney Mesa (area G). All measured displacements are shown relative to May 1997. I chose this reference image because it is central to the acquired data in time as well as baseline geometry. This allowed me to form a large number of displacement maps directly from interferograms involving this scene, rather than stacking interferograms as described in the previous section. Where decorrelation due to long temporal baselines or large perpendicular baselines prevented forming good interferograms, I combined other interferograms, each with a smaller perpendicular baseline, spanning a shorter time period, to form the displacement map. Each of these displacement maps is represented by one data point in each panel of figure 3-6. The error bar shown on the most recent data point in each panel are ± 5 mm to indicate a rough estimate of the achieved accuracy (section 3.3). The dashed line segments connect data points that span longer time periods (> 5 months) which cannot be used to estimate seasonal fluctuations. In the northwest subsidence bowl (top panel) a clear subsidence trend is observed, on which seasonal fluctuations are superimposed. The subsidence rate is decreasing in recent times. In the central subsidence zone (middle panel), strong seasonal displacements on the order of 20 mm are observed. Since summer 1995 there has been no significant long-term trend, as the subsidence occurring

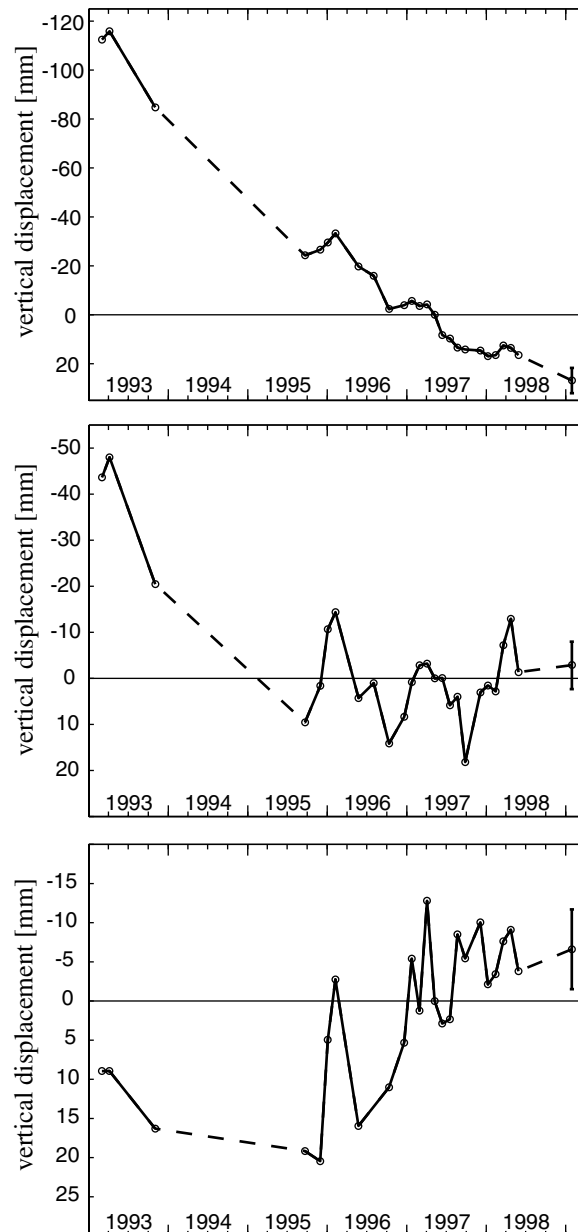


Figure 3-6: Measured vertical displacements at three locations in Las Vegas Valley: The panels show the displacements at the center of the northwest subsidence bowl (area A in figures 3-3-3-5), the central subsidence zone (2 km east of area H), and Whitney Mesa (area G) from top to bottom. The displacements are measured in millimeters relative to the May 1997 scene. The estimated accuracy of about ± 5 mm is indicated by the errorbar on the most recent data points.

during the summer seasons is generally recovered as uplift in the following winter season. Thus, the earlier subsidence in this area has been essentially arrested for the 4-year period from fall of 1995 to winter of 1998-99. At Whitney Mesa (bottom panel), a long-term uplift trend is observed with approximately 15 mm of uplift from fall of 1995 to winter of 1998-99. Seasonal fluctuations as well as the long term uplift rate are decreasing in more recent times.

3.2.2 Horizontal surface displacements

To interpret the InSAR observations discussed in section 3.2.1 in terms of vertical surface displacements I have assumed that the observed surface displacements are purely vertical. This assumption is commonly made in the context of compaction in aquifer systems and is usually justified by the very large horizontal extent of the compacting layers with respect to their vertical thicknesses. However, a horizontal displacement component is theoretically expected even if the gradient of the stress change is vertical (see section 2.1). Furthermore, the horizontal displacement component can become significant where the spatial gradient of the stress change is large or above structural heterogeneity in the subsurface. Helm [1994] argues that horizontal displacements can be of the same order of magnitude as vertical displacements. In this section I compare InSAR observations from two different orbits (ascending and descending) to test the validity of the assumption that the observed displacements are vertical. Because of the different acquisition geometry horizontal displacements project differently into the radar line of sight, while vertical displacements affect both acquisitions equally. In principle the deformation field derived from ascending and descending geometries should be the same if the displacements are truly vertical.

Unfortunately, this analysis is hampered by a number of difficulties. At least one pair of images for each of the two orbits must be available that allows forming an interferogram. Also, both image pairs must observe the same displacement field. In the case of ongoing surface deformation this can only be ascertained by choosing acquisition pairs that span the same time period. Furthermore, differences between the two resulting interferograms can also be caused by differences in the tropospheric

orbit number	date	B_{\perp}
Ascending		
12413	1997/09/04	-77 m
10409	1997/04/17	
Descending		
12735	1997/09/26	-118 m
10731	1997/05/09	

Table 3.2: Acquisitions used in comparing ascending and descending data to study horizontal displacements in Las Vegas Valley.

delay signal contained in the images.

The ERS ascending and descending acquisitions over Las Vegas Valley are separated by at least 11 days in time, which is too long to reliably exclude any seasonal displacements occurring during this time. At the time of this study, the best acquisition pair available spanned about 4.5 months during the summer of 1997 (table 3.2). However, the time period spanned by the ascending image includes about 3 weeks from April 17, 1997 to May 9 1997 that are not contained in the time period spanned by the descending image. Similarly, the descending image includes displacements during about 3 weeks from September 4 to 26 of the same year that are not contained in the ascending image. Unfortunately, this incongruence compromises the conclusions from the comparison of the observations.

Figure 3-7 shows the geocoded interferograms for the two acquisition pairs. There is a strong signal in the ascending image (3-7a), which is highly correlated with the topography. The signal is too strong to be explained by inaccurately known satellite orbits (2.2.2), as I used precise orbit information in the processing. Instead, a large part of the signal is probably due to the elevation-dependent atmospheric signal discussed in section 2.2.2. To correct for the elevation-dependent part of the signal using the equations presented by Delacourt et al. [1998] (eq. 2.35) requires knowledge of surface temperature, atmospheric pressure and relative humidity at the acquisition times of the images. Because these values vary over spatial distances much smaller than the area imaged, measurements from different locations in Las Vegas Valley would ideally have to be included in the estimation of the correction. These data

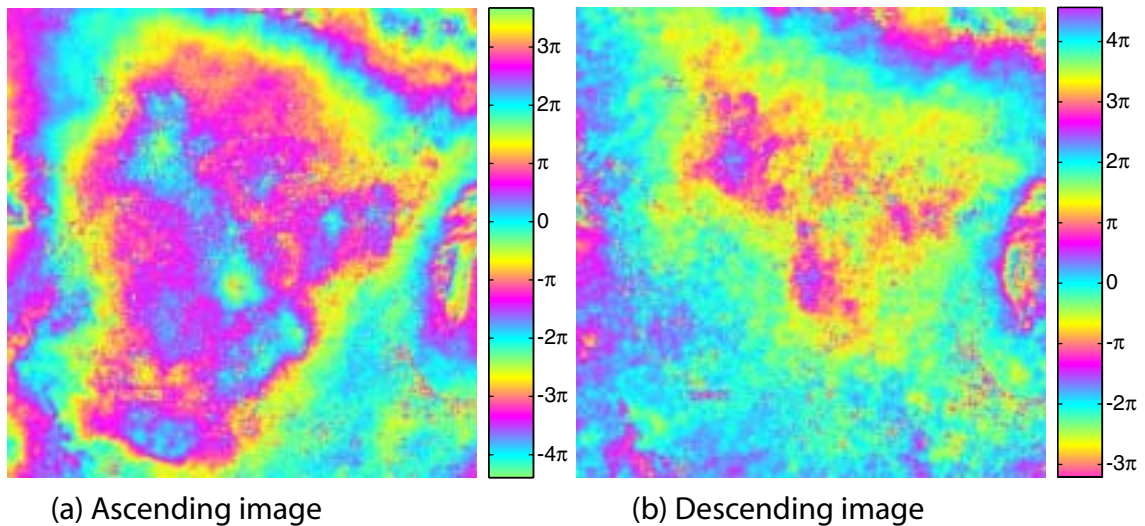


Figure 3-7: Ascending and descending interferograms (table 3.2) for Las Vegas Valley. The strong signal pattern in the ascending image is discussed in the text.

were not readily available and I therefore selected a simpler approach. Using the mean daily temperature and atmospheric pressures measured at a single station (McCarran International Airport) at the days of the acquisition, I found the difference in relative humidity between the two image acquisitions that best removed the observed elevation-dependent signal. All values were assumed to be constant for the entire image. The parameters used and the estimated relative humidity differences are summarized in table 3.3. Figure 3-8 shows the two interferograms in figure 3-7 after correction for the elevation-dependent signal. The images clearly differ (fig. 3-8). Particularly the ascending image (fig. 3-8a) seems to be strongly contaminated with signals deriving from turbulent atmospheric mixing, although the topographic dependence has been largely removed. The fact that the level of atmospheric disturbance is significantly higher in the interferogram formed from the ascending passes may be related to the different acquisition times of day. The ascending images were acquired at 10.22 p.m. local time, while the descending images were acquired at 10 a.m. local time. Differences in atmospheric dynamics between these times may explain these difference. Figure 3-9 shows the vertical surface displacement (assuming no horizontal displacements) along the three profiles shown in figure 3-8. The curve for the

	Ascending		Descending	
	Master	Slave	Master	Slave
Mean Temperature [K]	298.7	296.5	296.5	300.4
Mean Pressure [mb]	937.21	933.16	935.22	934.95
Min. rel. humidity	40%	11%	52%	14%
Max. rel. humidity	93%	24%	93%	33%
estimated rel. humidity difference	-73%		-54%	
temp. gradient [K/m]	0.008		0.008	

Table 3.3: Atmospheric data used to correct elevation-dependent phase signal in interferograms (fig. 3-7). The data were obtained from the National Climatic Data Center web site (<http://www.ncdc.noaa.gov>) and were measured at McCarran International Airport (elevation 660m). The Las Vegas latitude of 36 degrees north leads to interpolated values of the two empirical constants (see Baby et al. [1988]): $\gamma = 0.0224^{\circ}C^{-1}$ and $\nu = 0.7574$ mm.

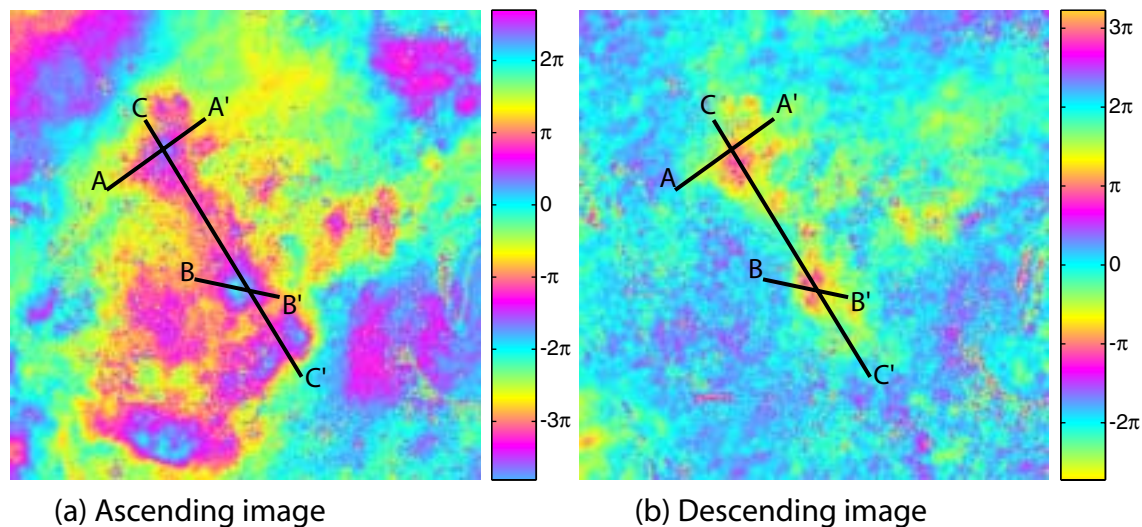


Figure 3-8: Ascending and descending interferograms after correction for best-fit elevation-dependent atmospheric signal (table 3.3, equation 2.35). A linear phase ramp was also removed. One color cycle in the images shown corresponds to 28.33 mm change in the radar line of sight. The phase values along the profiles indicated are shown in figure 3-9.

ascending data (blue) has been shifted to have the same mean as the curve for the descending data (red). While the observations along the profiles between the ascending and descending acquisitions are clearly highly correlated, their disagreement may point to the occurrence of horizontal displacements in Las Vegas Valley during the summer of 1997. Due to the relatively steep incidence angle of the ERS acquisition geometry ($\sim 23^\circ$), the measurement sensitivity to horizontal displacements is at most 42% of the sensitivity to vertical displacements, and even less if the angle between the satellite orbit and the direction of horizontal displacement is small. Despite the subsidence estimates derived from ascending and descending data differing on the order of 1 cm locally (fig. 3-9), this cannot be interpreted to indicate the presence of significant horizontal displacements. The low signal-to-noise ratio due to the small amount of displacements accumulating during a single summer season, the fact that the time periods spanned by the interferograms are not identical and the strongly obvious atmospheric contamination of the images make it impossible to discern the small signal expected from horizontal displacements. Using the radar data currently available for Las Vegas Valley I can therefore neither accept nor refute the presence of significant horizontal displacements.

A similar analysis using data acquisitions spanning several years in Antelope Valley, California (Chapter 6) indicates that horizontal surface displacements accompanying inelastic compaction are negligible. However, Bawden et al. [2001] observed seasonally fluctuating horizontal displacements exceeding 1 cm in the Santa Ana basin, California. Their observations suggest that elastic deformation processes in aquifers are accompanied by measurable horizontal displacements, particularly near the boundaries of the aquifer system.

3.3 Accuracy

Very small displacements must be detected reliably if we wish to successfully measure subtle seasonal variations in the displacement patterns in Las Vegas. Although the phase measurements used in the interferometric technique are accurate enough to detect millimeter-level variations, systematic errors introduced by uncertainties

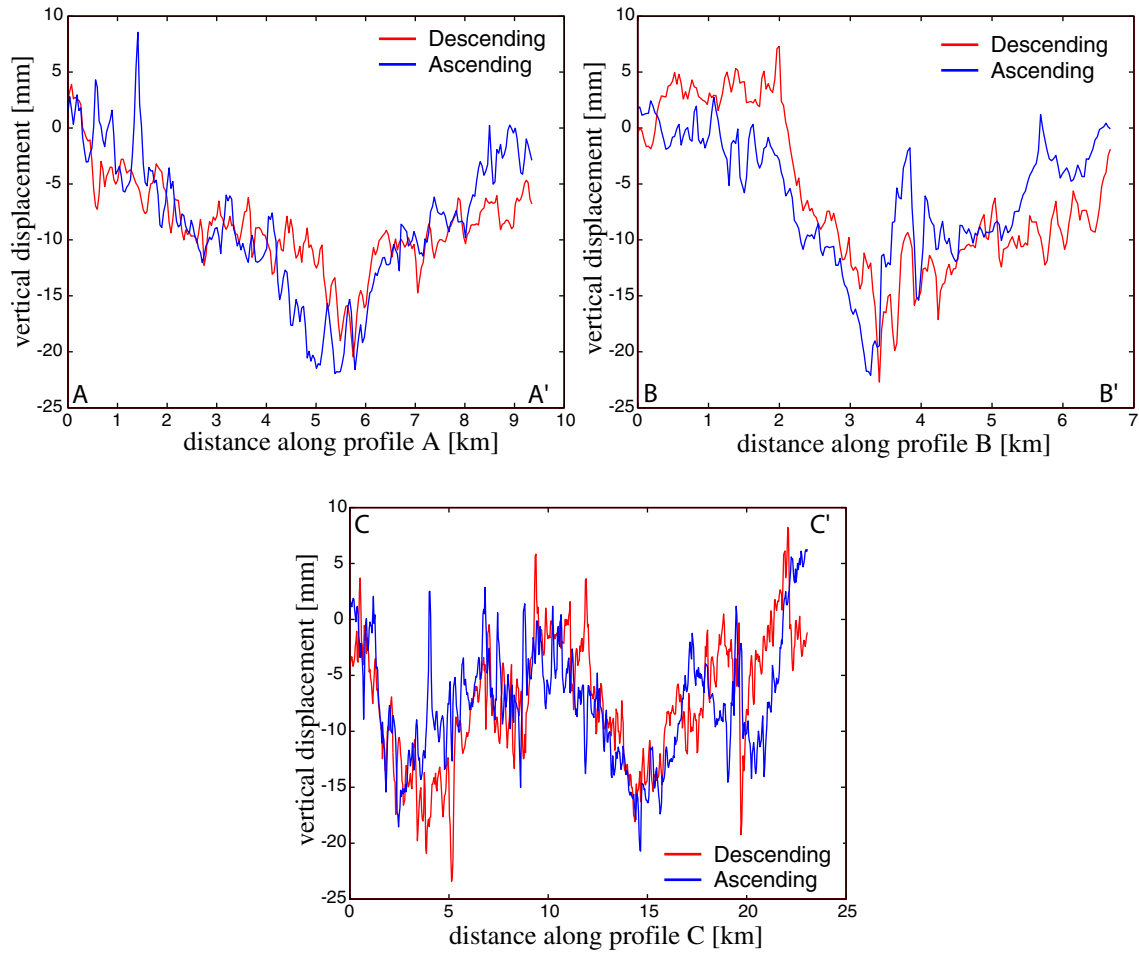


Figure 3-9: Vertical surface displacement along profiles shown in figure 3-8 assuming no horizontal displacements. The ascending curves (blue) have been shifted to have the same mean as the descending curves (red).

in the orbits and changes in tropospheric propagation may bias the InSAR-derived displacements. Because errors due to the imperfect knowledge of the orbits depend on topography and increase with elevation difference, they are less critical in the relatively flat Las Vegas Valley. Small inaccuracies in the satellite orbits introduce roughly linear phase trends across the image [Zebker et al., 1994]. Thus these can be corrected for by subtracting a plane from the image that minimizes these tilts in areas where no significant subsidence is observed. As the selection of these areas where subsidence is not expected is somewhat subjective, biases of the resulting displacements may result. However, the residual biases are likely small compared to possible errors introduced by tropospheric delays in the interferograms. I estimate that residual orbit errors are less than 1 mm over the flat areas of the valley.

Tropospheric errors are a more important concern in seasonal observations by InSAR. Where constant deformation rates persist over considerable time periods these tropospheric errors can often be decreased by averaging several interferograms. However, in Las Vegas seasonal displacement patterns change too rapidly to use this approach. A signal of localized subsidence and subsequent rebound may not be easily distinguished from tropospheric delay signals. One criterion that is frequently applied in interferometric studies to detect tropospheric artifacts, namely that they tend to appear only in individual interferograms [Massonnet and Feigl, 1998], could also represent a seasonal subsidence feature unique to one particular season.

Although it is easy to misinterpret some tropospheric signals as deformation (and vice versa) it is, nonetheless, usually possible to differentiate between tropospheric artifacts and subsidence. Most displacement patterns appear at the same area over several seasons, while tropospheric delays, which are statistical in nature, tend not to recur at exactly the same location in consecutive summer or winter seasons. Thus I assume that displacement patterns which are observable over several seasons, such as the subsidence bowl in the northwest or the displacements in the central subsidence zone, are true deformation signals. Conversely, patterns which do not seem to correspond to an area that has been observed before, are likely, though not certainly, due to tropospheric delay rather than deformation.

Images with strong tropospheric artifacts are easily identified due to characteristic

patterns and scales of tropospheric phenomena. These images can then be excluded from the interpretations or the values drawn from these images be assigned significantly greater uncertainties. From my experience with the large number of interferograms I processed over the area I estimate that tropospheric delays cause less than about 5 mm error in the measured vertical displacements within the valley, this being the level of easily recognized artifacts.

As discussed in section 2.2.2, atmospheric signal contributions are in fact not constrained to certain spatially localized “artifact”. A more thorough treatment would account for atmospheric effects at all spatial scales. I limit my analysis here to the much simpler argument of recognizable artifacts in the images. The spatial scales at which these occur are likely the most important. The very large wave number components are removed or strongly damped by the removal of a linear phase ramp in the correction for orbit inaccuracies. Similarly, the atmospheric signal energy at the small-wavelength end of the spatial spectra (high spatial frequencies) is suppressed by low-pass filtering of the signal to reduce phase noise in the processing. Although this argument cannot replace a more rigorous treatment for a formal error-analysis, it supports using the level of easily recognized artifacts in the interferograms as an approximate measure for the accuracy in this study. In some of the interferograms I observe a relatively strong phase signal, corresponding to about 20 to 30 mm of vertical displacement, in the areas of high relief surrounding Las Vegas Valley, especially at Frenchman Mountain, in the east, and the Spring Mountains, in the west (fig. 3-3b, 3-4d, 3-5a). These signals derive from changes in tropospheric conditions as a function of altitude (see section 2.2.1). Electromagnetic waves are affected by temperature as well as moisture content in the troposphere, which are functions of altitude. These tropospheric artifacts can mimic topographic residuals [Delacourt et al., 1998]. This has been discussed in some detail in section 2.2.2. On the valley floor, this effect does not constitute an important error source, because of the absence of significant topography.

Misinterpretations of measured displacements could also potentially be due to variations in soil moisture content, which can cause measurable displacements of the land surface (section 2.1.3). Higher soil moisture contents may cause relative

soil swelling and lower soil moisture contents soil shrinking. Therefore, more lawn watering in the summers would lead to swelling and less watering in the winters would cause shrinkage. However, as this effect is not observed anywhere outside the subsiding areas, I assume that it is negligible over the entire imaged area.

Because the radar measures changes in range, the distance between the satellite and the ground, to compute equivalent subsidence and uplift the measured range changes are projected into the vertical dimension under the assumption that no horizontal deformation occurs due to compaction of the aquifer system. According to Helm [1994], inhomogeneities in the aquifer system or steep gradients in the piezometric surface may cause horizontal displacements of the same order of magnitude as the vertical displacements. If there are horizontal displacements with a range component they will contribute to the error in the measurement. In Las Vegas Valley the occurrence of numerous tensional fissures at land surface provides clear evidence of localized horizontal displacements [Bell and Price, 1991]. I attempted to assess the importance of biases from horizontal displacements on the basin scale by comparing images from different acquisition geometries (section 3.2.2). However, due to limitations of data availability and strong atmospheric artifacts the results were inconclusive. It should be noted though, that due to the relatively steep incidence angle the phase measurement is at least 2.3 times more sensitive to vertical displacements.

3.4 Estimation of aquifer system storage coefficients

In this section I demonstrate, for six locations in Las Vegas Valley, how estimates of the aquifer system elastic storage coefficients can be derived from the InSAR displacement maps and contemporaneous measurements of water levels in wells, using equation 2.18. The elastic storage coefficient of aquifer systems is a bulk value that reflects the responses of the aquifer and aquitard fractions of the aquifer system to variations in head in those units. It is a critical hydraulic parameter that strongly influences the nonsteady flow of groundwater and is important to groundwater resource evaluations. Typically, these bulk values of the storage coefficient may be difficult to obtain and of questionable reliability. In situ values can be obtained

from measurements of drawdown rates in pumping tests, but these can be costly and often are representative of only the most permeable fraction of the aquifer system, the aquifers. Values can also be measured in the laboratory from core samples but these measurements generally are not representative of in situ conditions [Riley, 1998]. Most often the aquifer storage coefficient is estimated from the 'rule-of-thumb' relation, $S = 3 \cdot 10^{-6}b^*$, where b^* is the saturated aquifer thickness in meters [Todd, 1980]. I use S_{ke}^* to denote the elastic skeletal storage coefficient of the aquifer system as a whole, as opposed to S , the storage coefficient for the aquifer as defined by Jacob [1950]. For this analysis, I assume that the measured range changes are attributed only to vertical displacements of the surface. This assumption may bias the calculated elastic storage coefficients if horizontal displacements are significant. I calculated the elastic storage coefficient at the six observation wells shown in figure 3-1. At each site hydraulic head (measured as the depth to water level in the well below land surface) is monitored in wells penetrating the aquifer system at depths greater than 60 m. Water levels were measured at least every three months over the time period spanned by the InSAR observations. The water levels and InSAR-derived ground displacements were used to determine the stress-strain relationship at these sites (fig. 3-10). Water level variations, plotted on the y axis, represent the applied stresses and the ground displacements, plotted on the x axis, represent the vertical deformation of the aquifer system. Interferograms with large tropospheric residuals were excluded from the analysis. After Riley [1969], I computed an estimate of the elastic skeletal storage coefficient from the inverse slope of the best fitting line to the stress-displacement data. A weighted least squares approach was used, taking into account that the measurement errors in interferograms that share one radar acquisition are correlated. For each of the wells except the well at the Lorenzi Site, where water level was measured hourly, I linearly interpolated the water level values to the radar acquisition dates. The resulting storage coefficient estimates (Table 3.4) ranged from $4.2 \cdot 10^{-4}$ at well 22BDD in the northwest subsidence bowl to $3.4 \cdot 10^{-3}$ at well 32CDC in the central subsidence zone. Table 3.4 also compares the estimated values with estimates proportional to an estimate of the saturated thickness of the aquifer system [Todd, 1980]. As an approximation for the saturated thickness I used

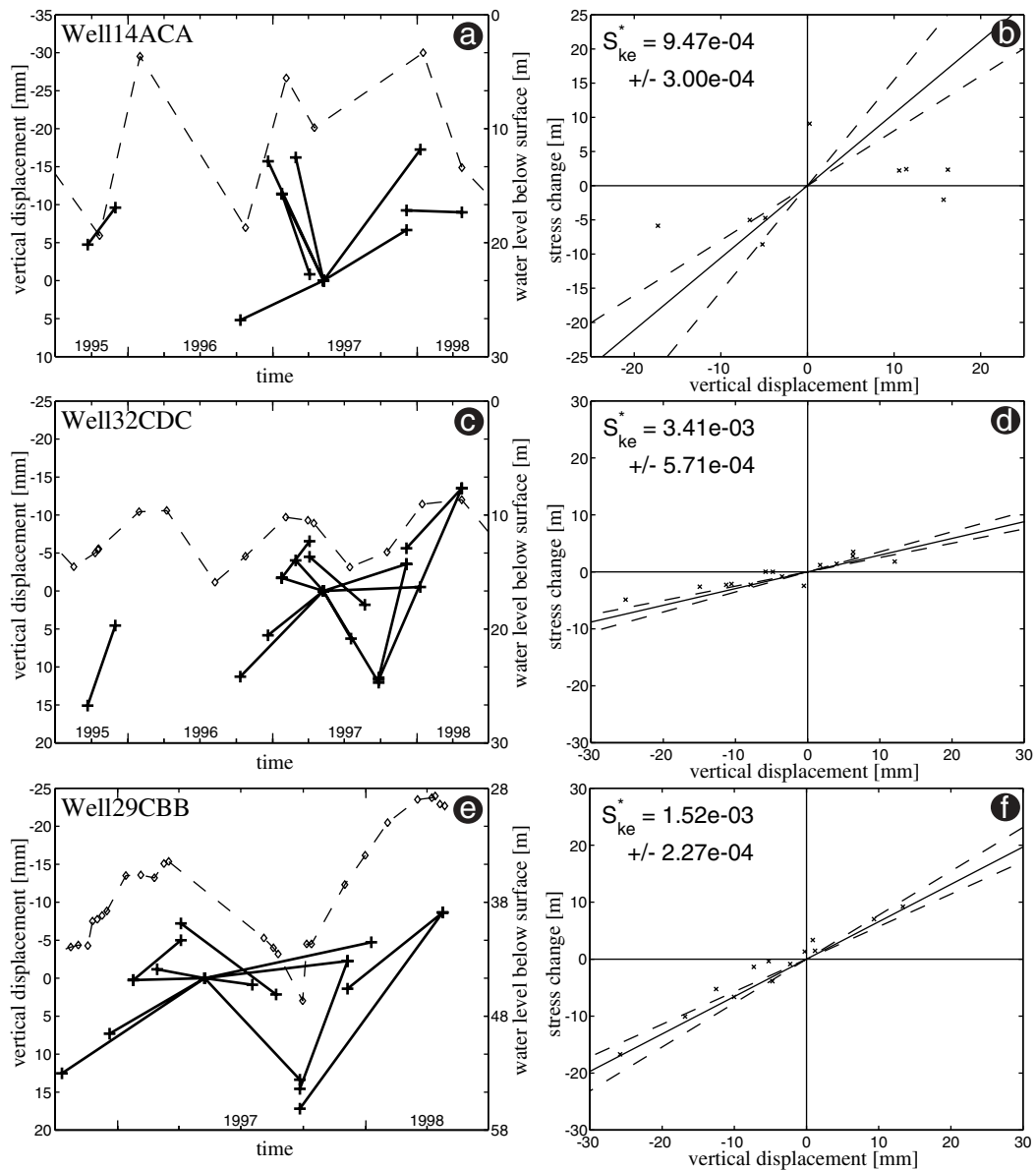


Figure 3-10: Calculating the skeletal elastic storage coefficient from stress-displacement analysis. On the left are time series plots for water level measurements (diamonds) in meters below land surface and vertical displacements, shown as changes in vertical elevation as measured in the interferograms. Each “+” corresponds to a radar acquisition. On the right these data are plotted in a stress-strain diagram. The slope of the solid line is the weighted least-squares estimate for the elastic storage coefficient S_{ke}^* . The dashed lines correspond to $\pm\sigma$ values, assuming a 5 mm standard deviation for the displacement measurement and exact interpolated water levels.

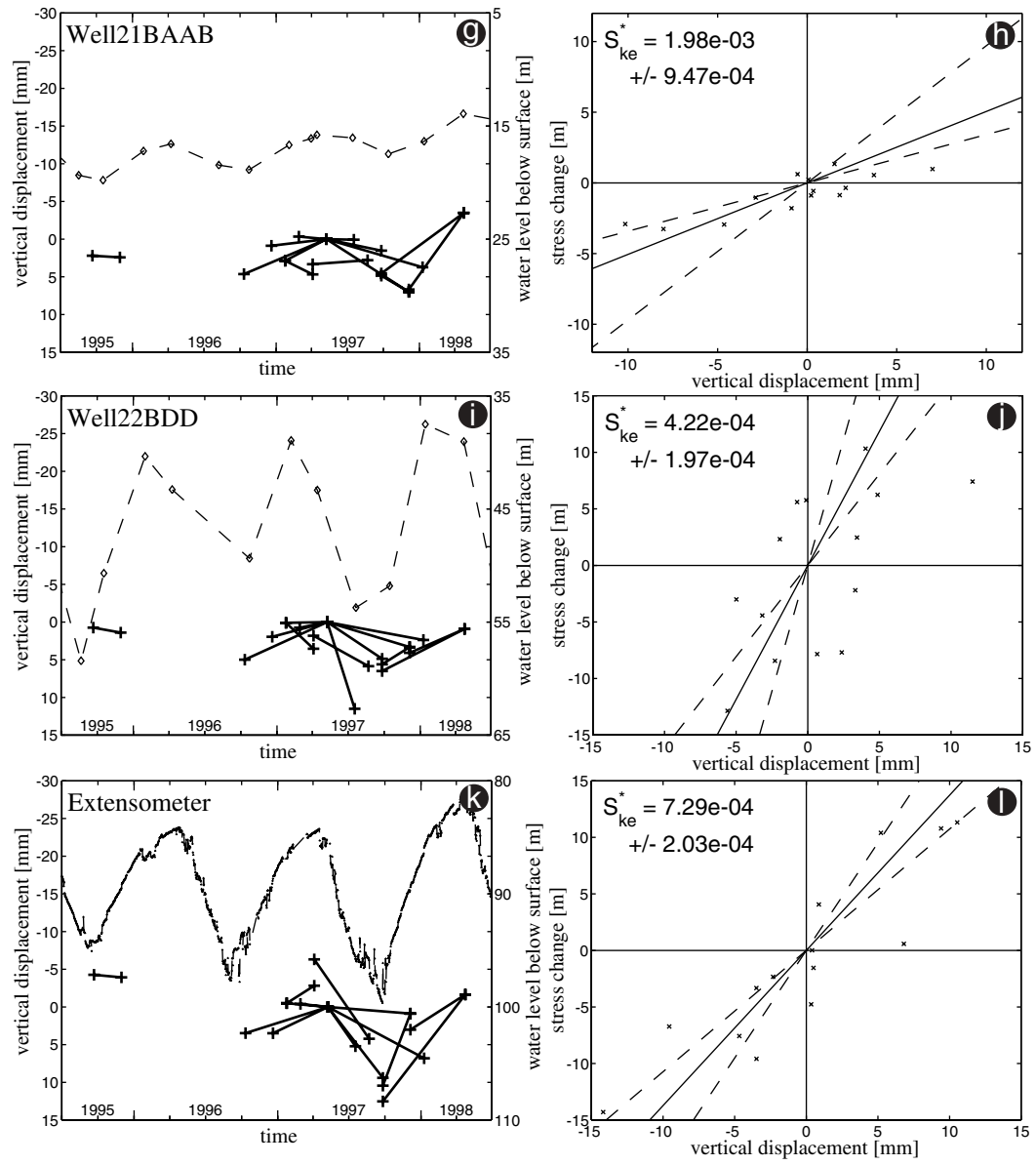


Figure 3-10: (continued)

Well name	monitored depth interval	S_{ke}^*	S
14ACA	152.4m – 227.4m	$9.47 \cdot 10^{-4}$	
32CDC	173.7m – 198.1m	$3.41 \cdot 10^{-3}$	$4.05 \cdot 10^{-4}$
29CBB	177.1m	$1.52 \cdot 10^{-3}$	$4.80 \cdot 10^{-4}$
21BAAB	61.0m – 120.4m	$1.98 \cdot 10^{-3}$	$5.40 \cdot 10^{-4}$
22BDD	61.0m – 121.9m	$4.22 \cdot 10^{-4}$	$5.10 \cdot 10^{-4}$
Extensometer	206.3m – 209.4m	$7.29 \cdot 10^{-4}$	$4.50 \cdot 10^{-4}$

Table 3.4: Elastic storage coefficients, S_{ke}^* , determined from displacements measured by InSAR and stress measured as water level change in the wells shown in figure 3-1. The aquifer storage coefficients S , derived from the commonly used relation $S = 3 \cdot 10^{-6}b^*$, where b^* is the saturated thickness of the aquifer system [Todd, 1980], are shown for comparison. (No thickness value was available for well 14ACA). Because the estimates for the saturated thickness of the aquifer system do not vary significantly between the different locations, they limit S to a very narrow range of values. The value for S_{ke}^* determined for the Lorenzi extensometer PZD well from compaction measured by the extensometer is $5.1 \cdot 10^{-4}$ (M. Pavelko, written comm. 1999).

the thickness of the “Las Vegas Springs aquifer” from Donovan [1996]. This includes most of the “developed-zone aquifers” defined by Morgan and Dettinger [1991]. This very rough estimate demonstrates very clearly, that the typically small variations in saturated thickness limit the estimated storage coefficients to a very narrow range, which cannot explain the observed spatial variability of the displacement field.

I tested the sensitivity of my estimates to the validity of the assumption that residual, inelastic compaction is negligible by calculating and removing a long-term subsidence trend for each location in the analysis. I found that the resulting estimates were insensitive to the removal of the very small trends, and thus conclude that any residual compaction that may still be occurring at these locations does not significantly bias my estimates.

In the described analysis, the water level changes measured in the observation wells were assumed to be representative for the aquifer system at the well locations. Unfortunately, the vertical distribution of hydraulic head in the aquifer system is generally unknown. If water levels in the observation wells do not represent the local average conditions in the aquifer system, the estimated value for the storage coefficient

will be inaccurate. Also, some of the water level measurements in the observation wells may reflect effects of transient water level fluctuations due to pumping. This would compromise the accuracy of the interpolation of these water level measurements to the radar acquisition times. In most cases the values probably are biased toward the low side, because of the delayed propagation of drawdown and recovery from the pumped or recharged aquifers, where water levels are measured. Thus, the unknown depth distribution of hydraulic head limits the accuracy of the computed storage coefficients to about ~ 0.5 orders of magnitude.

3.5 Discussion

The displacement maps in figures 3-3, 3-4 and 3-5 contain a wealth of information regarding the seasonal deformation of the aquifer system in Las Vegas Valley. Over the last few years, changes in the management of the aquifer system have led to changes in the character of the observed displacements. From late fall to mid-spring comprehensive groundwater recharge programs are now in effect, primarily in the central and northwestern parts of the valley. These programs, which began in the late 1980s and continue to grow, have helped stabilize groundwater levels in the northwest, which have been recovering slightly since the mid-1990s [Wood, 2000]. Over the longer term, increased water imports since the 1970s from Lake Mead have been used to meet water demand throughout the valley, making it possible to reduce groundwater pumping during the summer months in these areas. As a result, water levels in the central Las Vegas Valley have been recovering since the mid-1990s and are now well above their historic minimum levels [Pavelko et al., 1999]. During the time period 1992-99 a trend of increasing precipitation has been measured at stations in the recharge source areas of Las Vegas Valley [U.S. Geological Survey, 1992-99]. This increase in natural recharge could explain some groundwater level recovery and uplift in the valley occurring during this period. However, I believe that this effect is negligible where uplift and water level recovery are observed in the central portion of the valley. In this area, groundwater level recoveries of tens to a hundred feet are occurring in former subsidence areas, and near artificial recharge wells. I attribute

most of this water level recovery and uplift to artificial recharge.

3.5.1 Seasonal deformations

In the northwest subsidence bowl groundwater levels are recovering and InSAR-derived subsidence rates are declining (fig. 3-6, 3-11, 3-10i). Using InSAR, Amelung et al. [1999] observed 70 – 80 mm of subsidence in the northwest bowl between April 1992 and November 1993, a period spanning two summers. I measure a maximum subsidence in the northwest subsidence of 40 mm for the summer of 1993 and a decrease to about 25 mm for each of the summers 1996 through 1998 (fig. 3-3). There is no significant large-scale deformation detected for the winter of 1996-97, and some areas within the northwest subsidence bowl show small uplift for the winter of 1997-98 (fig. 3-4).

In the central subsidence zone, where Amelung et al. [1999] measured 30 – 50 mm of subsidence between April 1992 and November 1993, I measure a maximum subsidence of more than 30 mm for the summer of 1993 and somewhat smaller values for the summers, 1996 through 1998 (fig. 3-3). The surprisingly large uplift of more than 30 mm for the winter of 1997-98 is larger than for earlier winters, which also clearly show uplift in the central subsidence zone (fig. 3-4). These results are consistent with elastic expansion of the aquifer system in response to the overall recovery of water levels in the central Las Vegas Valley.

The absence of measurable subsidence in the northwest subsidence bowl during the more recent winter seasons (fig. 3-4) suggests that residual compaction due to the delayed dissipation of residual excess pore pressure occurring in the thick aquitards is masked by elastic expansion occurring in the thinner and/or more permeable aquitards and in the aquifers due to longer-term seasonal increases in hydraulic head. On the other hand, the net subsidence of about 10–20 mm/yr observed between 1996 and 1998 despite recovering water levels, suggests that some residual compaction is occurring in the aquifer system, causing further permanent subsidence. At the location of the northwest subsidence bowl Morgan and Dettinger [1991] estimated an aggregate clay thickness of approximately 50 – 100 m within the “developed-zone

aquifers” of the valley fill deposits. Little information is available on the thickness of individual aquitards. The boreholes drilled for the piezometers and the extensometer at the Lorenzi site penetrate three thick aquitards, two of which are below the current water table [Pavelko, 2000]. The presence of these thick aquitards presumably explains the residual compaction measured by the extensometer and perhaps some of the subsidence detected by InSAR in the northwest subsidence bowl.

The same reasoning applied to the absence of significant annual subsidence in the central subsidence zone leads to the conclusion that there is little or no residual compaction and therefore little or no residual excess pore pressure in the aquitards in the central subsidence zone. Water levels in the downtown area of Las Vegas have been stabilized or recovering since the mid-70s, allowing for dissipation or cancellation of the excess pressure from aquitards. In the central Las Vegas Valley the estimated aggregate clay thickness within the “developed-zone aquifers” is about 75 – 150 m [Morgan and Dettinger, 1991], but the thickness of discrete aquitards is unknown to us.

The InSAR-derived displacements suggest that the effective stress changes in the central portion of Las Vegas Valley have been predominantly in the elastic range of aquifer system compressibility since 1995. For aquifer systems, elastic compressibilities are generally one or two orders of magnitudes smaller than the inelastic compressibilities [Riley, 1998]. Though the magnitude of the maximum observed displacements in the central subsidence zone are seemingly large, they are roughly equivalent to maximum seasonal elastic deformations, 25 – 30 mm, measured by some extensometers in the Santa Clara [Ireland et al., 1984] and San Joaquin [Poland et al., 1975] Valleys in California. In the northwest subsidence bowl, the multi-year compaction rate of about 10 – 20 mm/yr is small compared to historical subsidence rates of 63 mm/yr measured between 1963 and 1986/87 [Bell and Price, 1991].

3.5.2 Land subsidence from December 1997 to January 1999

The trend of decreasing subsidence rates in the northwest subsidence bowl observed by Amelung et al. [1999] until December 1997 continues through January 1999. The

maximum average subsidence rate in the northwest subsidence bowl from December 1997 to January 1999 was 20 mm/yr, compared to about 25 mm/yr in the previous two years. This small apparent change in the subsidence rate could be due to measurement error.

The trend of decreasing subsidence rate is also observed in the central subsidence zone, where the average subsidence rate decreased from about 10 – 15 mm/yr from January 1996 to December 1997 to nearly zero from December 1997 to January 1999. Subsidence in the central subsidence zone seems to have been completely arrested during this period.

3.5.3 Elastic storage coefficient estimates

I computed an estimate of the skeletal elastic storage coefficient of the aquifer system, S_{ke}^* , for six locations in Las Vegas Valley (table 3.4). I argue in section 2.1 that the skeletal elastic storage coefficient is approximately equal to the elastic storage coefficient, S^* , for unconsolidated alluvial deposits as the ones found in Las Vegas Valley. The computed values are largest for sites in the central part of Las Vegas Valley and smallest for sites in the northwest part of the valley.

Stress-strain analyses using continuously measured displacements and water levels at the Lorenzi extensometer site yield estimates of the elastic storage coefficient of the aquifer system, S_{ke}^* , ranging from $1.1 \cdot 10^{-4}$ to $1.3 \cdot 10^{-3}$, averaging $5.1 \cdot 10^{-4}$ for a saturated depth interval of 183m (M. Pavelko, USGS, written communication, 1999). The InSAR derived value, $7.3 \cdot 10^{-4}$ compares favorably within the expected accuracy of the InSAR measurements. The values calculated for the well locations are within the range of elastic storage coefficients estimated for Las Vegas Valley on the basis of a calibrated groundwater flow model [Morgan and Dettinger, 1991] and others determined from pumping tests [Malmberg, 1965]. Given the uncertain vertical distribution of the stress changes in the aquifer system, due largely to the unknown distribution and magnitude of residual excess pore pressures, the elastic storage coefficients calculated on the basis of the InSAR measurements represent first-order estimates with an uncertainty I estimate at ~ 0.5 orders of magnitude. Because of

the time lag involved in the equilibration of aquitards, a substantial fraction of the aggregate thickness of aquitard material may experience significantly less stress change in a season than is imposed and measured in the interbedded aquifers. Consequently, the seasonally estimated values of S_{ke}^* probably do not fully reflect the material elastic compressibility and thus elastic storage of the aquifer system.

I estimated storage coefficients for six well locations in Las Vegas Valley. Using additional well data, this analysis could be extended to more locations. If hydraulic heads were calculated from a regional groundwater flow model, the InSAR-derived displacements could be used to create a map of elastic storage coefficients over the aquifer system. These could be used iteratively to improve the groundwater flow model by including the derived storage coefficients. This approach was pursued in estimating inelastic storage coefficients in Antelope Valley, California, in Chapter 4.

3.5.4 Comparison of InSAR and extensometer measurements

Figure 3-11 shows the time series of aquifer system compaction measured at the Lorenzi borehole extensometer (fig. 3-1) located on the southern rim of the northwest subsidence bowl, the InSAR-derived vertical displacements for the same location, and the fluctuation of aquifer head that represents the change in stress driving these displacements. The long-term trends and magnitudes measured by the extensometer and by InSAR are in good agreement. The trends of the seasonal fluctuations also agree very closely. However, the InSAR measurements show seasonal displacements consistently larger than those measured by the extensometer. This difference can be explained by the different thicknesses of deforming sediments that are measured by the two techniques. The extensometer measures vertical compaction and expansion only in the interval 4 to 244 m below land surface [Pavelko, 2000]. Any compaction or expansion of the aquifer system occurring at depths outside this range is not detected by the extensometer, but would be detected by the InSAR measurements.

It is unlikely that the seasonal variations measured by InSAR at the extensometer location are caused by deformation occurring in the uppermost 4 m. The most likely shallow mechanism would be soil shrinkage and swelling, but two factors argue against

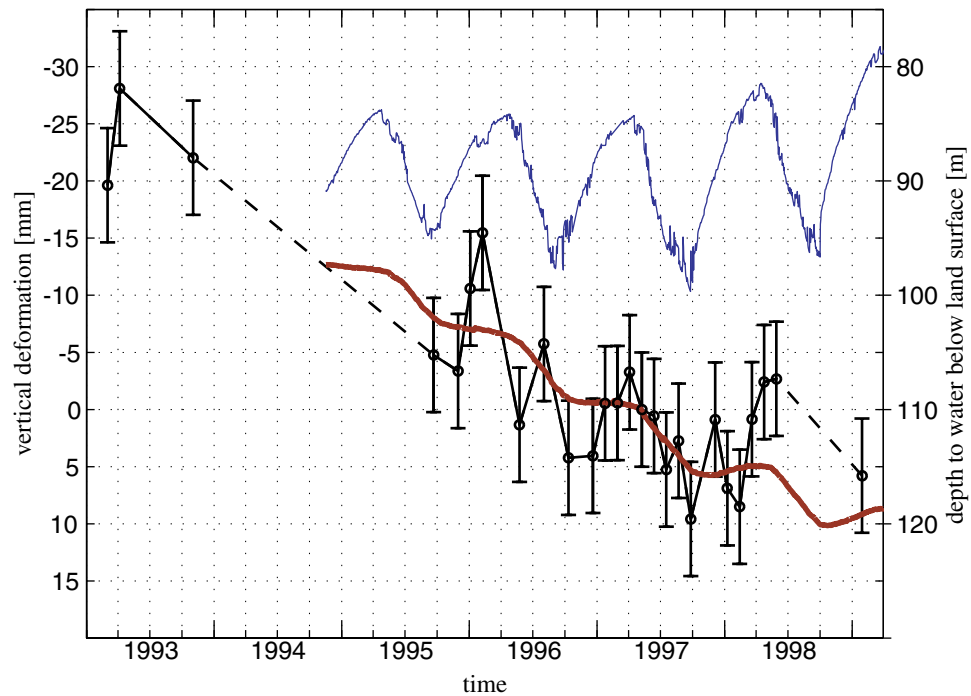


Figure 3-11: Comparison of vertical displacements measured by InSAR (with errorbars) and by the extensometer at the Lorenzi site (brown line) at southern the rim of the subsidence bowl (fig. 3-1), superposed with aquifer head measured is the depth to water below land surface (blue line) in a well (USGS-PZD) co-located with the extensometer. Although the two measurements are in good agreement, the magnitude of the seasonal responses are generally larger for the InSAR measurements. This is likely due to deformation below the depth interval monitored by the extensometer. The errorbars for the InSAR measurements are ± 5 mm.

this possibility. Firstly, the patterns of seasonal variation are not widespread as one might expect with seasonal climatic variations in soil moisture content. Secondly, if lawn watering practices were responsible for seasonal changes in soil moisture content one would expect to see relative uplift in summer and relative subsidence in winter, which is not present. Deep wells in the Las Vegas Valley penetrate to depths below 244 m, and more importantly, pressure transients extend into that region, providing the necessary stress changes to cause deformation at these depths.

Another possible source of discrepancy between the two measurements is the measurement “dead band” in the extensometer, the region in which reversing trends in the displacement are not detected. However, the dead band for the Lorenzi extensometer, which ranged between 0.15 and 0.3 mm during the period 1994 to 1999 (M. Pavelko, U.S. Geological Survey, written commun. 1999), is too small to explain the observed differences.

The stepwise seasonal variations in compaction rate measured by the extensometer (fig. 3-11) reflect elastic seasonal deformation superimposed on nonrecoverable residual compaction attributed to the delayed drainage and fluid-pressure equilibration of thick aquitards. The ongoing residual compaction results in small to no seasonal uplift (rebound) during the periods of groundwater level recovery, followed by accelerated compaction during the periods of drawdown. Despite the larger seasonal variations in the InSAR measurements the long-term trend is comparable to the extensometer record. This suggests that thick, slowly draining aquitards within the 244 m depth interval measured by the extensometer are chiefly responsible for the residual compaction occurring at this site. I thus conclude that the larger seasonal variations detected by InSAR are most likely caused by essentially elastic deformation of the aquifer system occurring at depths below 244 m. Altogether, the general agreement between the two methods is very encouraging, while the differences in the seasonal variations are an interesting topic for future investigations.

3.6 Conclusions

I have shown that InSAR can be used to measure seasonal variations in the displacement field over subsiding or elastically expanding aquifer systems, and how these variations can be used to estimate the elastic storage coefficient over the aquifer system, where measurements of stress change are available. In Las Vegas Valley, the seasonal variations in the displacement patterns are at least of the same order of magnitude as the multi-year displacements. In the central part of the valley in particular, the observed seasonal fluctuations far exceed the multi-year trend in magnitude. These seasonal displacement signals contain important information about the hydrogeologic properties of the aquifer system and are of considerable value in assessing the effectiveness of groundwater recharge programs. Although the errors in the displacement measurements due to tropospheric delays cannot be effectively corrected for at present, the derived vertical displacements seem to be accurate to about 5 mm. Thus this technique can be used to monitor ongoing subsidence and elastic uplift processes at very high spatial detail over time periods constrained primarily by the orbit repeat cycle of 35 days for the case of ERS-2.

The comparison between the displacements as measured by InSAR at the location of the Lorenzi extensometer located at the southern rim of the northwest subsidence bowl and the extensometer measurements show general agreement in both direction and magnitude of the long term subsidence. However, the seasonal variations derived from the InSAR measurements are more pronounced than expected from the extensometer data. This difference is best explained by elastic deformation below the base of the extensometer at 244 m. The general agreement between the two techniques supports the use of satellite radar interferometry for the routine monitoring of ongoing subsidence at the basin scale.

During the period 1995-1999 subsidence rates have diminished, stabilized or reversed in different parts of Las Vegas Valley (fig. 3-6). The maximum ongoing rate of 25 mm/yr occurred in the northwest subsidence bowl. During the winter months this subsidence is almost entirely compensated by elastic expansion of the aquifer system due to recovering hydraulic heads. However, residual compaction in the northwest

subsidence bowl will continue despite recovering hydraulic heads until the residual excess pore pressures at the center of the thickest clay beds have completely dissipated. The latter stages of this process may be completely masked by elastic responses in the remainder of the system.

In the central subsidence zone reduced pumping and artificial recharge seem to have successfully halted further permanent compaction. The deformations in this area are largely elastic, reflecting little or no residual compaction and excess pore pressures, even in the thicker clay beds. The observed seasonal variations of elastic deformation are somewhat larger than expected for Las Vegas Valley. This suggests that the elastic storage values for the aquifer system are somewhat larger than previously thought, as indicated by the values obtained at wells 32CDC, 21BAAB, and 29CBC. With recovering groundwater levels in Las Vegas, future deformations are expected to occur more and more elastically. To the south, in the Whitney Mesa area, almost 30 mm of uplift is indicated, suggesting that deformation in this area has become wholly elastic. Unfortunately, comparable data documenting the presumed recovery of water levels are not presently available.

I was unable to assess conclusively if horizontal surface displacements contribute significantly to the InSAR-derived subsidence signals. Strong atmospheric delay signals in at least one of the ascending image acquisitions used in comparing ascending and descending data as well as adverse data availability rendered the differences between the interferograms relatively unreliable. Horizontal displacements of 1 – 2 cm or more would not lead to a significant difference between them. Given that any expected horizontal displacements accompanying the observed vertical displacements would have been smaller than this, I was not able to complete this analysis at the necessary accuracy. Thus, notwithstanding the differences in the observations from ascending and descending orbits, given the limitations of the accuracy achieved they do not refute the assumption of purely vertical displacements made for this study.

Las Vegas Valley offers very good conditions for the application of radar interferometry. The absence of dense vegetation and the relatively small amount of precipitation over the valley floor limit the amount of temporal decorrelation and allow formation of interferograms spanning time periods of several years. Similarly favorable

conditions prevail over a large number of other aquifer systems in the southwestern United States and in similar climates globally. In these settings the technique used here would be applicable to the study of aquifer system mechanics. The method will become applicable to the study of subsidence in a wider range of environmental settings when radar systems using longer radar wavelengths (L-Band), which are less prone to decorrelation, become operational in the future.

I have shown that InSAR can be applied to study seasonal variations in the displacement field over aquifer systems at a valley-wide scale with great spatial detail. Where the stress changes in the aquifer system are known from well observations, the InSAR measurements can be used to estimate the elastic storage in the aquifer system, an important parameter for the management of groundwater resources. Although further study of the tropospheric and other systematic biases is necessary to confidently estimate the accuracy of the derived subsidence values, this case study emphasizes the potential for InSAR in hydrogeologic applications.

Chapter 4

Subsidence observations and estimation of parameters governing inelastic compaction in Antelope Valley, California

4.1 Introduction

In Chapter 3 I have demonstrated the utility of InSAR to characterize surface displacements in Las Vegas Valley both in space and time. I have also used these observations in conjunction with measurements of hydraulic head to estimate elastic storage coefficients at several locations and shown that these estimates vary spatially. In this chapter I will focus on the estimation of inelastic storage coefficients, which control inelastic compaction in the Antelope Valley (Mojave Desert, California) aquifer system. I will show that for the inelastic compaction process in Antelope Valley the observed subsidence is delayed with respect to the drawdowns of aquifer heads. The time delays associated with the slow dissipation of residual overpressures in interbedded aquitards or confining units are described by a compaction time constant. Here I show how both, the inelastic storage coefficients and the compaction time constants can be estimated in a regional groundwater flow model by calibrating these parameters to the available subsidence measurements. By employing a regional groundwater model I can dramatically increase the number of locations for which the storage coefficients are estimated.

Land subsidence in Antelope Valley, California as a result of extensive groundwater pumping was hypothesized by Snyder [1955], and was first observed in surveys between 1928 and 1960 [Mankey, 1963]. A number of studies have since addressed land subsidence in the area, documenting wide-spread sinking of the land surface and linking the deformation to groundwater level declines [e.g. Blodgett and Williams, 1992; Londquist et al., 1993; Ikehara and Phillips, 1994; Galloway et al., 1998; Sneed and Galloway, 2000; Nishikawa et al., 2001]. In this section I describe the geographical setting of Antelope Valley, summarize the history of its settlement, development of its water resources, and describe the aquifer system. A discussion of the observed land subsidence follows in section 4.2. Much of the material of this chapter has been accepted for publication [Hoffmann, Galloway, and Zebker, 2003a].

4.1.1 The lay of the land

Antelope Valley is located in southern California, about 80 km northeast of Los Angeles (fig. 4-1), in the southwestern reaches of the Mojave desert. Despite its name, Antelope Valley is not really a valley, but a topographically closed basin, roughly triangular in shape, and bounded by the San Gabriel and Tehachapi mountains in the southwest and west and lower hills and buttes in the north and east. The valley covers an area of about 6200 km², mostly within the Kern and Los Angeles counties. A small area in the eastern part of the valley is part of San Bernadino County.

The valley floor is very flat with elevations decreasing from about 1100 m at the foot of the San Gabriel and Tehachapi mountains to about 700 m at the playa surfaces of the Rogers and Rosamond Lakes (fig. 4-1). The mountain ranges in the west efficiently block precipitation from the Pacific ocean from reaching the Antelope Valley, making the area a semi-arid high-desert environment. Mean annual precipitations vary from 900 mm near the crests of the mountains to values as low as 80 mm on the valley floor [Rantz, 1969]. On average the valley receives less than 250 mm of precipitation a year, 80% of which falls during the winter months. Annual precipitations fluctuate significantly around these mean values. Mean daily temperatures vary

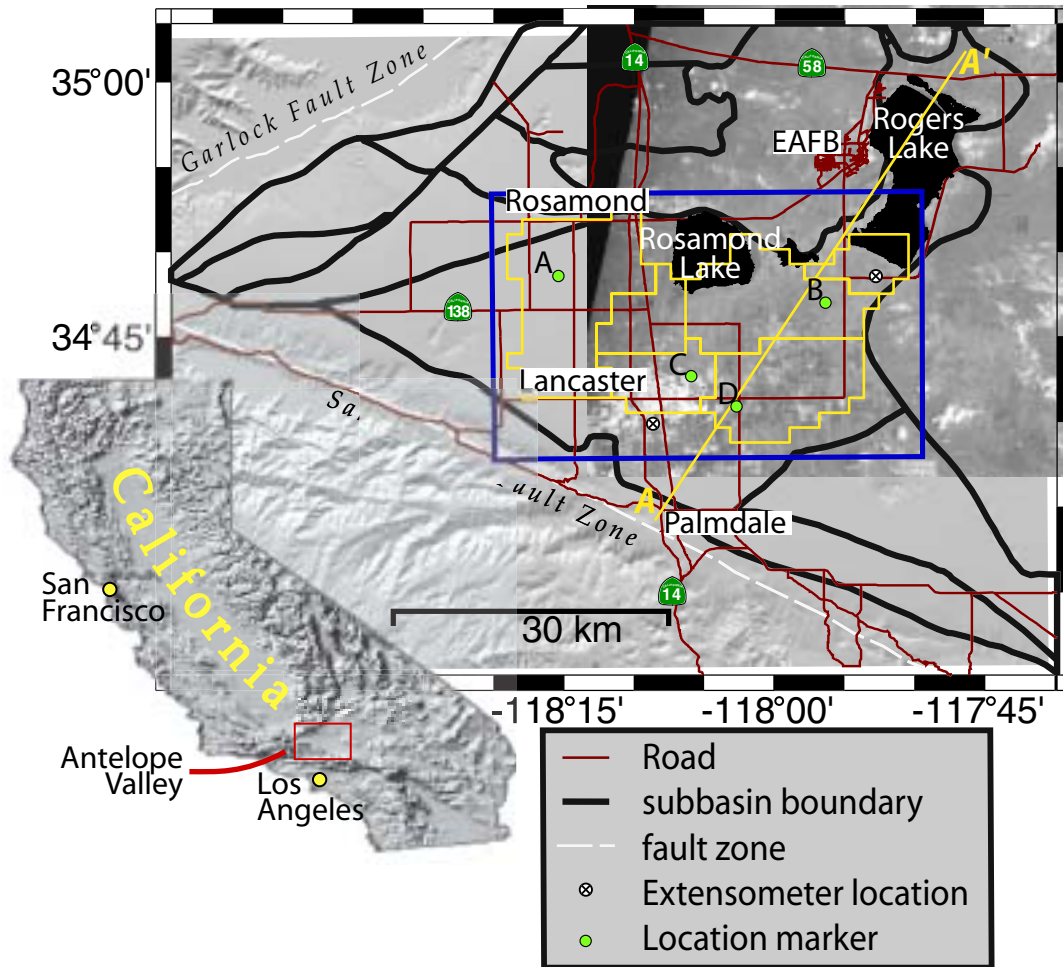


Figure 4-1: Overview of Antelope Valley, California. The radar amplitude image indicates the area included in the radar interferograms (fig. 4-6). The blue frame delineates the area shown in figure 4-9. Subbasin boundaries after Bloyd [1967] and Durbin [1978]. The yellow lines indicate parameter zones used for the estimation of the compaction time constants (see section 4.3). A schematic cross-section of the aquifer system along the profile $A - A'$ is shown in figure 4-3.

between 17 and 34 degrees Celsius during the summer, with peak temperatures frequently exceeding 40°C. During the winter, the mean daily temperatures are between 1°C and 14°C.

4.1.2 Historical settlement and water development

The settlement of the Antelope Valley and the accompanying development of the groundwater resource are part of the history of the settlement of the American West during the 19th and 20th centuries. The first documented permanent settlement in Antelope Valley is a Mexican Land Grant of 11 leagues of land to Jose M. Flores [Snyder, 1955]. The agricultural activity during the second half of the 19th century was probably mostly grazing of cattle. Starting in the south of the valley, near the foot of the San Gabriel mountains, extensive settlement occurred in the late 1800s, indicating the first efforts to farm in the valley. Initially this was mostly dry-farming, although a few artesian wells did exist as early as 1870 [Johnson, 1911]. After a brief period during which some orchards actually yielded some harvest, most of the orchards and livestock farms failed during a drought in the 1890s, leading to abandonment of the first homesteads along with the illusion of a reliable surface-water supply [Thompson, 1929]. By 1909 Johnson [1911] lists 353 water wells, 75% of which were flowing. Most of these wells were probably drilled primarily to get a title to the land under the 1877 Desert Land Act, which required proof of a water source to obtain the title. Many of these wells were drilled in highly alkaline soil, making successful agriculture difficult. Essentially no water was pumped from wells prior to 1900, and by 1910 only 800 ha land were under irrigation [Thompson, 1929]. After the irrigated area had reached an estimated 4,840 ha by 1919 with 500 wells drilled (though not all of them were in use) Thompson [1929] judged that “*Antelope Valley is one of the few areas in the Mohave Desert region in which irrigation has been successful to a considerable extent*”.

Even the earliest reports [Johnson, 1911; Thompson, 1929] recognized the fact that despite the vast areas of tillable land, the scarcity of water-resources would eventually limit agricultural development. Both reports strongly criticized the then common

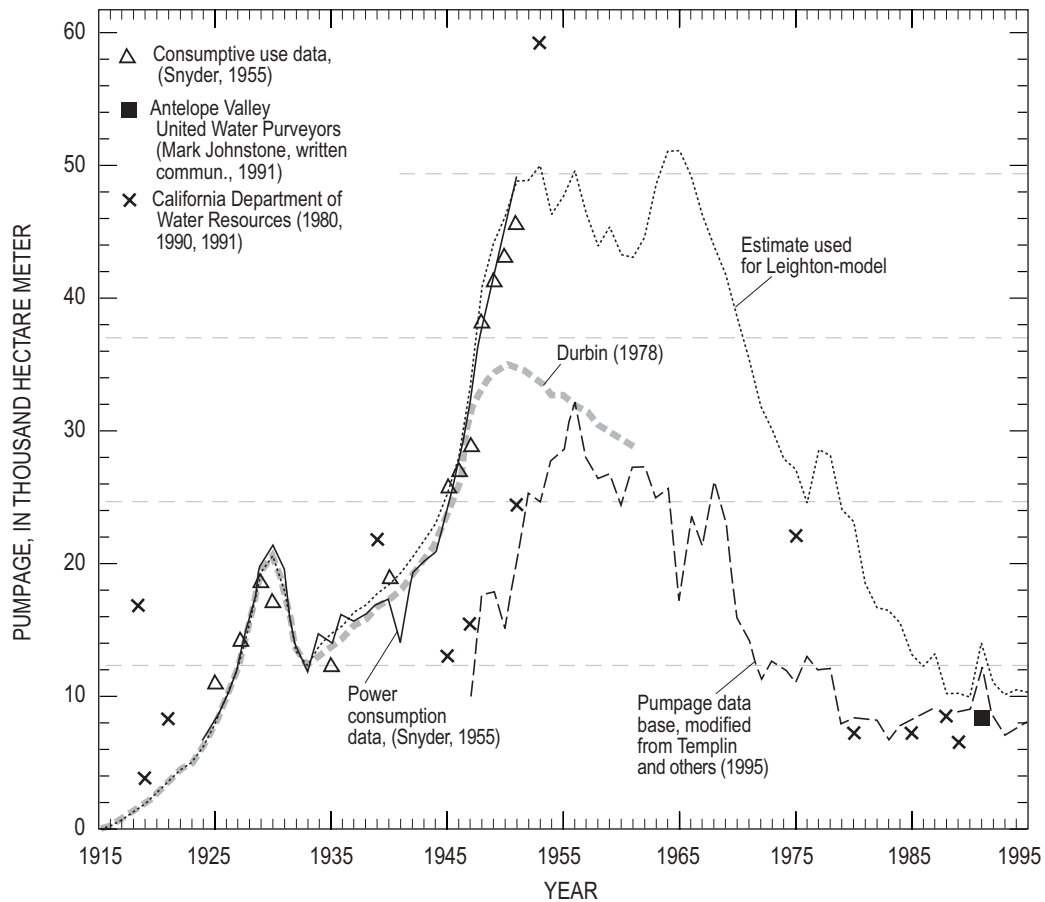


Figure 4-2: Estimates of groundwater pumpage in Antelope Valley during 1915-95. (Modified from Leighton and Phillips [2003]).

practice to leave artesian wells uncapped, letting large volumes of water evaporate and aggravating soil chemistry problems in some areas. Johnson [1911] estimated that 60 uncapped wells spilled over 10,000 m³ per day in 1909. The practice continued for many years despite existing laws requiring the well owners to control the flow. Nevertheless, Thompson [1929] did not believe that groundwater withdrawals yet exceeded the natural annual recharge, which he estimated at 6,167 hm. Snyder [1955] later estimated that groundwater withdrawals had exceeded the natural recharge since 1925. Figure 4-2 shows different estimates of groundwater pumpage in Antelope Valley between 1915 and 1995.

Higher crop prices after the economic depression in the 1930s led to a rapid expansion of agricultural activity in the Antelope Valley. Both the irrigated acreage and groundwater pumpage increased rapidly, to about 30,000 ha and 59,200 hm in the early 1950s (fig. 4-2) [Templin et al., 1995]. With estimates of annual natural recharge to the aquifer system ranging from 4,105 hm to 10,040 hm it was recognized at the time that these withdrawal rates were far from sustainable. Snyder [1955] stated that “... *long-run overdraft has become the most important feature of the Antelope Valley groundwater economy*”. With low-value, high water-demand crops like alfalfa being by far the most important component of the agricultural economy, Snyder [1955] also recognized that the farmers would be unable to afford realistically priced imported water from the then-planned State Water Project (SWP).

As predicted, the groundwater overdraft led to rapidly declining groundwater levels. These lowered groundwater levels, combined with an increased cost of electricity in the 1970s led to a dramatic increase in pumping costs, quickly rendering many farming operations uneconomical. Large areas of irrigated land went out of production and groundwater withdrawals reached a low of 6,560 hm in 1983 (fig. 4-2) [Templin et al., 1995]. This started shifting the traditionally agricultural use of water to a more urban usage pattern. Groundwater pumpage resumed slowly as the population in Antelope Valley grew. During 1980-2000 the population of the two largest communities in Antelope Valley, Lancaster and Palmdale, grew from 48,103 to 118,718 and from 12,277 to 121,413, respectively. The urbanization of the Antelope Valley is expected to continue and predictions indicate an almost complete cessation of agricultural activity by 2020 [Templin et al., 1995].

To meet the growing urban water demand the groundwater supply has been supplemented with water imported via the California Aqueduct and reclaimed wastewater. Recent projections predict this trend to continue, with imported water becoming more important than groundwater in meeting the water demands in Antelope Valley by 2010 [Templin et al., 1995]. It should be noted though that imported water cannot be considered a reliable supply any longer, as environmental concerns for the source region (the Sacramento-San Joaquin Delta) have created strong opposition to these large-scale water transmissions.

4.1.3 Description of the aquifer system

The topographical basin of Antelope Valley has been filled to depths exceeding 1 km with material eroded from the mountain ranges in the southwest and west [Londquist et al., 1993; Mabey, 1960]. The sediments forming the main water-bearing units are of Tertiary and Quaternary age and consist of gravel, sand, silt, and clays of granitic origin [Bloyd, 1967; Durbin, 1978]. Most of the aquifer-system sediments are unconsolidated to moderately indurated with older sediments being more consolidated than the overlying younger units [Dutcher and Worts, 1963; Durbin, 1978]. The basin has been conceptually subdivided into 12 subunits [Thayer, 1946]. Bloyd [1967] modified some of the subdivision boundaries. These boundaries, defined on the basis of known or inferred faults, bedrock boundaries or – in some cases – convenience [Bloyd, 1967] were adopted by Leighton and Phillips [2003] and are shown in figure 4-1. Among these subbasins the Lancaster subbasin (fig. 4-1) is the largest and most developed. Most of the pumping and all subsidence simulated in this study occur within the Lancaster subbasin. Vertically the aquifer system in the Lancaster subbasin has been conceptualized using either two or three aquifers. Earlier reports identified two aquifers, a principal and a deep aquifer [e.g. Bloyd, 1967; Durbin, 1978], which are vertically separated by a laterally extensive lacustrine unit, where this is present. The lacustrine unit extends from Rogers Lake, where it is exposed at the land surface, down dip to the south west. Near the southern end of the valley the lacustrine unit is overlain by over 200 m of alluvium [Sneed and Galloway, 2000]. Referring to more recent data, Sneed and Galloway [2000], Nishikawa et al. [2001] and Leighton and Phillips [2003] use a conceptual model with three aquifers termed the upper, middle and lower aquifer. Figure 4-3 shows an idealized cross-section of the aquifer system along the profile $A - A'$ in figure 4-1. According to Durbin [1978], most of the water is produced from the principal (unconfined) aquifer, while Sneed and Galloway [2000], Nishikawa et al. [2001] and Leighton and Phillips [2003] consider the upper aquifer as generally unproductive and the middle (confined) aquifer to be the most productive. Low-permeability interbeds consisting of compressible, unconsolidated deposits are present throughout the aquifer system. Compaction of these interbeds in response to declining hydraulic heads results in land subsidence. Exploiting the

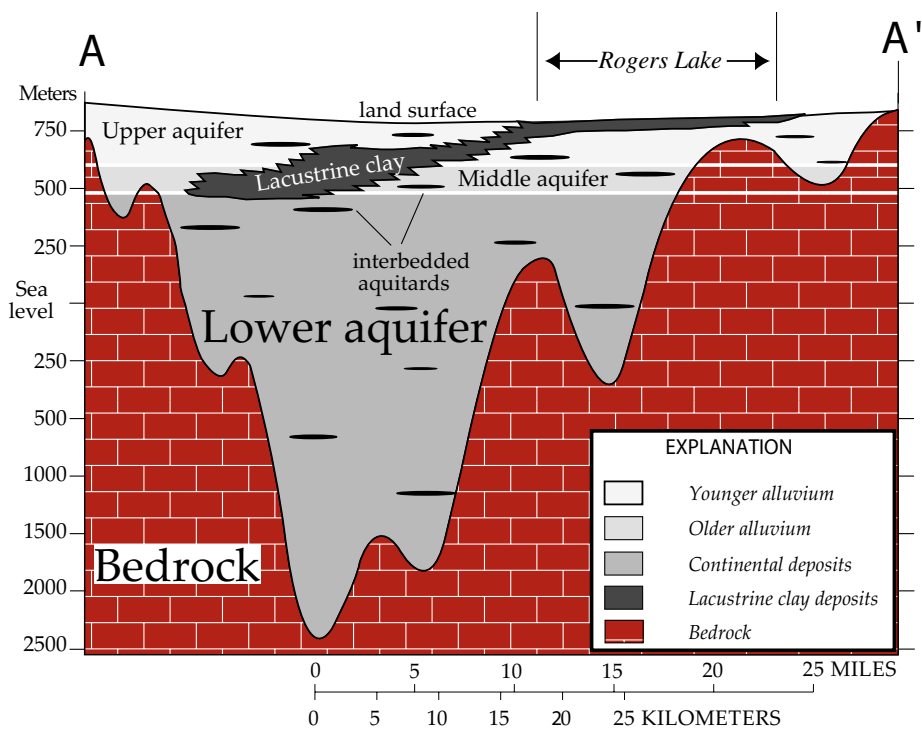


Figure 4-3: Generalized cross-section of the Antelope Valley aquifer system along the profile A – A' (fig. 4-1). (Modified from Sneed and Galloway [2000].)

observed subsidence to estimate the inelastic skeletal storage coefficients and delay properties of the compressible interbeds is the primary objective of this study.

4.2 Subsidence observations

4.2.1 Recent subsidence observations from InSAR and borehole extensometer data

A large number of ERS scenes have been acquired over the Antelope Valley largely due to the significant scientific interest in Southern California tectonics. In this way this study of the Antelope Valley benefits from the vicinity of the Antelope Valley to the Los Angeles metropolitan area. Table 4.1 lists the ERS scenes used for this study. These scenes were processed to form the interferograms shown in figure 4-5. As is obvious from this figure, most interferograms share one of two common scenes (a common “master”), to facilitate the compilation of deformation time series. However, any tropospheric signal contained in the shared acquisitions will affect all interferograms using this scene. The interferograms formed from the available radar acquisitions enable a detailed characterization of the land surface displacements between 1995 and 1999, both in terms of the spatial patterns and the temporal evolution (fig. 4-4). Due to the absence of dense surface vegetation cover over much of Antelope Valley and the scarcity of precipitation, the phase coherence is preserved for relatively long time series. I was able to form interferograms over time periods of years (fig. 4-5). As discussed in section 2.2.2 the radar only measures changes in distance along the radar line of sight and the three-dimensional displacement vector cannot be uniquely determined from the observations. In the following, I interpret range increase with time as surface subsidence and range decrease as uplift, assuming that the surface displacements are predominantly vertical. As mentioned before (section 2.2.2), horizontal displacements have been observed near pumping centers or near the boundaries of an aquifer system [Bawden et al., 2001; Watson et al., 2002] and neglecting these displacements may lead to an over- or underestimation of the vertical displacement where they are significant. The validity of this assumption of

Platform	orbit	asc/desc	date (yy/mm/dd)	comment
ERS-1	19697	D	95/04/21	
ERS-1	20198	D	95/05/26	atmosphere
ERS-1	21200	D	95/08/04	
ERS-1	23705	D	96/01/26	
ERS-2	4032	D	96/01/27	
ERS-1	24707	D	96/04/05	
ERS-2	5034	D	96/04/06	
ERS-2	6036	D	96/06/15	
ERS-2	7539	D	96/09/28	
ERS-2	9042	D	97/01/11	
ERS-2	9543	D	97/02/15	
ERS-2	10545	D	97/04/26	
ERS-2	11046	D	97/05/31	
ERS-2	11547	D	97/07/05	
ERS-2	12048	D	97/08/09	
ERS-2	12549	D	97/09/13	
ERS-2	13050	D	97/10/18	
ERS-2	14052	D	97/12/27	
ERS-2	15555	D	98/04/11	
ERS-2	17058	D	98/07/25	
ERS-2	17559	D	98/08/29	
ERS-2	19563	D	99/01/16	atmosphere
ERS-2	21066	D	99/05/01	
ERS-1	20148	A	95/05/22	
ERS-2	3982	A	96/01/24	
ERS-1	23655	A	96/01/22	
ERS-2	19012	A	98/12/09	
ERS-2	19513	A	99/01/13	

Table 4.1: Radar scenes of Antelope Valley.

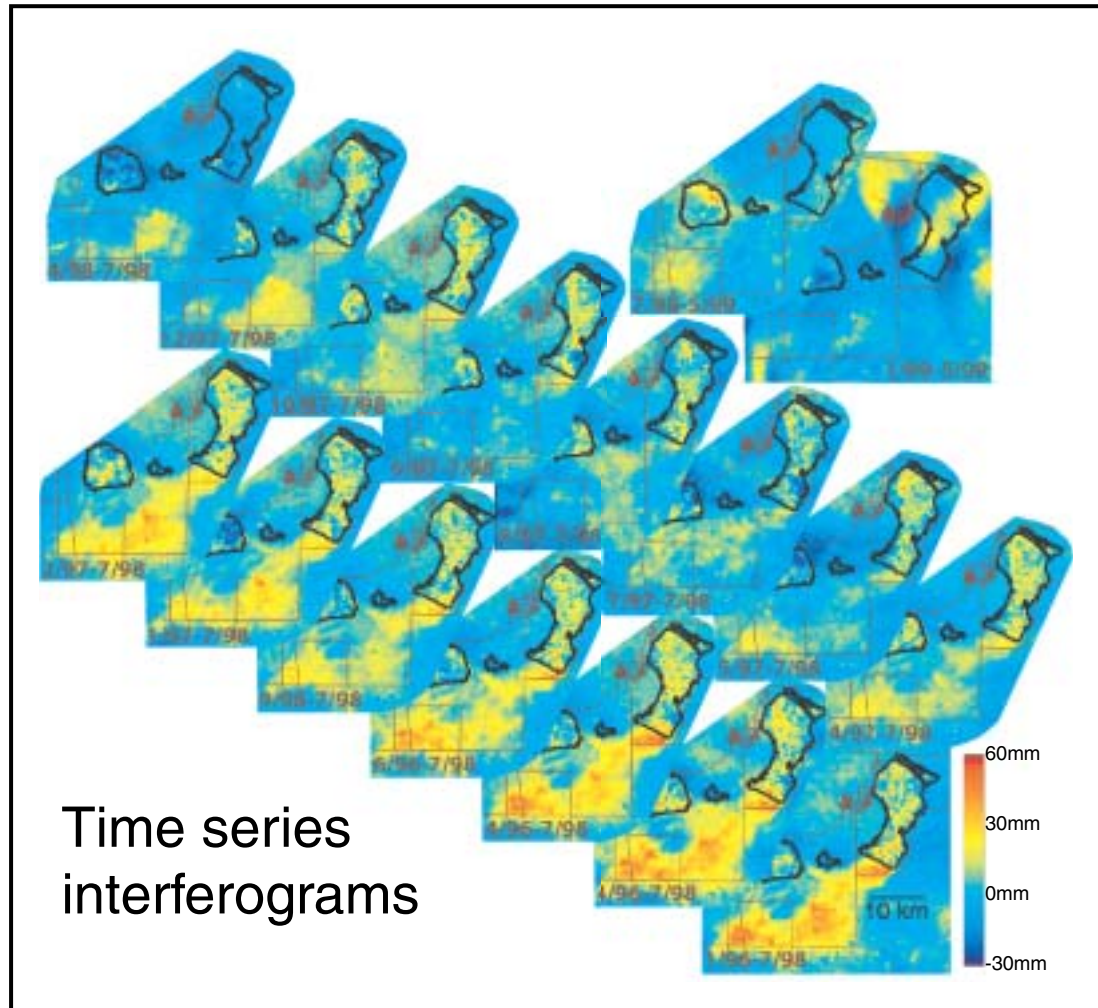


Figure 4-4: Interferogram time series showing subsidence between January 1996 and May 1999. Acquisition times and perpendicular baselines are listed in fig. 4-5.

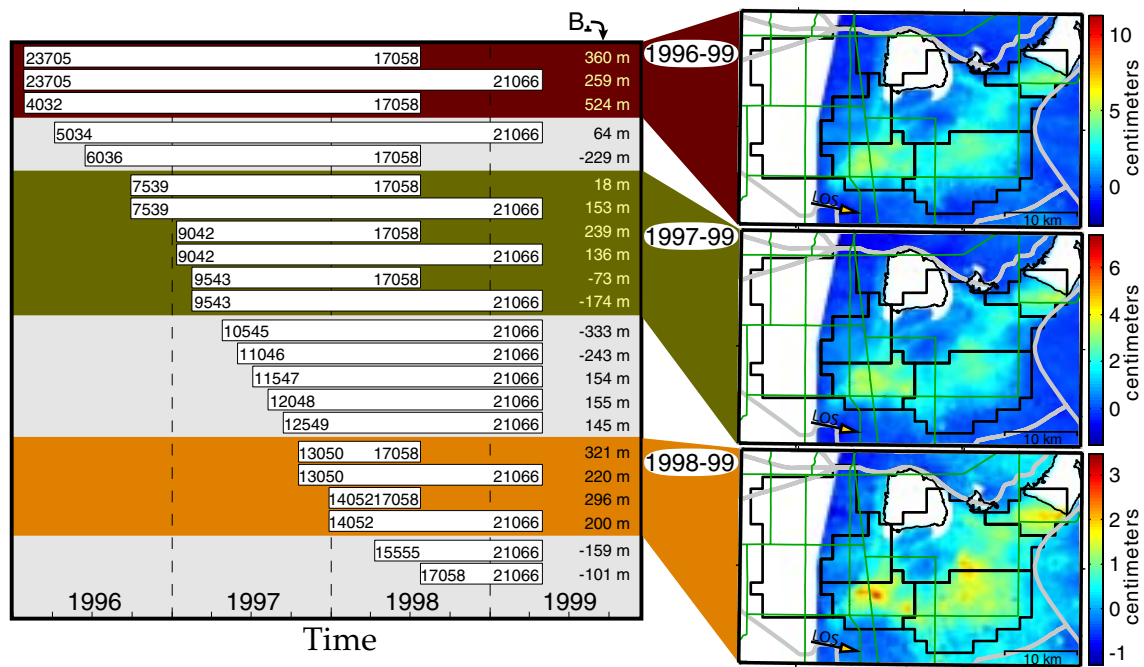


Figure 4-5: Interferograms formed for Antelope Valley, California. The bars on the left indicate the time spanned by the interferograms. The colored bands indicate which interferograms were included in the composite subsidence images covering one, two and three years, shown on the right.

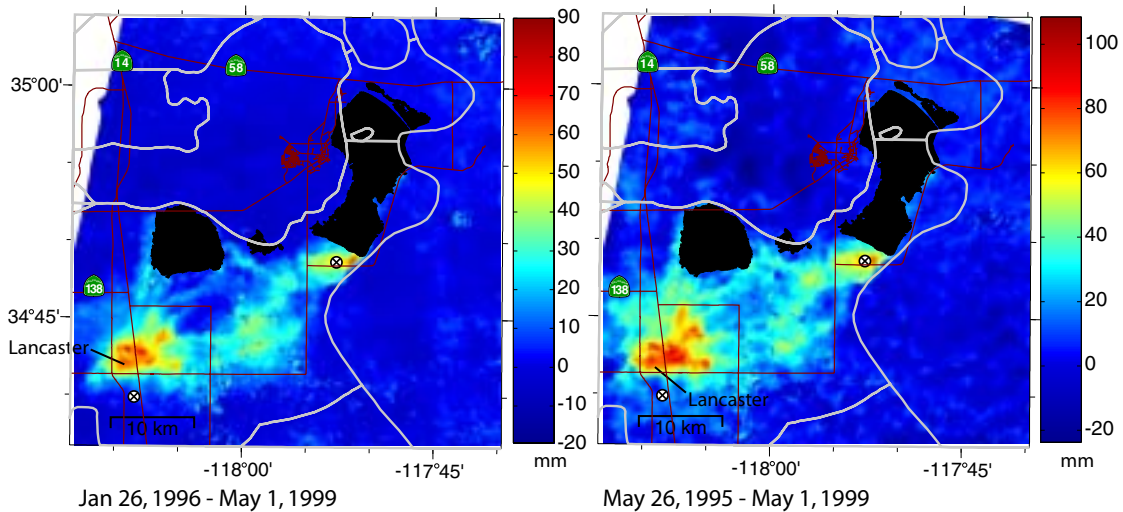


Figure 4-6: Two interferograms spanning long time periods highlight the spatial pattern of recent subsidence. Major roads, subbasin boundaries and the location of the two borehole extensometers are shown for reference.

negligible horizontal displacements is further investigated in Chapter 6. The spatial pattern of the subsidence is most easily observed in interferograms spanning longer time periods. Figure 4-6 shows the two interferograms spanning the longest time periods, January 26, 1996 to May 1, 1999, and almost four years between May 26, 1995 and May 1, 1999. The observed subsidence patterns are very similar in the two images. Subsidence maxima are located in and around the town of Lancaster, and at a very localized maximum at the southern tip of Rogers Lake. In both areas the average subsidence rate is about 20 mm/yr between 1995 and 1999. The large subsidence feature in Lancaster extends about 10 km from east to west and about 7.5 km from north to south. Approximately 78 km² in this area subside at a rate exceeding 10 mm/yr. The shape is that of a three-toed paw-print, with a large elliptical main part and three elongations in easterly, northeasterly and almost northerly directions. This structure is the same as that observed by Galloway et al. [1998] using one interferogram spanning the time from October 1993 to December 1995. The second prominent subsidence feature just south of Rogers Lake has a peak subsidence rate approximately equal to the peak subsidence rate in Lancaster, but the affected area

is significantly smaller. Here about 18 km^2 are affected south of Rogers Lake. Due to the loss of coherent signal above the lake playa itself (probably due to infrequent flooding), it is not possible to assess how much lake area is affected by the subsidence. A very interesting observation regarding this subsidence area is its very well defined eastern boundary. This exemplifies how the spatially dense InSAR data can visualize subsurface structure in a deforming aquifer system. In this case, the sudden change in subsidence rates approximately corresponds to the mapped boundary of the aquifer system [Durbin, 1978]. East of the subsidence boundary no significant thicknesses of compressible sediments are present, resulting in little or no deformation. The spatial pattern of the subsidence remains approximately constant over time, while the cumulative subsidence increases over longer time periods (fig. 4-4). This is consistent with an ongoing subsidence trend. Furthermore, the frequent data acquisitions allow to discern temporal patterns in the displacement field. During the winter months subsidence generally slows, in some areas changing to uplift. During the summer months, the observed displacements are all subsidence. While this can be qualitatively observed in figure 4-4, it is more easily seen for individual locations.

Figure 4-7 compares the InSAR-derived vertical displacements at the two borehole extensometers in Antelope Valley with the continuously recorded compaction data from these instruments. At the Lancaster extensometer, the multi-year subsidence trend of about 3 mm/yr is superposed with a strong seasonally fluctuating signal with an amplitude of about 5 mm . Note that the instrument is located just south of the much larger displacements in Lancaster (fig. 4-1). At the Holly extensometer the multi-year subsidence trend is much larger, about 15 mm/yr . A seasonal displacement signal is also clearly discernable, but it is not strong enough to reverse the sense of displacement in the extensometer data to uplift in the winter months. Instead, the compaction seen in the extensometer record merely slows, before accelerating again in the summer. The InSAR-derived surface displacements at the Lancaster site agree very well with the extensometer record. Most InSAR values fall within two millimeters of the extensometer values (fig. 4-7). Three values in the summer of 1997 deviate by 5 mm or a little more from the extensometer curve, but at least one of these values can be related to an obvious, probably tropospheric, artifact

in the corresponding image. Note that the InSAR values accurately track the seasonal compaction and expansion signal seen by the extensometer. The close agreement between these two measurements not only verifies the InSAR measurements, but also indicates that only insignificant compaction is occurring at depth ranges outside the depth interval spanned by the Lancaster extensometer ($\sim 5 - 363$ m below surface). At the Holly site, the long-term trends agree equally well between the InSAR and extensometer measurements, but the InSAR time-series indicates a stronger seasonal signal than recorded by the extensometer. As in the case of the Las Vegas extensometer (section 3.5.4) this can be explained by differences in the observed depth intervals of the aquifer system. The Holly extensometer measures changes in aquifer system thickness between 4.6 – 256 m below surface [Sneed and Galloway, 2000]. The InSAR measurements include compaction in both the very shallow and very deep intervals. Elastic (recoverable) displacements at depths below 256 m are the most likely explanation for the differences between the two observations. This seems to disagree with simulated compaction result at the site of the Holly extensometer by [Sneed and Galloway, 2000], who simulated that 99% of the compaction during 1990-97 occurred at depths measurable by the extensometer. However, Sneed and Galloway [2000] did not indicate whether their simulations showed transient elastic deformations outside the depth interval monitored by the extensometer, which is what the InSAR observations indicate.

4.2.2 Historical subsidence observations from repeated benchmark surveys

The earliest ERS SAR acquisitions of Antelope Valley date back to 1992 and no extensometer observations have been made there prior to 1990. However, the development of the Antelope Valley aquifer system occurred much earlier in the 20th century [Templin et al., 1995] and most of the over 2 m of cumulative subsidence in Antelope Valley occurred prior to 1990 [Ikehara and Phillips, 1994]. Traditionally, land subsidence has been measured by differential leveling of geodetic benchmarks.

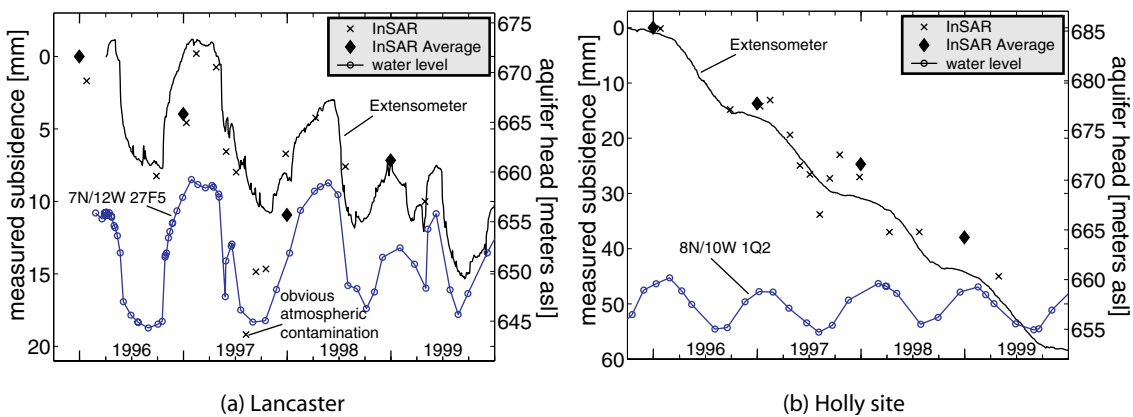


Figure 4-7: Comparison of compaction measured by the Lancaster and Holly extensometers (fig. 4-1) and the InSAR-derived subsidence. Each cross represents one SAR acquisition. The diamonds show the subsidence measured in the composite images (fig. 4-5) used for the inversion. Water-level observations from wells co-located with the extensometers are shown for reference (blue, labeled with well name). The surface displacement measurements at the Lancaster site agree well within the expected accuracies, suggesting that little compaction is occurring below the anchoring depths of the extensometers (363 m). At the Holly site, the seasonal displacement fluctuations are stronger in the InSAR-derived values, indicating elastic displacements below the anchoring depth of that extensometer (256 m).

period	variogram sill [cm ²]
1957-62	102.2
1962-65	139.4
1965-72	139.4
1972-75	32.5
1975-81	92.9
1981-92	51.1
1930-92	2972.9

Table 4.2: Variogram sills used for the kriging interpolation for the different time periods. The variogram model was gaussian with a range of 6.44 km and a nugget value of 1 mm² for all cases except the 1930-92 period, where the nugget was 7.7 cm².

These measurements have been made on an irregular basis since 1926, albeit by different national and regional agencies and according to different standards as well as relative to different geodetic data [Ikehara and Phillips, 1994]. Ikehara and Phillips [1994] conducted an extensive GPS survey in 1992 and collected the available historical benchmark data to determine historical subsidence in Antelope Valley for the time periods corresponding to the major surveys 1957-62, 1962-65, 1965-72, 1972-75, 1975-81 and 1981-92. They also estimated subsidence from 1930-92 on the basis of the available observations.

Spatial interpolation of the subsidence values at the benchmark locations can be accomplished by ordinary kriging [Deutsch and Journel, 1998]. This requires a model of the spatial covariance of the data. I used the available data to estimate the covariance structure. Figure 4-8 shows the resulting isotropic gaussian variogram¹ model with a range of 6.44 km and a nugget effect (essentially the variance of the measurement) of 1 mm². The experimental variograms from the data are shown for comparison. The nugget effect for the long-term estimate (1930-92) was estimated to be 7.7 cm², significantly less accurate than the measured values for the other time periods. The variogram sill varied for the different time periods (table 4.2). Using these variograms the benchmark observations and, in the 1930-92 case, estimates were used to perform kriging of the subsidence field (fig. 4-9). The maps shown in figure

¹The gaussian semi-variogram is given by $\gamma(h) = c(1 - \exp(-\frac{3h^2}{a^2}))$, where a is the range and c is the variogram sill.

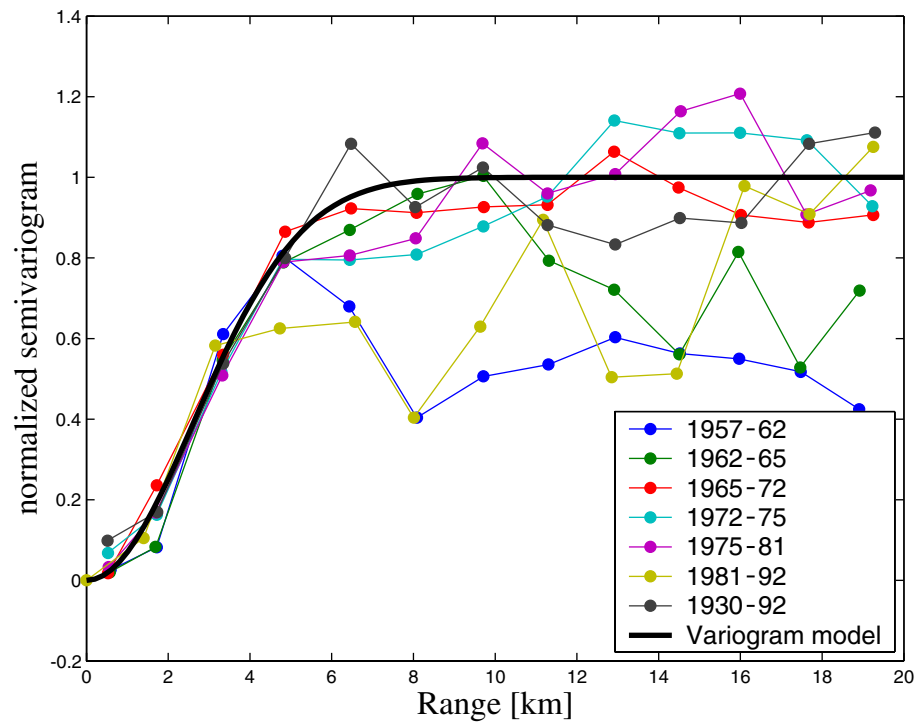


Figure 4-8: Experimental semivariograms for 7 time periods for benchmark subsidence data from Ikehara and Phillips [1994] normalized by the sill of the selected variogram model. The sills are listed in table 4.2. An isotropic gaussian variogram model with a range of 6.44 km was fit to the data (black line). This variogram model was used to create the kriged subsidence maps shown in fig. 4-9.

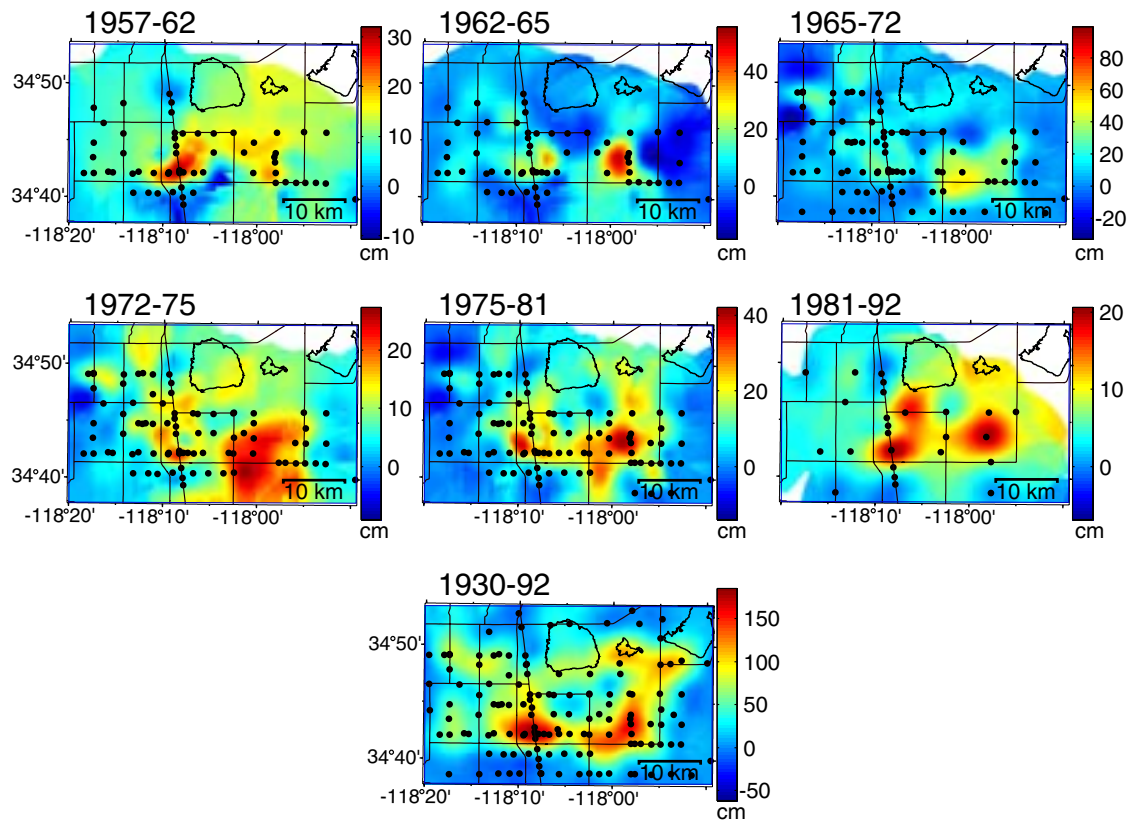


Figure 4-9: Historical subsidence maps for Antelope Valley derived from benchmark observations using ordinary kriging. The black dots indicate the location of the benchmarks for which a differential surface elevation observation was available.

4-9 suggest a spatially detailed knowledge of the subsidence field, which does not really exist. The reliability of the interpolated (kriged) estimate of the subsidence decreases with increasing distance from the benchmark data locations. This must be kept in mind when comparing kriged maps derived from point observations with InSAR observations, which are inherently much more complete. Nevertheless, the benchmark data indicate that about 2 meters of subsidence have occurred in Lancaster during the 20th century. Another subsidence center can be observed in an agricultural region further east. Comparing the maps in figure 4-9 with the recent subsidence observations from InSAR in figure 4-6 highlights some interesting differences. The historical subsidence center in Lancaster still shows the largest subsidence rates in the recent data. The additional structure of the displacement field visible in the InSAR data may or may not have existed previously but was impossible to determine from the sparse benchmark data. The second historical subsidence area further east has been subsiding at a much smaller rate than the Lancaster area during the time period covered by the InSAR images, although it has subsided even faster than the Lancaster area during several of the time periods between the leveling surveys.

Both types of observations, the InSAR observation presented in the previous section and the historical benchmark observations in this section were used in a nonlinear estimation of parameters governing inelastic aquifer system compaction. This is described in the following section.

4.3 Parameter estimation

The displacements of the land surface observed in Antelope Valley are an expression of compaction and expansion of the aquifer system at depth. The mechanics of aquifer system compaction have been presented in Chapter 2. In section 3.4 I have used InSAR subsidence observations together with knowledge of water-level changes measured in wells to estimate an elastic storage coefficient for the aquifer system at several locations. Similarly, information on parameters governing the aquifer system compaction in Antelope Valley can be extracted from the subsidence observations

presented in section 4.2, using additional information on water level changes. Knowledge of these parameters is essential to estimating the storage properties of the aquifer system and predicting future land subsidence.

4.3.1 The MODFLOW model

The most recent model of the Antelope Valley aquifer system is a MODFLOW [McDonald and Harbaugh, 1988] model developed by Leighton and Phillips [2003]. It simulates three-dimensional regional groundwater flow and vertical subsidence from 1915 to 1995 in annual time-steps. The model is based on a model grid with square 2.57 km^2 (1 mile²) grid cells extending 96.2 km (60 cells) from east to west and 69.0 km (43 cells) from south to north. Vertically the aquifer system is represented by three layers. The top layer is represented as “confined/unconfined” and the lower two layers are confined. (Additional detail on the Leighton and Phillips [2003] groundwater flow model is provided in Appendix A). Compaction is computed for the upper two layers, using the interbed storage package (IBS1) [Leake and Prudic, 1991]. The IBS1 package computes the amount of compaction ultimately resulting from a step decline in aquifer head (equations 2.17 and 2.22), neglecting any time delays in the equilibration of aquifer heads across the aquifer system. It uses three parameters for each cell, the elastic and inelastic skeletal storage coefficients and the preconsolidation head [Leake and Prudic, 1991].

Using data of groundwater pumping from 1996-98 (*Steve Phillips, U.S. Geological Survey, written comm.*) I extended the simulated time period up to the end of 1998. Figure 4-10 shows the simulated subsidence during 1995-99. The simulated subsidence shown in figure 4-10 differs from the InSAR observations in figure 4-6 in two respects. First, the magnitude of the subsidence maximum in the Lancaster area is overestimated by more than 100 percent, while it is underestimated in the second major subsidence feature south of Rogers Lake. Second, the simulation fails to reproduce any subsidence in the area between Lancaster and Rogers Lake, where widespread subsidence of about 1 cm/yr is observed in the InSAR image.

The differences between the model-simulated and observed subsidence indicate an

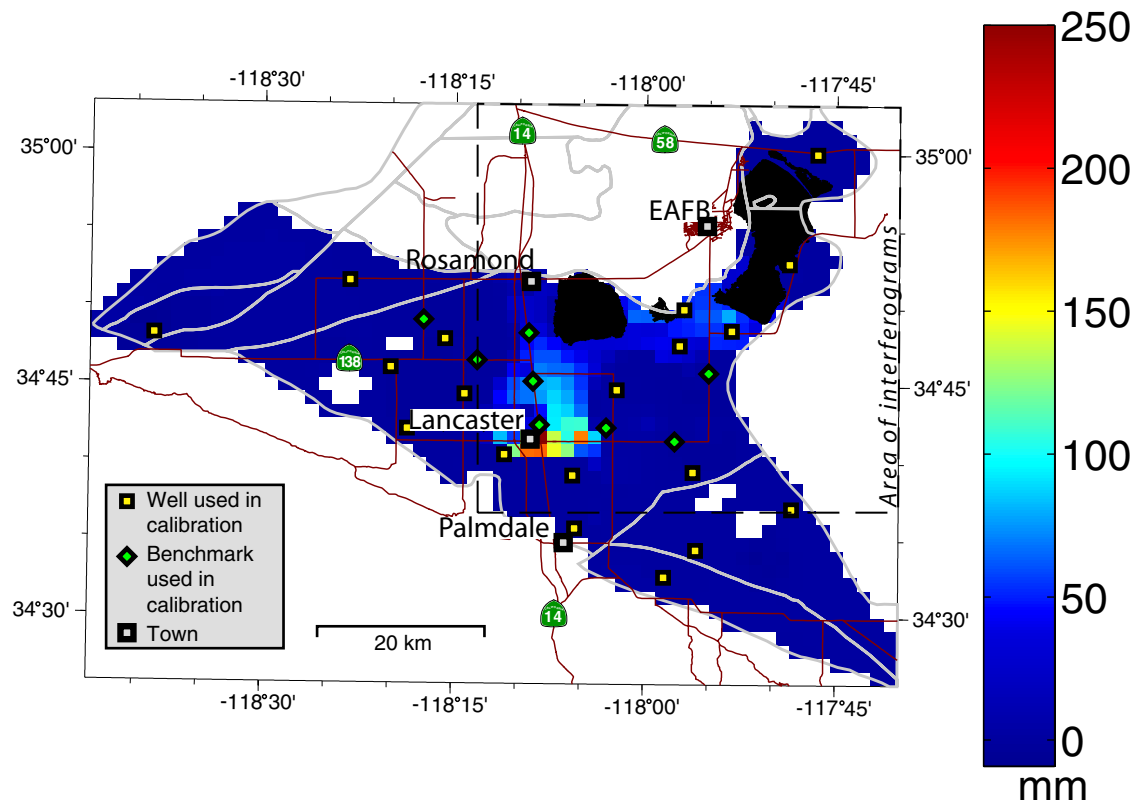


Figure 4-10: Subsidence between the beginning of 1995 and 1999 as computed by the original Leighton and Phillips-model. The locations of wells and benchmarks used in the model calibration are shown. Major roads, subbasin boundaries and lake playas from figure 4-1 are shown for reference. Note the pronounced differences between the simulated subsidence and the four-year subsidence observed in figure 4-6.

inadequate representation of the parameters governing the subsidence in the model. The original Leighton and Phillips model, hereafter referred to as simply “the original model”, was calibrated to hydraulic heads at 19 well locations and subsidence at 10 benchmark locations (fig. 4-10). While fairly typical for the calibration of regional groundwater flow models, the small number of benchmarks was obviously insufficient to reliably characterize the spatial subsidence pattern. Furthermore, due to the assumptions inherent in the IBS1 package the model cannot simulate continuing subsidence in the presence of stable or recovering hydraulic heads. However, this phenomenon is observed over significant areas of Antelope Valley, such as the area between Lancaster and Rogers Lake, where the simulation does not show any subsidence [Carlson et al., 1998]. As discussed in section 2.1.2, subsidence in the presence of recovering water-levels can be understood as residual compaction of poorly conductive compressible interbeds, in which the pore pressure has not yet equilibrated with the lower pore pressures in adjacent aquifers.

The goal of the work described here was to improve the agreement between the simulated and observed subsidence by employing all available subsidence data, including the spatially detailed InSAR observations. Furthermore, because the observed residual compaction suggests that it may be necessary to explicitly account for the process of delayed compaction in the simulation, I modified the parametrization of the interbed compaction in the model to do so.

4.3.2 Simulation of compaction

The simulation of delayed interbed compaction can be included in the MODFLOW-96 [Harbaugh and McDonald, 1996] simulation by replacing the IBS1 package with the IBS2 package, developed by Leake [1990]. The full functionality of IBS2 can be included in the more recent MODFLOW-2000 program [Harbaugh et al., 2000] with the SUB package [Hoffmann et al., 2003b]. Both packages require a different parametrization of the compacting interbed material. While the IBS1 package uses elastic and inelastic skeletal storage coefficients for each cell, the IBS2 and SUB packages use the elastic and inelastic specific skeletal storage of the interbed material,

IBS1		IBS2/SUB	
elastic skeletal storage coefficient,	S_{ke}	elastic skeletal storage coefficient for instantaneous compaction,	S_{ke_i}
inelastic skeletal storage coefficient,	S_{kv}	inelastic skeletal storage coefficient for instantaneous compaction,	S_{kv_i}
preconsolidation head,	h_{pc}	preconsolidation head,	h_{pc}
		specific elastic skeletal storage,	S_{ske}
		specific inelastic skeletal storage,	S_{skv}
		vertical hydraulic conductivity,	K_v
		number of individual interbeds,	N
		equivalent thickness of interbeds,	b_{eq}

Table 4.3: Comparison of input parameters required for the IBS1 and IBS2 or SUB packages.

the number of individual interbeds and an equivalent interbed thickness (eq. 2.14). The parameters required for the two packages are compared in table 4.3.

Estimated parameters

According to equation 2.15 the compaction in a system of interbeds due to a unit step decrease in hydraulic head depends on the time constant τ , the inelastic skeletal specific storage, S_{skv} , and the thickness of the compacting interbeds. The time constant only affects the timing of the compaction, but not the ultimate magnitude of the subsidence. The actual subsidence can be thought of as a convolution of the compaction in equation 2.15 and the drawdown history, assuming that the stress-dependence of K_v and S_{skv} is negligible. Although both K_v and S_{skv} have been shown to be stress-dependent for many geologic materials, the effect of neglecting this stress-dependence is small for stress-changes typical for water-level drawdowns in deep aquifer systems [Leake and Prudic, 1991]. Because different sets of K_v , S_{skv} and b_{equiv} result in the same time constant (eq. 2.13), and hence the same subsidence history, these parameters cannot be resolved independently using only land subsidence measurements to constrain the parameter estimation. Similarly, the inelastic skeletal specific storage, S_{skv} , of the interbeds cannot be separated from the interbed thickness using surface

subsidence measurements alone. I therefore chose to estimate the time constant, τ , and the inelastic skeletal storage coefficient of the compacting interbeds, S_{kv}^* , which is the product of S_{skv} and the cumulative interbed thickness (eq. 2.10).

Because the parameter estimation is only constrained by surface subsidence data, no information is available on the depth at which the compaction occurs. Furthermore, the drawdowns in the upper two model layers have similar time histories, so that the presence of compressible material in either layer would result in a very similar subsidence history. For these reasons it is impossible to estimate separate S_{kv}^* values for the different layers. Fortunately though, as will be discussed shortly, water dissipated from the compacting interbeds did not significantly change the drawdowns in the simulation. This suggests that all compressible interbeds can be simulated in one of the top two layers. Thus, I simulated all interbeds in the second model layer.

The estimated value for S_{kv}^* can be translated into an estimate of the cumulative interbed thickness if a value for S_{skv} is either assumed or available from independent information. For this study I used $S_{skv} = 1.148 \cdot 10^{-3} m^{-1}$, which is the value estimated for thick aquitards at the Holly site [Sneed and Galloway, 2000, table 3]. If the vertical hydraulic conductivity, K_v , is also assumed or known, the equivalent thickness of the interbeds can be computed from the compaction time constant (eq. 2.13). I used a value of $K_v = 4.23 \cdot 10^{-11} m s^{-1}$, which is the value estimated by Sneed and Galloway [2000] for the confining unit. Because of the spatial heterogeneity of the skeletal storage coefficient in the aquifer system it is of interest to derive spatially varying estimates rather than average values for the entire aquifer system. This is one of my principal objectives here and of particular importance in areas where relatively large subsidence gradients may point to heterogeneities. The InSAR-derived subsidence maps can afford the spatial detail necessary to make these spatially variable estimates. However, initial results of the parameter estimation showed that subsidence observations over periods on the order of the compaction time constants are necessary to reliably constrain the estimates of the time constants. Unfortunately, SAR data suitable for interferometry has only been acquired for about 10 years, and the data used in this study only cover about a three year period. This proved to be too short to constrain the large time constants in the study area. Thus, the regression

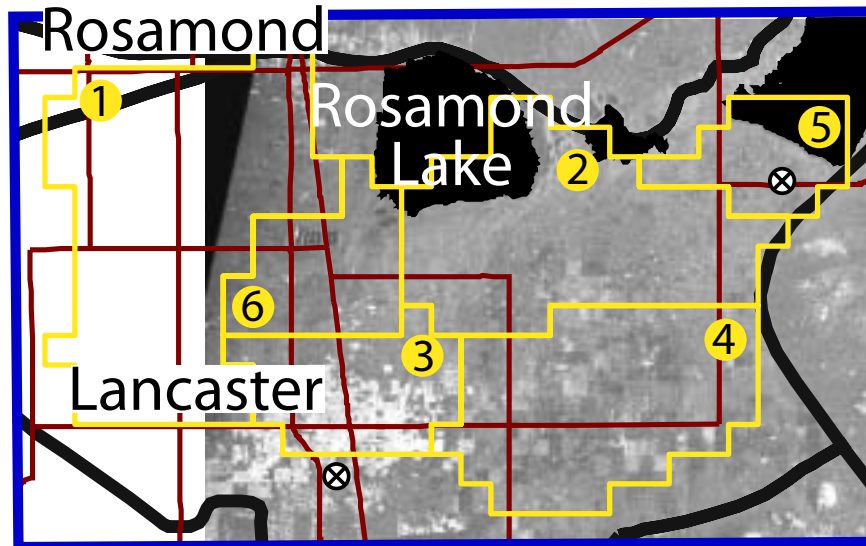


Figure 4-11: Six parameter zones used for the estimation of the compaction time constants.

of the compaction time constants has to rely primarily on benchmark data which cover a large part of the 20th century, but do not afford the high spatial detail of the InSAR maps. To overcome this problem I defined six parameter zones (fig. 4-11) by modifying a zonation in the original model based on spatial structure observed in the InSAR images and initial inversion results. These parameter zones were only used to estimate the time constants. The inelastic skeletal storage coefficient, S_{kv}^* , was allowed to vary at each of the 282 model cells within the 6 parameter zones. The number of estimated parameters is therefore 288 (282 storage coefficients and 6 time constants). A total of 2566 subsidence data were available to constrain the estimation of these parameters. It is more meaningful to compare the number of estimated parameters and the number of observational constraints for each parameter zone though, as the parameters in each parameter zone were estimated independently from the parameters in the other parameter zones (see section 4.3.3). These numbers are listed in table 4.4. The number of subsidence observations available at each location varies somewhat, as the conservatively extrapolated benchmark values did not yield a value for all time periods at every location (fig. 4-9). Also, the InSAR-derived displacement maps do not cover the entire area within the parameter zones (fig. 4-11) and in a few locations

Parameter Zone	no. of estimated parameters	no. of observational constraints
1	88	672
2	66	629
3	29	280
4	59	580
5	20	155
6	26	250

Table 4.4: Number of estimated parameters and observational constraints by parameter zone. The number of estimated parameters for each zone includes one compaction time constant and between 19 and 87 inelastic skeletal storage coefficients, S_{kv}^* .

did not provide a measurement due to decorrelation. For most locations, however, subsidence measurements were available for three time periods from InSAR and for 7 historical time periods from benchmark leveling.

4.3.3 Setting up the inverse model

Estimating 288 parameters in a non-linear parameter estimation quickly becomes computationally daunting, particularly if the forward model involves a significant number of computations. This is decidedly the case for this problem, as the forward model is the regional groundwater flow and subsidence model.

Fortunately, this can be alleviated by recognizing that the subsidence is linearly related to the inelastic skeletal storage coefficient for a given drawdown history and time constant (eq. 2.15). Although this is only approximately true in the presence of elastic deformation, it is a reasonable assumption for interbeds, where the ratio of S_{skv} to S_{ske} (the inelastic and elastic skeletal specific storage values) is generally large. The parameter estimation can then be performed in two interleaved estimations, one being an iterative non-linear estimation of the 6 time constants and the second one being a linear estimation of the 282 inelastic skeletal storage coefficients. This much more efficient approach is described in detail in the following paragraph. A flow diagram of the estimation approach is shown in figure 4-12.

After simulating the initial drawdown histories in a MODFLOW simulation using initial estimates for S_{kv}^* and τ , I used the general-purpose parameter estimation code

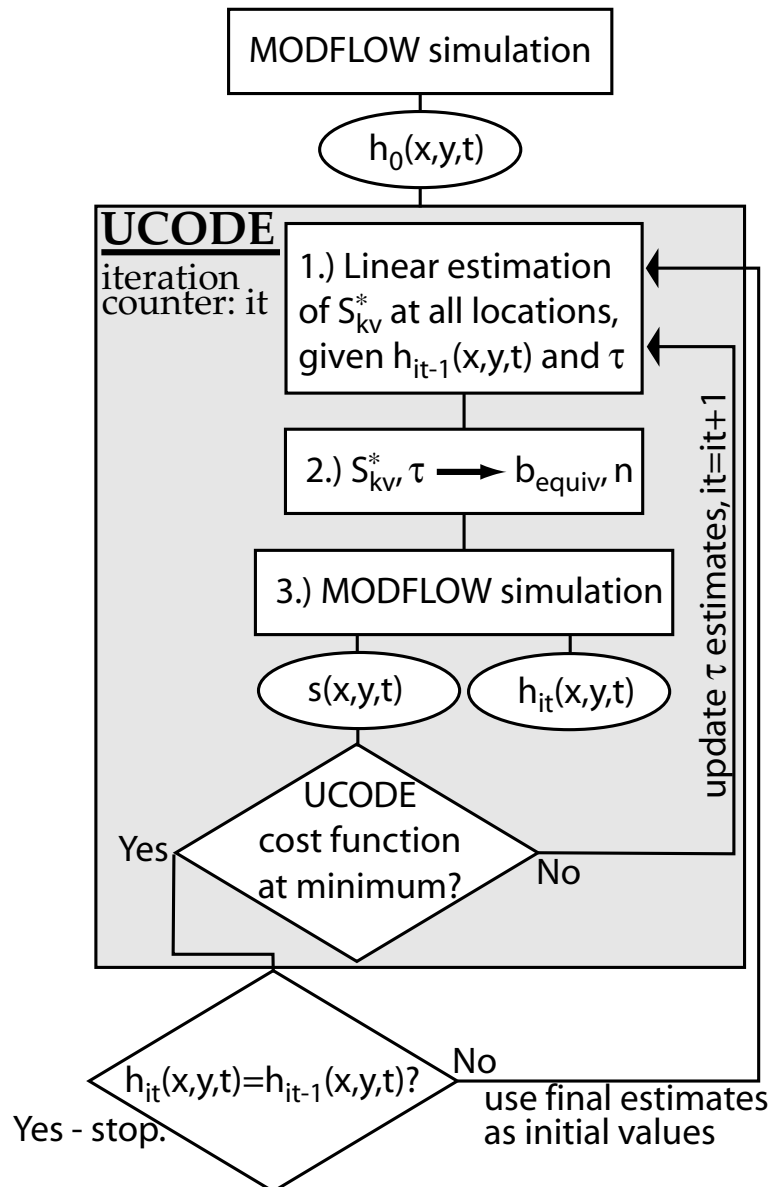


Figure 4-12: Flow-chart for the estimation of S_{kv}^* and τ . The S_{kv}^* values are estimated in a linear estimation (step 1) and the τ values are estimated non-linearly by UCODE. The aquifer heads, $h_{it}(x, y, t)$ are updated in every UCODE iteration (it) through a new MODFLOW simulation. The UCODE cost function is computed as the sum of the squared weighted residuals between the simulated subsidence, $s(x, y, t)$, and the subsidence observations.

UCODE [Poeter and Hill, 1998] to perform the non-linear parameter estimation of the time constants for the 6 parameter zones (grey box in fig. 4-12). UCODE employs a modified Gauss-Newton method to solve a general non-linear regression problem. Thus, UCODE minimizes the squared weighted differences between the simulation and the constraining observational subsidence data (section 4.2), repeatedly running the forward model in the process. Observations of hydraulic head in wells tapping the aquifer system were not used as observational constraints. The simulated aquifer heads proved to be very insensitive to changes of the interbed storage in the model during the estimation. Including head measurements as observational constraints would have forced the UCODE algorithm to improve the agreement between simulated and observed heads through large changes to the interbed storage. This would have quickly led to highly improbable values. Therefore, the simulated heads would need to be improved upon by modifying other parameters instead, which more directly affect the flow in the aquifers. This was beyond the scope of this investigation though. Here I focused on interbed properties in an existing groundwater flow model, which had already been calibrated to observations of hydraulic head.

Every model simulation run executed by UCODE is performed using a trial set of compaction time constants, yielding drawdown and subsidence histories for these values. Because of the approximately linear relationship between the subsidence and the skeletal storage coefficient (eq. 2.15), an optimal skeletal storage coefficient S_{kv}^* for the current drawdown history and time constant can be estimated at each model cell by linear least squares,

$$S_{kv}^* = (\bar{g}^T \Sigma_d^{-1} \bar{g})^{-1} \bar{g}^T \Sigma_d^{-1} \bar{s} \quad (4.1)$$

where \bar{s} is the vector of observed subsidence values for different time periods and \bar{g} is the numerically computed subsidence per unit S_{kv}^* during the time periods corresponding to the times of the available subsidence observations, given the drawdown history. Σ_d is the data covariance matrix, the structure of which is discussed below.

Equation 2.14 represents an upper limit on the time constant, τ for a given set of

K_v , S_{skv} and S_{kv}^* , because it follows from equation 2.14 that

$$b_{equiv} \leq b_{max}, \quad (4.2)$$

where b_{max} is the thickness of the thickest of the N interbeds. The equality holds if $b_n = b_{max}$ for all n . However, b_{max} is constrained by equation 2.10 if the storage coefficient and the specific storage are fixed. Thus, the time constant physically cannot exceed a maximum value, τ_{max} , given by

$$\tau \leq \tau_{max} = \frac{\left(\frac{b_{max}}{2}\right)^2 S_{skv}}{K_v} = \frac{\left(\frac{S_{sk}^*}{2S_{skv}}\right)^2 S_{skv}}{K_v}. \quad (4.3)$$

The time constant τ assumes the value τ_{max} only where the compaction is caused by a single interbed. Because I assumed K_v and S_{skv} to be constant (table 4.5), it is possible that the value of τ (for the entire parameter zone) exceeds this maximum value locally for the locally estimated S_{kv}^* . This can be resolved in several ways. Rather than locally varying K_v or S_{skv} I chose to locally decrease the value for the time constant by 10% and repeat the estimation of S_{kv}^* , until equation 4.3 was satisfied. This leads to some spatial variability in the estimated time constants within a parameter zone.

These parameters are then converted to the input parameters required by SUB,

$$b_{eq} = 2\sqrt{\frac{\tau S_{kv}^*}{K_v}} \quad (\text{from eq. 2.14}) \quad \text{and} \quad (4.4)$$

$$N = \frac{S_{kv}^*}{S_{skv} b_{eq}}, \quad (4.5)$$

using constant values for K_v and S_{skv} as described above. The preconsolidation head, h_{pc} was chose as uniformly 1.2 m below the initial aquifer head. Table 4.5 summarizes the SUB input parameters used. More detail on these input parameters is presented in Appendix A.

Finally, UCODE executes the MODFLOW model and computes the cost function as the sum of the squared weighted differences between the simulated subsidence and the subsidence observations used to constrain the regression. In summary, every UCODE

parameter	value
S_{ke_i}	original S_{ke} , spatially variable
S_{kv_i}	original S_{ke} , spatially variable
h_{pc_i}	original h_{pc_i} , spatially variable
h_{pc_d}	1.2m below starting head, spatially variable
S_{ske}	$5.577 \cdot 10^{-6} m^{-1}$
S_{skv}	$1.148 \cdot 10^{-3} m^{-1}$
K_v	$4.233 \cdot 10^{-11} m/s$

Table 4.5: Constant SUB input parameters used in MODFLOW simulation. The values for S_{ske} , S_{skv} and K_v were taken from Sneed and Galloway [2000, table 3].

iteration consists of the following steps (fig. 4-12):

1. Estimate the best S_{kv}^* value for all locations inside the parameter zones using linear least-squares (eq. 4.1) and an auxiliary program to compute one-dimensional subsidence for the local drawdown history. Also, ensure that the values of τ and S_{kv}^* satisfy equation 4.3 at every location.
2. Convert these S_{kv}^* estimates and the time constants to the input parameters required by the SUB package.
3. Run the MODFLOW model to simulate groundwater flow and land subsidence for the entire model domain.

Several points should be noted regarding these steps. Employing a linear inversion to estimate the inelastic skeletal storage coefficients (step 1) makes this approach much more efficient than performing a fully non-linear estimation of all parameters. However, it inherently decouples the interbed compaction from the flow system, which is affected by the water expelled from – or taken up by – the interbeds. The coupled system is solved in the MODFLOW simulation. To avoid biasing the final solution I compared the initial drawdown history for the final estimates (used to compute the subsidence in step 1) with the final MODFLOW-computed drawdown history. As long as significant differences remained, I updated the drawdown history used in the linear estimation of S_{kv}^* and repeated the estimation. After 2 iterations the maximum difference in the drawdowns was less than 1 cm.

The parameter estimation was constrained by the two types of subsidence data presented in section 4.2. Interpolated (kriged) subsidence maps based on benchmark observations or estimates (in the 1930-92 case) were available for seven time periods. Interferometric SAR was available for about four years at a temporal spacing on the order of months. However, because the model uses annual stress periods, I combined (stacked) several interferograms to approximate the inter-annual subsidence in 1996-98, 1997-98 and 1998. The individual data included in these composite images are indicated in figure 4-5. This also reduces the influence of random error due to tropospheric variations in the composite images.

It is important in both the UCODE parameter estimation and the linear least-squares estimation to assess the relative weights given to the different subsidence observations. Both the UCODE objective (cost) function and the least-squares estimation weight the data residuals according to the variance of the corresponding observation. Note though, that while the least-squares estimation uses the entire covariance matrix, including the off-diagonal elements, the objective function computed by UCODE only takes into account the variances of the observations, inherently assuming the data covariance matrix to be diagonal. It is difficult to assess measurement variances that adequately account for all error sources. Because of the high accuracy in precision leveling surveys the variance in the benchmark observations is dominated by the interpolation and averaging over spatially varying values. I therefore used the spatially varying kriging variance at the center of each model cell as the measurement variance of the benchmark values at that location. This accounts for the increasing uncertainty distant from the actual benchmarks. I also specified a minimum variance for the interpolated subsidence values at each grid cell. This accounts for the fact that the average or representative subsidence value within each grid cell generally differs from the interpolated value at the center of the cell. An estimate for the variability of the subsidence field is provided by the variogram model (see section 4.2.2). I used the theoretical variance of the interpolated subsidence values within each grid cell according this variogram model as the minimum variance. This avoided the occurrence of unreasonably small variances where a benchmark was close to the cell center.

For the InSAR-derived subsidence values I assumed a spatially constant variance of 50 mm^2 . While this is a subjective choice it addresses an attempt to include two separate error sources. The first is the measurement variance mostly due to atmospheric disturbances. As the importance of random atmospheric errors in the images is reduced by the stacking of several individual interferograms to produce the composite images and the comparison of InSAR-derived values with the extensometer values (fig. 4-7) implies a low noise-level in the InSAR data, I assumed a variance of 25 mm^2 for this error source. The second error source is related to the variance of the actual subsidence values within each model grid cell. In the parameter estimation this is represented by a single value (the median of the InSAR-values within that cell). Again, I assigned a variance of 25 mm^2 to this error source. All three InSAR-derived displacement maps share a common reference year (1999) and common data acquisitions. This correlation is accounted for in the covariance matrix used in the linear inversions for S_{kv}^* at each location.

In principle both all available subsidence data and the available aquifer head data should be adequately reproduced by the simulation. Also, as both are affected by changes to the interbed storage parameters, the aquifer heads could be included in the set of observations used to constrain the parameter estimation. However, while this is true in principle, I found the changes in the aquifer heads caused by the interbed storage changes to be very small. This is due to the fact that the water derived from the interbeds constitutes only a small part, on the order of 5% (see section 4.4.3), of the water budget for the flow system. Including the water-level data as constraining data in the estimation of interbed storage parameters implies that any water-level residuals can and should be reduced by changes to the interbed parameters. However, the aquifer heads are much more sensitive to other parameters, which are not estimated. On the other hand, because of the low sensitivity of the aquifer heads to changes in the interbed storage parameters, these data could easily cause large biases in the estimated parameters. For these reasons I decided to exclude the aquifer head data and assume the simulated water-levels to adequately represent the actual drawdowns.

4.3.4 Notes on the reliability of the resulting parameter estimates

UCODE computes non-linear 95%-confidence intervals for the estimated parameters based on the locally linearized slope of the objective function and the linear least-squares estimator can provide a covariance matrix for the S_{kv}^* estimates. However, these values do not represent a good indication of the actual error in the estimates as their computation does not account for important systematic errors in the parameter estimates. Specifically, two important error sources that are excluded are (1) errors in the conceptualization of the aquifer system, including the geometry of the different units and (2) errors in the parameters that were held constant with respect to the original model. Both of these influences are difficult to quantify and more than likely result in deviations of the simulated aquifer heads from the actual conditions in the aquifer system.

As the simulated aquifer heads are used to drive the subsidence simulations in the model, these deviations directly affect the resulting parameter estimates. An alternative approach, circumventing the problem of inaccurately simulated aquifer heads, would be to use water-level observations instead. However, while this would ensure an adequate representation of the water-level at the well location, the problem would then be to spatially and temporally interpolate sparse observations. This is exactly what a groundwater flow simulation is designed to do, presumably better than simple geostatistical methods.

Nevertheless, I repeated the parameter estimation approach using kriged draw-down histories, which I derived from observations at 389 wells. The number of observations available varied significantly for these wells. Also, although I was careful to only use wells which appeared (by their depth or observed water levels) to sample the confined part of the aquifer system, few of the wells were classified as “observation wells”. For many wells adequate well-construction information, such as their depth or the depth intervals in which they are open to the formations, was unavailable. Also, water levels observed in wells used for groundwater pumping may be severely affected by recent pumping activity. It is therefore questionable how representative these well

zone	τ [d]	(τ [yr])	95% confidence interval [d]
1	14909	(40.8)	[14000, 15900]
2	104056	(284.9)	[75900, 201000]
3	28247	(77.3)	[26700, 29800]
4	34580	(94.7)	[33400, 35700]
5	7485	(20.5)	[3730, 11200]
6	14274	(39.1)	[10600, 18000]

Table 4.6: Estimated time constants and confidence intervals for the six parameter zones in Antelope Valley.

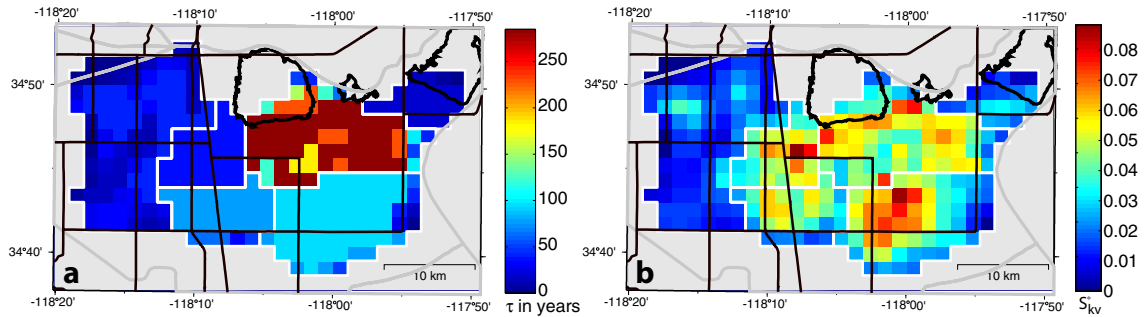


Figure 4-13: Estimated compaction time constants, τ (a) and inelastic skeletal storage coefficients, S_{kv}^* (b) for the Antelope Valley aquifer system. Large values of S_{kv}^* indicate large potential for land subsidence.

observations are of the actual hydraulic head in the aquifer.

If the difference between the kriged and MODFLOW-simulated aquifer heads is viewed as an indication of the range of likely drawdown histories, the differences in the resulting estimated parameters can at least give a qualitative impression of the reliability of the estimated parameters. This is examined in section 4.4.4.

4.4 Results

4.4.1 Final parameter estimates

The resulting parameter estimates for τ and S_{kv}^* show significant spatial variability (fig. 4-13, table 4.6). The corresponding input parameters for the final MODFLOW model are shown in Appendix A. The estimated compaction time constants range

from 20.5 years in zone 5 to 284.9 years in zone 2 (table 4.6). Non-linear 95% confidence intervals for the estimated time constants computed by UCODE are listed in table 4.6. The estimated compaction time constants are not strictly constant within each parameter zone and time constants as low as 3 years occur in the final results (fig. 4-13a), because the time constant was locally decreased to ensure physically reasonable results (i.e. satisfy eq. 4.3). Using the S_{skv} and K_v estimates from Sneed and Galloway [2000] (table 4.5), these values correspond (eq. 2.14) to an equivalent thickness between 3.8 m and 36.4 m. The time constants are bracketed by time constants estimated by Sneed and Galloway [2000] for the Holly site, ranging from less than 1 year estimated for thin (1.7 – 6 m) doubly-draining interbeds to 60 years for one thick (21 m) doubly-draining interbed, and 350 years for the 23 m-thick singly draining confining unit. The large time constant determined for the confining unit suggests that compaction in this unit may have biased the time constants resulting from the inversion. As discussed in more detail below, unrepresentative drawdown histories may also have biased the time constant estimates. Although the numerically determined confidence intervals in table 4.6 indicate the reliability of the parameter estimates, more insight is gained by considering the objective functions as a function of the six estimated time constants (fig. 4-14). Note that the cost functions for zones 1, 3, 4, and 6 have clearly defined minima. However, the cost function for zone 2 (red line in fig. 4-14) flattens out towards increasing time constants. This occurs due to a trade-off between τ and S_{kv}^* . Depending on the local drawdown and subsidence history these two parameters are not independent of each other, given a limited set of subsidence observations. In this case, the effect of increasing the time constant on the subsidence occurs after the most recent subsidence observation. The reduction in simulated subsidence for an increased time constant in the short term is balanced by an increase in S_{kv}^* . This means that it is not possible to constrain the parameters independently of each other for zone 2, given the constraining data available. However, the available data do put a lower bound on the time constant, which is about 150 years (fig. 4-14). The value for zone 5 (black line) is also poorly constrained, in this case primarily due to the lack of data. No benchmark data were available for that area. The extrapolated (kriged) “observation” values are therefore

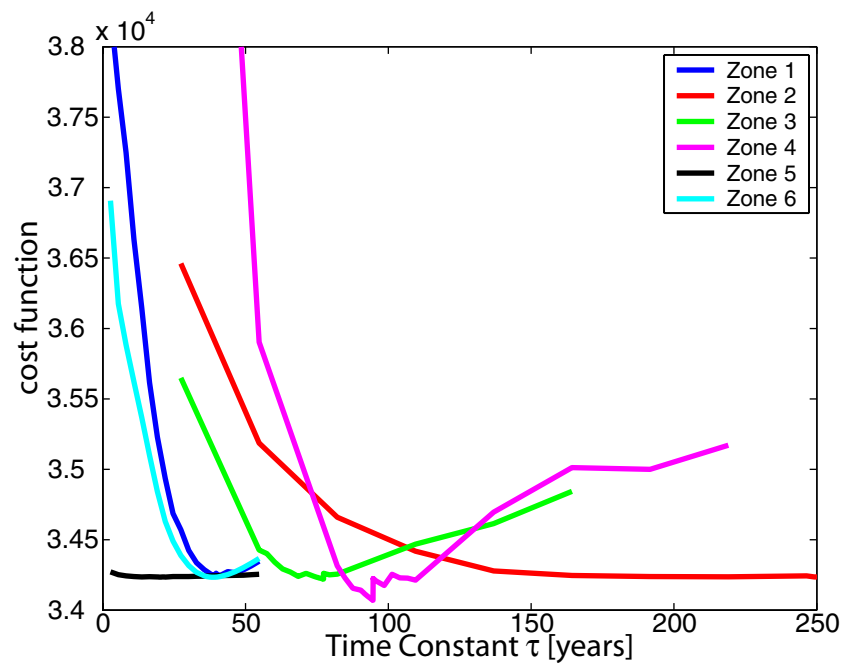


Figure 4-14: The objective (cost) function computed by UCODE as a function of the six time constants. The values for zones 2 and 5 are poorly constrained towards higher values.

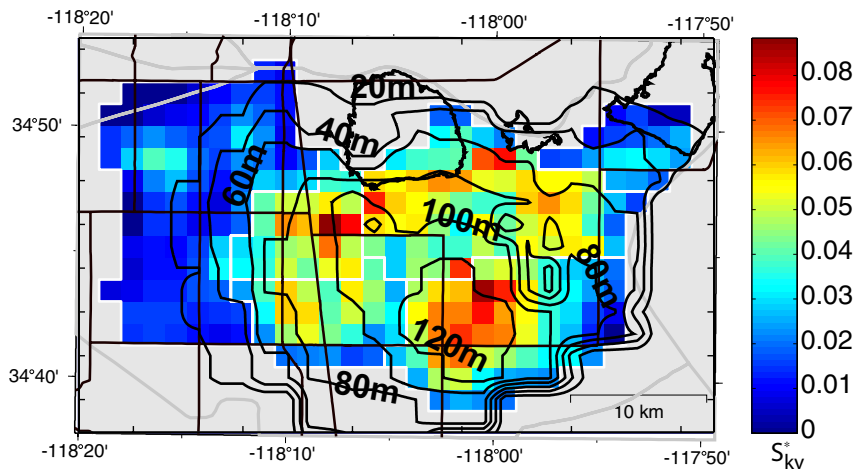


Figure 4-15: Comparison of final estimate of inelastic skeletal storage coefficients with the thickness of the lacustrine clay unit as mapped by Durbin [1978] (contours).

relatively uncertain, leading to low weights on the residuals in the computation of the cost function. The InSAR data, although available for the area, leaves the parameters relatively unconstrained for the same reasons discussed with regard to zone 2.

The final estimates of the inelastic skeletal storage coefficients, S_{kv}^* range from zero at the boundaries of the estimation domain to almost 0.09 in zone 6 (fig. 4-13b). Again using S_{skv} from Sneed and Galloway [2000] (table 4.5) this translates (eq. 2.10) to cumulative interbed thicknesses up to 77 m. Another result afforded by the linear inversions is a spatially varying estimation variance (not shown). This variance reflects the spatially variable variances of the observational data and the goodness of fit but does not include any uncertainties related to imprecise or unrepresentative drawdown histories used in the inversions.

The resulting parameter estimates reflect the spatial heterogeneity of interbed storage in the aquifer system, which causes the observed uneven distribution of subsidence when sufficiently large and widespread drawdowns occur. It is important to observe that the subsidence pattern is not solely due to the spatial distribution of drawdowns, but clearly reflects the spatial variability of the skeletal storage coefficients of the interbeds.

An interesting observation can be made when comparing the distribution of the

final S_{kv}^* -estimates with the thickness of the lacustrine clay unit mapped by Durbin [1978] (contours in figure 4-15). The observed correlation between the two distributions suggests that compaction of the lacustrine clay, which confines the underlying part of the aquifer system, may be responsible for part of the observed subsidence. This unit was not represented separately (as one or more model layers) in the model by Leighton and Phillips [2003]. Sneed and Galloway [2000] estimated that the confining unit was responsible for 31% of the historical land subsidence at the Holly site in their simulation. During 1990-97 this fraction increased to 42%. By not explicitly accounting for the compaction in this confining unit the model needs to approximate it as an interbed. The validity of this approximation depends on the validity of the interbed-assumptions for the case of the lacustrine clay unit, particularly that the top and bottom interface of the unit are exposed to the same head. Where this assumption is violated the resulting parameters are going to be biased. The lacustrine unit would be better represented by several model layers [Nishikawa et al., 2001].

4.4.2 Model fit

The simulated subsidence computed for the final parameters is compared with the kriged benchmark values during the seven time periods in figure 4-16 and with the InSAR-derived subsidence maps in figure 4-17. The subsidence values simulated using the original model are shown for comparison (column 3 in fig. 4-16 and 4-17). In all cases the agreement between the kriged values and my simulations was improved with respect to the original model. Both the magnitude and spatial extent of the observed subsidence are reproduced much better in the modified model. This improvement is quantified by the objective function (computed as the sum of squared weighted residuals) shown as blue numbers in figures 4-16 and 4-17. The total cost decreased by over 70% with respect to the original model. But although the simulated subsidence captures the timing and magnitude of the main subsidence features, some important differences remain. These differences highlight limitations of the approach presented here. Particularly over time periods of only a few years the simulation does not adequately reproduce the observed subsidence (fig. 4-17). Apart from being simply

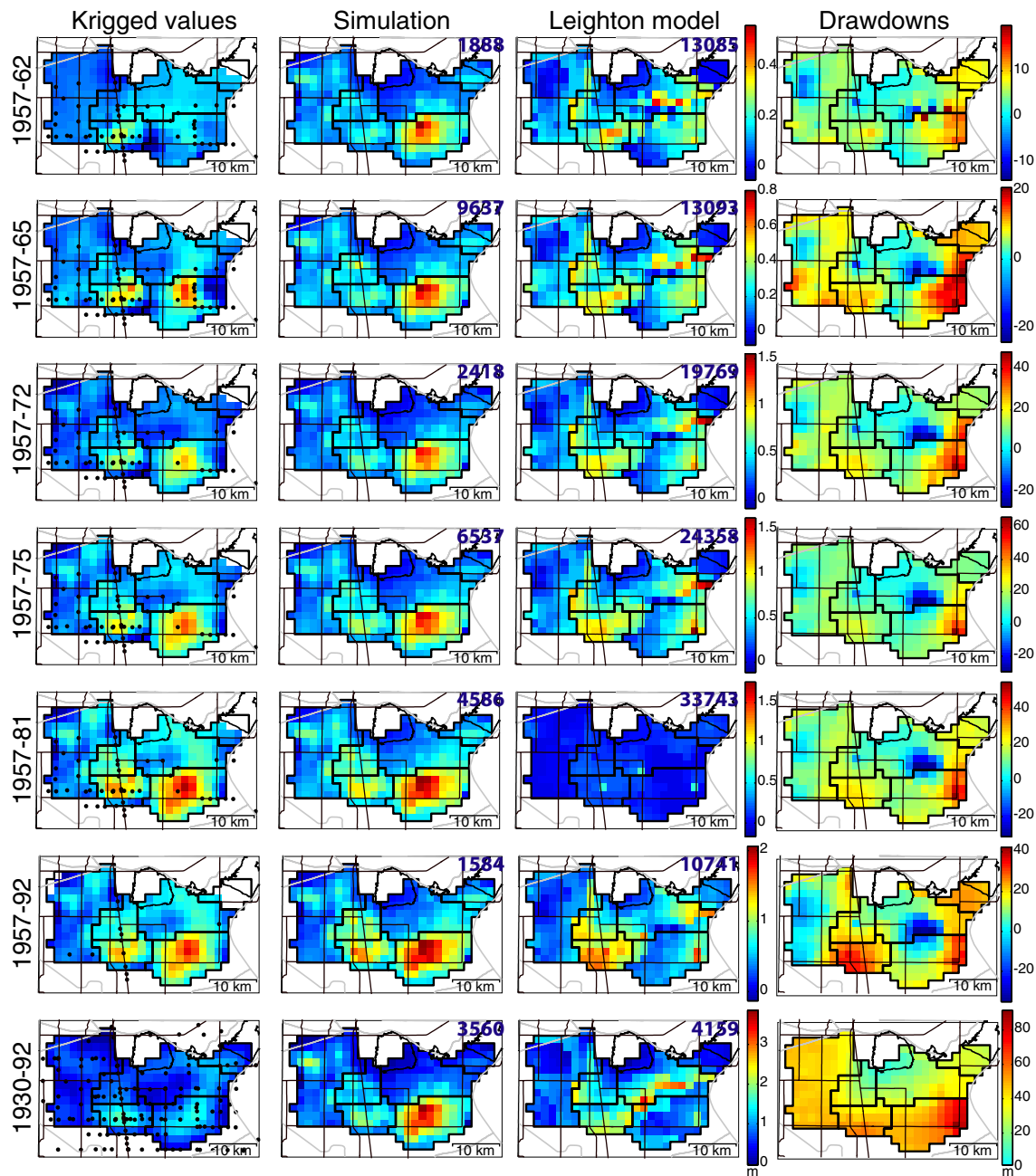


Figure 4-16: Comparison of kriged benchmark data (first column) with the final model simulations (2nd column) and the original model (3rd column). The MODFLOW-simulated drawdowns are shown for reference (4th column). The sum of the squared weighted residuals of the simulated data values are indicated for each time period (blue numbers).

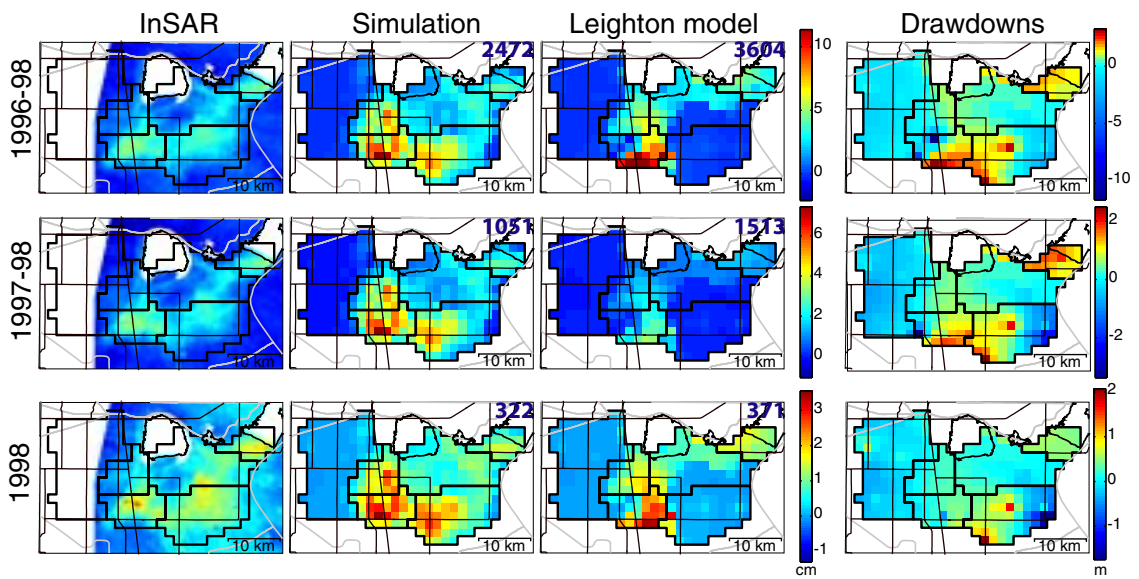


Figure 4-17: Comparison of InSAR-derived displacements (first column) with the final model simulations (2nd column) and the original model (3rd column). The MODFLOW-simulated drawdowns are shown for reference (4th column). The sum of the squared weighted residuals of the simulated data values are indicated for each time period (blue numbers).

the effect of a lower signal-to-noise ratio, this is likely caused by short-term and seasonal fluctuations in hydraulic head that are not adequately represented in the flow simulation. In calibrating the regional flow model emphasis was placed on simulating regional-scale and long-term trends in groundwater flow at the expense of local or short-term changes. In the context of the approach used here this can severely bias the short-term subsidence simulations and the parameter estimates resulting from the inversions. The relatively strong disagreement between the kriged subsidence map and the simulations for the 1930-92 time period (4-16, last row) is probably to a large extent due to errors in the underlying subsidence data for that time period. The subsidence estimate for this time period [Ikehara and Phillips, 1994] was derived from a combination of historic benchmark surveys and old subsidence maps. The small number of reliable data for this period compromise the estimate (*Steven Phillips, USGS Sacramento, priv. communication, 2001*). This has been accounted for by assigning a significantly higher variance to this estimate, which reduces the weight of the estimate in the parameter estimation. In many locations the subsidence measured during 1957-92 amounts to the entire subsidence estimated for the 1930-92 period. This would suggest that almost no subsidence occurred prior to 1957. Given the dramatic declines of hydraulic head in some areas during this time this appears highly unlikely. Instead, the published 1930-92 subsidence estimate is likely too conservative. The MODFLOW-simulated drawdowns during these time periods are shown in the rightmost columns in figures 4-16 and 4-17.

A comparison of the simulated subsidence with the available observations at the four locations marked by the green dots labelled *A – D* in figure 4-1 is shown in figure 4-18. Here it is obvious that the match to the *observed* data is generally much better than that to the 1930-92 subsidence *estimate* by Ikehara and Phillips [1994]. This can be explained by the relatively uncertain estimated subsidence values. Furthermore, it becomes intuitively clear from figure 4-18 that the time period covered by currently available InSAR data is extremely short compared to the time span over which the subsidence occurred. The comparison between the water level observations in wells and the simulated hydraulic heads (fig. 4-18, right) gives an indication of the reliability of the simulated heads. While the flow simulation (dashed line) doubtlessly

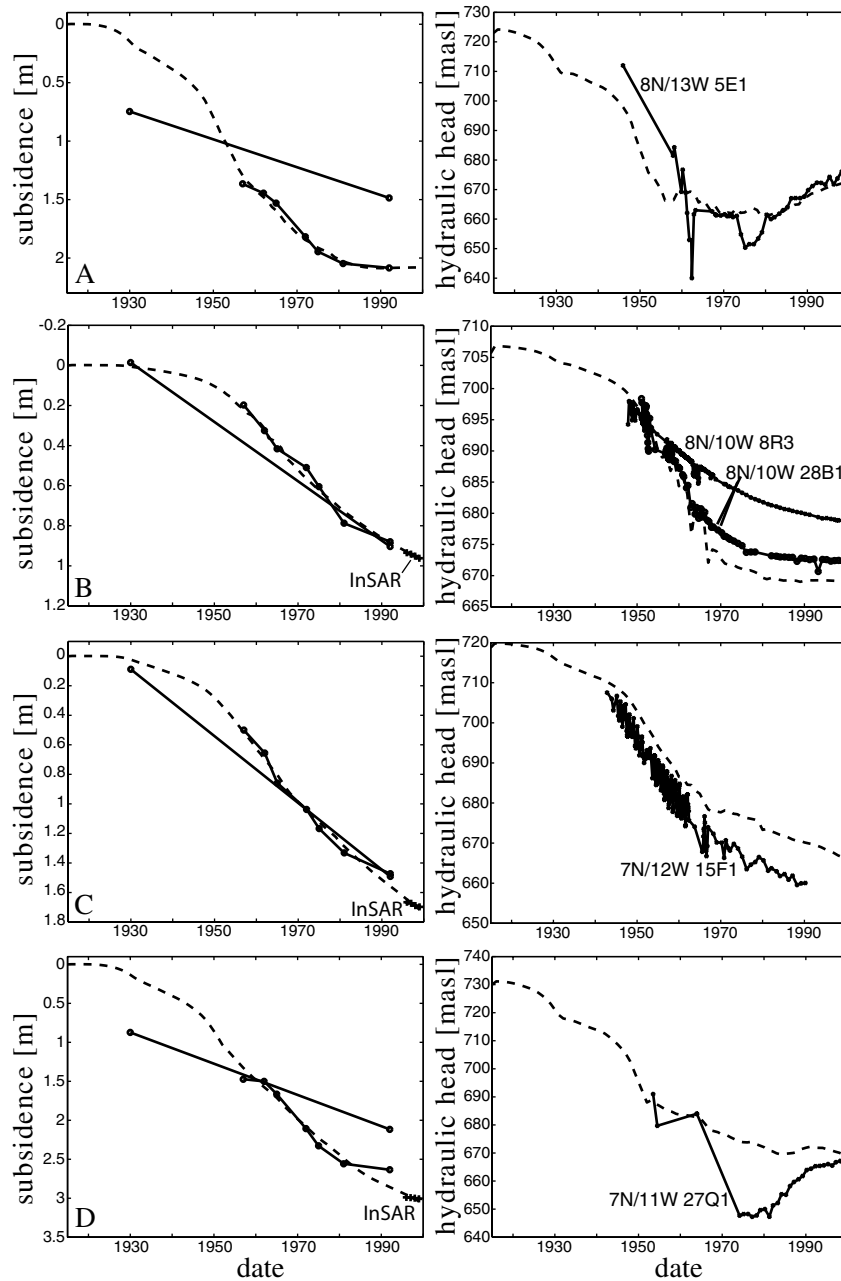


Figure 4-18: Subsidence history (left) and drawdowns (right) at the four locations marked A – D in figure 4-1. The dashed lines show the simulated values, while the solid lines show observational data. The subsidence estimate for the 1930-92 period is shown separately from the other subsidence data due to its much higher uncertainty. The hydraulic head records shown are observations from nearby wells. Note that slow drainage from thick interbeds causes continuing subsidence despite stabilizing or recovering hydraulic heads in most wells.

approximates the observed heads, significant differences remain between the simulated and observed heads. This difference between the simulated drawdowns (driving the subsidence simulation) and the actual drawdowns in the aquifer system probably constitute the most important limitation of the described inversion approach. While it was beyond the scope of this study to improve on the simulated heads in the flow-model, the resulting parameter estimates are strongly biased where the simulated heads in the aquifers are not representative of the head at the boundaries of the compacting interbeds. An alternative approach circumventing difficulties related to the simulation of the hydraulic head history would be to replace the simulated heads with measured heads in wells. However, the relatively few well observations would have to be interpolated in both space and time, introducing new, likely larger, inaccuracies. Nevertheless this approach is investigated for comparison in section 4.4.4. The role of the groundwater flow simulator in the approach described here can essentially be seen as a sophisticated way to interpolate the hydraulic heads at locations where a sufficient number of observations is not available.

4.4.3 Aquifer heads

An interesting observation during the parameter estimation procedure was that the changes in interbed storage during the estimation did not significantly alter the flow field or resulting hydraulic heads in the aquifers, although the interbeds supply large volumes of water to the wells. Over the 84 years of the simulation, an average of 5% of the water pumped from wells originated from interbeds, with peak values of 10% in some years. Note however that these values are significantly higher locally. The effect of introducing delay in the interbed drainage resulted in larger initial drawdowns in the aquifer after the onset of pumping. These larger drawdowns increase the head gradient across the interbeds, causing them to drain at a higher rate. However, within a few years the head in the modified model returned to the level found in the original model. This indicates that despite the hydrologic coupling of the compacting interbeds with the regional flow field the long-term drawdowns can be computed without explicitly accounting for the delay in the drainage process. However, if the

short-term response of hydraulic head to changes in pumping are to be simulated, the presence of delayed interbeds must be accounted for. The increased drawdown that occurs after the onset of pumping when delayed drainage of the interbeds is simulated has been observed previously by Leake [1990]. It occurs in response to the prescribed pumping rates and the slow release of water from storage in the interbeds. More water is initially required from storage in the aquifer to supply the pumping wells, resulting in larger drawdowns in the aquifer than would occur without delayed drainage of interbeds. These large drawdowns increase the hydraulic gradient between the centers of the interbeds and the aquifers, thereby accelerating the drainage. After some time (depending on the time constants of the interbeds) the aquifer drawdowns approach those for the aquifer system with no-delay interbeds.

Another implication of the weak coupling between long-term drawdowns and interbed storage properties may be even more important here. Specifically, it may, in many cases, be possible to separate the flow simulations from subsidence simulations. A flow-model could then be used to provide the drawdown history, which could be used in a separate model to simulate the subsidence. This would simplify the simulations as the flow-field does not have to be recomputed at every iteration.

4.4.4 Results using kriged aquifer heads

Errors in the simulation of aquifer heads by the MODFLOW program and the fact that they may not adequately represent the drawdowns in the confined depth interval of the aquifer system, have been identified as probably the primary limitation of the presented approach to estimate the interbed material properties. I have pointed out before, that using observations of aquifer heads in wells would enable an estimation without the use of a groundwater flow model. Unfortunately, avoiding the flow model comes at the cost of having to interpolate well observations both in space and time, adding a different source of uncertainty, as hydrological conceptualizations in the flow model are replaced with statistical assumptions of the spatio-temporal distribution of the aquifer heads. For these reasons using interpolated well observations in the

estimation cannot be considered a better or more accurate approach. To the contrary, the results are probably less reliable than results using a carefully calibrated groundwater flow model.

If the differences between the aquifer heads simulated by the groundwater flow model and the interpolated well observations are used as a rough indicator of the accuracy of the simulated heads, the differences in the respective estimated parameters can be regarded as a qualitative measure of reliability of the estimates. Although this approach admittedly does not amount to a rigorous error estimation it allows at least an approximate quantification of the effect of the inaccurately simulated aquifer heads.

The critical issue in replacing the MODFLOW-simulated heads with well observations is the spatial and temporal interpolation of reliable head observations. Kriging is well suited for this problem as it does not require the input data to be regularly sampled. Using a kriging interpolator, the construction of the spatially variable draw-down history includes the following steps:

1. Select reliable head observations from wells that are considered representative of the confined part of the aquifer system.
2. Determine a spatial and temporal covariance functions of these data. This is needed in the kriging.
3. Perform a three-dimensional (2 spatial and 1 temporal dimensions) interpolation of the observations selected in 1.

A database of water-levels observed at wells is maintained by the U.S. Geological Survey (*Steven Phillips, USGS Sacramento, written comm.*). I inspected all wells for which data were available and selected 389 wells which I considered reliable enough to be used in the kriging (fig. 4-19).

I chose the wells on the basis of (a) their open depth interval (where known), (b) the similarity of the observed water level with the water level in nearby wells of known depth interval and (c) water-level and water-level fluctuations suggesting confined conditions. This selection was necessarily very subjective and certainly has

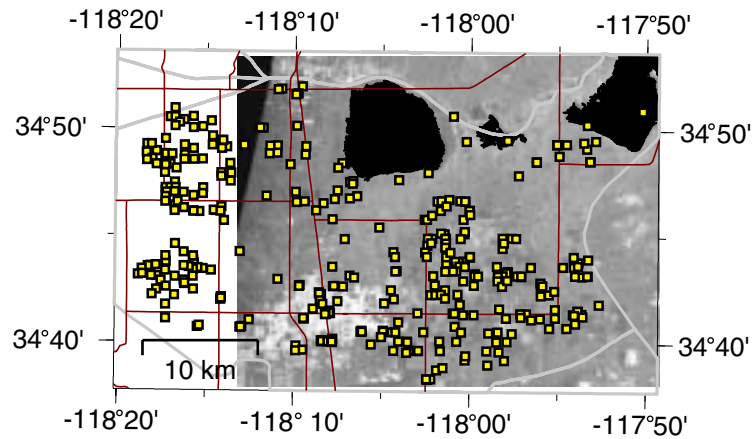


Figure 4-19: Locations of the 389 wells used in the kriging of the aquifer head in space and time.

to be considered one of the weak points in deriving reliable aquifer head distributions from observations. Another difficulty in estimating water levels representative of a larger volume in the confined aquifer system are that lithologic and well-construction information are often unavailable and measurements may in many cases be severely affected by recent or nearby pumping operations. Only 24 (6%) of the 389 wells used in the kriging were classified as “observation” wells. The majority (232 (60%)) of the selected wells were classified as “withdrawal” wells, for which well-construction information was often unavailable. Also, water level observations in withdrawal wells are often severely affected by the pumping operations and may only give a poor representation of the aquifer head outside the immediate surroundings of the well. Another 107 (28%) wells were classified “unused” and 26 (7%) were classified as “destroyed”. (Presumably these had been mostly withdrawal wells previously). Using only the 24 observation wells in the kriging to ensure the quality of the water level observations would not have sufficed to interpolate the piezometric surface in space and time. For the purpose of this study I relied on all observations from the 389 wells without attempting to weight or correct potentially less representative observations. There were 8112 water level observations available in these wells.

I fit these observations with an isotropic exponential semivariogram model in space and a gaussian semivariogram model in time. The semivariogram γ used in the kriging

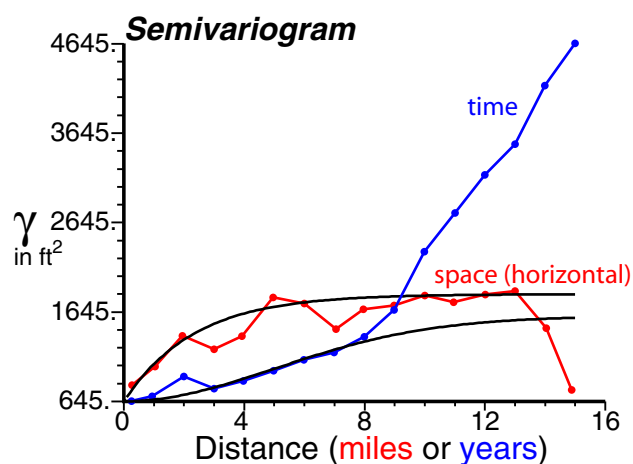


Figure 4-20: Variogram model (black lines) and experimental variograms in space (red) and time (blue).

was

$$\gamma(h) = 111.48m^2 \left(1 - \exp\left(-\frac{3h}{11265m}\right)\right) \quad \text{horizontally, and}$$

$$\gamma(\Delta t) = 83.055m^2 \left(1 - \exp\left(-\frac{3\Delta t^2}{(12.33\text{years})^2}\right)\right) \quad \text{in time.}$$

I used a “nugget” effect of $\gamma(\varepsilon) = 59.83m^2$. This variogram model is compared to the experimental variogram in figure 4-20.

The kriged estimate of the annual aquifer heads for the confined part of the aquifer system differed markedly from the MODFLOW-simulated values at many locations (fig. 4-21, 4-22, 4-23).

Repeating the parameter estimation using the kriged drawdowns results in the time constants listed in table 4.7 and shown in figure 4-24a. The resulting S_{kv}^* values are shown in figure 4-24b. Interestingly, none of the estimates for the time constants using the kriged drawdowns fall within the non-linear 95% confidence intervals computed for the final values using the MODFLOW heads. The significant changes in the resulting time constants is partly due to the fact that these values are relatively poorly constrained by the available subsidence data for the kriged drawdown histories (see discussion in section 4.4.1). However, they also suggest that the estimation of

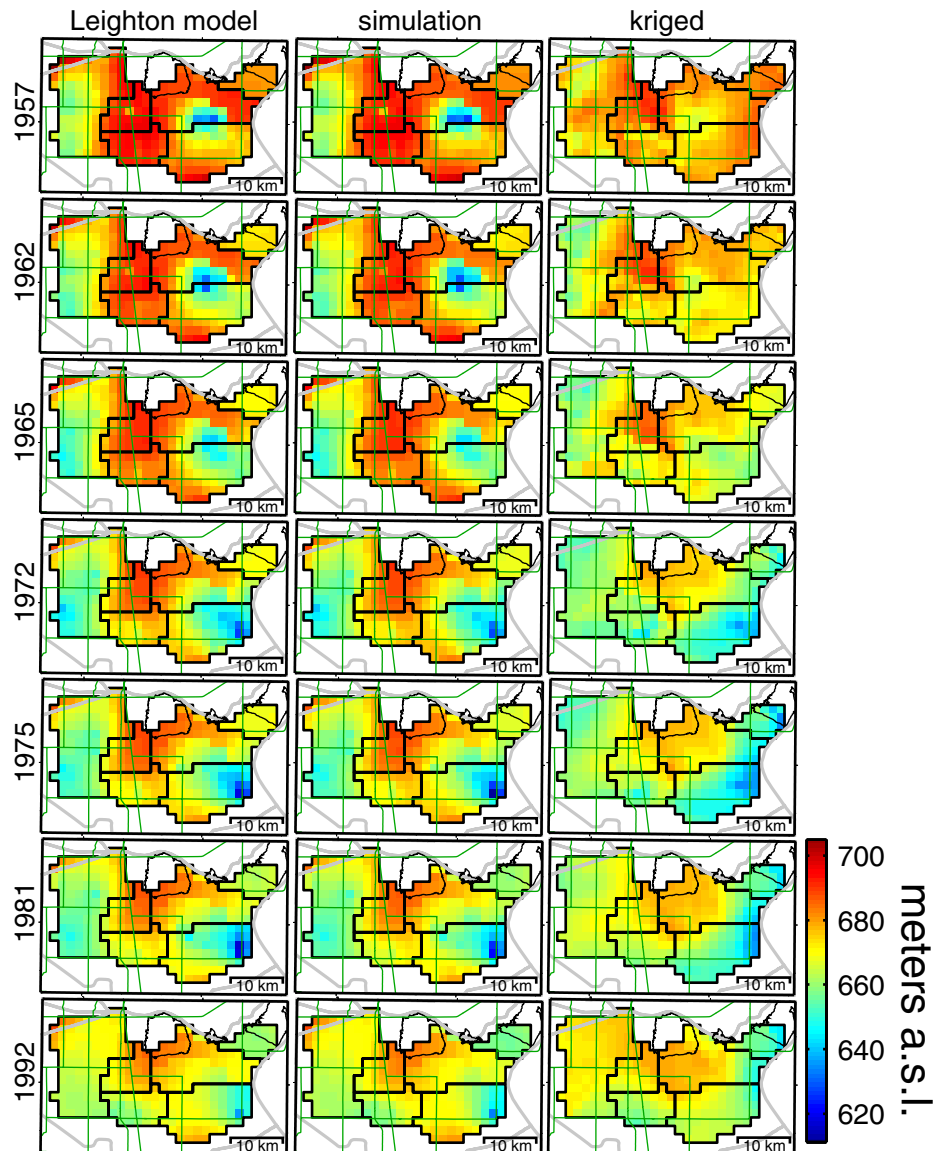


Figure 4-21: Comparison of hydraulic heads simulated by the original Leighton and Phillips model (first column), the model incorporating the estimated storages (second column), and kriged using observations of hydraulic head in wells. The changes in interbed storage had little effect on the hydraulic heads, while the kriging resulted in markedly different results.

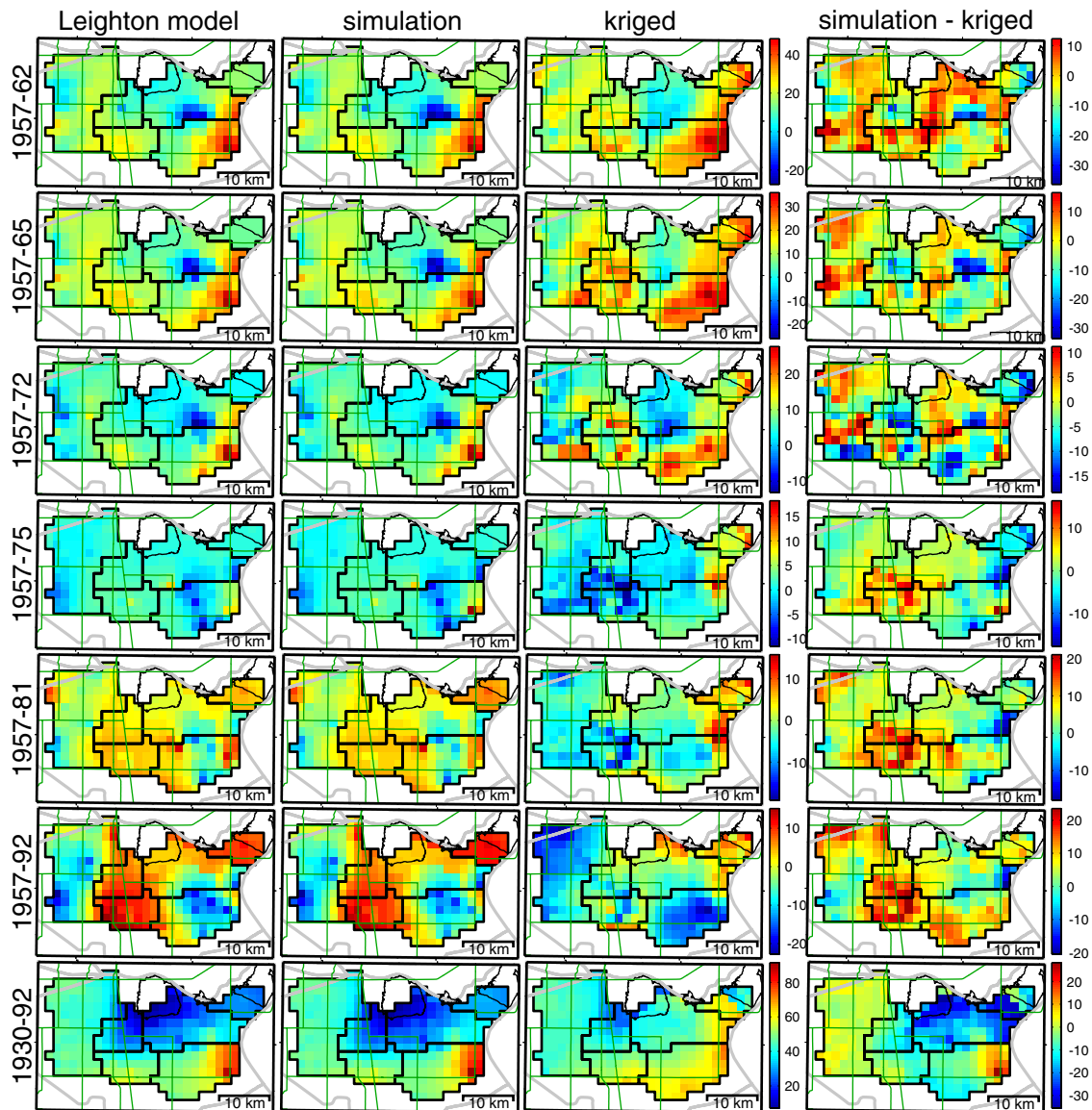


Figure 4-22: Comparison of drawdowns simulated by the original Leighton and Phillips model (first column), the model incorporating the estimated storages (second column), the derived from the kriged hydraulic heads (third column). The fourth column shows the difference between columns 2 and 3. Values are in meters (positive for declining water levels).

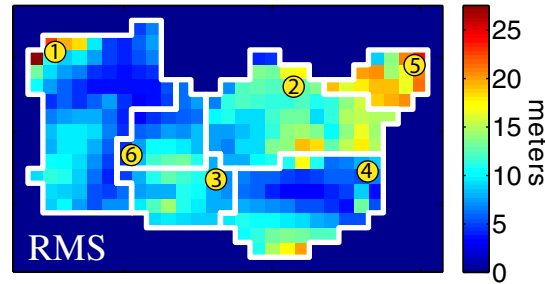


Figure 4-23: Root-mean-squared (RMS) difference between MODFLOW-simulated and kriged heads.

zone	τ [d]	(τ [yr])	95% confidence interval [d]
1	24730	(67.7)	[22800, 26600]
2	78580	(215.1)	[65100, 92100]
3	61724	(169.0)	[59200, 64300]
4	43512	(119.1)	[41600, 45400]
5	67179	(183.9)	[46100, 88300]
6	57792	(158.2)	[-6010, 122000]

Table 4.7: Estimated time constants and confidence intervals for the six parameter zones in Antelope Valley, using kriged head values instead of MODFLOW-simulated heads.

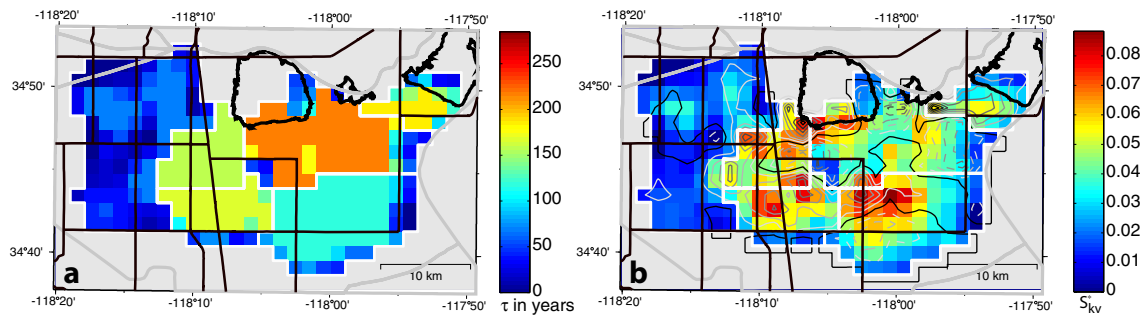


Figure 4-24: Estimated compaction time constants, τ (a) and inelastic skeletal storage coefficients, S_{kv}^* (b) for the Antelope Valley aquifer system, using kriged aquifer heads. The contours in (b) show the difference between these results and the results obtained using the MODFLOW-simulated heads (fig. 4-13). Contour interval is 0.005. The solid black contour is zero difference. Dashed contours mean that the new values are smaller than the values in fig. 4-13.

the time constants is highly sensitive to the drawdown histories – assumed or measured – used in the regression. The change in the estimated S_{kv}^* values using kriged heads with respect to the estimates using MODFLOW-simulated heads is shown by the contours in figure 4-24b. The contour interval is 0.005. Solid contours denote areas where the estimates using kriged heads were larger than the estimates using MODFLOW-simulated heads; dashed contours denote the opposite case.

If the differences between the kriged heads and the MODFLOW-simulated heads are assumed to be representative for the deviation of the simulated heads from the values that would adequately represent the hydraulic heads at the boundaries of the compacting interbeds, the difference between the estimated parameters resulting using the MODFLOW-simulated and kriged heads, respectively (contoured in figure 4-24), can be viewed as a systematic error resulting from the uncertainty in hydraulic head. This systematic error is significantly larger than the standard deviation estimated in the linear estimation of the S_{kv}^* values. However, if these two contributions are combined by taking the square root of the sum of their squares, an estimate of the total error ($1-\sigma$) can be obtained (fig. 4-25). It must be emphasized that this error estimate is not the result of a rigorous error analysis but has to be viewed as a rather crude approximation to the true error distribution. However, because of difficulties in parameterizing the error in the drawdown histories a more formal error analysis seems elusive.

4.5 Conclusions

In this chapter I have presented a newly developed approach to estimate spatially varying parameters controlling interbed compaction using observations of the subsidence field in Antelope Valley over different time periods. The estimated parameters were the compaction time constant τ and the total inelastic skeletal storage coefficient, S_{kv}^* of the interbeds. The observations of the subsidence field were derived from recent InSAR observations and historical observations at benchmarks. A previously calibrated regional MODFLOW model was used to simulate hydraulic heads in the aquifer system. The subsidence package (IBS2) was included to simulate subsidence,

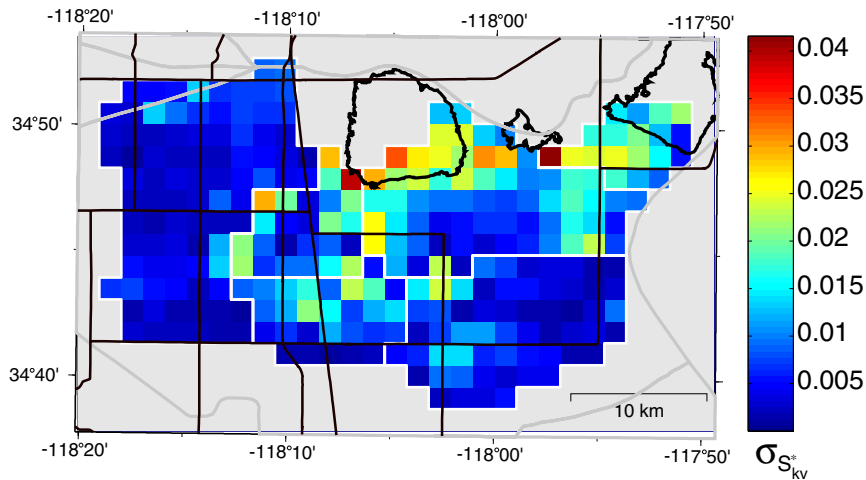


Figure 4-25: Estimate for the total standard deviation ($1-\sigma$) of the final S_{kv}^* estimate based on the difference between the estimates resulting from using kriged and MODFLOW-generated aquifer heads and the estimation variance from the linear estimation.

explicitly accounting for slow drainage of the interbeds. The resulting parameter estimates show a heterogeneous parameter distribution across the Antelope Valley aquifer system. Estimated time constants range from 3 years to 285 years. The estimated inelastic skeletal storage coefficients range from near zero to 0.09. Although the estimations used here also provided an error estimate for the final parameter values, these exclude the likely most important error contributions, namely errors in the conceptualization of the aquifer system and inaccurately simulated aquifer drawdowns. The large estimated time constants may in some areas be due to compaction in a laterally-extensive, thick confining unit or biased by inaccurately simulated drawdown histories. Reliable and accurate knowledge of the drawdown history is essential to estimate both storage coefficients and compaction time constants reliably. In addition, the estimates of the interbed time constants would have been better constrained if sufficient historical subsidence data had been available at all locations. Because of the difficulties in quantifying errors in the conceptual hydrogeologic model or the simulated drawdown histories it is difficult to assess a reliable confidence level for the resulting parameter estimates.

Nevertheless, the parameter estimation procedure developed in this study led to a notable improvement of the original groundwater flow and subsidence model. The resulting parameter estimates significantly improved the agreement between the model-simulated subsidence and the observations. The agreement was better over longer time periods. This can in part be explained by a higher signal-to-noise ratio as larger drawdowns and subsidence accumulate over time, but is likely aggravated by the fact that the model-simulated heads generally match the long-term head changes better than short-term head fluctuations which strongly influence subsidence over short periods. Interestingly, the long-term drawdown histories were relatively little affected by the modifications to the interbed storage, suggesting that regional groundwater flow in Antelope Valley is relatively insensitive to groundwater contributed by the compacting interbeds. The most important improvement this work has yielded was the added spatial heterogeneity of the parameter estimates that for the first time exploited the spatial detail provided by InSAR subsidence observations. These observations have afforded an unprecedented knowledge of the spatial distribution and magnitude of ongoing land subsidence. The heterogeneous parameter estimates enabled a much better reproduction of the spatial extent and structure of the subsidence field. Where the subsidence field and aquifer system structure are highly heterogeneous, understanding this heterogeneity (and being able to simulate it) is critical to making informed management decisions. Additionally, the timing of the observed subsidence was simulated more realistically by explicitly accounting for slowly draining interbeds. This added complexity proved necessary in parts of Antelope Valley to reproduce the observed subsidence history.

Due to the currently limited temporal coverage of SAR data the large time constants found in Antelope Valley cannot be estimated from InSAR alone. Subsidence observations on the order of the compaction time constant (tens to hundreds of years in Antelope Valley) are necessary to constrain the time constant estimates. The presently available InSAR data has proven useful in mapping and monitoring ongoing land subsidence, defining structural boundaries in aquifer systems, defining parameter zones within models, and estimating storage parameters where time constants are small. As more SAR data become available in the future, the importance of InSAR in

the study of aquifer-system properties, including compaction time constants, is likely to increase. The lower precision of the vertical displacement measurement using InSAR compared to precision leveling does not limit their applicability, as inaccuracies in the hydrogeological conceptual models currently cannot exploit more accurate observations and the need for interpolation in a heterogeneous displacement field adds an error source that has been eliminated from InSAR observations.

Where InSAR techniques can be applied to measure and characterize the subsidence field above compacting aquifer systems the spatially sparse or infrequent observations of surface displacements cease to be the limiting factor in the analysis of aquifer mechanics. The wealth of data provided by InSAR is in contrast to the much sparser sampling of the distribution of hydraulic heads (and hydraulic head changes). Difficulties in reliably estimating stress changes given the incomplete knowledge of the subsurface geology now constitute the primary limitation of this kind of analysis.

Chapter 5

Limitations in estimating inelastic compaction parameters

5.1 Introduction

Almost all SAR data suitable for interferometry have been acquired after 1992. The SAR sensors on the ERS, J-ERS and RADARSAT satellites have provided data enabling an explosion of applications for InSAR technology in the earth sciences in recent years and the recent successful launch of the ENVISAT satellite and other planned radar missions are expected to ensure the continuing availability of interferometric radar data.

In estimating hydrologic parameters of the Antelope Valley aquifer system (Chapter 4) I found the time constants of the interbed compaction process to be on the order of decades to centuries. This severely limited the usefulness of InSAR data – spanning only a few years – in estimating the parameters governing land subsidence over the compacting aquifer system.

I show here that data sets likely to become available in the future will be able to improve this situation provided that reliable information on the aquifer drawdowns histories is available. InSAR will thus be of greater utility in the characterization of aquifer system compaction with large time constants. I demonstrate this with a set of simulations described in this chapter.

For the purpose of these simulations, I assumed the model for one-dimensional interbed compaction (section 2.1) to describe aquifer system deformation adequately.

This means specifically that all interbeds that contribute to the compaction of the aquifer system are exposed to the same head at their boundaries and have the same (constant) specific storage values and vertical hydraulic conductivity. To assess both, the importance of the availability of frequent observations and the possible inaccurate estimation of aquifer drawdowns I then performed the parameter inversion as described in section 4.3.3 for a variety of scenarios representing different drawdowns and InSAR data sets of different sizes. The subsidence data used to constrain the parameter estimation were computed using the numerical forward model. There was one minor difference in the parameter inversion approach employed in this case with respect to the approach described in section 4.3.3. In the parameter estimation for the Antelope Valley aquifer system I estimated the time constants for parameter zones and subsequently adjusted the values locally, if they violated the condition in equation 4.3. As for each scenario here I estimated one compaction time constant τ and one inelastic skeletal storage coefficient S_{kv} , this was not necessary. Instead, I enforced the constraint that

$$S_{kv} \geq 2\sqrt{\tau K_v S_{skv}}, \quad (5.1)$$

which is equivalent to equation 4.3.

To evaluate the robustness of the parameter estimation approach with respect to the often imperfect knowledge of the hydraulic head I simulated subsidence using several systematically biased drawdown histories, while always assuming the same drawdown history in the parameter inversions. In practice such systematic differences between the actual heads and those measured in wells might be due to several effects. An observation well might be influenced by heads in more than one aquifer, or nearby pumping or recharge, for example. The scenarios used here (described in section 5.2) represent idealized cases of what might be observed in practice. By systematically varying both the error in the head observations and the size of the subsidence data set I was able to determine whether the sheer volume of subsidence data can to some extent make up for deficiencies in the knowledge of hydraulic head.

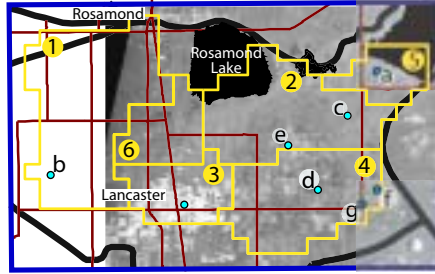


Figure 5-1: Map of eight locations (a-g) in Antelope Valley model (see Chapter 4) for which drawdown histories were used for simulations in this chapter. Parameters are listed in table 5.1.

5.2 Description of the simulated scenarios

I selected eight different locations with different storage coefficients and different drawdown histories from the Antelope Valley model described in Chapter 4 (fig. 5-1). Each location is characterized by an inelastic skeletal interbed storage coefficient, S_{kv} , an elastic skeletal storage coefficient for the aquifer system, S_{ke} , and a preconsolidation head, h_{pc} . The corresponding parameter values are summarized in table 5.1. The elastic and inelastic skeletal specific storages for the interbeds were assumed to be constant and equal to $S_{ske} = 5.6 \cdot 10^{-6} m^{-1}$ and $S_{skv} = 1.15 \cdot 10^{-4} m^{-1}$, respectively. The vertical hydraulic conductivity of the interbeds was assumed to be $K_v = 3.66 \cdot 10^{-6} m/s$.

For each of the locations, I used 13 different drawdown scenarios to compute subsidence. The first scenario constitutes the base case. For all other scenarios the drawdown histories were modified versions of this drawdown history, $h_1(t)$. The “observed” drawdown history used in the parameter estimation for all scenarios, was equal to $h_{obs}(t) = h_1(t)$. For the other 12 scenarios the actual drawdown history (used to simulate subsidence) differed systematically from the “observed” drawdowns. In scenarios 2 – 5 the change in hydraulic head in any time period was the original change in hydraulic head during that time period multiplied by a factor α between 0.8 and 1.2:

$$\frac{\partial h(t)}{\partial t} = \alpha \frac{\partial h_1(t)}{\partial t}. \quad (5.2)$$

location	$S_{kv}[10^{-3}]$	$\tau[\text{days}]$	$S_{ke}[10^{-3}]$	$h_{pc}[\text{m}]$	$madr[\text{m/yr}]$	AV (row, col)
a	16.5	7453	1.20	687.05	0.409	(16, 47)
b	9.6	4861	1.39	720.58	0.665	(23, 25)
c	47.1	67298	1.30	705.64	0.449	(19, 45)
d	50.8	27266	1.44	728.50	0.778	(24, 43)
e	40.1	67298	1.33	712.35	0.522	(21, 41)
f	8.4	4092	1.17	732.16	0.964	(24, 47)
g	41.4	25159	1.37	717.53	0.800	(25, 34)
h	13.4	7702	1.46	733.38	1.001	(25, 46)

Table 5.1: Parameter values for the eight simulated locations. The values are taken from the final results from the final Antelope Valley MODFLOW model. The last column indicates the model location they correspond to (see fig. 5-1). h_{pc} is the pre-consolidation head for the interbed material and $madr$ is the mean annual drawdown rate computed from the simulated heads for that location.

This approximates a situation where the observation well is influenced by effects that either dampen or accentuate the head changes in the compacting aquifer system. In scenarios 6 – 9 a linear drawdown trend has been added or subtracted to the original drawdown history. For each location the magnitude of the trend was proportional to the mean annual drawdown rate ($madr$) for that location (table 5.1) over the entire observation period:

$$h(t) = h_1(t) + \alpha \cdot madr \cdot t. \quad (5.3)$$

The scenarios are therefore relatively similar to scenarios 2 – 5 over long time periods, but do not emphasize changes on shorter time-scales as much. They may represent a case where the observation well is either strongly influenced by nearby pumping activity or somewhat hydraulically isolated from the main aquifer. In scenarios 10–13 a sinusoidal seasonal head fluctuation of different amplitudes was added to the original drawdown history. The amplitude of the sinusoidal signal was proportional to the mean annual drawdown for each location:

$$h(t) = h_1(t) + \alpha \cdot madr \cdot \sin\left(\frac{2\pi}{1 \text{ year}}t\right) \quad (5.4)$$

These scenarios correspond to a case where seasonally fluctuating water levels may affect the subsidence history, but are not accounted for in the parameter estimation,

scenario	type of bias	α
s1	no bias	
s2	head changes accentuated (eq. 5.2)	0.8
s3		0.9
s4		1.1
s5		1.2
s6	linear trend added (eq. 5.3)	-0.2
s7		-0.1
s8		0.1
s9		0.2
s10	seasonal signal added (eq. 5.4)	0.5
s11		1.0
s12		2.0
s13		5.0

Table 5.2: Drawdown scenarios used in simulating the land subsidence. In all cases the parameter regression used the same drawdown history – the one of scenario 1. The different meanings of α are defined in equations 5.2, 5.3, and 5.4.

either because the model time periods are too long, or because water level observations at seasonal time scales are not available. The thirteen scenarios are summarized in table 5.2.

For all eight locations and 13 drawdown scenarios I estimated the inelastic skeletal interbed storage coefficient, S_{kv} , and the compaction time constant τ as described above. The estimations were constrained by the simulated subsidence data. In order to assess the importance of the frequency of SAR observations I used four different subsets of the simulated subsidence data, using one observation every one, five, ten and twenty years. I added a Gaussian noise with a standard deviation of $\sigma = 5$ mm to the simulated subsidence to account for measurement uncertainty.

5.3 Results

A total of 416 parameter estimations were performed for the 8 locations, 13 drawdown scenarios, and 4 different subsidence data subsets. In most cases the UCODE routine converged on a solution within about 4 iterations. However, in some cases

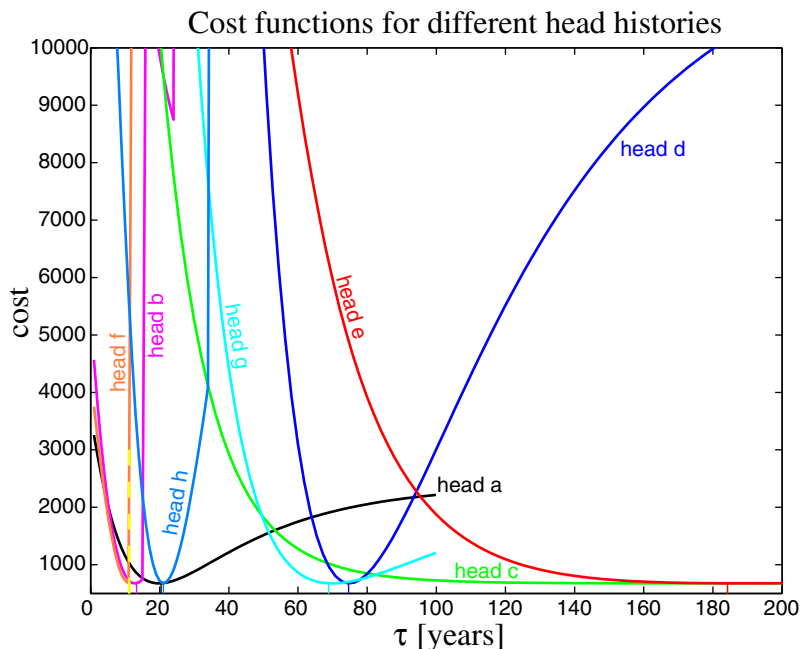


Figure 5-2: Objective (cost) functions for different head histories in parameter inversions using scenario 1 (correct drawdowns). Note that for locations **c** and **e** a trade-off between increasing τ and decreasing S_{kv} results in poorly constrained estimates.

the algorithm failed to converge to a solution. For these cases I determined the optimal parameters by mapping out the cost function (computed as the sum of weighted squared residuals) as a function of τ . I found that in these cases τ was poorly constrained towards larger values. This can be seen clearly for the heads at locations **c** and **e** in figure 5-2.

For certain drawdown histories there can be a strong trade-off between τ and S_{kv} . The effect of increasing τ is to decrease the amount of subsidence occurring at early times and increase the amount of subsidence occurring at later times. An increase in S_{kv} linearly increases the observed subsidence for a given drawdown history. If the time constant is increased above a certain value, the effect of increasing subsidence at later times is moved beyond the times for which measurements are available. For these situations S_{kv} and τ become highly correlated.

The estimated parameters for all scenarios are compared to the true values in figures 5-3, 5-4, and 5-5. Using the correct drawdown histories (scenario 1), the

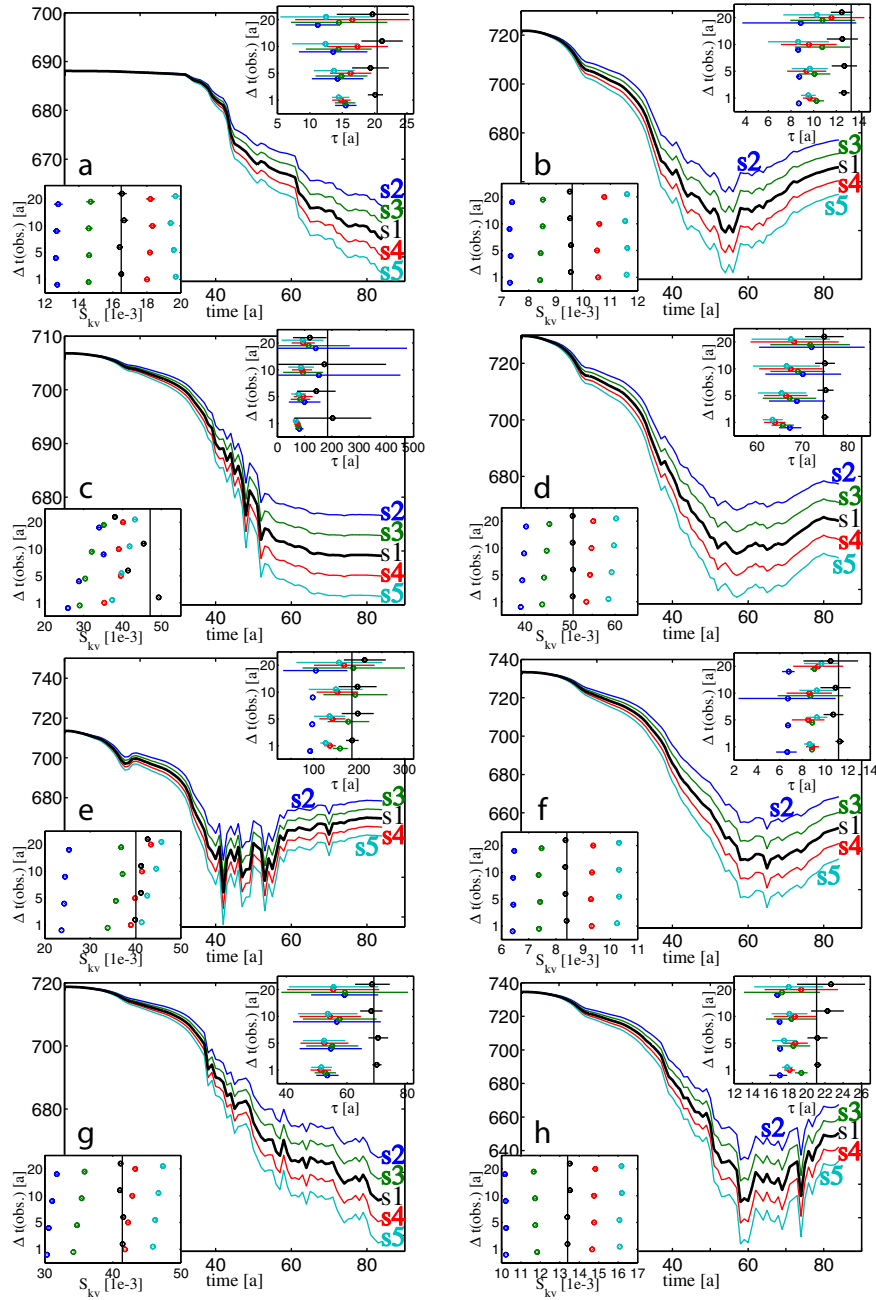


Figure 5-3: Drawdown scenarios $s1 - s5$ for the eight locations. The black drawdown curve ($s1$) is the drawdown history used for all parameter estimations. The insets at the top right show the estimated time constants (abscissa) for InSAR observations available every 1, 5, 10, and 20 years (ordinate); the horizontal bars indicate the UCODE -estimated 95% confidence intervals and the vertical black lines indicate the true value. The insets at the bottom left of the graphs show the estimated S_{kv} values of the interbeds; the $1-\sigma$ error bars of the linear parameter estimation are mostly too small to see at this scale; the vertical black lines indicate the correct value.

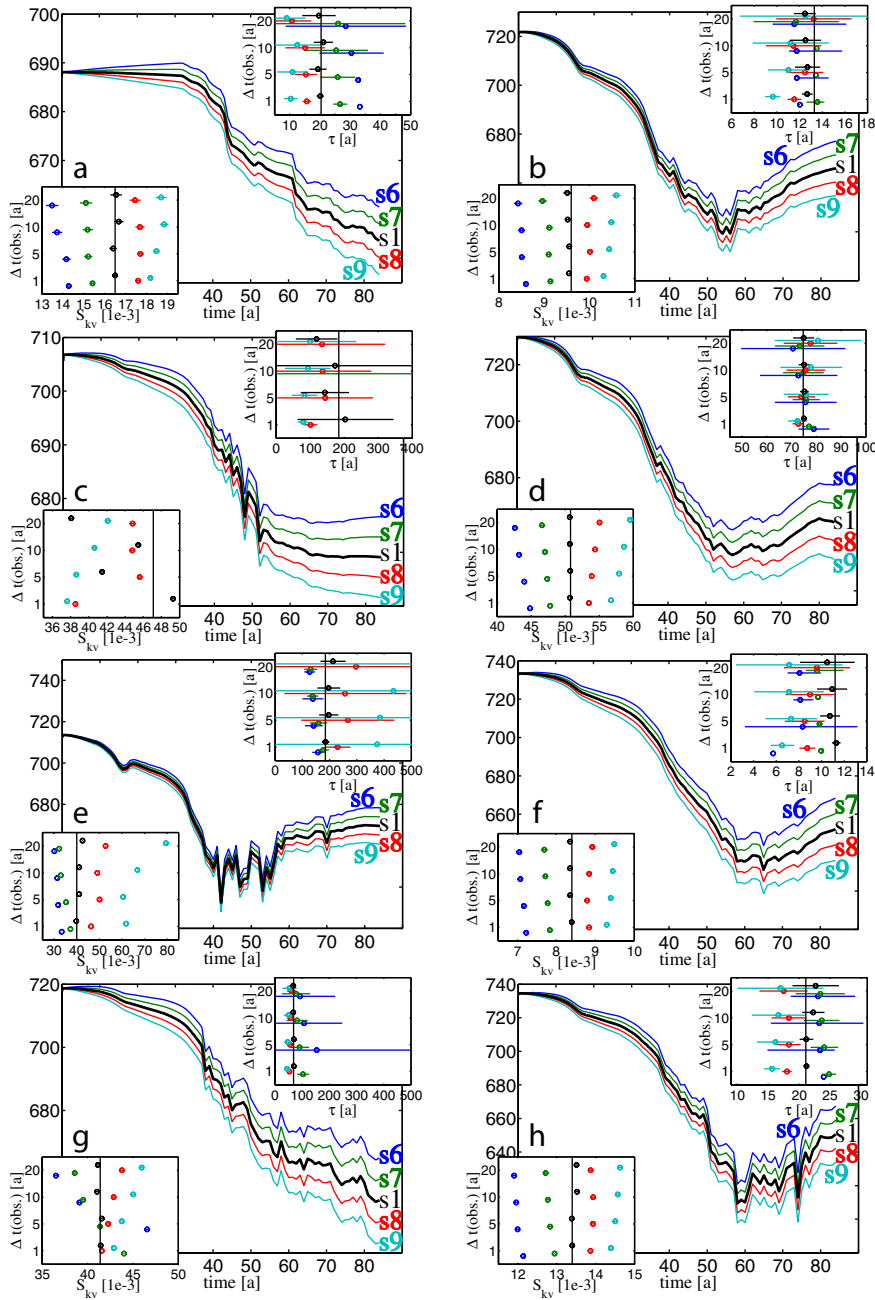


Figure 5-4: Drawdown scenarios s_6 – s_9 for the eight locations. The black drawdown curve (s_1) is the drawdown history used for all parameter estimations. The insets at the top right indicate the estimated time constants (abscissa) for InSAR observations available every 1, 5, 10, and 20 years (ordinate); the horizontal bars indicate the UCODE -estimated 95% confidence intervals and the vertical black lines indicate the true value. The insets at the bottom left of the graphs show the estimated S_{kv} values of the interbeds; the 1- σ error bars of the linear parameter estimation are mostly too small to see at this scale; the vertical black lines indicate the correct value.

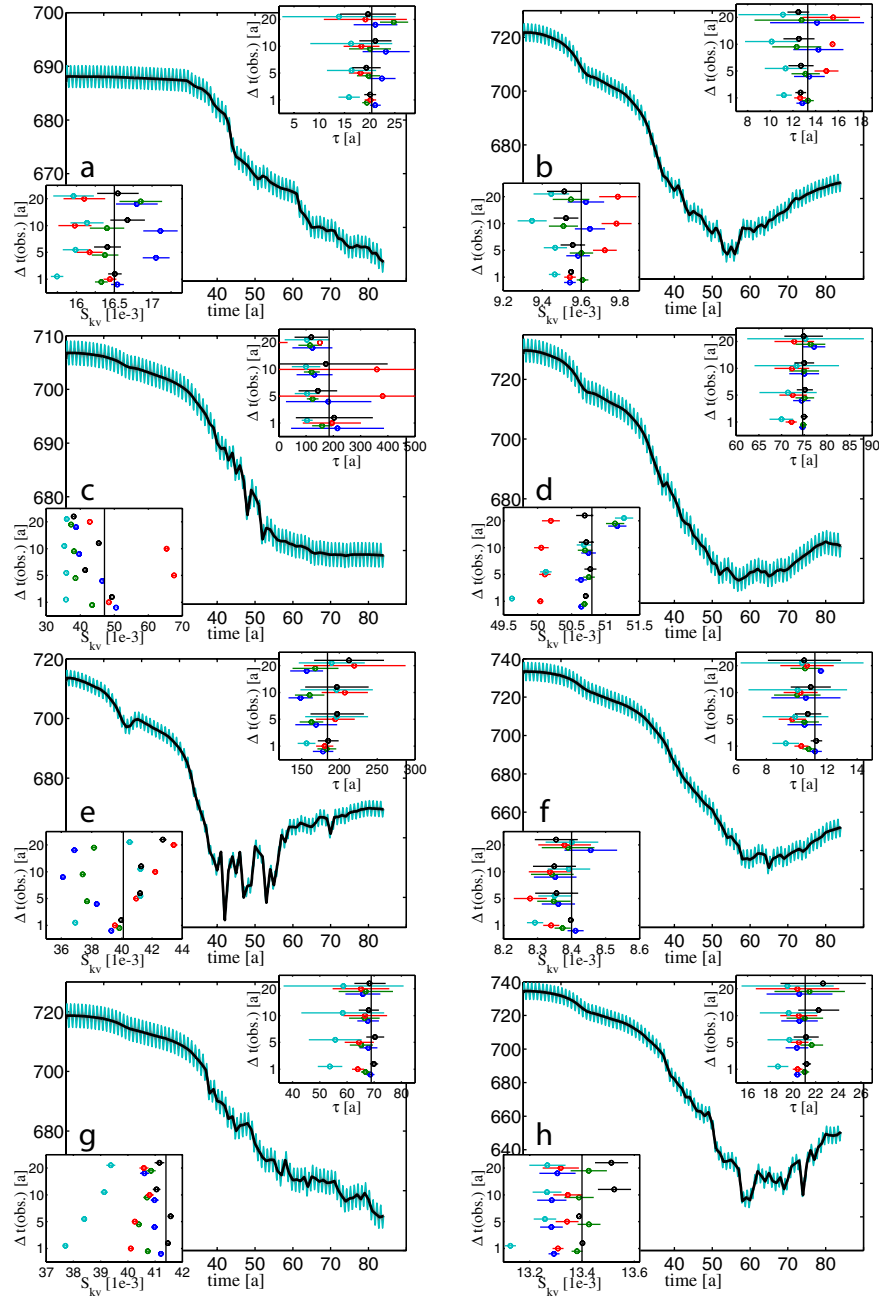


Figure 5-5: Drawdown scenarios s_{10} – s_{13} for the eight locations. The black drawdown curve (s_1) is the drawdown history used for all parameter estimations. The insets at the top right indicate the estimated time constants (abscissa) for InSAR observations available every 1, 5, 10, and 20 years (ordinate); the horizontal bars indicate the UCODE -estimated 95% confidence intervals and the vertical black lines indicate the true value. The insets at the bottom left of the graphs show the estimated S_{kv} values of the interbeds; the horizontal bars indicate the 1- σ error bars of the linear parameter estimation; the vertical black lines indicate the correct value.

parameter estimation successfully retrieves the correct time constants within the 95% confidence levels (black curves in figures 5-3, 5-4, and 5-5). The S_{kv} values are also estimated accurately. Note however, that the formal error variances for S_{kv} are generally very small, underestimating the error of the estimate. This is due to the fact that the estimated variance of the S_{kv} value does not account for propagated errors of an inaccurately estimated time constant. Thus, deviations in the estimated time constant from the true value causes a systematic bias of the estimated skeletal storage coefficient.

Reducing the number of subsidence observations used to constrain the estimations primarily renders the parameter estimates less certain. This is indicated by the widening error bars for increasing time intervals between observations of the τ -estimates in the top right insets of figures 5-3, 5-4, and 5-5. However, the resulting estimate is not significantly biased with respect to the true value. The effect of the frequency of subsidence observations over the 84-year time span simulated is negligible compared to the errors introduced by biased assumptions (or observations) of the hydraulic head history.

Even relatively small deviations of the true hydraulic heads from the heads used in the parameter estimation have a large effect on the estimated time constants. The estimated S_{kv} are not as severely affected by small biases in the hydraulic heads directly, but their accuracy depends on the accurate estimation of τ . If τ is accurately estimated, the error in the S_{kv} values remains relatively small. Conversely, even for small biases in the hydraulic heads, large errors in the S_{kv} estimate result from inaccurate estimates of τ .

In the scenarios I investigated the time constants were more often over- than underestimated. This seemed to depend on the details of the drawdown histories in a complex way and I was unable to identify specific criteria to predict in which way the estimate will be biased.

For most scenarios the estimated time constants were within a factor of 2 of the true value. The S_{kv} values were mostly within 25 – 30% of the true value, depending primarily on the deviation of the estimated τ value from the true time constant.

Finally, neglecting seasonal fluctuations in hydraulic head (scenarios 10 – 13) only

caused very modest biases of the resulting estimates of τ and S_{kv} . For the majority of simulations the true τ was within the confidence interval of the estimate and the error in the inelastic skeletal storage coefficient was small (fig. 5-5).

5.4 Conclusions

I have estimated the time constant τ and the inelastic skeletal storage coefficient for the interbeds, S_{kv} , using the parameter estimation approach developed for the Antelope Valley aquifer system (Chapter 4) for 416 different combinations of (1) the aquifer drawdown history causing compaction in the interbeds, (2) systematic misrepresentations of these aquifer drawdowns in the parameter estimation, and (3) the number of subsidence data available to constrain the inverse model. Interpreting the effect of the different combinations on the robustness of the parameter estimations and the biases of the resulting estimates, several conclusions can be drawn.

I have found that accurate knowledge of the drawdown history is of singular importance to estimate the compaction time constant of the interbeds reliably. Systematic overestimation or underestimation of the drawdowns causing the compaction of interbedded material can severely bias the resulting estimate of τ . The error of the S_{kv} values is correlated to the error of the τ values, so biases of the former due to misrepresented drawdowns will also contaminate the storage coefficient estimates. However, if the true drawdowns differ from the observed drawdowns only by a seasonally fluctuating signal, this likely will not prevent the accurate estimation of the two parameters, if the compaction time constant is sufficiently large. Time constants are generally large for inelastic compaction of interbeds.

Compared to the significant biases introduced by inaccurate knowledge of the drawdowns, the effect of the frequency of subsidence observations is negligible. While increasing the frequency of subsidence observations can reduce the formal uncertainty of the parameter estimates, it cannot reduce the systematic bias due to uncertain drawdowns. Thus, compared to the effects of inaccurate knowledge of the drawdowns, neither the measurement uncertainty in the subsidence observations, nor relatively

infrequent observations (every few years) are likely to severely deteriorate the parameter estimates. However, because the parameter estimation interprets stress (head) changes and surface displacements, measurements of both must be available over a sufficiently long time period for appreciable drawdowns (and corresponding surface displacements) to be measured.

Subsidence measurements at accuracies achievable with InSAR techniques made every few years are therefore well suited to estimate compaction time constants and inelastic skeletal storage coefficients where the drawdowns are very well known or at least not systematically misrepresented and measurements have been made for a sufficiently long time. Due to their spatial completeness InSAR data are superior to currently available alternative surface geodetic techniques for providing these subsidence data.

However, the correct interpretation of these data requires an adequate understanding of the compacting units in the subsurface. Specifically, any compacting confining units that cannot be treated mathematically as a compacting interbed must be adequately accounted for. Furthermore, accurate knowledge of the drawdown history in the aquifer containing the compacting interbeds is imperative to estimate the controlling parameters. Where simultaneous compaction in several aquifers contributes significantly to the observed subsidence signal it will generally not be possible to estimate storage coefficients or time constants for the different depths. Only where the vertical variations in the drawdown histories are negligible in such more complex settings can composite values (for the aquifer system) be estimated from surface subsidence observations and aquifer drawdowns. Unfortunately, as seen by example in the discussion of the parameter estimation in Antelope Valley (Chapter 4), it can be exceedingly difficult to obtain reliable and accurate estimates of the drawdown history. Although obtaining these data will generally be more feasible for smaller areas where substantial amounts of well observations are available, in most practical cases the uncertain spatial and temporal characteristics of drawdown will likely remain the single most important limitation of the discussed parameter estimation approach.

Chapter 6

Horizontal displacements in Antelope Valley, California from ascending and descending SAR acquisitions

As discussed in section 2.1, poroelastic theory predicts three-dimensional displacements in response to stress changes. Horizontal displacements of the same order of magnitude as seasonal (elastic) vertical displacements have been reported by Bawden et al. [2001] in the Santa Ana basin in southern California. Most studies of land subsidence to date, including the previous chapters of this dissertation, have neglected horizontal displacements, mostly on the basis of geometrical considerations regarding the compacting units (see 2.1). As discussed previously (section 3.2.2) the importance of horizontal displacements in the subsidence field can be assessed by combining InSAR observations from ascending and descending satellite passes. Performing this analysis for the long-term subsidence field in Antelope Valley is the topic of this chapter.

Because the line-of-sight (LOS) vectors differ for the ascending and descending acquisition geometries, any horizontal displacements are projected differently onto the LOS vectors. This contrasts the projection of vertical displacements, which only depends on the incidence angle, and is therefore identical for both tracks. Thus, horizontal displacements can be inferred where displacement maps derived from interferograms spanning the same time period differ significantly for the two acquisition geometries. If these differences are also spatially correlated with the areas affected by

land subsidence attributable to aquifer system compaction, they can be interpreted as an observation of horizontal aquifer system deformation. On the other hand, identical phase differences derived from data of different acquisition geometries indicate purely vertical displacements.

A similar analysis for the Las Vegas Valley (3.2.2) was inconclusive due to the lack of adequate available data. For Antelope Valley the acquisition dates for ascending and descending passes are separated by only 3 days. Furthermore, the acquired data available enable the comparison of displacement over three years, from January 1996 to January 1999, resulting in a relatively large displacement signal. Nevertheless, several of the limitations discussed in 3.2.2 still apply. In particular, atmospheric signal contributions are quite strong in a number of the image acquisitions that had to be used in this analysis, making it difficult to interpret observable differences confidently in terms of horizontal displacements.

The analysis of the displacement maps does not identify significant differences for the two acquisition geometries. Despite the fact that inaccuracies in the interferometric measurement and atmospheric delay signals preclude any conclusion regarding the existence of horizontal displacements up to about two centimeters, the absence of spatial correlation between the observable differences and the known subsidence structures indicates that horizontal displacement are indeed negligible for inelastic aquifer system compaction in Antelope Valley.

6.1 Sensitivity to horizontal displacements

Because of the steep incidence angle for ERS data ($\sim 23^\circ$) the interferometric phase measurement is more sensitive to vertical than horizontal displacements. Depending on the angle between the projection of the satellite LOS onto the ground and the horizontal displacement vector, a horizontal displacement of 1 cm is observed as a change of the round-trip path-length of up to 7.8 mm, while a 1 cm vertical displacement is observed as an 18.4 mm change. The difference of the round-trip path-length changes for ascending and descending acquisitions depends on the angle between the satellite LOS vectors for the acquisitions. The round-trip path-length change caused

by a horizontal displacement of d_h is given by

$$dr = 2d_h \sin \Theta_i \cos(\phi - \alpha), \quad (6.1)$$

where Θ_i is the incidence angle, ϕ is the azimuth of the displacement vector and α is the azimuth angle of the satellite line of sight projected onto the ground. The difference of the round-trip path-length differences between the ascending and descending acquisitions is thus

$$\Delta dr = 2d_h \sin \Theta_i (\cos(\phi - \alpha_a) - \cos(\phi - \alpha_d)), \quad (6.2)$$

where α_a and α_d are the azimuth angles for the ascending and descending LOS projections, respectively. The maximum sensitivity to horizontal displacements is found for $\phi = (\alpha_a + \alpha_d)/2 \pm 90^\circ$, where

$$\Delta dr_{max} = \pm 4d_h \sin \Theta_i \sin\left(\frac{\alpha_a - \alpha_d}{2}\right). \quad (6.3)$$

For $\phi = (\alpha_a + \alpha_d)/2$ there is no observable path-length difference. The azimuth of the projected LOS vectors for the ascending and descending passes used for Antelope Valley are $\alpha_a = 76.4^\circ$ for the ascending images and $\alpha_d = 283.6^\circ$ for the descending images. Thus in comparing ascending and descending acquisitions the sensitivity is highest for horizontal displacements in the east-west direction. North-south displacements are projected identically into both LOS vectors and therefore do not cause any differences (fig. 6-1). The following section describes the interferograms used in this analysis and the quantification of the estimation error. The observations and results are discussed in section 6.3.

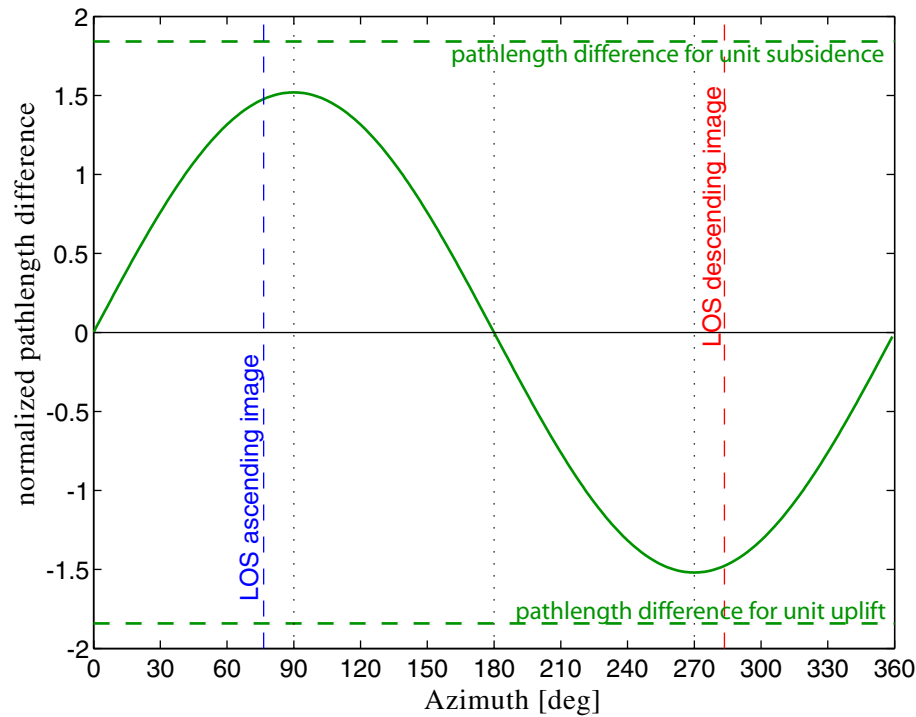


Figure 6-1: Difference in round-trip path-length changes caused by a unit horizontal displacement between ascending and descending acquisitions for Antelope Valley. Horizontal displacements at 90° and 270° azimuth (east and west) result in the largest differences. The path-length difference *in a single interferogram* caused by a unit vertical displacement is shown for comparison.

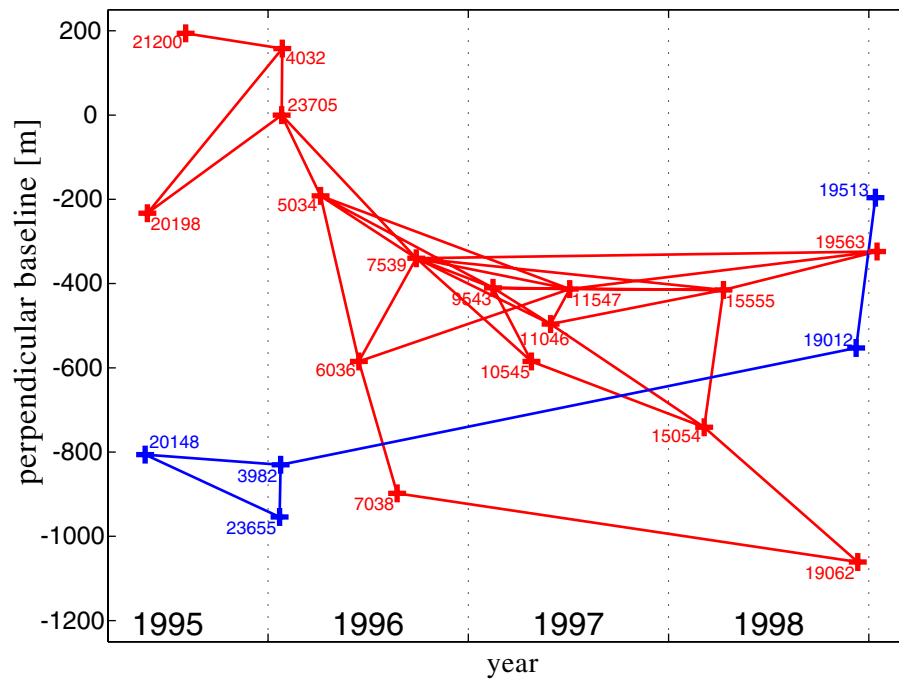


Figure 6-2: Ascending (blue) and descending (red) acquisitions and interferograms used to estimate displacements. The pluses indicate acquisitions, labeled with the orbit number. The lines indicate the interferograms formed (see also tables 6.1 and 6.2).

6.2 Displacement estimation

6.2.1 Available SAR acquisitions

One of the difficulties in the analysis presented in this chapter are the very specific requirements for the acquired data. The ascending and descending acquisitions have to span an identical or nearly identical time period. Furthermore, to derive interferometric displacement estimates from these acquisitions their temporal and spatial (baseline) distribution must allow the formation of interferograms with sufficiently high interferometric correlation (section 2.2.2). Most ERS SAR data over land areas has been acquired on descending passes, while only relatively few ascending acquisitions over land exist. This severely restricts the choice of data useful for the analysis described here. Figure 6-2 shows the data used for both ascending and descending

Acquisition 1			Acquisition 2			Interferogram
date	orbit	$\sigma_a^2[\text{rad}^2]$	date	orbit	$\sigma_a^2[\text{rad}^2]$	$\sigma_a^2[\text{rad}^2]$
1999/01/13	19513	0.4716	1998/12/09	19012	0.4716	0.9431
1996/01/24	3982	0.3023	1998/12/09	19012	0.4716	1.8194
1998/12/09	19012	0.4716	1995/05/22	20148	0.2649	2.6352
1996/01/24	3982	0.3023	1996/01/22	23655	0.2649	0.6654
1996/01/24	3982	0.3023	1995/05/22	20148	0.2649	0.6047
1996/01/22	23655	0.2649	1995/05/22	20148	0.2649	0.5298

Table 6.1: Ascending interferograms used to study horizontal displacements. The atmospheric variance estimates are given for the individual acquisitions and for the interferograms. The variances for the individual acquisitions are used as covariances for interferograms sharing the acquisition.

satellite tracks. The blue and red lines indicate the interferograms formed using ascending and descending data, respectively (fig. 6-2), which are also listed in tables 6.1 and 6.2. Unfortunately, the ascending acquisition on January 13, 1999 (orbit 19513) and the descending acquisitions on May 26, 1995 (orbit 20198) and January 16, 1999 (orbit 19563) contain strong atmospheric delay signals. To derive the best estimate of the surface displacements during May 1995 - January 1996, January 1996 - December 1998, and January 1996 to January 1999 for both ascending and descending imaging geometries, using the interferograms shown in figure 6-2, I employed a variance-weighted least-squares estimation, described in the following paragraph.

6.2.2 Estimating displacements from several interferograms

Even if it were possible to form interferograms between the image acquisitions May 1995, January 1996, December 1998 and January 1999 for both ascending and descending images, combining interferograms using intermediate image acquisitions may result in more accurate displacement maps if shorter perpendicular baselines and/or shorter time spans can be exploited to reduce the effects of spatial and temporal decorrelation in the interferograms. For the available data presented in the previous section, some of the perpendicular baselines between acquisitions spanning the above time periods are excessively large, necessitating the combination of interferograms with shorter baselines. This section describes a least-squares approach to obtain an

Acquisition 1			Acquisition 2			Interferogram
date	orbit	$\sigma_a^2[\text{rad}^2]$	date	orbit	$\sigma_a^2[\text{rad}^2]$	$\sigma_a^2[\text{rad}^2]$
1999/01/16	19563	1.6309	1998/04/11	15555	0.8840	4.4279
1999/01/16	19563	1.6309	1997/07/05	11547	0.6095	3.6187
1999/01/16	19563	1.6309	1996/09/28	7539	0.1349	3.2618
1998/12/12	19062	1.1923	1998/03/07	15054	0.5685	2.3845
1998/12/12	19062	1.1923	1996/08/24	7038	0.5838	4.6650
1998/04/11	15555	0.8840	1998/03/07	15054	0.5685	3.3844
1998/04/11	15555	0.8840	1997/07/05	11547	0.6095	2.2233
1998/04/11	15555	0.8840	1997/05/31	11046	0.5955	1.7681
1998/04/11	15555	0.8840	1997/02/15	9543	0.2143	1.8834
1998/04/11	15555	0.8840	1996/09/28	7539	0.1349	2.0766
1998/03/07	15054	0.5685	1997/05/31	11046	0.5955	1.7868
1998/03/07	15054	0.5685	1997/04/26	10545	0.1526	1.1369
1997/07/05	11547	0.6095	1997/05/31	11046	0.5955	2.2833
1997/07/05	11547	0.6095	1997/02/15	9543	0.2143	1.7085
1997/07/05	11547	0.6095	1996/09/28	7539	0.1349	1.2190
1997/07/05	11547	0.6095	1996/06/15	6036	0.2742	1.6024
1997/07/05	11547	0.6095	1996/04/06	5034	0.1349	1.3338
1997/05/31	11046	0.5955	1997/02/15	9543	0.2143	1.5274
1997/05/31	11046	0.5955	1996/09/28	7539	0.1349	1.1911
1997/04/26	10545	0.1526	1997/02/15	9543	0.2143	0.5263
1997/04/26	10545	0.1526	1996/09/28	7539	0.1349	0.3052
1997/02/15	9543	0.2143	1996/09/28	7539	0.1349	0.4286
1997/02/15	9543	0.2143	1996/04/06	5034	0.1349	1.0868
1996/09/28	7539	0.1349	1996/06/15	6036	0.2742	0.5484
1996/09/28	7539	0.1349	1996/04/06	5034	0.1349	0.2698
1996/09/28	7539	0.1349	1996/01/26	23705	0.1820	1.1595
1996/08/24	7038	0.5838	1996/06/15	6036	0.2742	1.1676
1996/06/15	6036	0.2742	1996/04/06	5034	0.1349	2.6211
1996/04/06	5034	0.1349	1996/01/26	23705	0.1820	0.3639
1996/01/27	4032	0.3792	1996/01/26	23705	0.1820	0.7584
1996/01/27	4032	0.3792	1995/08/04	21200	1.7951	3.5901
1996/01/27	4032	0.3792	1995/05/26	20198	0.8669	3.6565
1996/01/26	23705	0.1820	1995/05/26	20198	0.8669	1.7338

Table 6.2: Descending interferograms used to study horizontal displacements. The atmospheric variance estimates are given for the individual acquisitions and for the interferograms. The variances for the individual acquisitions are used as covariances for interferograms sharing the acquisition.

optimal estimate of the displacements during any given time period spanned by the acquisitions. A similar method has been applied by Usai [2001], who used a least-squares scheme to merge several interferograms. The approach presented here differs primarily in the variance weighting I applied to give more weight to measurements of higher accuracy.

If \vec{d}_i is the vector of displacement measurements at pixel i of all interferograms \vec{m}_i is the vector of the displacements at that pixel location during the time periods of interest, the problem can be written as

$$\vec{d}_i = \mathbf{G}\vec{m}_i, \quad (6.4)$$

where \mathbf{G} is a matrix containing zeros, ones and minus ones specifying the relation between the data and the estimated model parameters. For example, for the ascending data this is

$$\begin{pmatrix} d19513_19012 \\ d3982_19012 \\ d19012_20148 \\ d3982_23655 \\ d3982_20148 \\ d23655_20148 \end{pmatrix} = \begin{pmatrix} 1 & -1 & 0 \\ 0 & -1 & 0 \\ 0 & 1 & 1 \\ 0 & 0 & 0 \\ 0 & 0 & 1 \\ 0 & 0 & 1 \end{pmatrix} \begin{pmatrix} d(\text{Jan}96 - \text{Jan}99) \\ d(\text{Jan}96 - \text{Dec}99) \\ d(\text{May}95 - \text{Jan}96) \end{pmatrix}, \quad (6.5)$$

where I assumed that no deformation is occurring during the two days spanned by the interferogram between orbit numbers 3982 and 23655. If Σ_{d_i} is the data covariance matrix containing an estimate of the variances and covariances at pixel i , the displacements can be obtained from variance-weighted least squares:

$$\vec{m}_i = \mathbf{G}_g^{-1}\vec{d}_i, \quad \text{with} \quad \mathbf{G}_g^{-1} = (\mathbf{G}^T \Sigma_{d_i}^{-1} \mathbf{G})^{-1} \mathbf{G}^T \Sigma_{d_i}^{-1} \quad (6.6)$$

and

$$\Sigma_{m_i} = \mathbf{G}_g^{-1} \Sigma_{d_i} \mathbf{G}_g^{-1T} \quad (6.7)$$

as the estimation covariance matrix. The diagonal elements of $\Sigma_{\mathbf{m}_i}$ contain the variances of the displacement estimates at location i .

A critical issue using this approach is the estimation of the covariance matrix $\Sigma_{\mathbf{d}_i}$ which varies as a function of image location. The two important processes affecting error or uncertainty in the processed interferograms are the locally highly variable image noise, which is mostly governed by the interferometric correlation, and signal delays from a turbulent atmosphere that introduce an error signal into the measurement (see section 2.2.2).

Spatial filtering in the image processing reduces the noise level in the final displacement maps, but the accuracy of the final estimate depends on the variance of the original, unfiltered estimate. This local variance has to be computed prior to phase unwrapping, because images often cannot be successfully unwrapped without prior filtering. I computed the variance of the wrapped phase locally on the sample of the 69 pixels within 4.5 pixels of each pixel location. The 2π -ambiguity was resolved by assuming that all phase values are within π radians of the local mean phase value. For larger variances this assumption biases the computed variance towards lower values. Assuming that the unwrapped phase values are normally distributed, the variance of their wrapped values can be computed (fig. 6-3). Using this relationship I determined the variance of a Gaussian distribution of the (unwrapped) phase values from the variance computed on the wrapped values. The correction for small variances is negligible (fig. 6-3). For larger variances the mapping becomes non-unique in the presence of a noisy sample, as the measured variance approaches the theoretical value for a uniformly distributed sample in $[-\pi, \pi)$, 3.29 rad^2 . I considered variances of the wrapped values exceeding a threshold variance of 2.8 to be infinite. These values indicate completely decorrelated areas where the measured phase does not contain any information on the displacement. Assigning a large variance to the observation results in zero weight in the estimation (eq. 6.6). Alternatively to computing the phase statistics on the phase values themselves, they could be estimated from the image correlation [Bamler and Just, 1993; Just and Bamler, 1994]. I chose to compute the phase statistics on the actual phases though, as the relationship between correlation and phase variance depends on the statistics of the scatterers in the image, which

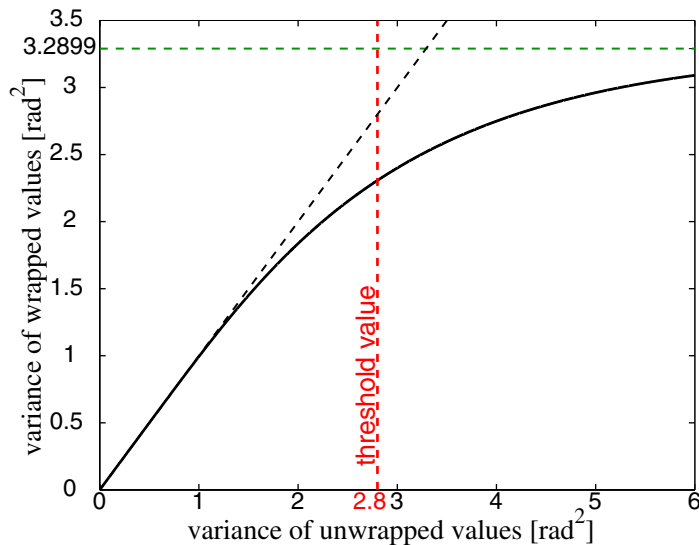


Figure 6-3: Relationship between the variances of unwrapped and wrapped phase values. Wrapped variances above the threshold value of 2.8 rad^2 were assumed to be infinite.

generally has to be assumed [Usai, 2001].

The variance due to noisy phase measurements is a property of the interferometric phase difference and not the individual SAR acquisitions. It therefore does not contribute to the covariances between interferograms. In contrast, atmospheric delay signals are contained in individual SAR image acquisitions, even though they only become noticeable in the interferometric phase differences. To estimate the variance of the atmospheric signal in each interferogram I computed the variance of the unwrapped phase values in the area that was not known to deform. To limit the contribution of small-scale noise to the variance, as this contribution was already accounted for as described above, I computed the variance in the final, spatially filtered images, using only pixels with correlation values exceeding 0.5. I assumed this “atmospheric” variance to be spatially constant for each interferogram. Thus, the variance for each image pixel was the sum of the spatially constant atmospheric variance and the spatially variable variance due to decorrelation noise.

Because the atmospheric delay signal contained in any SAR acquisition will equally affect all interferograms sharing this acquisition, the errors in these interferograms are

correlated. This must be accounted for in the off-diagonal elements of the data covariance matrices $\Sigma_{\mathbf{d}_i}$. The covariance between two interferograms sharing an acquisition with the atmospheric variance σ_a^2 is either σ_a^2 , if the acquisition is master or slave in both interferograms, or $-\sigma_a^2$, if the acquisition is the master image in one and the slave image in the other interferogram. I used half the minimum variance found in all interferograms sharing one particular acquisition as an estimate for the atmospheric variance in this individual SAR acquisition. This guarantees that the sum of two acquisition variances never exceeds the variance computed for an interferogram using these two images. However, the highest variances will be underestimated while the lowest variances will be overestimated. Tables 6.1 and 6.2 list the atmospheric variances for all interferograms shown in figure 6-2 and the estimates for the individual acquisitions. Using the spatially variable covariance matrices in equation 6.6 resulted in the displacement estimates shown and discussed in the following section.

6.3 Comparison of ascending and descending images

The estimated vertical subsidence derived from ascending and descending acquisitions for the time periods January 1996 to December 1998 and January 1996 to January 1999 agree very closely (fig. 6-4), both in magnitude and the detailed structure of the observed subsidence. In agreement with the observations presented in section 4.2, the two main subsidence features are the subsidence bowl in Lancaster and a smaller area south of Rogers Lake. Due to strong atmospheric delay signals in the descending acquisitions in January 1999 (orbit 19563) and May 1995 (orbit 20198), the corresponding images show strong atmospheric noise signals (fig. 6-4, top and bottom right), making a straightforward visual comparison of the ascending and descending images difficult. To visualize more subtle differences in the area of the Lancaster subsidence bowl (yellow frame in fig. 6-4) the displacement maps are also displayed with a wrapped colormap (fig. 6-5). Although this representation results in a much noisier appearance, the visible differences appear to be related to atmospheric effects,

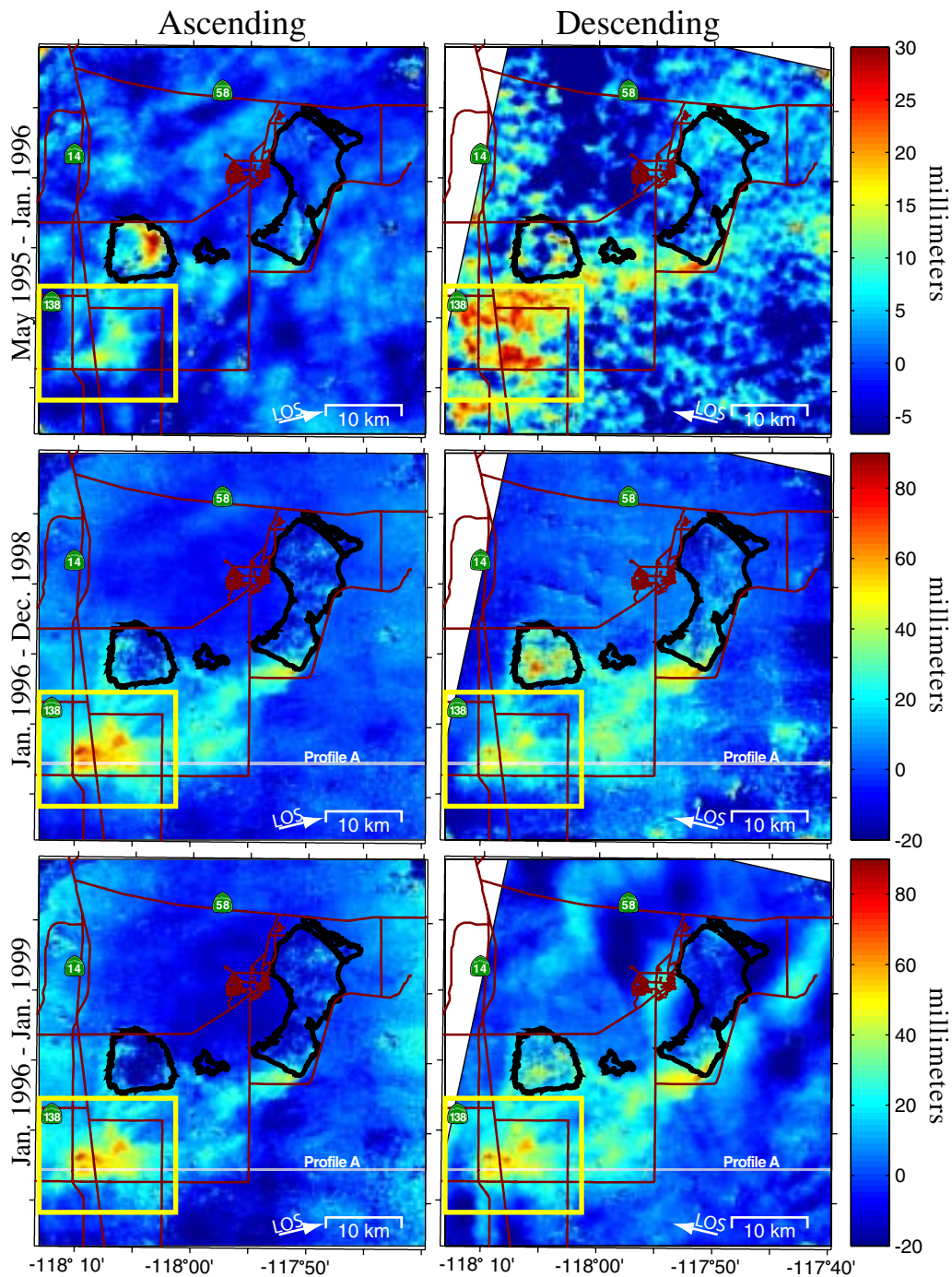


Figure 6-4: Comparison of displacement maps derived from ascending and descending observations for three time period. The values are shown in terms of equivalent vertical displacement assuming no horizontal displacement. The yellow frame indicates the area shown in figures 6-5, 6-6 and 6-7.

not horizontal displacement. The most apparent spatially coherent difference is the fringe spacing on the southern side of the subsidence bowl in the three-year images. The fringes are further apart in the descending image than in the ascending image (fig. 6-5). However, horizontal displacements in this area are expected to be directed to the north, and consequently not appear differently in these images (see fig. 6-1). It is therefore more likely that this difference is also of atmospheric origin. Although differences in the ascending and descending images in many locations exceed one or even two centimeters (fig. 6-6, 6-8, 6-9, 6-10), the spatial patterns of these differences do not appear to be correlated with the subsidence bowl. Their spatial distribution strongly suggests atmospheric delays as their origin. Furthermore, in most areas the differences are within one standard deviation of the difference estimate (fig. 6-6, 6-7). The significance of the difference between the vertical displacement estimates can be tested using a statistical T-test [Davis, 1986]. Figure 6-7 shows the difference between the ascending and descending displacement estimate normalized by the standard deviation (the t-value) and the locations where the vertical displacement estimates are different at a 5% significance level. The result indicates that the observations from the two orbital tracks are not significantly different given the variance of the estimates. The displacements along the profiles indicated in figures 6-4 and 6-5 are shown in figures 6-8, 6-9 and 6-10. Again, although differences of one or two centimeters equivalent vertical displacements are not uncommon, they are not correlated with the sides of the subsidence bowl, where horizontal displacements are expected to be greatest. The relatively large differences during January 1996 to December 1998 along the first six kilometers of profile C (fig. 6-10) are unlikely to be due to horizontal displacements, because of the unfavorable expected orientation of horizontal displacements (fig. 6-1) and the absence of these differences in the January 1996 to January 1999 observations.

While the displacement maps derived from ascending and descending observations are not significantly different given the variances of the displacement estimates, it should be pointed out that horizontal displacements of more than a centimeter may occur even in the east-west direction, where the difference measurement is most sensitive to these displacements, without being reliably detected. For displacements at

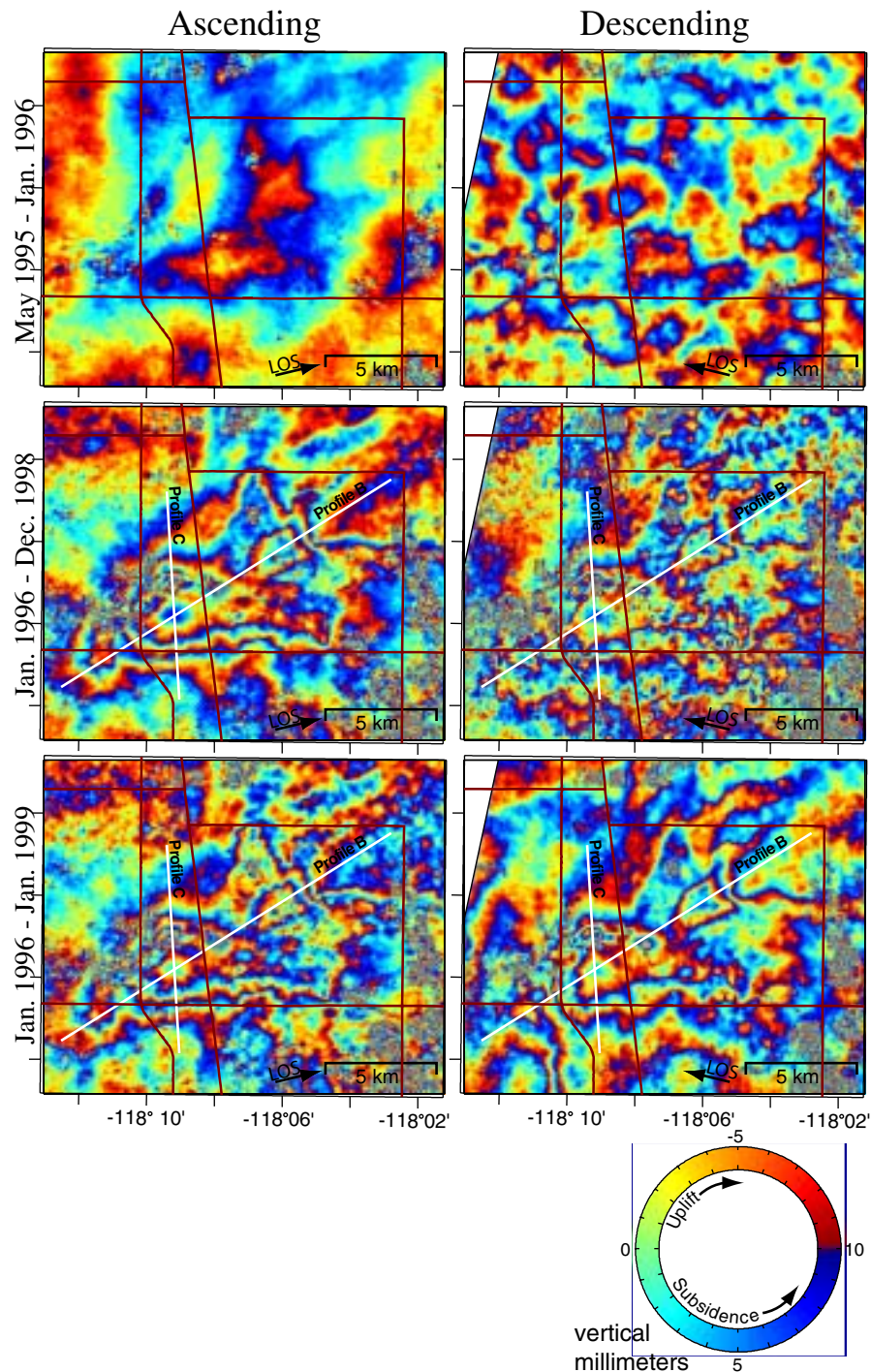


Figure 6-5: Comparison of displacements in area indicated by yellow frame in figure 6-4. The values are shown using a wrapped colorscale to enhance the visibility of small-scale features. Also, the descending values were adjusted by up to 5mm to make the color patterns more easily comparable by eye.

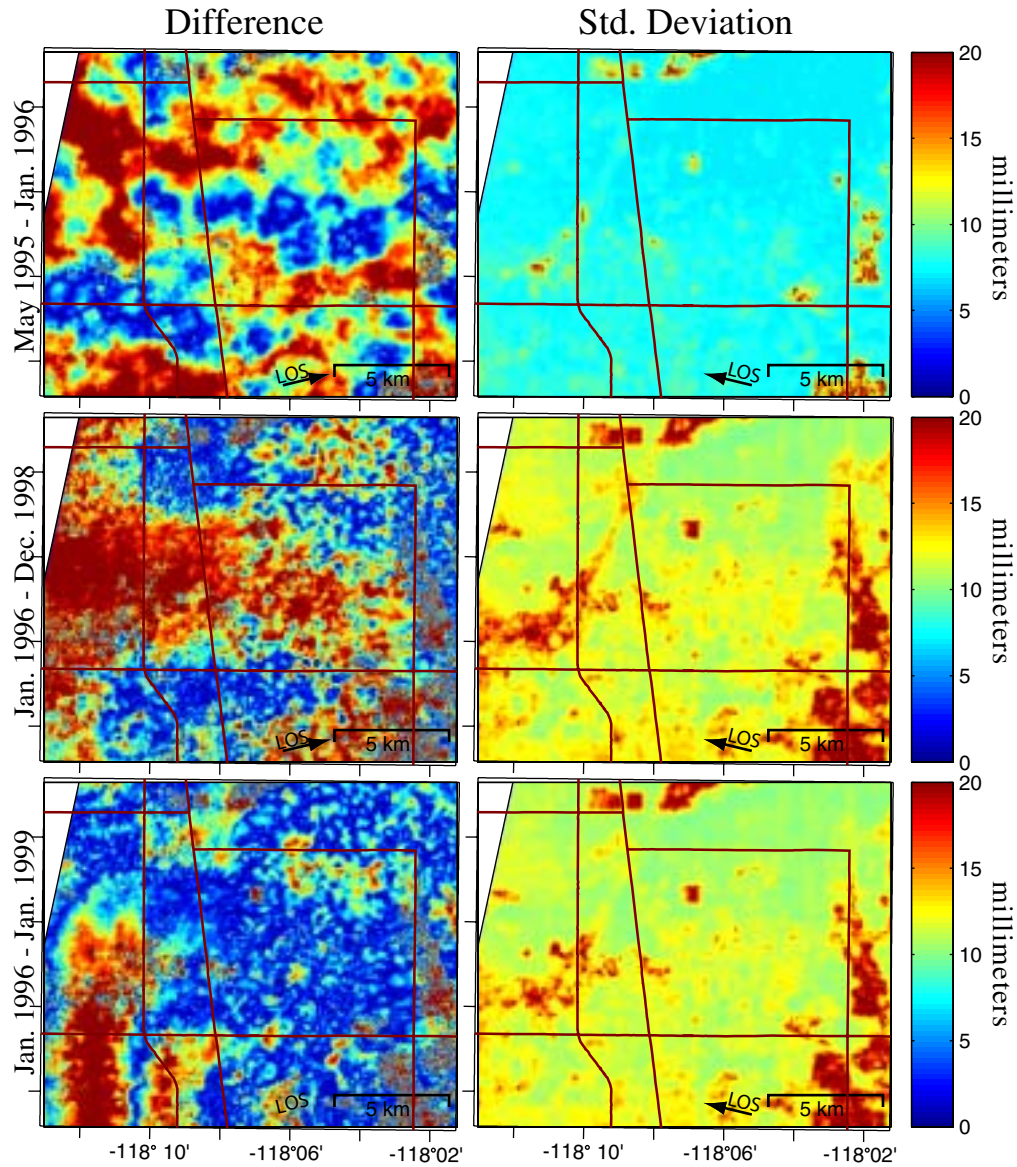


Figure 6-6: Absolute difference between displacement maps derived from ascending and descending acquisitions. The patterns suggest an atmospheric process causing these differences. For large areas the difference is smaller than one standard deviation of the estimates (see also fig. 6-7).

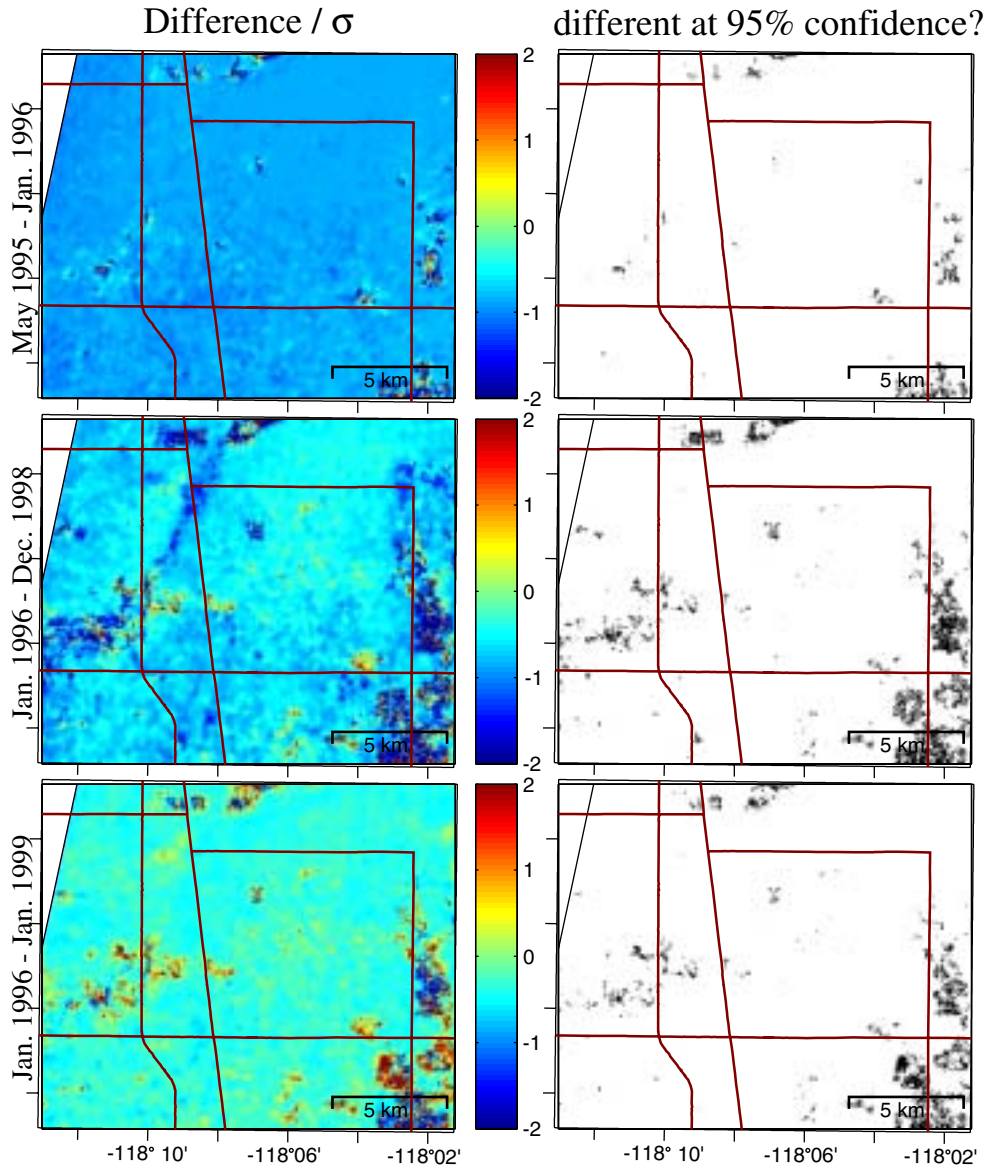


Figure 6-7: Left: Differences between displacement maps from ascending and descending acquisitions normalized by the standard deviation. For most locations the difference is below one standard deviation. Right: Result of a T-test testing the hypothesis if the values from ascending and descending images are different at a 5% significance level. In the white areas the hypothesis cannot be accepted. The few locations where the hypothesis is accepted (black dots) do not appear to be correlated with the subsidence bowl.

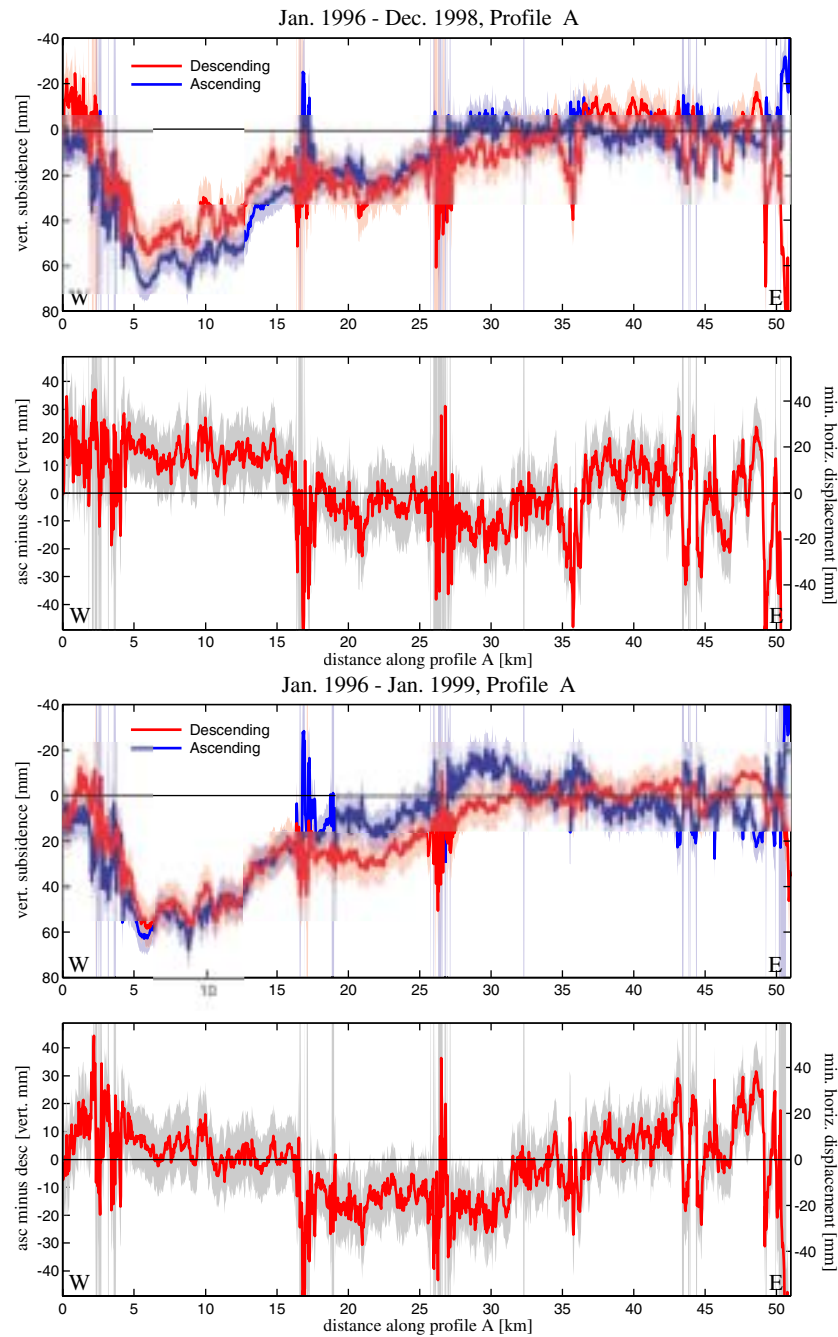


Figure 6-8: Comparison of displacements from ascending and descending acquisitions along profile A (fig. 6-4). The shaded areas around the lines indicate 1- σ error bars. The right ordinate on the bottom indicates the equivalent optimally oriented horizontal displacement.

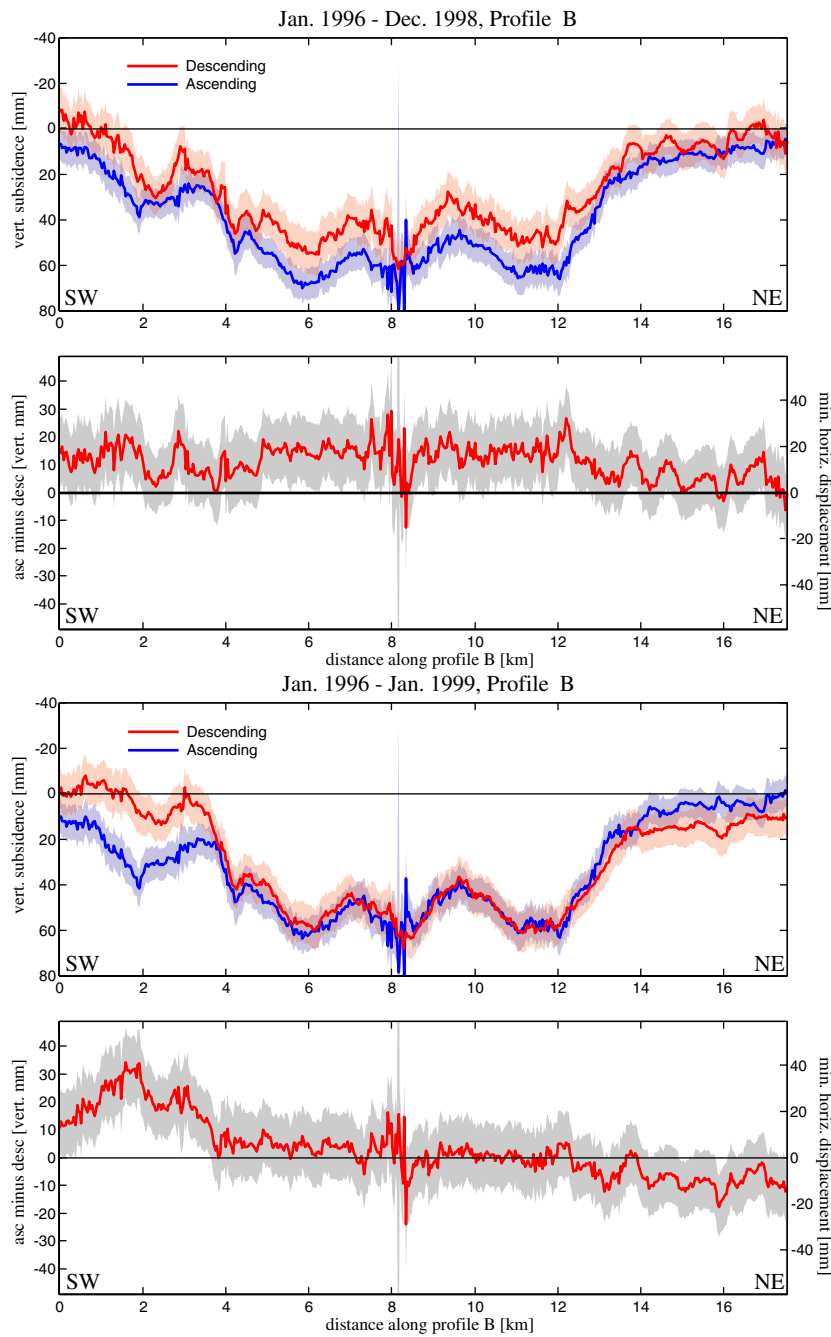


Figure 6-9: Comparison of displacements from ascending and descending acquisitions along profile B (fig. 6-5). The shaded areas around the lines indicate 1- σ error bars. The right ordinate on the bottom indicates the equivalent optimally oriented horizontal displacement.

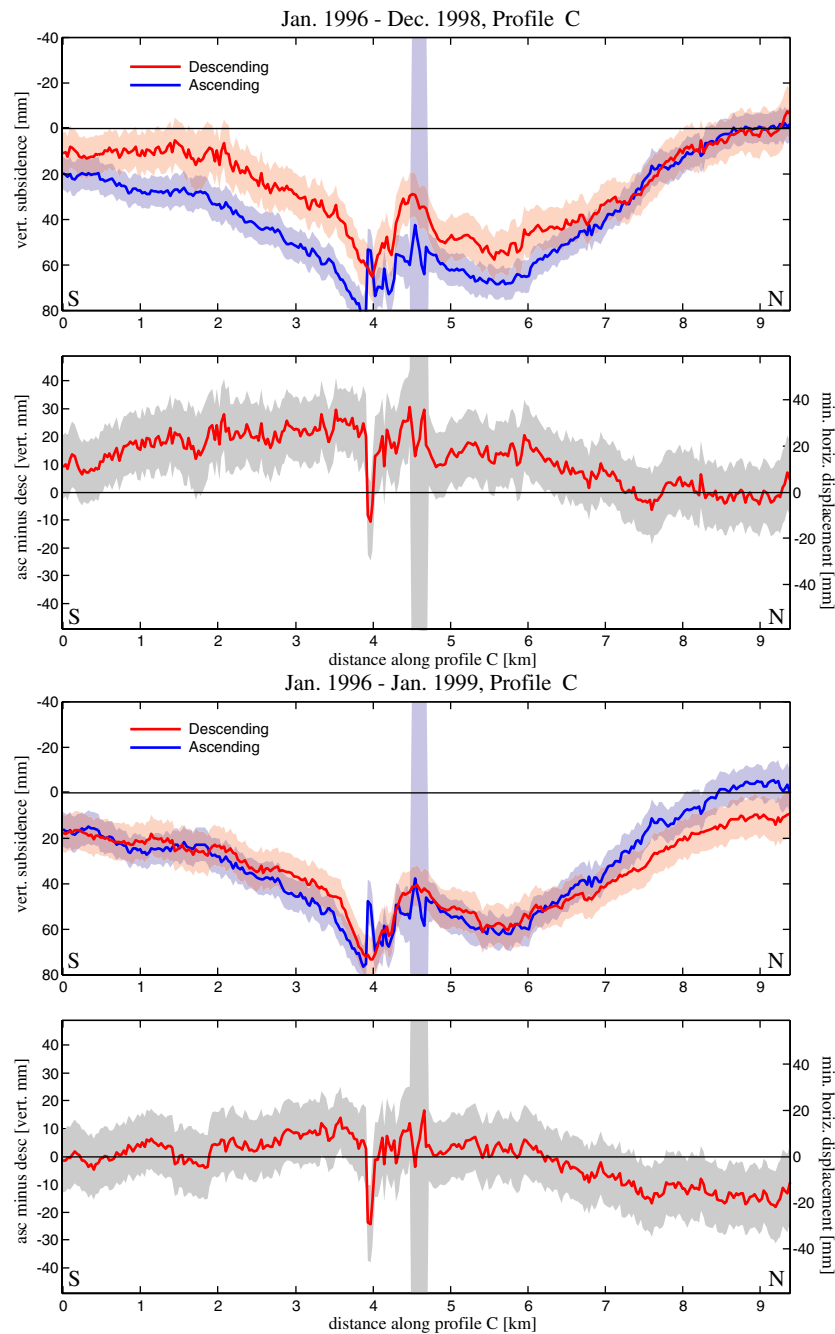


Figure 6-10: Comparison of displacements from ascending and descending acquisitions along profile C (fig. 6-5). The shaded areas around the lines indicate 1- σ error bars. The right ordinate on the bottom indicates the equivalent optimally oriented horizontal displacement.

larger angles to this direction, even much larger displacements may not be detectable at the level of statistical significance. However, notwithstanding the relatively large uncertainty of the absolute difference values, the absence of differences that are spatially correlated with the subsidence bowl does in fact support the hypothesis that horizontal surface displacements accompanying inelastic aquifer system compaction are small and probably negligible. This may not be true for elastic displacements such as those observed by Bawden et al. [2001], which occur primarily in the aquifers. Unfortunately, the lack of more ascending SAR acquisitions prevented an investigation of horizontal displacements in connection to seasonal elastic deformation in Antelope Valley here.

Chapter 7

Conclusions

This chapter summarizes my general conclusions from the work presented in the previous chapters. Detailed conclusions for the individual case studies have already been presented in the respective chapters. In this chapter I focus on conclusions pertaining to the general questions and problems I set out to address in Chapter 1 (p. 5), placing this work in the larger context of applying InSAR technology to the study of aquifer systems.

7.1 Results and implications

I have found InSAR techniques to be well suited to measure and monitor ground surface displacements over the two aquifer systems studied. The dry and bare or urbanized land surfaces permitted forming interferograms spanning several years without prohibitive loss of signal due to decorrelation. The achievable accuracies were generally on the order of 1 cm or less and the spatial resolution was significantly higher than the spatial resolution of any other data, such as the hydraulic head or material properties, available for these aquifer systems. Beyond simply studying surface deformation itself, any analysis requiring conjunctive interpretation of different data is therefore no longer restricted by the paucity of surface displacement data, but by the scarcity of other data. For example, the estimation of spatially variable elastic (Chapter 3) or inelastic (Chapter 4) skeletal storage coefficients was limited by the lack of more detailed and more reliable knowledge of the hydraulic heads in the aquifer system.

The accuracy of InSAR-derived displacement maps for the aquifer systems studied proved to be limited primarily by the presence of atmospheric phase signals in the interferograms. The measurement error for detailed interpretations of these displacements therefore depends on the ability to remove or at least reliably identify these atmospheric signals. Furthermore, deviations of the displacement from the assumed (vertical) direction can bias the displacement estimates. However, investigating displacement maps derived from acquisitions on different satellite tracks I did not find an indication of significant horizontal displacements related to several centimeters of subsidence in Antelope Valley. This indicates that horizontal surface displacements may be negligible for inelastic aquifer system compaction at the regional scale.

I have found that displacement observations over long time periods were necessary to constrain estimations of the compaction time constants in Antelope Valley (Chapter 4). Although the available catalog for ERS SAR data now contains acquisitions over the past 10 years this remains insufficient to constrain the estimation of time constants on the order of decades to centuries. Thus, the newness of the technique and the correspondingly limited amount of available historical data currently restricts the usefulness of InSAR in the interpretation of delayed deformation processes.

The very high spatial resolution of ERS SAR imagery permits the observation of the surface deformation patterns with great spatial detail. This can be extremely useful in determining the exact location of structural boundaries, such as faults, sudden changes in subsurface composition or sediment thickness, provided that stress changes induce differential displacements to highlight these boundaries.

One of the most important observational advances using InSAR is the ability to characterize the time-variability of the deformation process at much higher temporal resolution than previously possible using geodetic observations from benchmark surveys or campaign GPS. The 35 day orbit repeat cycle of the ERS satellites enables the detection of displacement transients down to almost monthly time-scales. Even though not every acquisition may be usable for conventional InSAR in practice, due to excessively long perpendicular baselines or strong atmospheric artifacts, the temporal frequency of observations exceeds that of most other techniques available today. If an even higher observation frequency is required, observations from different sensors or

satellite tracks might be used. In both aquifer systems studied I observed temporal variability of the displacement field at the shortest observable time scales. Long-term displacement trends were usually superposed with a seasonally fluctuating signal. In some locations even shorter transients are observable. These are probably caused by local pumping operations. Both seasonal and transient displacement signals are an important aspect of the displacement field and can be analyzed in terms of aquifer system properties, such as the elastic storage coefficients. Seasonal and transient surface displacements over aquifer systems have not received much attention prior to this work, primarily due to the lack of adequate observations. Chapter 3 constitutes the first detailed investigation of seasonal displacement signals over an aquifer system and the first estimation of spatially variable elastic aquifer system storage coefficients from InSAR data. The subsidence observed over the Antelope Valley aquifer system (Chapter 4) can also not be described by a constant subsidence rate. Any attempt to interpret the surface displacements in terms of the underlying physical process must adequately account for the true complexity of the subsidence signal. However, it seems to be possible to neglect seasonal fluctuations of both pore pressures and surface subsidence in the estimation of inelastic skeletal storage coefficients.

I have shown how the elastic skeletal storage coefficient of the aquifer system, the inelastic skeletal storage coefficient of interbeds and compaction time constants can be estimated from surface displacement observations and known changes of hydraulic head in a confined aquifer system. I have further demonstrated for the first time that these parameters can be estimated for many locations across an aquifer system if both subsidence and head change observations are available for an extended area. However, while the subsidence observations derived from InSAR yielded sufficiently accurate and detailed measurements of the surface displacements, the reliability of the estimated parameters was impaired by inaccurate or unreliable estimates of the stress changes in the aquifer systems and biased by conceptual misrepresentations of the aquifer system. Smaller study sites with densely spaced observation wells and detailed data on the geometry of the hydrogeologic units would provide a more controlled experiment, enabling more reliable parameter estimations. Particularly in site-scale studies, however, one-dimensional observations of surface displacement may

not suffice to characterize the surface displacements adequately, necessitating more realistic models for the mechanical behavior of the subsurface materials.

7.2 Future research and applications

The application of InSAR to studies of developed aquifer systems is still in its infancy. Developments of the processing tools will make these data more easily accessible to a larger community of scientists and engineers. The advanced capability of measuring surface displacements will allow them to develop and constrain more complex geomechanical models of the aquifer systems. Parallel advances in the tools for numerical simulation will enable the development of sophisticated geomechanical models of developed aquifer systems, providing a powerful tool for optimizing groundwater pumping with respect to land subsidence problems.

Routine InSAR mapping can play an important role in siting structures that are particularly sensitive to ground displacements such as the routing of pipelines or aqueducts over terrain susceptible to deformation. Where such infrastructure is already in place, InSAR-derived deformation maps can be used to assess the risk of breakage and identify most vulnerable locations.

In this work I have used the available subsidence data in conjunction with observed or simulated changes in hydraulic head to estimate storage coefficients and compaction time constants. Where additional information on the aquifer system is available it may be possible to estimate additional parameters from these data. If the geometry of the aquifer system, in particular the thicknesses of compacting layers, is known accurately, the vertical diffusivity of the compacting interbeds can be determined from the compaction time constants. In relatively simple, elastically deforming aquifer systems it should also be feasible to estimate changes in subsurface pore pressure (i.e. hydraulic head) from surface displacement observations, after the parameters governing the elastic deformation process have been calibrated. This would provide a uniquely powerful tool to monitor changes in hydraulic head at the unprecedented detail of SAR images. Such an approach would also be a valuable supplement to gravity studies to monitor changes in basin-wide water storage, such as the GRACE

satellite mission [Rodell and Famiglietti, 1999].

The applicability of InSAR techniques is severely curtailed in densely vegetated areas due to the loss of signal by decorrelation. This problem may be at least partly overcome by future sensors operating at longer radar wavelengths, which are not as strongly affected by vegetation. Also, recent developments indicate that interferometry can be performed on a sparse grid of highly coherent individual scatterers (“permanent scatterer”), vastly extending the applicability of InSAR in vegetated areas.

Finally, InSAR data acquired over aquifer systems can be useful beyond the measurement of deformation. Some studies have attempted to relate interferometric phase signatures to soil moisture [Fatland and Nolan, 2001]. Furthermore, a largely untapped opportunity is the use of InSAR correlation maps as a mapping tool for change detection. These maps might be used for surface classification or verification of land following agreements, for example.

7.3 Closing remarks

Where the technique is applicable, InSAR is rapidly developing into an indispensable tool for monitoring ongoing surface displacements over deforming aquifer systems. The surface displacement observations provide an additional constraint in calibrating groundwater flow and subsidence models. With observational data for their calibration available, deformation processes are likely to be routinely included in numerical models, particularly where land subsidence is a concern in groundwater management decisions. On the previous 179 pages I have demonstrated some of the analyses enabled by the wealth of surface displacement data available from InSAR. Hopefully my results will encourage future applications and research, using one of today's most sophisticated space-borne imaging technologies to study one of our most vital and valuable resources: water.

Appendix A

Details of the Antelope Valley groundwater flow model

This appendix contains detailed information on the groundwater flow and subsidence model used for the simulation and parameter inversion described in Chapter 4. The model was developed by Leighton and Phillips [2003], who provided me with their input files. I refer to their model as “the original model” herein. I modified this original model in the following three aspects:

1. The original model was based on MODFLOW-88 [McDonald and Harbaugh, 1988]. I changed the original input files to run my simulations using MODFLOW-96 [Harbaugh and McDonald, 1996]. This represents a minor change and only affected the format of some of the input file, but not the computations performed in the simulation or the simulation results.
2. The original model used annual stress periods for the time period from 1915 through 1995. Using more recent pumping data for the years 1996 to 1998 (*Steve Phillips, U.S. Geological Survey, written comm.*) I extended the simulated time period to the end of 1998.
3. The original model used the interbed storage package (IBS1) [Leake and Prudic, 1991] to simulate aquifer system compaction and land subsidence. For my simulations I used the IBS2 package, developed by Leake [1990]. The calibration of the required input parameters for this package is the topic of Chapter 4.

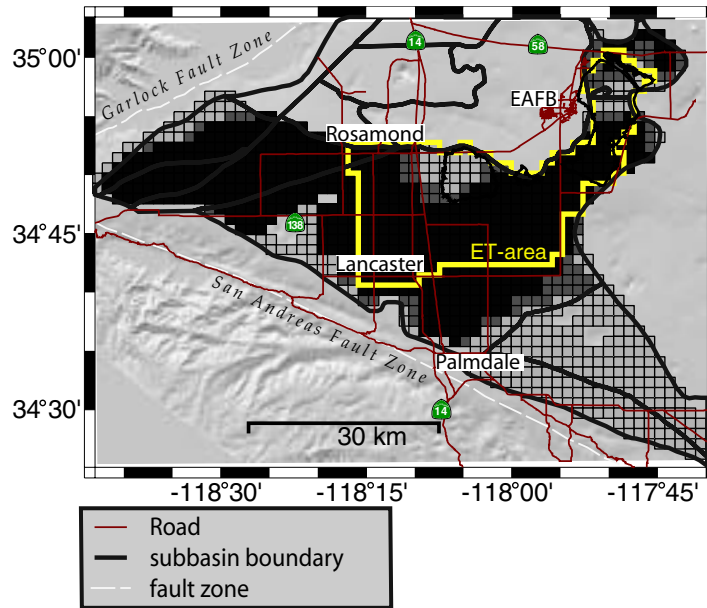


Figure A-1: Area covered by model grid. Shown are only the active cells in the model layers. Black cells are active (IBOUND value 1) in all three model layers. The dark gray cells are only active in the top and middle layers and the light gray cells are only active in the top layer. All active cells in the model are variable head cells. All boundaries are no-flow boundaries. Any inflow and outflow across the model boundaries is simulated through wells in the boundary cells. The cells for which evapotranspiration is simulated are indicated by the yellow frame.

The development and calibration of the original model to aquifer heads at 19 wells and subsidence at 10 benchmark locations is reported in detail by Leighton and Phillips [2003]. Rather than mirroring their work here, I will merely present the resulting groundwater flow model (including my modifications).

A.1 Model grid

The model uses a regular finite difference grid with 43 rows (east-west), 60 columns (north-south) and three model layers. Each model cell extends 1 by 1 mile horizontally. The thicknesses of the model cells vary spatially. The total area covered by this model grid is shown in figure A-1. Groundwater flow is only simulated for a subset of the cells. The active cells for the three model layers are defined by the MODFLOW

IBOUND arrays (fig. A-1). All active cells in the model are variable head cells. All model boundaries are no-flow boundaries.

A.2 Flow properties

A.2.1 Horizontal groundwater flow

The model uses the block-centered flow package (BCF) [McDonald and Harbaugh, 1988] for the groundwater flow computations. The upper model layer is identified as confined/unconfined and the middle and lower layers are specified as confined. The BCF package requires different input parameters for these two cases. For the confined/unconfined (top) layer the horizontal hydraulic conductivity needs to be specified (fig. A-2). The transmissivity is then computed by the package as the product of the hydraulic conductivity and the saturated thickness in the layer. For confined layers the saturated thickness does not change during the simulation. The BCF package requires the transmissivity to be specified directly for these layers (fig. A-2).

Several faults in the Antelope Valley aquifer system are represented in the model using the horizontal flow barrier (HFB) package [Hsieh and Freckleton, 1992]. The faults (fig. A-2) are assigned a “hydraulic characteristic”, defined as the hydraulic conductivity or transmissivity (for unconfined/confined and confined layers, respectively) divided by the width of the fault zone (or, more generally, horizontal-flow barrier) [Hsieh and Freckleton, 1992]. The values used for the different faults are indicated in figure A-2.

A.2.2 Vertical groundwater flow

The BCF package parameterizes the vertical flow properties by using a quantity called the “vertical leakance” [McDonald and Harbaugh, 1988] instead of using a vertical hydraulic conductivity, K_v and the layer thickness, z . The vertical leakance is defined

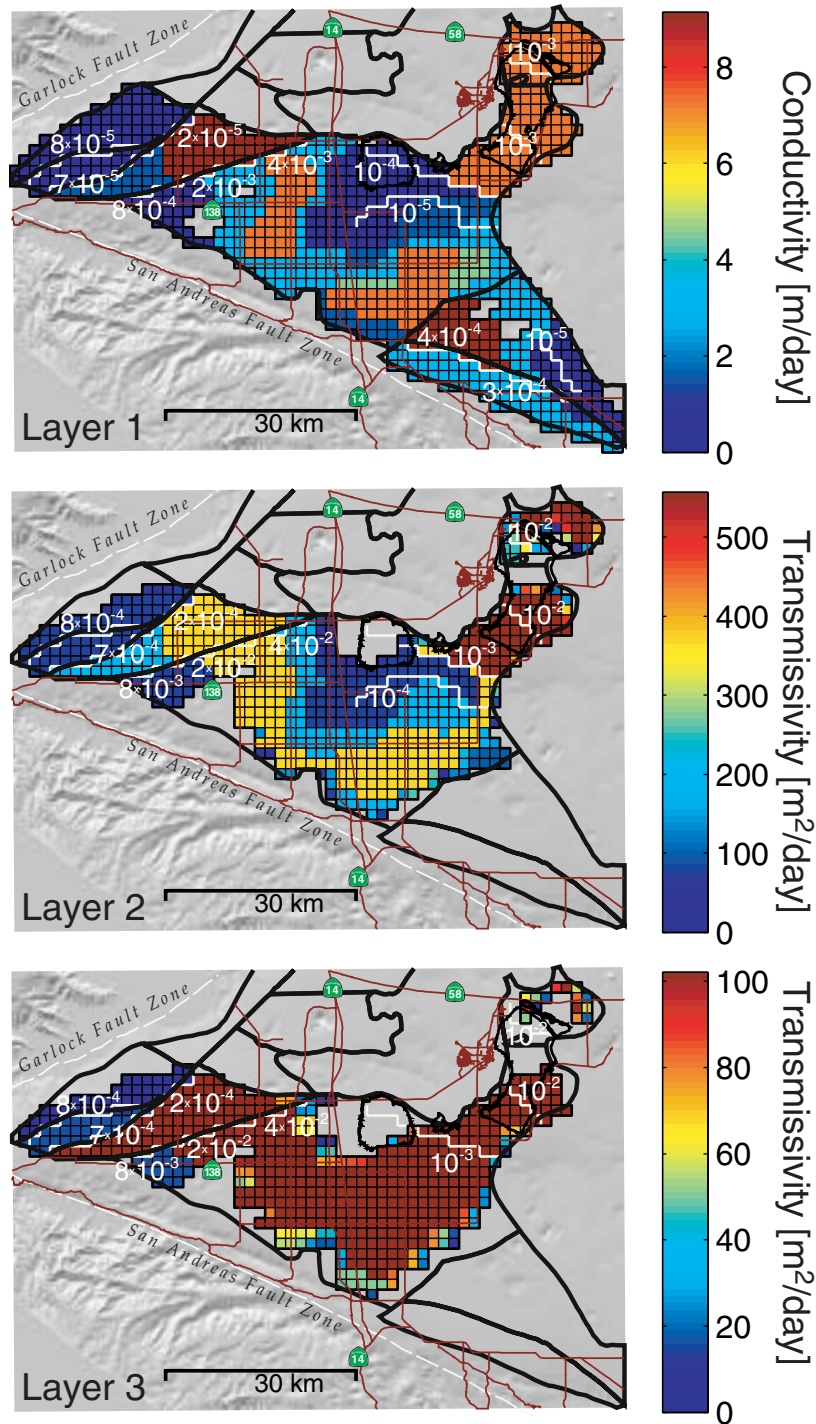


Figure A-2: Horizontal hydraulic conductivity (layer 1) and transmissivity (layers 2 and 3) in the model. A number of horizontal-flow barriers (using the HFB package) are also specified (white lines). The “hydraulic characteristic” (see text) in day^{-1} is indicated for each flow barrier by the white numbers.

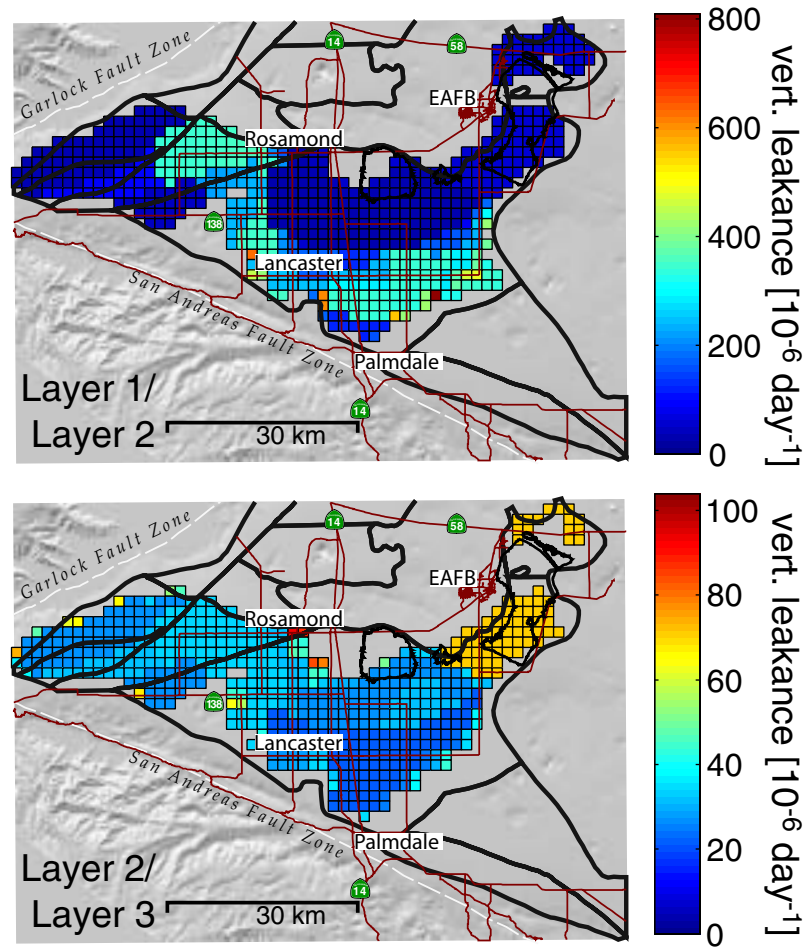


Figure A-3: Vertical leakance between layers 1 and 2 and layers 2 and 3.

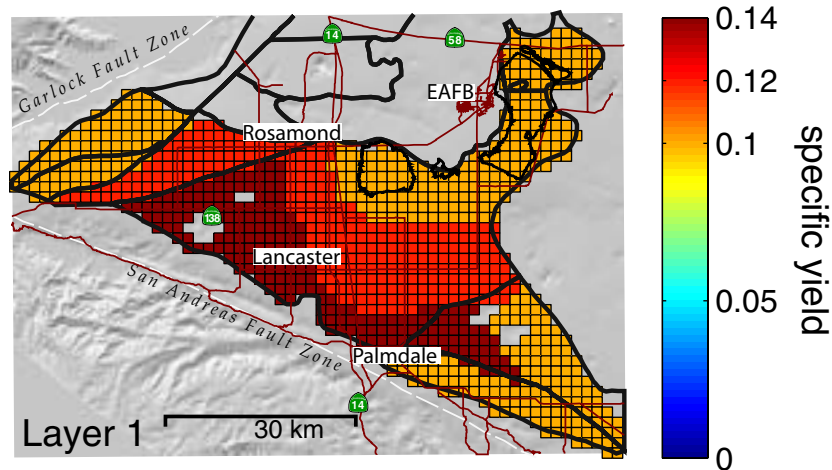


Figure A-4: Specific yield specified for layer 1. The value is used for cells in which the aquifer is not fully saturated during a stress periods. For saturated (confined) conditions the storage coefficient (fig. A-5) is used.

as [McDonald and Harbaugh, 1988]

$$\text{VCONT}_{k+1/2} = \frac{1}{\frac{z_k}{2(K_v)_k} + \frac{z_{k+1}}{2(K_v)_{k+1}}}, \quad (\text{A.1})$$

where $\text{VCONT}_{k+1/2}$ is the vertical leakance between layers k and $k + 1$, z_k and z_{k+1} are the local layer thicknesses and the K_v are the local vertical hydraulic conductivities for layers k and $k + 1$. These vertical leakance values specified between the top and middle layers and the middle and bottom layers are shown in figure A-3.

A.2.3 Storage

Storage in the aquifer system is simulated in two separate packages. The BCF package accounts for storage in the aquifers. Storage and storage changes in confining units and interbeds are accounted for in the interbed storage package (IBS2) or subsidence package (SUB). This is discussed in detail in section 4.3.2.

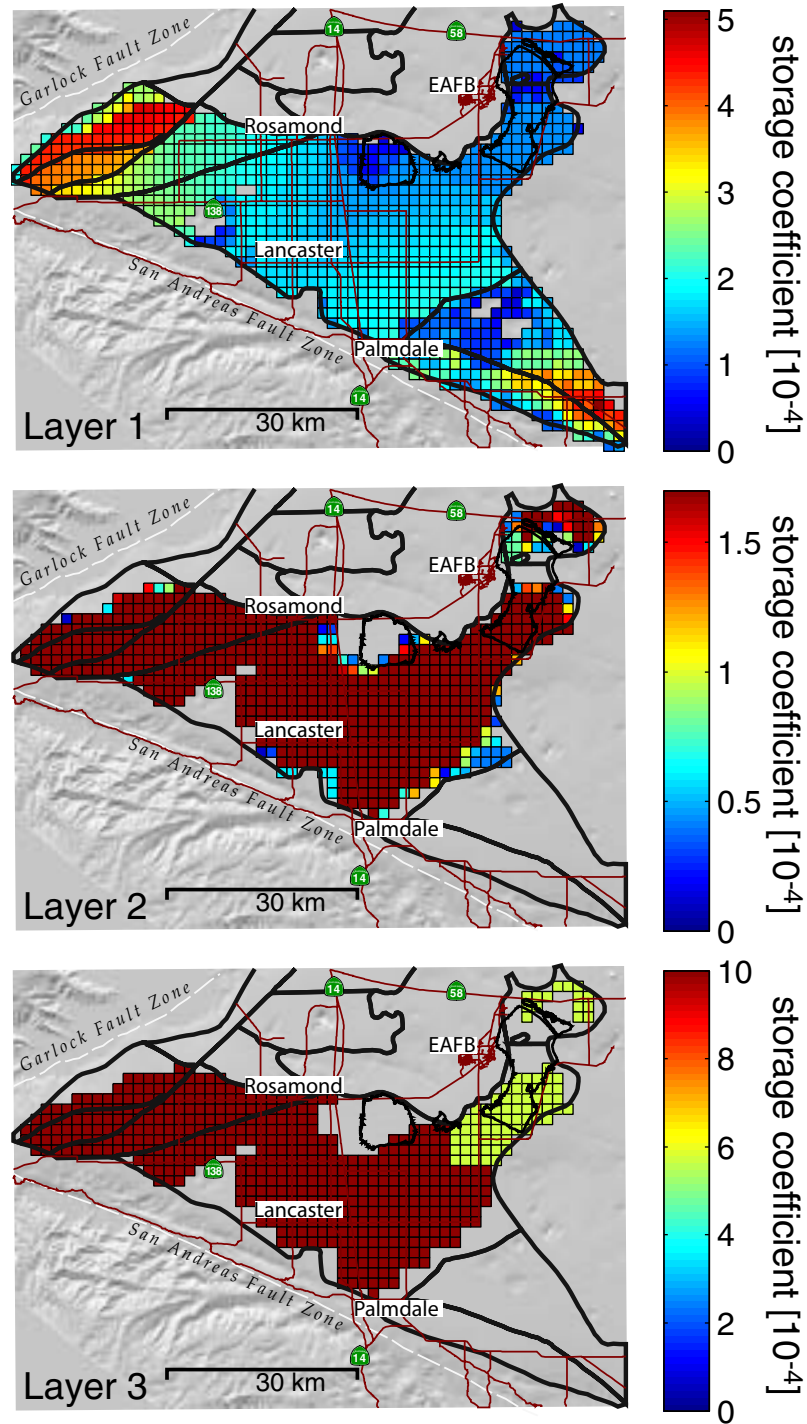


Figure A-5: Primary aquifer storage coefficients specified in the model. For cells that become unsaturated (only in the upper layer), the specific yield is used instead (fig. A-4).

Aquifer storage

The BCF package requires a dimensionless storage coefficient to be specified for each model layer. This is the storage coefficient (eq. 2.10) for the confined layers (layers 2 and 3, fig. A-5) and the specific yield for the unconfined layers. For the top layer, which is specified as confined/unconfined, both values are provided as input to the package (figs. A-4 and A-5).

Interbed storage

As I discussed in detail in section 4.3.2, the IBS2 package [Hoffmann et al., 2003b] uses two different parameterizations for storage in interbeds. For interbeds in which the hydraulic heads are assumed to equilibrate with the heads in the aquifers instantaneously two storage coefficients, S_{ke} and S_{kv} , for elastic and inelastic deformation, respectively, must be specified (figs. A-6 and A-7). For interbeds in which the heads can equilibrate only very slowly with the changing heads in the surrounding aquifers and elastic and inelastic specific storage (S_{ske} and S_{skv} , respectively) and their vertical hydraulic conductivity, K_v , are specified for the interbeds. In the model these values were constant over the entire model domain (table 4.5). The storage in these interbeds is then computed using the other input parameters, namely the equivalent thickness, b_{eq} , and the number of individual interbeds, N (table 4.3). In the model interbed storage is only assigned to the upper two model layers. Only the middle model layer (layer 2) is assigned interbeds with delay properties. The elastic and inelastic storages are set to identical values for each of the two layers (i.e., the inelastic storage for interbeds in the top layer is equal to the elastic storage; similarly for the middle layer). Thus, all inelastic interbed storage is simulated in interbeds with delay properties in layer 2. The elastic and inelastic storage, and the initial preconsolidation head for interbeds without delay properties in the upper two layers are shown in figures A-6 and A-7. The values for b_{eq} and N in the middle model layer are shown in figure A-8. The initial preconsolidation head for the delayed interbeds in that layer is uniformly 1.2m below the starting head in that layer (fig. A-11).

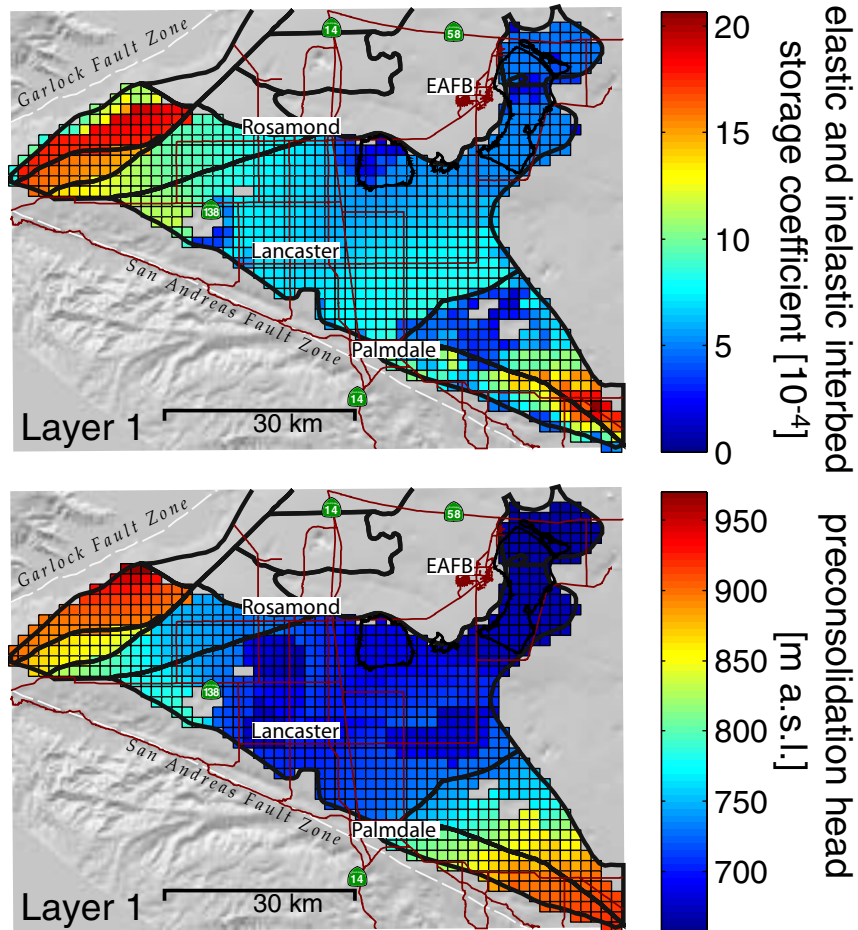


Figure A-6: Elastic and inelastic storage and the initial preconsolidation head for the upper model layer. The values for inelastic and elastic instantaneous interbeds were equal as inelastic compaction was simulated only for interbeds with delay properties in layer 2 (section 4.3.2). The properties of these interbeds are shown in figure A-8.

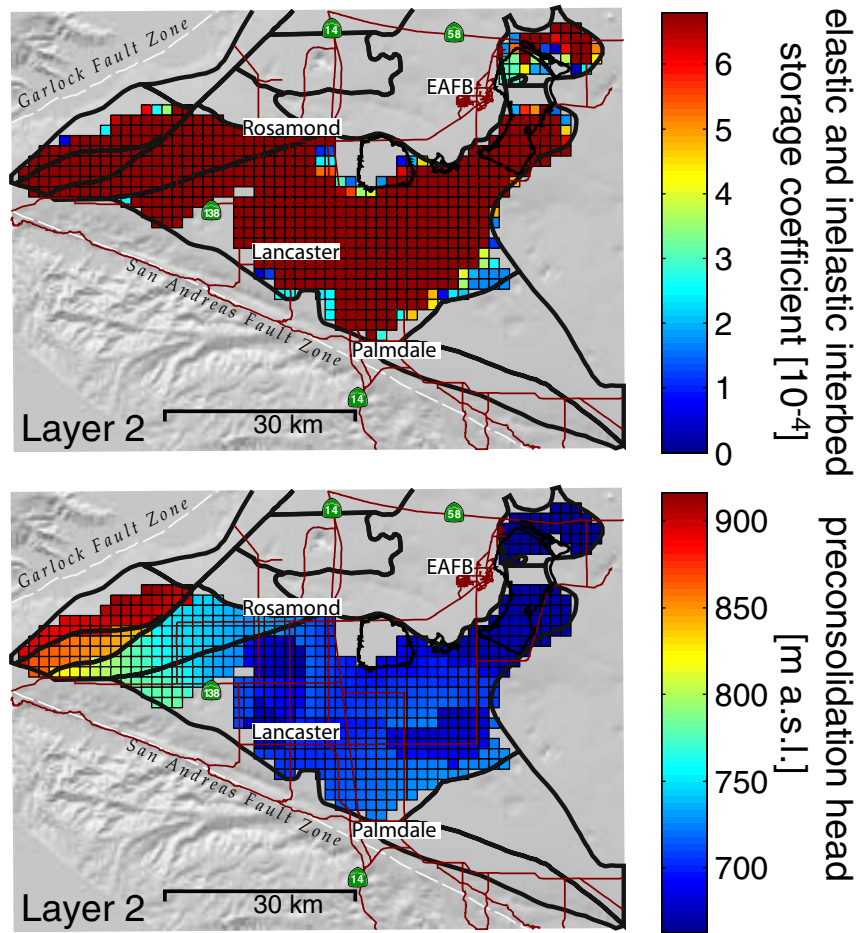


Figure A-7: Elastic and inelastic storage and the initial preconsolidation head for the middle model layer. Interbeds with delay properties require additional parameters (fig. A-8). By setting the inelastic storage of interbeds without delay properties equal to the elastic storage all inelastic compaction is simulated in interbeds with delay properties.

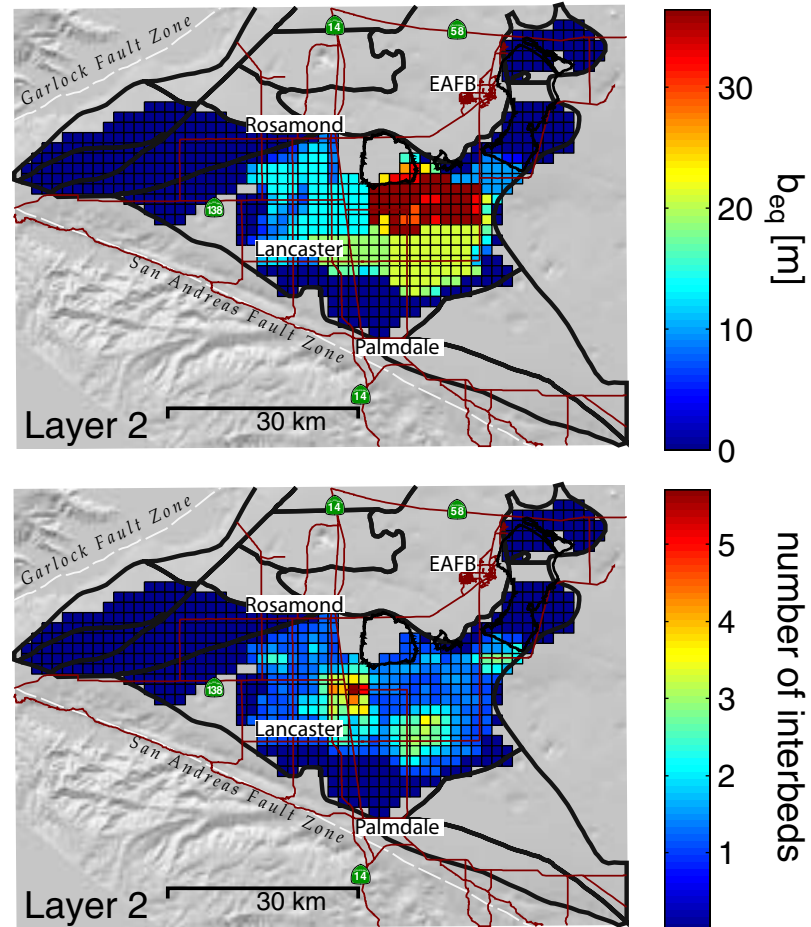


Figure A-8: Equivalent interbed thickness (b_{eq} , see eq. 2.14) and the number of individual interbeds, N for interbeds with delay properties in the middle model layer. The resulting total inelastic storage coefficients and time constants are shown in figure 4-13.

A.3 In- and outflow

Because only variable-head cells are used in the model, all outer model boundaries represent no-flow boundaries. Water enters the model domain as recharge (using the recharge (RCH) package) or through wells (using the well (WEL) package) [McDonald and Harbaugh, 1988]. Water leaves the model via evapotranspiration (ET), negative recharge (simulating outflow), or pumping wells.

A.3.1 Evapotranspiration

The area for which evapotranspiration is considered is indicated by the yellow frame in figure A-1. The ET flux in this area depends on the depth of the water table below the surface. It decreases linearly from $5 \cdot 10^{-4} m/d$ for a water table at the land surface to zero for a water table more than $3.05m$ below the land surface.

A.3.2 Recharge

Recharge to the model by means of the recharge (RCH) package is simulated primarily along the foot of the mountain ranges in the southwest and northwest, corresponding to runoff from the mountains. This recharge pattern (fig. A-9) remains constant during the first 69 stress periods (1915-1984). After that, an additional artificial recharge, increasing from $1,792m^3/d$ in stress period 70 to $2,873m^3/d$ in stress period 84 is applied at the cell indicated in figure A-9.

A.3.3 Groundwater pumping

Groundwater pumping represents the by far most important sink of water in the Antelope Valley aquifer system and varied significantly over time (fig. 4-2). Figure A-10 shows the total withdrawals at each model grid location.

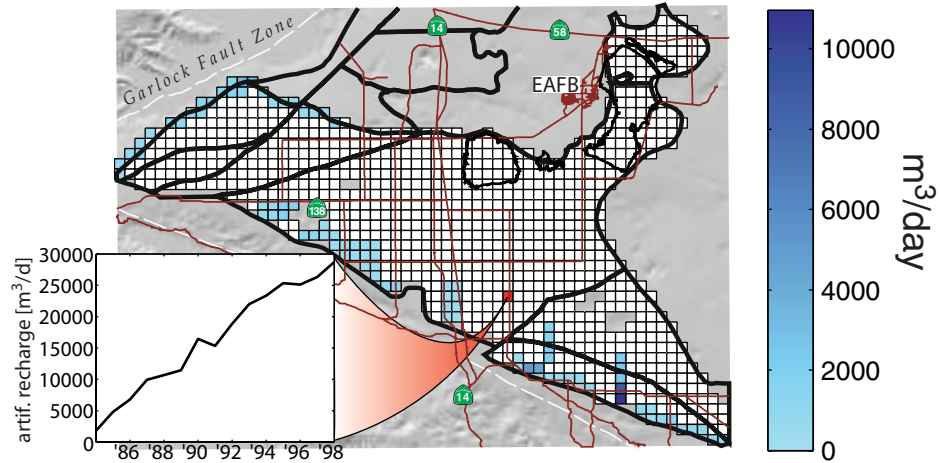


Figure A-9: Natural and artificial groundwater recharge. Natural recharge is simulated along the mountains in the southwest and northwest. Artificial recharge occurs in a single model cell starting in 1984.

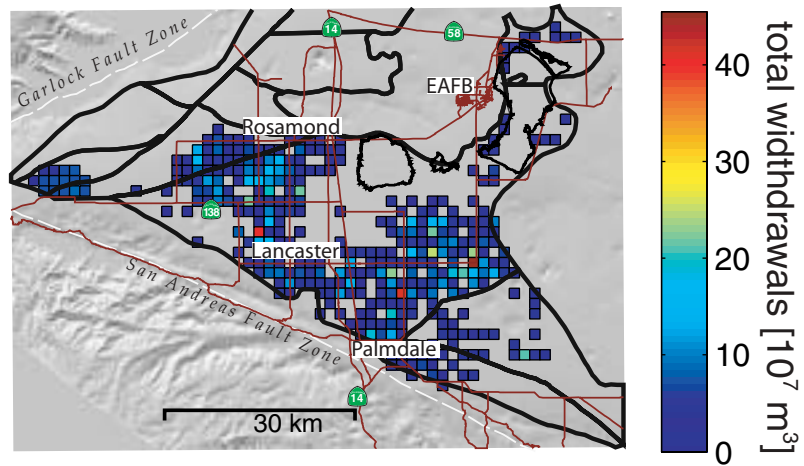


Figure A-10: Total withdrawals from wells over the 84 years in the simulation. 30% of the water withdrawn from wells was returned as irrigation return after a 10 year time delay.

A.3.4 Irrigation return

Some fraction of the water pumped for irrigation percolates back down to the water table. In the model this is simulated by returning 30% of the water pumped from wells to the top model layer after a time delay of 10 years to account for the time required for the irrigation water to reach the water table. The water is added to the top model layer through the pumping wells using the well (WEL) package [McDonald and Harbaugh, 1988].

A.4 Starting heads

The starting heads were obtained by Leighton and Phillips [2003] through a steady state simulation for the model. They were not modified in this work as changes in storage do not affect the steady state solution. Figure A-11 shows the starting heads for the three model layers.

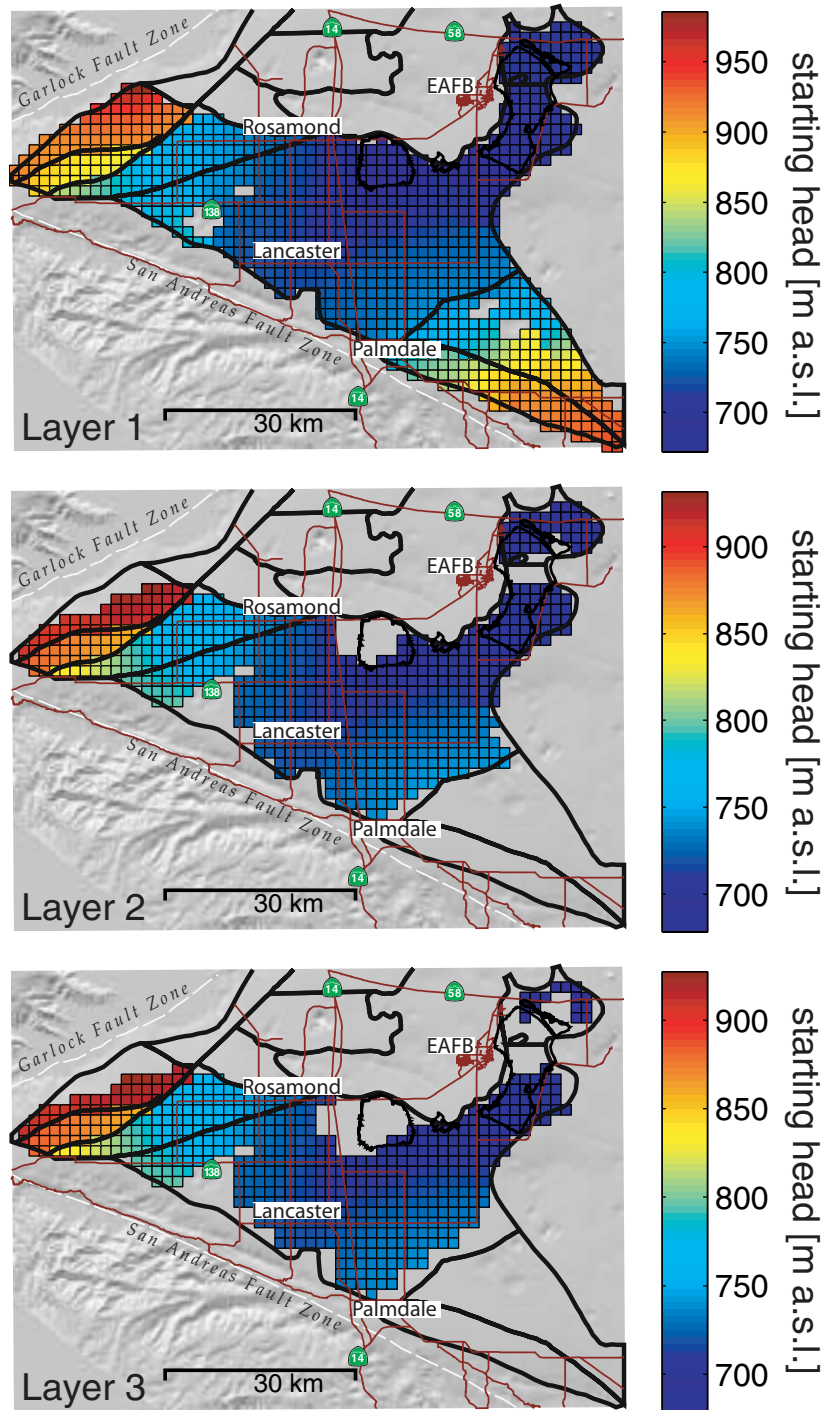


Figure A-11: Starting heads for the three model layers.

References cited

- Falk Amelung, Devin L. Galloway, John W. Bell, Howard A. Zebker, and Randell J. Laczniaik. Sensing the ups and downs of Las Vegas: InSAR reveals structural control of land subsidence and aquifer-system deformation. *Geology*, 27(6):483–486, June 1999.
- Falk Amelung, Sigurjón Jónsson, Howard A. Zebker, and Paul Segall. Widespread uplift and trapdoor faulting on Galápagos volcanoes observed with radar interferometry. *Nature*, 407:993–996, 2000.
- H. Berrada Baby, P. Golé, and J. Lavergnat. A model for the tropospheric excess path length of radio waves from surface meteorological measurements. *Radio Science*, 23(6):1023–1038, 1988.
- Richard Bamler and Dieter Just. Phase statistics and decorrelation in SAR interferograms. In *Geoscience and Remote Sensing Symposium, IGARSS 1993*, volume 3, pages 980–984, 1993.
- Gerald W. Bawden, Wayne Thatcher, Ross S. Stein, and Ken Hudnut. Tectonic contraction across Los Angeles after removal of groundwater pumping effects. *Nature*, 412:812–815, 2001.
- John W. Bell and J. G. Price. Subsidence in Las Vegas Valley, 1980-91: Final project report. Open-File Report 93-4, Nevada Bureau of Mines, 1991.
- M. A. Biot. Theory of elasticity and consolidation for a porous anisotropic solid. *Journal of Applied Physics*, 26(2):182–185, February 1955.

- Maurice A. Biot. General theory of three-dimensional consolidation. *Journal of Applied Physics*, 12:155–164, February 1941.
- James C. Blodgett and J. S. Williams. Land subsidence and problems affecting land use at Edwards Air Force Base and vicinity, California, 1990. Water-Resources Investigations 92-4035, U.S. Geological Survey, 1992.
- R. M. Bloyd, Jr. Water resources of the Antelope Valley East-Kern water agency area, California. Open-file report, U.S. Geological Survey, 1967.
- James W. Borchers, editor. *Land Subsidence Case studies and current research: Proceedings of the Dr. Joseph F. Poland Symposium on Land Subsidence*, number 8 in Special Publication, 1998. Association of Engineering Geologists.
- T. J. Burbey. Pumpage and water-level change in the principal aquifer of Las Vegas Valley, 1980-90. Nev. Div. of Water Resour. Inf. Rep. 34, State of Nevada, Carson City, 1995. 224pp.
- Carl S. Carlson, David A. Leighton, Steven P. Phillips, and Loren F. Metzger. Regional water table (1996) and water-table changes in the Antelope Valley groundwater basin, California. Water-Resources Investigations Report 98-4022, U.S. Geological Survey, 1998.
- Claudie Carnec, D. Massonnet, and C. King. Two examples of the application of SAR interferometry to sites of small extent. *Geophysical Research Letters*, 23(24): 3579–3582, December 1996.
- M. C. Carpenter. Earth-fissure movements associated with fluctuations in groundwater levels near the Picacho Mountains, south-central Arizona, 1980-84. Professional Paper 497-H, U.S. Geological Survey, 1993.
- J. J. Carrillo-Rivera. Monitoring of exploited aquifers resulting in subsidence. example: Mexico City. *Studies and reports in hydrology*, 57:151–165, 1999.
- M. M. Carroll. An effective stress law for anisotropic elastic deformation. *Journal of Geophysical Research*, 84(13):7510–7512, December 1979.

- H. S. Carslaw and J. C. Jaeger. *Conduction of heat in solids*. Oxford at the Clarendon Press, 2 edition, 1959.
- Curtis W. Chen. *Statistical-Cost network-flow approaches to two-dimensional phase unwrapping for radar interferometry*. PhD thesis, Stanford University, Stanford, California, June 2001.
- R. Coache. Las Vegas Valley water usage report, Clark County, Nevada, 1998. Nev. Div. of Water Resour. rep., State of Nevada, Carson City, 1999. 137pp.
- Mario Costantini. A novel phase unwrapping method based on network programming. *IEEE Transactions on Geoscience and Remote Sensing*, 36(3):813–821, May 1998.
- Michele Crosetto, Carl Christian Tschering, Bruno Crippa, and Manuel Castillo. Subsidence monitoring using SAR interferometry: Reduction of the atmospheric effects using stochastic filtering. *Geophysical Research Letters*, 29(9): 10.1029/2001GL013544, 2002.
- John C. Curlander and Robert N. McDonough. *Synthetic Aperture Radar*. Wiley Series in Remote Sensing. John Wiley, 1991.
- John C. Davis. *Statistics and data analysis in geology*. Wiley, New York, 2 edition, 1986.
- C. Delacourt, P. Briole, and J. Achache. Tropospheric corrections of SAR interferograms with strong topography. Application to Etna. *Geophysical Research Letters*, 25(15):2849–2852, August 1998.
- Clayton V. Deutsch and André G. Journel. *GSLIB Geostatistical software library and user's guide*. Applied Geostatistics Series. Oxford University Press, 2 edition, 1998.
- David J. Donovan. Hydrostratigraphy and allostratigraphy of the cenozoic alluvium in the northwestern part of Las Vegas Valley, Clark County, Nevada. Master's thesis, University of Nevada, Department of Geoscience, August 1996.

- Timothy J. Durbin. Calibration of a mathematical model of the Antelope Valley ground-water basin, California. Water-Supply Paper 2046, U.S. Geological Survey, 1978.
- L. C. Dutcher and G. F. Worts, Jr. Geology, hydrology, and water supply of Edwards Air Force Base, Kern County, California. Open-file report, U.S. Geological Survey, 1963.
- D. R. Fatland and M. Nolan. Measurements of soil moisture on 50m postings using InSAR. *Eos Transactions*, 82(47), 2001. Fall Meet. Suppl., Abstract H41E-0314.
- A. Ferretti, C. Prati, and F. Rocca. Multibaseline InSAR DEM reconstruction: The wavelet approach. *IEEE Transactions on Geoscience and Remote Sensing*, 37(2): 705–715, March 1999.
- A. Ferretti, C. Prati, and F. Rocca. Nonlinear subsidence rate estimation using permanent scatterers in differential SAR interferometry. *IEEE Transactions on Geoscience and Remote Sensing*, 38(5):2202–2212, September 2000.
- A. Ferretti, C. Prati, and F. Rocca. Permanent scatterers in SAR interferometry. *IEEE Transactions on Geoscience and Remote Sensing*, 39(1):8–20, January 2001.
- E. J. Fielding, R. G. Blom, and R. M. Goldstein. Rapid subsidence over oil fields measured by SAR interferometry. *Geophysical Research Letters*, 25:3215, 1998.
- A. K. Gabriel and R. M. Goldstein. Crossed orbit interferometry: theory and experimental results from SIR-B. *Int. J. Remote Sensing*, 9(5):857–872, 1988.
- A. K. Gabriel, R. M. Goldstein, and H. A. Zebker. Mapping small elevation changes over large areas: Differential radar interferometry. *Journal of Geophysical Research*, 94(B7):9183–9191, July 1989.
- Devin L. Galloway, K. W. Hudnut, S. E. Ingebritsen, S. P. Phillips, G. Peltzer, F. Rogez, and P. A. Rosen. Detection of aquifer-system compaction and land subsidence using interferometric synthetic aperture radar, Antelope Valley, Mojave Desert, California. *Water Resources Research*, 34(10):2573–2585, October 1998.

- Devin L. Galloway, David R. Jones, and S. E. Ingebritsen. Land subsidence in the United States. Circular 1182, United States Geological Survey, 1999.
- G. Gambolati. A one-dimensional model of the subsoil for computing the surface subsidence. Technical Report CRV002, International Business Machines Science Center, Venice, Italy, 1970.
- G. Gambolati. Estimate of subsidence in Venice using a one-dimensional model of the subsoil. *International Business Machines Journal of Research and Development*, 16(2):130–137, 1972a.
- G. Gambolati. A three-dimensional model to compute land subsidence. *Bulletin of the International Association of Hydrological Sciences*, 17(2):219–226, 1972b.
- G. Gambolati and R. A. Freeze. Mathematical simulation of the subsidence of Venice. *Water Resources Research*, 9(3):721–733, 1973.
- R. M. Goldstein, T. P. Barnett, and H. A. Zebker. Remote sensing of ocean currents. *Science*, 246:1282–1285, 1989.
- R. M. Goldstein, E. R. Caro, and C. Wu. *Method and apparatus for contour mapping using synthetic aperture radar*. United States Patent, 1985. No. 4551724.
- R. M. Goldstein, H. Engelhardt, B. Kamb, and R. M. Frolich. Satellite radar interferometry for monitoring ice sheet motion: Application to an antarctic ice stream. *Science*, 262:1525–1530, 1993.
- R. M. Goldstein and H. A. Zebker. Interferometric radar measurement of ocean surface currents. *Nature*, 328:707–709, 1987.
- R. M. Goldstein, H. A. Zebker, and C. L. Werner. Satellite radar interferometry: Two-dimensional phase unwrapping. *Radio Science*, 23(4):713–720, 1988.
- L. C. Graham. Synthetic interferometer radar for topographic mapping. *Proceedings of the IEEE*, 62(6):763–768, 1974.

- Ramon F. Hanssen. *Atmospheric heterogeneities in ERS tandem SAR interferometry*. Delft University Press, 1998.
- Ramon F. Hanssen. *Radar Interferometry – Data Interpretation and Error Analysis*. Kluwer Academic Publishers, 2001.
- A. W. Harbaugh, E. R. Banta, M. C. Hill, and M. G. McDonald. Modflow-2000, the U.S. Geological Survey modular ground-water model - User guide to modularization concepts and the ground-water flow process. Open-File Report 00-92, U.S. Geological Survey, 2000.
- A. W. Harbaugh and M. G. McDonald. User's documentation for MODFLOW-96, an update to the U.S. Geological Survey modular finite-difference ground-water flow model. Open-File Report 96-485, U.S. Geological Survey, 1996.
- Donald C. Helm. One-dimensional simulation of aquifer system compaction near Pixley, California 1. constant parameters. *Water Resources Research*, 11(3):465–478, June 1975.
- Donald C. Helm. One-dimensional simulation of aquifer system compaction near Pixley, California 2. stress-dependent parameters. *Water Resources Research*, 12(3):375–391, June 1976.
- Donald C. Helm. Horizontal aquifer movement in a Theis-Thiem confined system. *Water Resources Research*, 30(4):953–964, April 1994.
- Edward W. Hoen. *A Correlation-based Approach to Modeling Interferometric Radar Observations of the Greenland Ice Sheet*. PhD thesis, Stanford University, 2001.
- Jörn Hoffmann, Devin L. Galloway, and Howard A. Zebker. Inverse modeling of interbed storage parameters using land subsidence observations, Antelope Valley, California. *Water Resources Research*, 2003a. in press.
- Jörn Hoffmann, Devin L. Galloway, Howard A. Zebker, and Falk Amelung. Seasonal subsidence and rebound in Las Vegas Valley, Nevada, observed by synthetic

- aperture radar interferometry. *Water Resources Research*, 37(6):1551–1566, June 2001.
- Jörn Hoffmann, Stanley A. Leake, Devin L. Galloway, and Alicia M. Wilson. MODFLOW-2000 ground-water model – user guide to the subsidence and aquifer-system compaction (SUB) package. Open-file report, U.S. Geological Survey, 2003b. in press.
- T. L. Holzer. Ground failure induced by ground water withdrawal from unconsolidated sediment. In T. L. Holzer, editor, *Man-induced land subsidence*, volume 6 of *Reviews in Engineering Geology*, pages 67–105. Geological Society of America, 1984.
- Thomas L. Holzer. The history of the aquitard-drainage model. In J. W. Borchers, editor, *Land subsidence case studies and current research: Proceedings of the Dr. Joseph F. Poland symposium on land subsidence*, number 8 in Special Publication, pages 7–12. Association of Engineering Geologists, 1998.
- Paul A. Hsieh and John R. Freckleton. Documentation of a computer program to simulate horizontal-flow barriers using the U.S. Geological Survey’s modular three-dimensional finite-difference ground-water flow model. Open-File Report 92-477, U.S. Geological Survey, 1992.
- Marti E. Ikehara and S. P. Phillips. Determination of land subsidence related to ground-water-level declines using Global Positioning System and leveling surveys in Antelope Valley, Los Angeles and Kern counties, California, 1992. Water-Resources Investigations Report 94-4184, U.S. Geological Survey, 1994.
- R. L. Ireland, J. F. Poland, and F. S. Riley. Land subsidence in the San Joaquin Valley, California as of 1980. Professional Paper 437-I, U.S. Geological Survey, 1984.
- C. E. Jacob. On the flow of water in an elastic artesian aquifer. *Trans. Amer. Geophys. Union*, 2:574–586, 1940.

- C. E. Jacob. Flow of groundwater. In H. Rouse, editor, *Engineering Hydraulics*, pages 321–386. John Wiley, New York, 1950.
- H. R. Johnson. Water resources of Antelope Valley, California. Water-Supply Paper 278, U.S. Geological Survey, 1911.
- Sigurjón Jónsson. *Modeling volcano and earthquake deformation from satellite radar interferometric observations*. PhD thesis, Stanford University, June 2002.
- R. L. Jordan, E. R. Caro, Y. Kim, M. Kobrick, Y. Shen, F. V. Stuhr, and M. U. Werner. Shuttle radar topography mapper (SRTM). In G. Franceschetti, C. J. Oliver, J. C. Shiue, and S. Tajbakhsh, editors, *Microwave Sensing and Synthetic Aperture Radar*, SPIE, pages 412–422, 1996.
- D. G. Jorgensen. Relationships between basic soils - engineering equations and basic ground-water flow equations. Water-Supply Paper 2064, U.S. Geological Survey, 1980.
- I. R. Joughin, D. P. Winebrenner, and M. A. Fahnestock. Observations of ice-sheet motion in Greenland using satellite radar interferometry. *Geophysical Research Letters*, 22:571–574, 1995.
- Dieter Just and Richard Bamler. Phase statistics of interferograms with applications to synthetic aperture radar. *Applied Optics*, 33(20):4361–4368, 1994.
- S. A. Leake. Interbed storage changes and compaction in models of regional ground-water flow. *Water Resources Research*, 26(9):1939–1950, September 1990.
- S. A. Leake and D. E. Prudic. Documentation of a computer program to simulate aquifer-system compaction using the modular finite-difference ground-water flow model. Techniques of Water-Resources Investigations, U.S. Geological Survey, 1991. Book 6, Chapter A2.
- D. A. Leighton and S. P. Phillips. Simulation of ground-water flow and land subsidence in the Antelope Valley ground-water basin, California. Water-Resources Investigations Report 03-4016, U.S. Geological Survey, 2003.

- F. Li and R. M. Goldstein. Studies of multi-baseline spaceborne interferometric synthetic aperture radar. In *International Geoscience and Remote Sensing Symposium, Ann Arbor, 18-21 May 1987*, pages 1545–1550, 1987.
- F. Li and R. M. Goldstein. Studies of multi-baseline spaceborne interferometric synthetic aperture radars. *IEEE Transactions Geoscience Remote Sensing*, 28:88–97, 1990.
- B. E. Lofgren. Land subsidence due to the application of water. In D. J. Varnes and G. Kiersch, editors, *Reviews in engineering geology, Vol. II*, pages 271–303. Geological Society of America, 1969.
- C. J. Londquist, D. L. Rewis, D. L. Galloway, and W. F. McCaffrey. Hydrogeology and land subsidence, Edwards Air Force Base, Antelope Valley, California, January 1989-December 1991. Water-Resources Investigations Report 93-4114, U.S. Geological Survey, 1993.
- Don R. Mabey. Gravity survey of the western Mojave Desert, California. Prof. Paper 316, U.S. Geological Survey, 1960.
- G. T. Malmberg. Available water supply of the Las Vegas groundwater basin, Nevada. Water Supply Paper 1780, U.S. Geological Survey, 1965.
- E. T. Mankey. Tabulation of elevation differences for earth movement study in Antelope Valley from 1928 to 1960. J.N. 0301.02, County of Los Angeles, Department of County Engineer, Survey Division, 1963.
- D. Massonnet, P. Briole, and A. Arnaud. Deflation of Mount Etna monitored by spaceborne radar interferometry. *Nature*, 375:567–570, 1995.
- D. Massonnet, K. L. Feigl, M. Rossi, and F. Adragna. Radar interferometric mapping of deformation in the year after the Landers earthquake. *Nature*, 369:227–230, 1994.
- D. Massonnet, T. Holzer, and H. Vadon. Land subsidence caused by the East Mesa geothermal field, California, observed using SAR interferometry. *Geophysical Research Letters*, 24(8):901–904, 1997.

- D. Massonnet, M. Rossi, C. Carmona, F. Adragna, G. Peltzer, K. Feigl, and T. Rabaute. The displacement field of the Landers earthquake. *Nature*, 364:138–142, 1993.
- Didier Massonnet and Kurt L. Feigl. Radar interferometry and its application to changes in the Earth's surface. *Reviews of Geophysics*, 36(4):441–500, November 1998.
- G. B. Maxey and C. H. Jameson. Geology and water resources of Las Vegas, Pahrump, and Indian Springs Valleys, Clark and Nye counties, Nevada. Nev. State Eng. Water Resources Bulletin 5, State of Nevada, Carson City, 1948. 121pp.
- M. G. McDonald and A. W. Harbaugh. *A modular three-dimensional finite-difference groundwater flow model*. Techniques of Water Resources Investigations. U.S. Geological Survey, Reston, Va., 1988. book 6, chapter A1.
- D. F. McTigue. Thermoelastic response of fluid-saturated porous rock. *Journal of Geophysical Research*, 91(9):9533–9542, August 1986.
- O. E. Meinzer. Compressibility and elasticity of artesian aquifers. *Econ. Geology*, 23(3):263–291, 1928.
- O. E. Meinzer and H. A. Hard. The artesian-water supply of the Dakota sandstone in North Dakota with special reference to the Edgeley quadrangle. Water-Supply Paper 520-E, U.S. Geological Survey, 1925.
- D. S. Morgan and M. D. Dettinger. Ground-water conditions in Las Vegas Valley, Clark County, Nevada, part 2, hydrogeology and simulation of ground-water flow. Water-Supply Paper 2320-B, U.S. Geological Survey, 1991.
- T. N. Narasimhan and P. A. Witherspoon. Numerical model for saturated-unsaturated flow in deformable porous media, 1, Theory. *Water Resources Research*, 13:657–664, 1977.

- S. P. Neuman, C. Preller, and T. N. Narasimhan. Adaptive explicit-implicit quasi three-dimensional finite element model of flow and subsidence in multiaquifer systems. *Water Resources Research*, 18(5):1551–1561, 1982.
- T. Nishikawa, D. L. Rewis, and P. M. Martin. Numerical simulation of ground-water flow and land subsidence at Edwards Air Force Base, Antelope Valley, California. Water-Resources Investigations Report 01-4038, U.S. Geological Survey, 2001.
- Amos Nur and J. D. Byerlee. An exact effective stress law for elastic deformation of rock with fluids. *Journal of Geophysical Research*, 76(26):6414–6419, September 1971.
- V. V. Palciauskas and P. A. Domenico. Characterization of drained and undrained response of thermally loaded repository rocks. *Water Resources Research*, 18(2): 281–290, April 1982.
- Michael T. Pavelko. Ground-water and aquifer-system compaction data from the Lorenzi Site, Las Vegas, Nevada, 1994-1999. Open-File Report 00-362, U.S. Geological Survey, 2000.
- Michael T. Pavelko, David B. Wood, and Randell J. Laczniak. Las Vegas, Nevada gambling with water in the desert. In Devin L. Galloway, David R. Jones, and S. E. Ingebritsen, editors, *Land subsidence in the United States*, number 1182 in Circular, pages 49–64. U.S. Geological Survey, 1999.
- Eileen P. Poeter and Mary C. Hill. Documentation of UCODE, a computer code for universal inverse modeling. Water-Resources Investigations Report 98-4080, U.S. Geological Survey, Denver, Colorado, 1998.
- J. F. Poland, B. E. Lofgren, R. L. Ireland, and R. G. Pugh. Land subsidence in the San Joaquin Valley, California, as of 1972. Professional Paper 437-H, U.S. Geological Survey, 1975.
- Joseph F. Poland. Guidebook to studies of land subsidence due to ground-water withdrawal. Technical report, Unesco, 1984.

- C. Prati and Rocca F. Limits to the resolution of elevation maps from stereo SAR images. *Int. J. Remote Sensing*, 11(12):2215–2235, 1990.
- W. E. Pratt and D. W. Johnson. Local subsidence of the Goose Creek oil field. *Journal of Geology*, 34(7):577–590, 1926.
- Perry H. Rahn. *Engineering Geology*. Prentice Hall PTR, Upper Saddle River, New Jersey 07458, 2 edition, 1996.
- S. E. Rantz. Mean annual precipitation in the California region. Open-file report, U.S. Geological Survey, 1969.
- Eric Rignot. Fast recession of a West Antarctic glacier. *Science*, 281:549–551, 1998.
- Francis S. Riley. Analysis of borehole extensometer data from central California. In *Land Subsidence*, pages 423–431. International Association of Scientific Hydrology, Publication 89, September 1969.
- Francis S. Riley. Mechanics of aquifer systems - the scientific legacy of Dr. Joseph F. Poland. In J. W. Borchers, editor, *Land subsidence case studies and current research: Proceedings of the Dr. Joseph F. Poland symposium on land subsidence*, number 8 in Special Publication, pages 13–27. Association of Engineering Geologists, 1998.
- M. Rodell and J. S. Famiglietti. Detectability of variations in continental water storage from satellite observations of the time dependent gravity field. *Water Resources Research*, 35(9):2705–2723, September 1999.
- Paul Rosen, C. Werner, E. Fielding, S. Hensley, S. Buckley, and P. Vincent. Aseismic creep along the San Andreas fault northwest of Parkfield, California, measured by radar interferometry. *Geophysical Research Letters*, 25:825–828, 1998.
- R. Scharroo and P. Visser. Precise orbit determination and gravity field improvement for the ERS satellite. *Journal of Geophysical Research*, 103(C4):8113–8127, 1998.

- David A. Schmidt and Roland Bürgmann. Transient tectonics of the Hayward, Calaveras and Mission fault junction. In *AGU Fall Meeting Suppl.*, volume 82 of *EOS Transactions*, page F264, 2001.
- R. F. Scott. *Principles of soil mechanics*. Addison-Wesley Pub. Co., Palo Alto, California, 1963.
- E. K. Smith, Jr. and S. Weintraub. The constants in the equation for atmospheric refractivity index at radio frequencies. In *Proceedings of the I.R.E.*, volume 41, pages 1035–1037, 1953.
- Michelle Sneed and Devin Galloway. Aquifer-system compaction and land subsidence: Measurements, analyses, and simulations - the Holly site, Edwards Air Force Base, Antelope Valley, California. Water-Resources Investigations Report 00-4015, U.S. Geological Survey, 2000. 65p.
- J. H. Snyder. Ground water in California – the experience of the Antelope Valley area, Los Angeles and Kern counties, California. Giannini Foundation Ground-Water Studies 2, University of California, Berkeley, Div. Agri. Sci., 1955.
- William E. Templin, Steven P. Phillips, Daniel E. Cherry, Myrna L. DeBortoli, et al. Land use and water use in the Antelope Valley, California. Water-Resources Investigations 94-4208, U.S. Geological Survey, 1995.
- Karl Terzaghi. *Erdbaumechanik auf Bodenphysikalischer Grundlage*. Deuticke, Wien, 1925.
- W. N. Thayer. Geologic features of Antelope Valley, California. Report, Los Angeles County Flood Control District, 1946.
- D. G. Thompson. The Mohave Desert region, California: A geographic, geologic, and hydrologic reconnaissance. Water Supply Paper 578, U.S. Geological Survey, 1929.
- David Keith Todd. *Groundwater Hydrology*. John Wiley & Sons, New York, 2 edition, 1980.

- C. F. Tolman and J. F. Poland. Ground-water infiltration, and ground-surface recession in Santa Clara Valley, Santa Clara County, California. *Transactions American Geophysical Union*, 21:23–34, 1940.
- U.S. Census Bureau. Metropolitan area rankings by population size and percent change for July 1, 1998 to July 1, 1999 and April 1, 1990 to July 1, 1999. Technical Report MA-99-4, U.S. Census Bureau, 2000. <http://eire.census.gov/popest/archives/metro/ma99-04.txt>.
- U.S. Geological Survey. Water resources data, Nevada, water years 1991-98. Water Data Reports NV-91-1 to NV-98-1, U.S. Geological Survey, 1992-99. published annually.
- Stefania Usai. *A New Approach for Long Term Monitoring of Deformations by Differential SAR Interferometry*. PhD thesis, Technische Universiteit Delft, 2001.
- Arnold Verrujit. Elastic storage of aquifers. In Roger J. M. De Wiest, editor, *Flow through porous media*, pages 331–376. Academic Press, New York, 1969.
- M. Watson, Karen, Yehuda Bock, and David T. Sandwell. Satellite interferometric observations of displacements associated with seasonal groundwater in the Los Angeles Basin. *Journal of Geophysical Research*, 107(0):10.1029/2001JB000470, 2002.
- D. B. Wood. Water use and associated effects on ground-water levels, Las Vegas Valley and vicinity, Clark County, Nevada, 1980-95. Nevada Department of Conservation and Natural Resources Inf. Report 35, State of Nevada, Carson City, 2000.
- Howard A. Zebker and R. Goldstein. Topographic mapping from interferometric SAR observations. *Journal of Geophysical Research*, 91:4993–5001, 1986.
- Howard A. Zebker and John Villasenor. Decorrelation in interferometric radar echoes. *IEEE Transactions on Geoscience and Remote Sensing*, 30(5):950–959, September 1992.

Howard A. Zebker, Charles L. Werner, Paul A. Rosen, and Hensley Scott. Accuracy of topographic maps derived from ERS-1 interferometric radar. *IEEE Transactions on Geoscience and Remote Sensing*, 32(4):823–836, July 1994.